Modelling of MOF/Graphene oxide composites and their performances for CO2 capture

Anusha Lalitha

THÈSE POUR OBTENIR LE GRADE DE DOCTEUR DE L'UNIVERSITÉ DE MONTPELLIER

En Chimie et Physico-chimie des Matériaux

École doctorale Sciences Chimiques Balard

Unité de recherche Institut Charles Gerhardt Montpellier (ICGM) – Equipe DAMP

En partenariat international avec [EU Project H2020 Gramofon, CNRS]

MODELLING OF MOF/GRAPHENE OXIDE COMPOSITES AND THEIR PERFORMANCES FOR CO_2 CAPTURE

Présentée par Anusha LALITHA
Le 13 Mars 2020

Sous la direction de Guillaume MAURIN

Devant le jury composé de

Prof. Patrick SENET, Professeur, ICB, Université de Bourgogne	Rapporteur
Prof. Göktug AHUNBAY, Professeur, Istanbul Technical University	Rapporteur
Dr. Anne JULBE, CNRS-Directrice de Recherche, IEM, Université de Montpellier	Examinatrice
Prof. Nathalie STEUNOU, Professeur, ILV, Université Versailles St Quentin en Yvelines	Examinatrice
Dr. Dorothée BERTHOMIEU, CNRS-Directrice de Recherche, IGCM, Université de Montpellier	Examinatrice
Prof. Guillaume MAURIN, Professeur, IGCM, Université de Montpellier	Directeur de thèse

UNIVERSITÉ DE MONTPELLIER

Acknowledgements

First and foremost, I would like to thank my supervisor Prof. Guillaume Maurin for his time, patience and scientific guidance throughout this doctoral journey. He introduced me to a diverse set of problems and provided incredible assistance and environment of academic freedom. Also, I would like to specially thank Prof. S Devautour-Vinot, and Prof. N Ramsahye for all their scientific and non-scientific discussions.

I am grateful to the jury members, first, Prof. Patrick Senet and Prof. Göktug Ahunbay for their time to read this manuscript as reviewers, along with Dr. Anne Julbe, Prof. Nathalie Steunou, Dr. Dorothée Berthomieu for agreeing to be part of my doctoral thesis committee.

I would like to appreciate my EU H2020 GRAMOFON partners for their successful collaborations, especially Prof. Ho bum Park and his group members (from Korea) for their valuable scientific exchanges.

My dissertation would be incomplete without sincerely acknowledging the support from CNRS, the current and former colleagues at DAMP: Satya, Rocio, Wahid, Paulo, Carla, Renjith, Ioannis, Kiran, Pierre, Francoise for their fruitful work and non-work-related discussions. Moreover, all those who contributed directly and indirectly to this dissertation.

Furthermore, I wish to express my gratitude to my former colleague at Mainz, Santosh, for motivating me to be in this field of simulations. It would be unfair not to acknowledge the support of all my friends outside of the professional life who keep inspiring me at every step be it my colleagues at IGCM or Montpellier city or India through fun and distraction from boredom. Notably, special thanks to my best friend, Deepika, who have been there thick and thin in this journey with immense patience and unflinching hand, and Suman for his constant encouragement and endless support both personally and professionally.

Lastly, I want to thank my parents, Mr. Chandrasekhar Gopalan and Mrs. Lalitha Chandrasekhar and my family members, for believing in me and letting me choose my path to success. With their unwavering love and care, I was able to maintain a peaceful and healthy state of mind.

Finally, I would like to dedicate this thesis to my late grandparents who left for their heavenly abode during this journey.

Table of Contents

GENERAL INTRODUCTION

Global warming has gained widespread attention due to its negative impact on our planet. Recently several international organisations and industries have announced collaborative programs, such as SET-Plan and a series of International Climate Change Conferences(Madrid 2019)[1] to cater this problem. Among greenhouse gases, CO_2 contributes 60% to Global warming therefore the main challenge is to selectively capture and store CO_2 at low cost in an energy-efficient way[2]. A central low-carbon technology like Carbon Capture and Storage (CCS) has been established to achieve the reduction of such greenhouse gases through EU's 2050 goal. CCS would enable reduction of 90-95% CO_2 emissions in power generation, fossil fuels transformation and energy-intensive industrial processes, e.g. cement, iron and steel production[3]. However much effort needs to be deployed worldwide in terms of embedding CCS in future policy frameworks[4,5].

Adsorption using adsorbents is currently one of the most promising technologies for CO_2 capture. Hence in October 2016, '**GRAMOFON**[6]", a 3.5-year EU H2020 RIA project was launched with the aim to develop and prototype a new cost-competitive, energy efficient dry separation process for post-combustive CO_2 (generated from flue gases) based on the use of hybrid porous solids like Metal organic frameworks (MOFs) and Graphene Oxide (GO). The objective is also to optimize the CO_2 desorption process by means of Microwave Swing Desorption (MSD)[7] and Joule effect that will surpass the efficiency of the conventional heating procedures[7].

In GRAMOFON, three main active nanostructured materials were considered as shown in Figure 1 for effective post-combustion CO_2 adsorption/desorption processes.

- Shaped MOFs
- Functionalized graphene oxide aerogel (meso- and microporous structures)
- Shaped MOFs/functionalized graphene oxide composites.

These selected systems are expected to show large CO_2 adsorption capacity, high CO_2 selectivity and can be easily regenerated. Indeed, MSD is an effective technology for the desorption of captured CO_2. The energy efficiency and cost saving inherent of this MSD process is expected to be enhanced by the consideration of GO owing to its superior microwave susceptor behavior. In the same way, Joule effect is also responsive to conductive carbonaceous nanomaterials like GO. Joule heating describes the process where the energy of an electric current is converted into heat as it flows through a resistor.

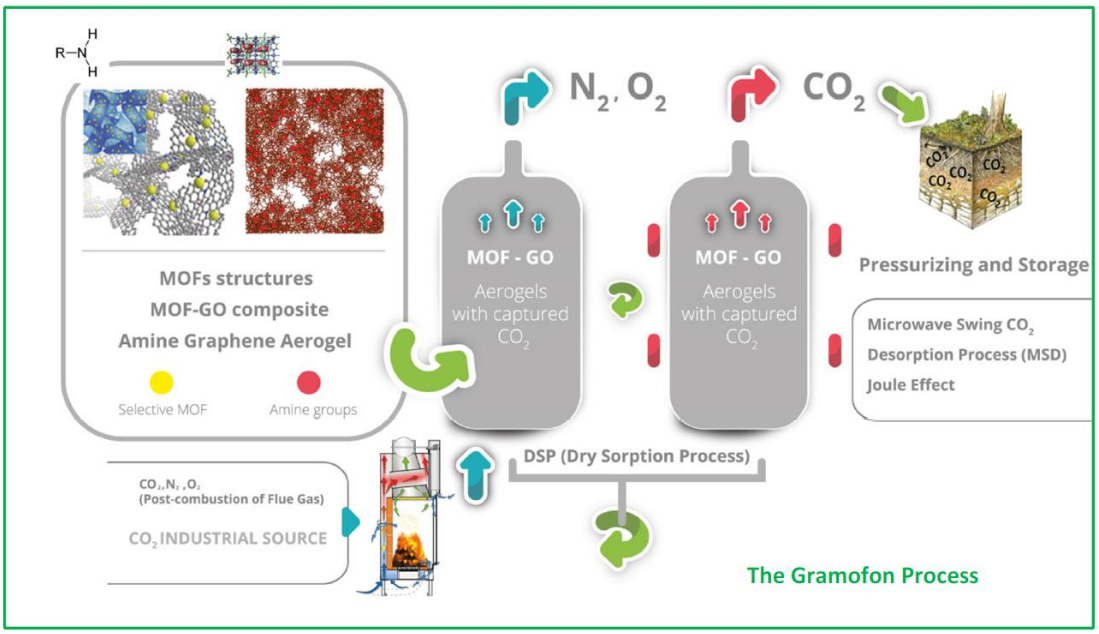

Figure 1 Presentation and Objectives of the EU H2020 RIA GRAMOFON

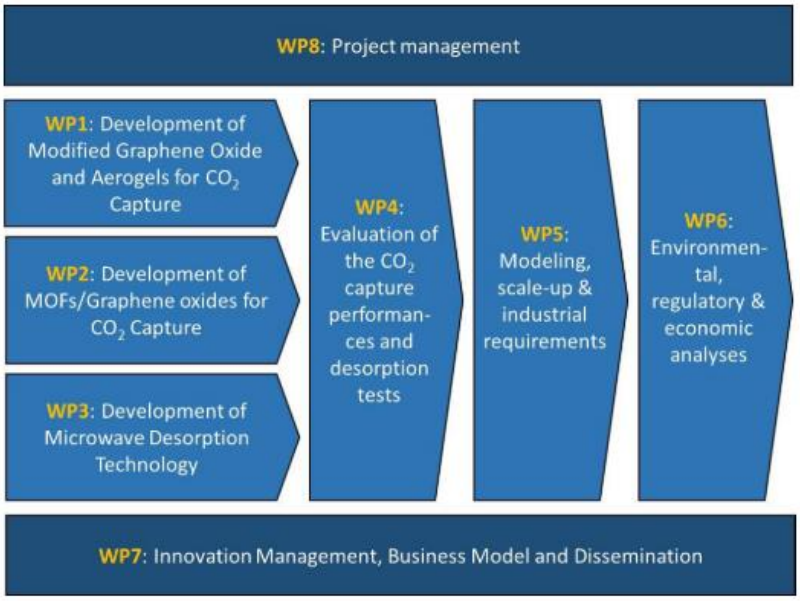

Figure 2 Workflow under EU H2020 RIA GRAMOFON project

To accomplish the ambitious targets of the GRAMOFON, several work packages (WPs) were settled (Figure 2) with key objectives mentioned below:

- Development (shaping and scale-up) of water stable MOFs with high CO_2 /N_2 selectivity
- Optimization of mesoporous morphology of GO aerogel structure

- Design of MOFs/functionalized GO composites specifically targeted for CO_2 capture.
- Economic and ecological assessment of these innovative adsorbents for an optimal cost/benefit ratio
- Improvement of the long-term cycle life of these novel adsorbents
- Development of an Effective desorption process based on improved microwave heating technology
- Exploration of alternative heating routes based on Joule effect

GRAMOFON assembled experts from different field of synthesis, adsorption, characterization and modelling as well as from process design and economics. All have been listed below:

(i) 4 European research organizations (AIMPLAS, **CNRS**, ICT and UMONS) and 1 Korean R&D partner (KRICT), for materials design and MSD process development.
(ii) 3 SMEs + 1 IND partners developing, and providing the required materials (GRAPHENEA, MOF-Tech), as well as, scale-up and validating processes (PDC, E2V).
(iii) 3 Korean Research organizations (Chonnam National University, Graduate School of EEWS, KAIST, Korea University) for twinning activities implementation.

My contribution in GRAMOFON was to provide theoretical predictions on the interfacial interactions between MOF and GO in the resulting composites (WP2) and their CO_2 adsorption and CO_2/N_2 separation performances (WP4). In this context, microscopic descriptions of both the composites and the adsorption phenomena are required. With the recent advancements of computer performances and algorithms, modelling of such large systems and the characterization of their properties have become feasible. To achieve this objective, I developed a computational strategy integrating quantum calculations and force field-based Molecular Dynamics to construct for the first time a series of MOFs-GO and MOFs-amine grafted-GO composites and analyse carefully their interfacial affinity. This systematic computational exploration was conducted in tandem with a series of experimental techniques including diverse spectroscopy, microscopy and mechanical testing. The adsorption and separation performances of these composites were further predicted by using force field-based Monte Carlo simulations.

The manuscript is divided as follows:

Chapter 1 provides an introduction of the individual components i.e. MOFs and GOs as well as of their resulting composites with a special focus on their properties of importance for many applications and in particular for CO_2 capture.

Chapter 2 introduces the basic principles of the molecular simulation techniques used in this work, i.e. the Density Functional Theory as well as the force field Monte Carlo and Molecular Dynamics techniques.

Chapter 3 focuses on the computational methodology I developed to model GO and the resulting MOF/GO composites with an illustration on the ZIF-8/GO system where ZIF-8 is considered as a model MOF for a proof-of-concept.

Chapter 4 delivers a systematic exploration of the MOF/GO composites and the compatibility between the two components by considering a series of different MOFs that includes MIL-69(Al) and MIL-91(Ti).

Chapter 5 explores the amine functionalization of GO on the interface of the ZIF-8/GO composite as well as on their CO_2 adsorption performances.

Finally, **General Conclusions and Perspectives** summarizes the main conclusions of this work and proposes perspectives for further development of this work.

REFERENCES

1. https://unfccc.int/cop25. *UN* (**2019**).
2. Albo, J., Luis, P. & Irabien, A. Carbon dioxide capture from flue gases using a cross-flow membrane contactor and the ionic liquid 1-ethyl-3-methylimidazolium ethylsulfate. *Ind. Eng. Chem. Res. 49*, 11045–11051 (**2010**).
3. Orr, F. M. CO2 capture and storage: Are we ready? *Energy Environ. Sci. 2*, 449–458 (**2009**).
4. https://www.zeroemissionsplatform.eu/policy-and-regulation.html.
5. Leung, D. Y. C., Caramanna, G. & Maroto-Valer, M. M. An overview of current status of carbon dioxide capture and storage technologies. *Renew. Sustain. Energy Rev. 39*, 426–443 (**2014**).
6. Muñoz, G. GRAMOFON : New process for efficient CO2 capture by innovative adsorbents based on modified graphene aerogels and MOF materials. (**2016**).
7. Chronopoulos, T., Fernandez-Diez, Y., Maroto-Valer, M. M., Ocone, R. & Reay, D. A. CO2 desorption via microwave heating for post-combustion carbon capture. *Microporous Mesoporous Mater. 197*, 288–290 (**2014**).

CHAPTER 1 – OVERVIEW ON MOFs, GOs AND MOF/GO COMPOSITES

1.1. Introduction

The family of MOFs encompasses a wide range of porous materials with promising properties for many applications in the fields of gas adsorption[1–4], separation[5–7], catalysis[8–10], biomedicine[5,11], molecular sensing[12] etc. due to their modular nature[11,13,14]. However certain drawbacks such as a limited thermal and mechanical stability have pushed scientists further to associate MOFs with materials like GO acting to address such challenges[15]. MOF/GO composites synergistically enhance their global properties and cater drawbacks of individual components especially in many applications that will be showcased here[16,17]. Indeed, the objective of this chapter is to introduce the general concept of MOFs and GOs. The various MOFs explored in this work have been particularly detailed. The synthesis strategies to fabricate MOFs as well as GOs have been discussed prior to describe their individual properties and applications since the EU H2020 GRAMOFON project I was involved in, assembled expert in the synthesis of the two systems. This is followed by a presentation of the methods currently used to prepare the MOF/GO composites and its favourable attributes leading to its enhanced properties. The chapter finishes with detailed data on the applications of the MOF/GO composites especially catering to CO_2 capture, the focus of EU H2020 GRAMOFON.

1.2. Metal Organic Framework

1.2.1. Introduction to Porous Solids

Porous solids are very important adsorbents intensively used in industries these days. They are majorly classified as activated carbons[18], zeolites[19,20], mesoporous silica[21] and coordination polymers[22]. Control of the pore size/shape is an important design element for any porous solid and hence tuning it from micro to meso-scale range is a must for its development for adsorption application. In particular, zeolites and activated carbons are one of the traditional porous adsorbents[23] for CO_2 capture but they have either low uptake capacities or have inefficient regeneration process[24,25]. Activated carbons show relatively large pore volumes but they lack long-range order in their structures[26]. Also, zeolites are difficult to tune due to rigid bonds and limited chemistry with only a few constituting elements (Si, Al, O, P, extra-framework cations)[27]. Mesoporous silica functionalised with amine groups show drawbacks in terms of regeneration

owing to the chemisorption process for CO_2 capture[28]. On the other hand, MOFs, which is a subclass of coordination polymers, counterbalance these with an unprecedented chemical and structural versatility, high surface area as well as long-range order that make these solids highly attractive for many adsorption/separation applications[29–32]. MOF family is a combination of metal cluster nodes which are linked together through organic moieties[33]. All metals from the periodic table can be incorporated i.e., metal being di-valent (Cu, Zn, Mg, etc.), tri-valent (Al, Cr, Ga, Fe, In, etc.) or even tetra-valent (V, Zr, Ti, Hf, etc)[34]. Similarly, many organic linker moieties like carboxylate, imidazolate, phosphonate, pyrazolate families can be combined[35,36]. The choice of metal and linker dictates not only the structure but also the functionality of the resulting MOFs and hence their resulting properties. The MOF structure can thus be described and organized by subunits called secondary building units (SBU) that impart thermodynamic and mechanical/architectural stability via strong covalent and directional bonds that can lock down the position of metal centers[37]. The inorganic and organic SBUs have distinctive coordination geometries with few examples shown in Figure 1.1 adapted from the paper published by O. Yaghi in Nature 2003[38]. The organic nature of linkers can provide variety of chemical variations and number of linker structures through bi-, tri- or tetra-topic carboxylates shown in Figure 1.1.

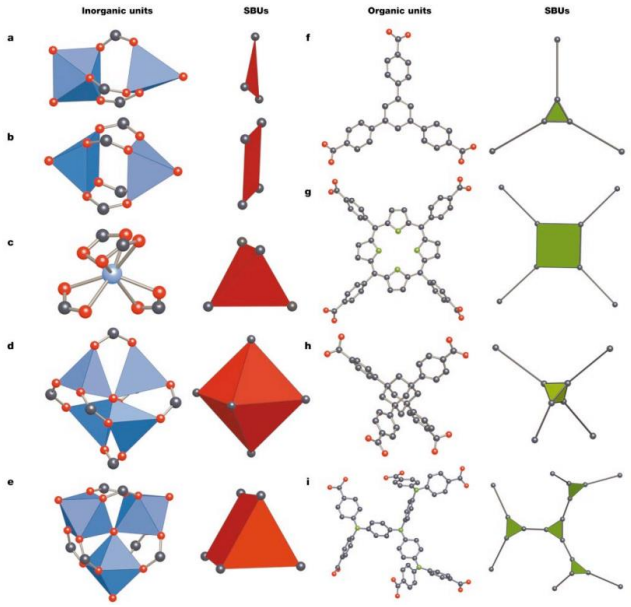

Figure 1.1 (a-e) Inorganic SBUs of carboxylates MOFs with colour scheme O, red; N, green; C, black. Here the metal-oxygen polyhedral are blue and the carboxylate carbon polyhedron atoms SBUs are red (f-i) Organic SBUs the polygons to which linker are shown in green with the last geometry i.e., (i) is a tertiary building unit with four SBUs. Adapted from Ref.[38]

The MOF linkers are supported by aromatic or olefinic backbone and typically anionic carboxylates groups which balance the charge of the cationic metal nodes or additional counter

anions are present in the structure like charged framework zeolite[39,40]. MOF structure can have different type of mixed linkers or metals or different groups in the linker in the same structure[41,42]. Depending on the connectivity and geometry of metal nodes and ligands in space, directional growth of the framework can be achieved[1,43]. Dimensionality refers to the connectivity of the inorganic sub-networks. They are classified into zero dimensional (0D)[44], one dimensional (1D)[45], two dimensional (2D)[46] and three dimensional (3D)[47]. 0D MOFs are finite in all spatial directions and are comprised of one or more voids. While 1D MOF extends in one direction with pores generated by stacked chains generating a channel-like structure. 2D MOFs exhibit infinite layers in two directions with pores generated by pillared windows. In 3D, pores extend to all three spatial dimensions. Here the pores are like cages in 3D as shown in Figure 1.2. According to Yaghi. et. al.[38] , dimensionality was the spatial extension of node-linker-node while according to Férey. et. al.[48], inorganic sub-lattices constitute dimensionality. All in all, the concept of dimensionality is important for the categorization of the MOF complex structures like for instance the MILs (Materials of Institut Lavoisier), some of them being represented in Figure 1.2.

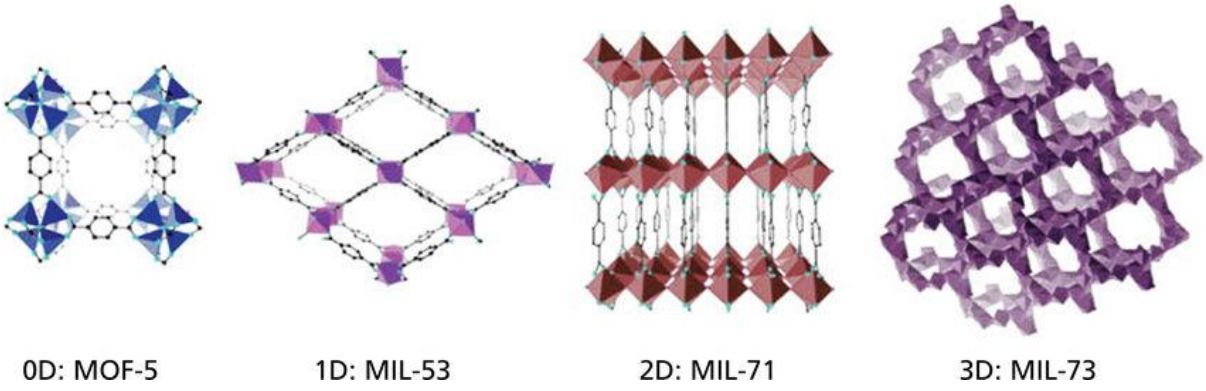

Figure 1.2 0D, 1D, 2D and 3D dimensionality in MOFs. Adapted from Ref.[48]

Depending on the synthesis conditions, thousands of diverse MOF structures can be obtained. Past decades have shown an exponential increase in number of frameworks being synthesized and studied for diverse properties (see Figure 1.3). The Cambridge Structure Database (CSD) assembles more than 800,000 MOF structures[49], and many authors including R. Snurr[50], D. Sholl[51] and B. Smit[52] reported thousands of hypothetical MOF architectures still to be synthesized.

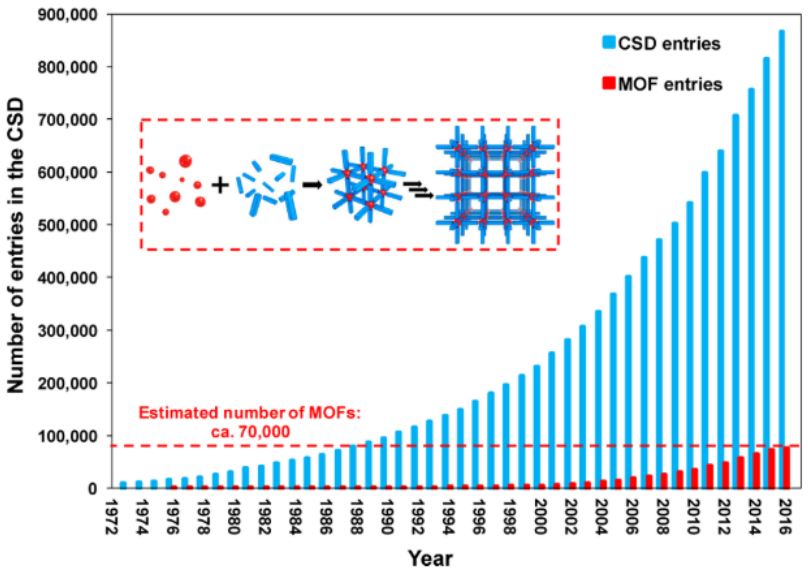

Figure 1.3 Number of MOF research papers published from 1972 to 2016 emphasizing the high-level of research interest. Inset shows the MOF self-assembly. Adapted from Ref.[49]

1.2.2. Family of MOFs explored in this work

As mentioned above, due to the large diversity of MOFs reported so far, it is impossible to make a full list of all MOF structures in this thesis, so I will merely focus on the family of MOFs which have been explored in my work i.e., ZIFs (ZIF-8(Zn)) and MILs (MIL-69(Al) and MIL-91(Ti)).

Zinc (Zn)-MOFs: The most common Zn^{2+}-based MOFs are Zeolitic imidazolate frameworks (ZIFs). ZIFs are composed of transition-metal ions (M) mostly Zn^{2+} (ZIF-1 to -4, -6 to -8, and -10 to -11)[53,54] and also Co^{2+} (ZIF-9 and -12)[53,55,56] bridged by ditopic azolates like imidazolate(Im), methylimidazolate, methyltriazolate or phenylimidazolate anions ligands to form a 3D tetrahedral frameworks in a manner similar to the Si–O bond found in zeolites[53,57]. Azolate derived frameworks represent a rich diversity of structural topologies. Zeolites have silicon as bivalent cations and forms an angle of ~145°(Si-O-Si) while ZIFs form the same with M-Im-M. Because of this resemblance, ZIFs possess the advantages of both structures with relatively high surface areas, unimodal micropores, high crystallinity and relatively high thermal and chemical stabilities[58] useful for application in gas uptake-separation, size- and shape-selective catalysis and they are also stable in liquids (organic solvents, water, and aqueous alkaline solutions)[58,59]. Some of the most representative ZIFs are shown in Figure 1.4.

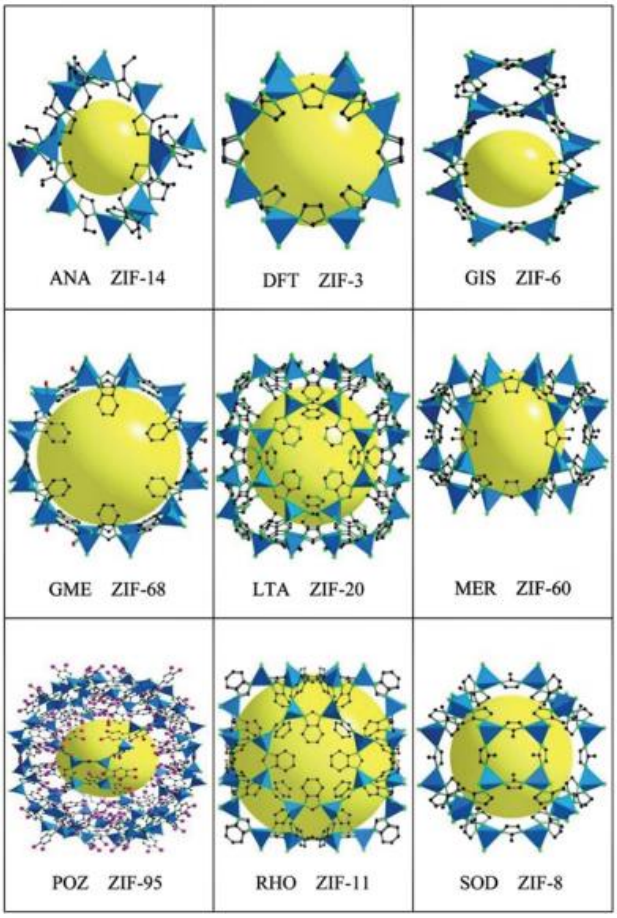

Figure 1.4 Crystal structure of different ZIFs with first three letters showing zeolite structure code. Adapted from Ref.[60]

In this thesis, I have worked with the most prototypical ZIF i.e., ZIF-8 to prepare the composite with GOs. This framework is built from Zn^{2+} ions and uses 2-methyl-imidazolate (MeIm) as the linker. It shows a relatively large micropore of diameter ~11.6 Å highlighted in yellow (Figure 1.5) and this micropore is surrounded by eight six-membered hexagonal apertures associated with a gate size of 3.4 Å[53] which is highly interesting to control the pore entrance for molecules depending on their dimensions. The tetrahedral metal centres are coordinated by nitrogen atoms in the 1,3-positions of the imidazolate ligand (Im = $C_3N_2H_3$) same as found in zeolite structures SOD (sodalite). Figure 1.5 shows the representation of the ZIF-8 {Zn $(MeIm)_2$} with the formation of a cage like unit cell. ZIF-8 shows a significant degree of flexibility through the rearrangement of its organic linker upon adsorption which is often called "pore gating". This flexibility is associated with a significant guest-induced change of the dihedral angle Zn-Zn-Zn-CH_3 also called swing angle (Figure 1.6) of the imidazole linkers[61] which can cause a gate size variation of more than 10% (0.3 Å). This local flexibility is at the origin of several molecular

separations driven by diverse mechanisms including molecular sieving, entropy (conformational) and kinetics consideration[61–63]. Furthermore, the adsorption sites that were identified in ZIF-8 are directly associated with the organic linkers, instead of the triangular faces of the ZnN_4 tetrahedra. This suggests that tuning the nature of the linkers rather than metal types in ZIFs is more important to optimize these materials for gas adsorption/separation[64].

Aluminium (Al)-MOF: Thousands of MOF structures reported are built up from divalent cations (Zn^{2+}, Cu^{2+}, Co^{2+}, Ni^{2+}, Cd^{2+}...) not often of higher valence cations (+III, +IV...)[34,65]. This is mainly due to high chemical reactivity of these highly charged cations and this often leads to uncontrolled crystallization process compared to lower valence metals. Still efforts are being made to develop such high valence MOFs since they usually show high hydrothermal stability which is useful for real applications. Also, these charged cations can enhance the intrinsic properties of the MOFs for various redox, photo-activity and catalysis applications[34]. Al-MOFs shows great potential in clean energy and environment-related applications due to their low formula weight, good oxophilicity and hydrophilicity of Al^{3+} at room temperature[65]. Al-MIL-53 is one of the most intensively studied MOF due to its outstanding thermal stability and structural "breathing" character upon external stimuli[66]. CAU-10[67] (Christian-Albrecht-University), MIL-160[68] and CAU-23[69] are other aluminium MOF with square-shaped micropores showing great promise for water-adsorption based chiller application while MOF-303 is efficient for water production under desert air conditions[70].

In particular, MIL-69(Al), is an analogue of the terephthalate-based MIL-53 (Al), which is built by infinite chains of corner-sharing octahedral $AlO_4(OH)_2$ units combined with 2,6-naphthalenedicarboxylate ligand (2,6-ndc)[71]. Aluminium atoms are coordinated to four carboxylic oxygen and two hydroxyl groups located in trans position. This forms one-dimensional rhombic channels along the c axis with pore size of around ~2.7Å for the non-porous form obtained by hydrothermal synthesis[72]. A representation of the MIL-69(Al) structure is depicted in Figure 1.5. A recent work undertaken by the group evidenced that MIL-69(Al) shows high selectivity for CO_2/N_2 via a molecular sieving but with a lower permeability due to its small pore size. The CO_2 adsorption uptake at 1 bar for MIL-69(Al) is 1.5 mmol/g at 283 K.

Titanium(Ti)-MOFs are the least explored family of MOFs because of its complex Ti^{4+} chemistry in solution[34]. Thanks to its potential photo-responsive properties, more effort has

been made in Ti-MOFs from both direct synthesis and post synthetic metal-exchange processes[73]. Ti-MOF is of great interest for its green production. For the limited number of Ti-MOFs obtained from direct synthesis using simple Ti precursors, including MIL-91[74], MIL-125[17], NTU-9[75], MIL-101[76] COK-69[77], Ti-CAT-5[78], MIL-167[79],MIL-25[80], MIL-177[81], MIL-100[82], Ti-TBP[83], and ZSTUs[84], their inorganic building units range from discrete Ti-O clusters to infinite chains, showing the highly unpredictable feature of Ti reaction. In this regard, only post-synthetic cation exchange between MOFs built with various metal centres of known secondary building units (SBUs) and Ti ions has led to Ti-MOFs in a structure-controlled manner[85–87].

In particular, MIL-91(Ti) is a 3D hybrid structure that consists of trans corner-sharing chains of TiO_6 octahedra linked together in two directions via the diphosphonate groups(N,N'-piperazine-bis-methylene-phosphonate) to form small channels with pore size ~3.5×4.0 $Å^2$ [74]. Metal phosphonates are not so common in MOFs[34]. Two reasons explain this observation: a) non-commercial availability of its linker and b) the need to connect three oxygen atoms of phosphonates (unlike carboxylates with two oxygen) leading to a non-open structure or a pillared non-porous structure like in MIL-25[34]. However, in MIL-91(Ti), the presence of diphosphonate groups leads to a 3D structure with ultra-small pores of about 4 Å that has been shown very promising for CO_2 capture versus molecules of larger size like N_2 and CH_4[88,89]. The MIL-91(Ti) structure is analogous to its Al counterpart MIL-91(Al) with the absence of hydroxyl groups between adjacent metal centres (Ti_{IV}–O–Ti_{IV} *vs.* Al_{III}–OH–Al_{III}). While the guest molecules induce structural rearrangement of MIL-91(Al) leading to a S-shaped CO_2 adsorption isotherm below 1 bar, it was demonstrated that this was not anymore the case for the Ti-version[88].

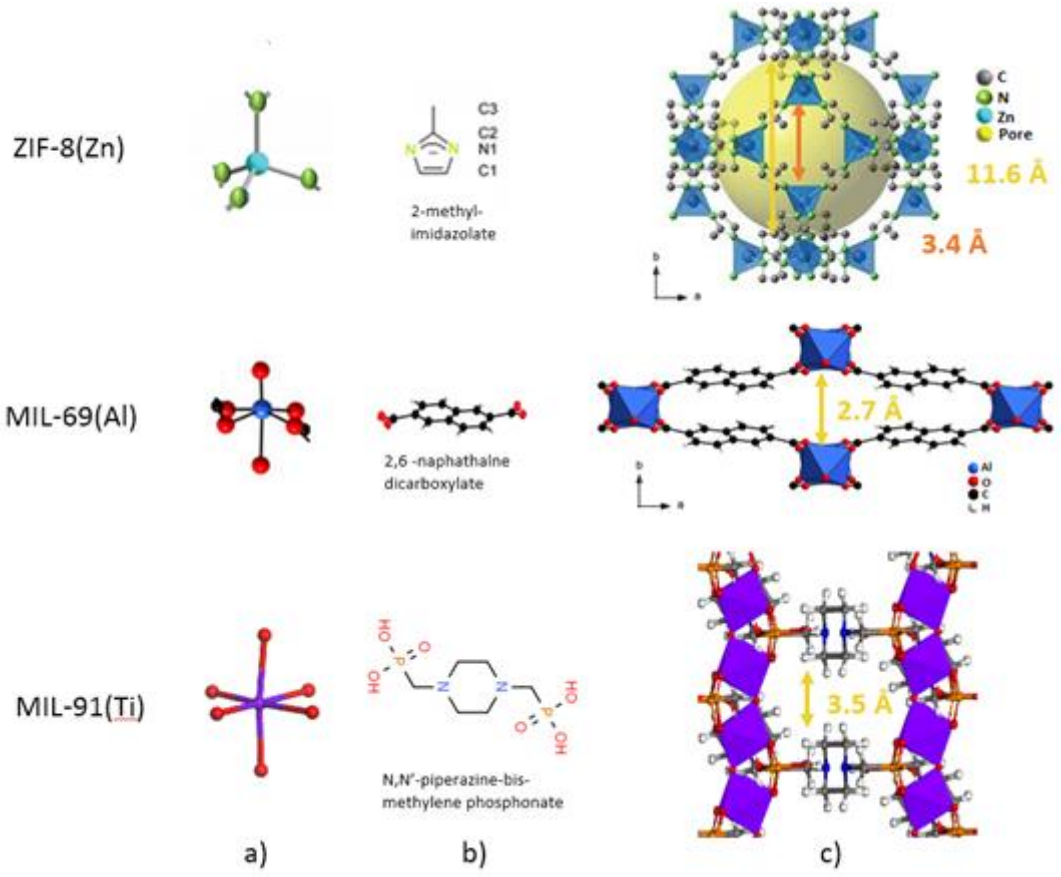

Figure 1.5 Representation of the MOF structures explored in this thesis a) metal centre, b) ligand and c) unit cell of MOFs with pore sizes mentioned in yellow

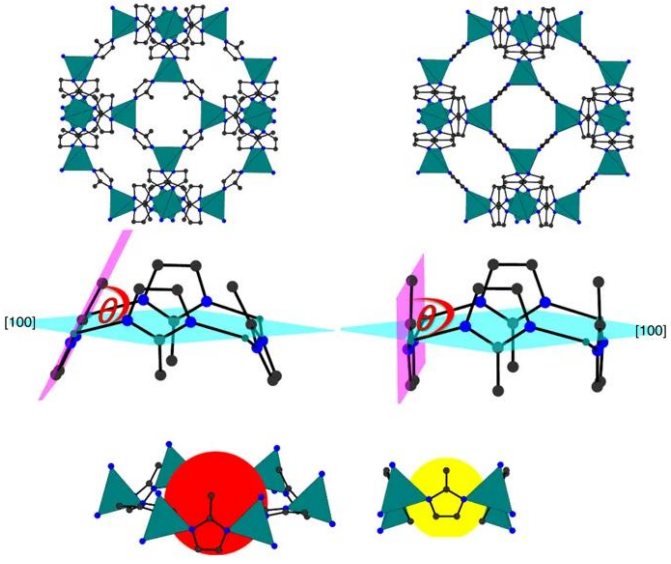

Figure 1.6 Structural difference of ZIF-8 structures from left to right, with mIm linker rotated by 30° angle leading to changes in pore diameter (shown as sphere of red and yellow). Adapted from Ref.[[90]]

1.2.3. Main strategies to prepare MOFs

Conventionally MOFs are synthesized using hydro or solvothermal batch reactions. Here metal salts and organic linker are usually heated above the boiling point of the solvent and retained under auto-genus pressure for up to one week[91]. This synthesis approach shows inherent limitation in terms of reduced crystallinity and non-uniform particle size and morphology[92].

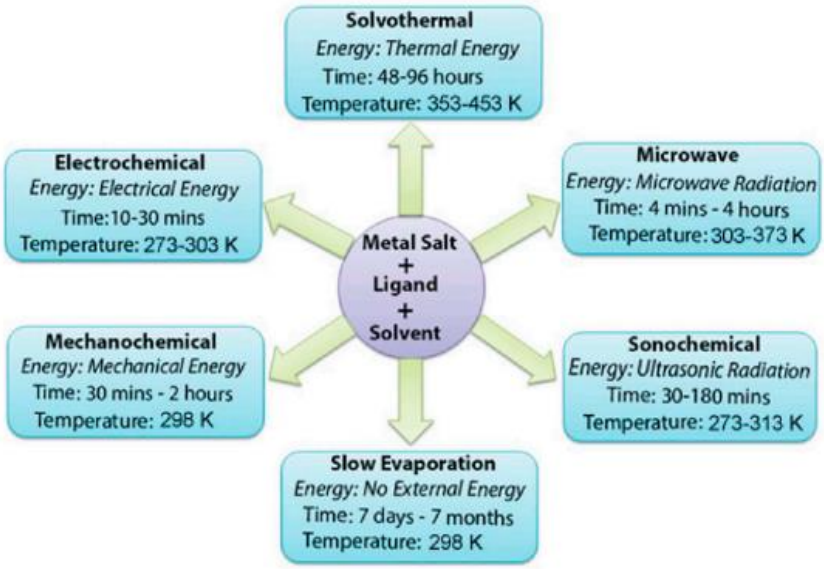

Figure 1.7 Synthesis methods of MOFs preparation. Adapted from Ref.[93]

Past two decades have seen a growth in microwave technology (a superior heating method[92]). Microwave assisted synthesis is based on the interaction of electromagnetic waves with polar solvent molecules and/or ions in a solution. The direct interaction of electromagnetic waves with the solution/reactants results in high heating rates and homogeneous heating with high energy efficiency. It has many advantages like reduced synthesis times (from hours to seconds) which significantly reduced energy consumptions[94]. Also highly controlled properties like particle size, morphology, and phase-selectivity are usually obtained. However, research in the field of microwave synthesis of MOFs is dominated by using commercially available multi-mode microwave systems. And the understanding of the interactions of reactants or MOFs with the electric field is still lacking and needs to be addressed prior envisaging further scale up processes[92]. Now with the advancement of technology various new methods are also emerging in the fields of mechano-, sono-, and electrochemical synthesis (Figure 1.7) and their details can be found elsewhere[91].

1.2.4. Functionalization of MOFs

The main trademark of MOF is its permanent porosity. Modifications of linker geometry, length, ratio, and functional groups can tune the size, shape, and internal surface property of a MOF for a targeted application. Growing number of publications states that for application purposes, it is even more important to tune existing MOFs rather than discovering novel architectures[95,96]. Indeed, the length and degree of functionalization of the organic linkers have been varied enormously. Tuning the nature of the linkers can not only affect the pore dimension of the MOFs by expanding the length of the linkers but also modulate the strength of interactions with the guest molecules by grafting certain functional groups. The functionalization of the MOFs is usually performed in two ways: (i) using linkers containing functional groups in pre-synthesis of MOF[97] or (ii) post-synthetic modification (PSM) of MOFs[98]. In the former case, when using modified linkers, crystallization can be impeded by differing solubility, ligand properties and steric demands and change of synthesis conditions during ligand employment. Also, the linkers are prepared with electron donor or acceptor pending groups such as $-NH_2$, $-OC_3H_7$, $-OC_5H_{11}$, $-C_2H_4$, and $-C_4H_4$ or $-NO_2$, -Br, -F etc. which can be less stable at higher temperature. In the latter approach, which is by far more popular, the already synthesized MOF solid is subjected to further chemical reactions by covalent modification to metal nodes/clusters or to ligands.

Metal nodes are present in MOFs as Coordinatively Unsaturated Sites (CUS) or Open-Metal Sites (OMS). These sites can attach covalently to other materials leading to MOF hybrids exhibiting superior properties. Depending on the nature of metal, these sites can have more or less affinity toward small gas molecules such as CO_2. Typically, the cage-structured Cr-MIL-101 was made by grafting electron-rich ethylene diamine (ED) to the Cr^{3+} nodes as shown in Figure 1.8a. The chelating amines coordinate to the Cr(III) nodes of the MOF while free amines act as Lewis base catalysts in this ED-MOF hybrid[98]. Also, atomic layer deposition (ALD) technique is useful to covalently attach metals and metal clusters to the metal nodes of MOFs exhibiting unique catalytic properties. Typically, Figure 1.8b illustrates successful installation of aluminium metal on the nodes of NU-1000 using ALD[98,99].

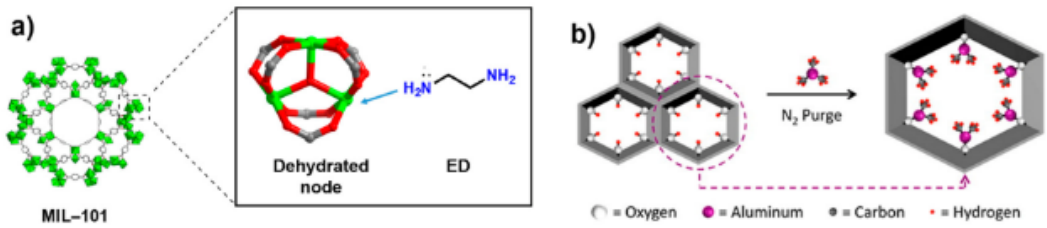

Figure 1.8 a) The preparation of ED-MIL-101, b) AlOx clusters on NU-1000 using ALD. Adapted from Ref.[98]

Ligands modification can be performed by covalently attaching other functions to MOF ligands. Functionalization of organic linkers has been typically performed to alter the chemistry of the pores thus affecting the affinity of guest molecules towards the framework. Like functionalization with polar substituents such as $-NH_2$, $-CO_2H$ or SO_3H results in more favourable binding sites for gas molecules like CO_2 due to lone pair electrons or hydrogen bond like interactions.

1.2.5. MOFs for CO_2 Capture

MOFs can be implemented in all three major carbon capture areas of coal fired power plants i.e., pre-combustion, post-combustion, and oxy-combustion[3]. The easiest retrofit is in the post combustion that is where my focus is on with the EU H2020 GRAMOFON Project. The post combustion flue gas contains different gases CO_2 (3-33%) depending on the process, N_2 more than two third, sulfuric oxides (SOx), nitrogen oxides (NOx), carbon monoxide (CO) and water (H_2O) among others. The operating conditions in the post combustive setup are between 15 to 190 °C in temperature and 1.0-1.25 bar in pressure. Hence, the targeted adsorbents should be optimized for such industrial needs and characteristics.

MOFs are promising for carbon capture because of their large surface areas typically ranging from few hundreds to 7,000 m^2/g, thus exceeding those of traditional porous materials such as zeolites and carbons. Moreover, they are chemically stable which make them even more important candidates for flue gas applications[100]. At high pressures, CO_2 capacities depend on surface areas and pore volumes of the MOFs while at low pressures it depends on the heat of CO_2 adsorption which measures the affinity of the porous solid for this guest molecule[27]. So, tuning the surface areas, pore volume for former cases and tuning unsaturated metal centres or appropriate functional groups grafted to the linkers for later cases can enhance its CO_2

adsorption capacity and/or affinity. Especially ultra-microporous MOFs (with pore aperture size below 5–7 Å) has remarkable selective CO_2 gas adsorption performances. This is due to their defined structural and chemical features like ultra-small pore size/diverse shapes and different degree of flexibility/rigidity in close correlation with the intrinsic properties of the adsorbate molecule like their size, shape and chemical/electronic properties[100]. Complexity of gas separation in MOFs is dependent on the difference of kinetic diameter between two adsorbates[100]. The kinetic diameter difference of about 0.3 Å between CO_2 and N_2 makes ultra-small pore MOFs attractive for separation by molecular sieving in addition to the possible thermodynamics effect driven by the different strength of host/guest interactions.

1.2.5.1. Main strategies to enhance the CO_2 adsorption performances of MOFs

There are many strategies followed to improve the CO_2 adsorption performances of MOFs: a) Pore structure control, b) Incorporation of CUS sites or c) functionalization of the organic linker by groups with high affinity for CO_2 e.g. amine-based functions.

a) Pore structure control: To enhance the affinity for CO_2, it is possible to introduce a modifier or smaller size metal centre which at the end reduces the pore dimension. Typically, the partial replacement of Zr^{4+} ions(~0.159 nm atomic radius) with smaller Ti^{4+} ions(~0.147 nm) in UiO-66 decreases the pore sizes of the architecture leading to an enhancement of the CO_2 adsorption capacity at low pressure by 81% (at 273 K)[101]. Another approach is to devise interpenetrating structures like SIFSIX-Cu-2-I which is discovered by Eddaoudi et al[102] and is an polymorph isostructural to SIFSIX-2-Cu. Structural interpenetration is useful for molecular separation process. Here the strength of the host/guest interactions is thermodynamically-driven via control of the degree of confinement, and also a size exclusion via a strict control of the pore size to selectively adsorb only the smaller molecule of the mixture[103]. The other approach is to select MOFs with an ultra-small pore like the ALFFIVE-1-Ni[104] or MIL-69(Al)[105] showing a pure molecular sieving of CO_2 over molecules of larger sizes.

b) Incorporation of CUS sites: These adsorption sites strongly enhance the affinity of MOFs towards CO_2. These sites are usually saturated by solvent molecules used in the synthesis of the corresponding MOFs. Techniques like solvent exchange, heating or freeze drying, can remove the coordinated solvent molecules to make these CUS sites free to interact with the guest molecules[6,106]. In particular the study reported by Llewellyn et al[107] on MIL-100 containing CUS

sites of chromium or iron evidenced a very high adsorption enthalpy for CO_2 at low coverage associated with a huge uptake at higher pressure owing to the mesoporosity of the material.

c) Functionalization of the organic linkers: Appropriate chemical modification of MOFs can also improve the adsorption capacity and selectivity for CO_2 with respect to other gases. The UIO-66(Zr) MOF with parent bdc linker was substituted with large variety of linkers like 40-BPDC, TPDC and AzoBDC to create other analogues MOFs like UiO-67(Zr), UiO-68(Zr) and Zr-AzoBDC solid with ultra-high porosity promising to enhance the CO_2 adsorption capacity[108]. Adding polar functional groups to the linkers like $-NH_2$, $-NO_2$, $-(OH)_2$, $-SO_3H$ and $-CO_2H$ allow strong interactions between polar groups and CO_2 leading to enhancement of the CO_2 affinity and separation ability[109]. Amine functionalized MOF especially the case of MIL-53(Al)-NH_2 synthesized by Gascon et al[110] has shown to be ideal for selective adsorption of CO_2. This is due to delicate interplay of amine functionalization and controlled pore size upon breathing.

1.2.5.2. Selection of MOFs as CO_2 adsorbents within GRAMOFON

The basic requirements to select MOFs for CO_2 capture under the framework of EU H2020 GRAMOFON were: (i) stability in the presence of water, (ii) a high CO_2 /N_2 selectivity, (iii) a large CO_2 uptake at 0.15 bar (called also working capacity) and (iv) a moderate CO_2 adsorption enthalpy which directly determines the energy of regeneration process, higher the heat of adsorption more the energy needed for regeneration.

Following this list of criteria, the project identified a series of MOFs for CO_2 capture offering the best compromise between the four items from (i) to (iv) mentioned above. The cost of the materials as well as their environmental impacts were also considered leading to the list of selected MOFs summarized in Table 1.1. From this list, I focused my attention on the 3 MOFs mentioned above which were successfully incorporated into GO matrix experimentally.

Table 1.1 : Performances of best MOF materials

MOF	CO_2/N_2 Selectivity at 0.15 bar	Maximum capacity at 0.1 bar and 298-323K (mol/kg)	Heat of adsorption (kJ/mol)	Ref.
MIL-53(Al)	>1000	~0.38-0.5 mol/kg (303 K) ~ 0.1 (314 K)	26.4	111,112
MIL-3(Al)_NH_2	>1000	~0.7 (298 K)	38.4	113
MIL-96(Al)	High (30-50)	~ 1.2 (303 K)	38	114
SIFSIX family – CuSiF6-Pyrazine ZnSiF6-Pyrazine	Exceptional (Higher for Cu)	(Cu): 2.45 (298 K); 2.4 (318 K) (Zn): 2.38 (298 K); 2.25 (318 K)	(Cu): 54 (Zn): 45	102,115
MIL-91(Ti)	High (100)	1.25 (303K)	47.1	88
MIL-69(Al)	>5000	0.2 (303 K)	37.5	unpublished
ZIF-8(Zn)	9.5	0.09(298 K)	25	116

1.3. Graphene Oxide (GO)

1.3.1. Structural/chemical features of GO and carbon materials

GO was first reported in 1840 and 1859 by Schafhaeutl[117] and Brodie[118] respectively. There are many synthesis methods being developed over the years, however the most standard approach is based on the method proposed by Hummers and Offeman[119]. This consists of oxidizing graphite to graphite oxide in a mixture solution made of concentrated sulfuric acid, sodium nitrate and potassium permanganate. This method has been further refined and labelled as modified Hummers method while the basic strategy remains the same[120,121]. GO is insulating, but disordered, like conducting crystalline graphene. The structure of GO is still debatable. Early investigations have proposed structural models of GO with a regular lattice composed of discrete repeat units[122], but the widely accepted GO model was proposed by Lerf and Klinowski[123] based on an in-depth nuclear magnetic resonance (NMR) study. The model incorporates carbon grid of aromatic or aliphatic six membered rings with sp^2/sp^3 regions having basal hydroxyl and epoxy functional groups, as well as carbonyl groups present as carboxylic acids along the sheet edge as shown in Figure 1.9.

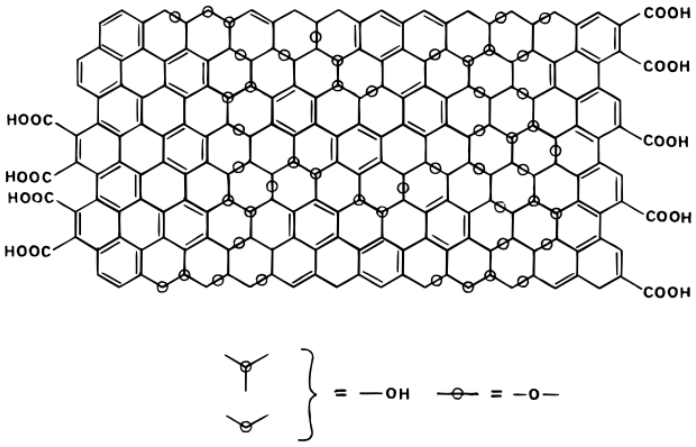

Figure 1.9 Lerf–Klinowski structural model of GO. Adapted from Ref.[123]

Before going further, a clear understanding of the carbon nanostructures like graphene, graphite, graphene oxide, graphite oxide etc. is necessary as depicted schematically in Figure 1.10. A single layer carbon grid arranged in 2D hexagonal lattice (crystalline) due to sp^2 hybridized carbon is termed as **Graphene**[124](Figure 1.10a)**.** Graphene has strong σ bonds (in plane) but weak π bonds (out of plane). The former assigns to graphene high mechanical strength and flexibility while the later a thermal carrying, electrical charge, and transparency[125]. **Graphite** is a layered structure of graphene stacked together by van der Waals forces of attraction. Graphite is widely available, inexpensive material can be obtained from synthetic or natural sources[126](Figure 1.10b). **Graphite oxide** is synthesized by oxidation of natural graphite powders through various oxidants in acidic media[124](Figure 1.10b). It can be also prepared through different chemical routes like Schafhaeutl[117] and Brodie[118] etc. Its final structure is very debatable and depends on the chemical oxidation process used. As reported in various literature, it consists of several groups like epoxy, hydroxyl, carboxyl and carbonyl[122,127,128]. It is important to note that graphite oxide is not identical to GO, it is similar in chemistry but very different structurally. **Graphene oxide** (mono- or few-layered stacks) is obtained from oxidation of graphite and subsequent exfoliation of Graphite oxide (as shown in Figure 1.10b). The C/O and C/H ratios of graphene oxide strongly depend on the starting graphite material and on the oxidation process used during synthesis i.e., the chemical composition and relative amount of the oxidizing agent, the temperature and duration of the process, the presence and character of the activation factor (e.g. $SOCl_2$ or a carbodiimide which activates the edges carboxylic acid group). It is adorned with covalently bound oxygen-containing groups. The sheet of graphene oxide has both partly arranged trigonal bonded sp^2 carbon atoms (perfectly flat) like graphene and tetrahedrally

bonded sp^3 carbon atoms, which are displaced slightly above or below the graphene plane (atomically rough)[129]. Studies using high-resolution annular dark field in scanning transmission electron microscope (ADF-STEM), scanning tunnelling microscopy (STM) showed that the oxidation degree of GO monolayer fluctuates at the nanometre-scale with random size of sp^2 and sp^3 clusters and the highly defective regions due to oxygen functional groups displacing the carbon[130,131]. Although the structure of GO has only three chemical elements (C, H and O), many oxygen containing functional groups can be attached to the nanosheet thus modulating the properties of GOs for various applications. The chemical composition of GO and in particular the nature of the chemical groups can be determined by various techniques like X-ray photoemission spectroscopy (XPS), nuclear magnetic resonance (NMR) spectroscopy, Fourier transform infrared (FT-IR) spectroscopy, electrochemical methods etc. XPS is used to assess the functional groups present in samples. Analysis of the C1s spectra obtained from the sample allows the identification of hydroxyl, epoxide, and carboxyl groups attached to the carbon backbone. NMR measurements are used to confirm the elemental analysis in particular the C/O and H/O ratios. Functional groups can also be identified by Raman spectra. Finally, XRD allows the determination of the interlayer distances of GOs. As already mentioned above, while many techniques are currently employed to characterize GO, its structure has been the subject of debate for several years. The widely adopted Lerf–Klinowski model is also not unanimously accepted, probably due to i) variation in the preparation routes of GO (Staudenmaier[132], Brodie[118], Hofmann[133], Hummers[119], and Tour method[134]), ii) the use of diverse oxidation conditions, iii) the use of many different graphite material [135] and iv) the relative low thermal stability and the resulting decomposition above 60–80°C[136]. Due to these reasons, characterizing the structure of GO and quantifying the content of its various functional groups are very challenging. Indeed, the use of harsh oxidizing conditions and work up treatments can lead to oxidize the epoxides, create defects, or other functionality on the carbon surface, and can also result in the formation of holes in the plane, smaller flake sizes, and highly oxidized species (e.g., $-CO_2H$) on the edge of the sheets[135]. Thus, GO varies in compositions/stoichiometry and should be appropriately characterized using multiple experimental techniques.

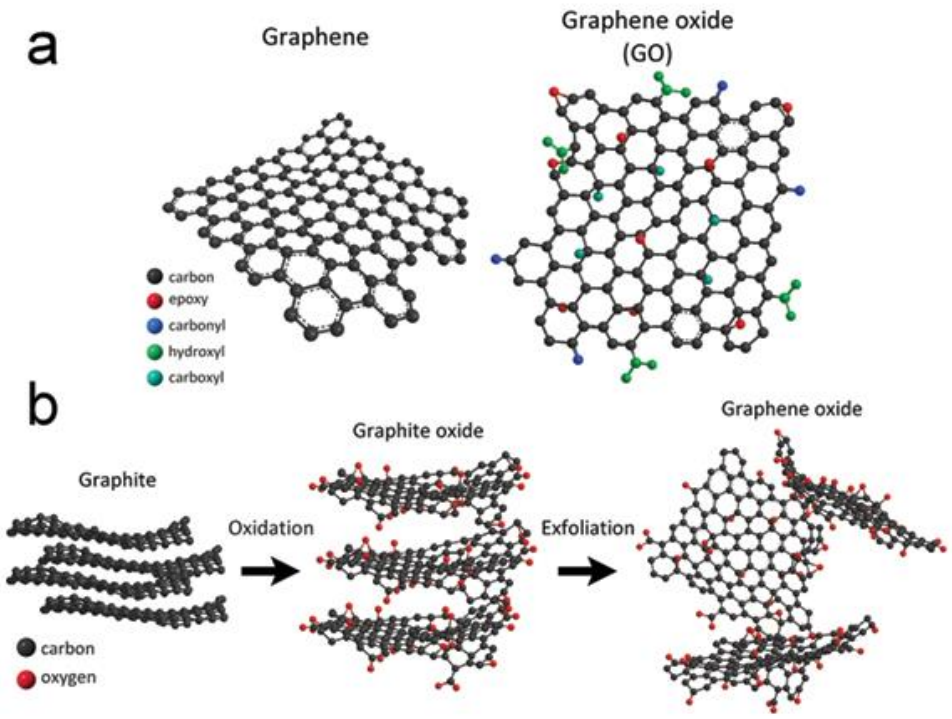

Figure 1.10 Schematic showing a) chemical structures of graphene and graphene oxide b) preparation method from graphite to graphene oxide. Adapted from Ref.[125]

Molecular modelling can provide unique insights into the mechanisms involved in the reactivity, stability and chemical modification of GO. However, modelling of GO is quite challenging since its structure and chemical composition are far to be universal in the literature. There are some structural models available in the literature like Rosas et. al[137], Shih et. al[138]etc. While Rosas et al.[137] studied the finite structure at DFT level with few functional groups, i.e. three hydroxyl and one epoxide groups on the basal plane and one carboxyl group at the edge), they did not take into account the real experimental atomic percentages and C/O ratios. Similarly, Shih et. al[138] studied the aggregation and surface activity of GO structure in aqueous solutions using molecular dynamics. They have used uncharged Lennard-Jones (LJ) spheres for carbon atoms with random ratios of functional groups. The GO used here were not sufficiently oxidized which nonetheless are important to build the right structural representation of the GO and further study its various interactions with other materials or solvents. Similarly, so far, there is no atomistic model reported for the amine-functionalized GO which has been catered in my thesis.

1.3.2. Properties of GO

i. **Reduction**: Due to their disrupted sp^2 bonding networks, GO are electrically insulating materials. Their electrical properties can be tuned using reduction processes. The product of this reaction is reduced graphene oxide (r-GO), chemically reduced graphene oxide (CReGO), and graphene. These reduction methods can be achieved through chemical, thermal, or electrochemical reduction pathways. All these methods lead to varying degrees of electrical, thermal and mechanical properties, as well surface morphology.

ii. **Chemical functionalization**: To incorporate different functionalities targeted for specific applications, GOs can be modified by grafting a range of functional groups by means of various chemical reactions that lead to either covalent or non-covalent attachments. Carboxylic acid groups at their edges, epoxy and hydroxyl groups on the basal planes or defects acts as chemically reactive oxygen species to functionalize one site or others. Sometimes reactions with multiple functionalities are also possible. Epoxy groups are in part expected to be sterically hindered and nucleophiles may more likely react with carboxylic acids[139]. Here below is the list of potential functionalization of the different species present in GOs.

    a. At the carboxylic group: Activation of carboxylic groups by using $SOCl_2$ for instance and later addition of nucleophilic species, such as amines or hydroxyls, produce covalently attached functional groups via the formation of amides or esters. XPS, FT-IR, and NMR spectroscopies are commonly used for the characterization of these systems. Using covalent functionalization, introduction of amines through substitution reaction is the most common method and this has been investigated for various applications in optoelectronics[140], biodevices[141], drug-delivery vehicles[142], and polymer composites[143]. Porphyrin-functionalized primary amines have been attached to GO in order to enhance their optical properties[144,145]. Aliphatic diamine to EDC-activated graphene oxide produced amine-functionalization at the carboxylic acid groups. Using an atom transfers radical polymerization (ATRP) initiator, α-bromoisobutyryl-bromide was covalently attached to carboxylic groups, as well as the hydroxyl groups on the basal plane[146,147]. Carboxyl groups can also be converted to reactive groups via ester linkages[143].

b. At the epoxy bridge: The chemically reactive epoxy groups can be easily modified through ring-opening reactions under various conditions. The mechanism usually involves a nucleophilic attack at the alpha-carbon by the amine (aliphatic, aromatic, and polymeric variants). Here the amine is heated in the presence of exfoliated GO in a polar solvent and purification/isolation involves either filtration or centrifugation. Like covalent attachment of 3-amino-propyltriethoxysilane (APTS) through nucleophilic displacement reaction of epoxy and APTS amine group[148].

c. At the hydroxyl group: This group acts as a nucleophile species and can condense with an exogenous carboxylic acid. It was shown that the hydroxyl groups of GO can be easily capped with a chain transfer agent (CTA). Like Poly(N-vinyl-carbazole) is grafted on the CTA-functionalized GO surface (CTA used is S-1-dodecyl-S'trithiocarbonate) in a controlled manner to yield electrical switching and memory effects when fabricated into an optoelectronic device[149].

d. Non-covalent: GO can show non-covalent binding on the sp^2 grids via π-π stacking, cation-π or van der Waals interactions. Yang et. al. prepared hybrid material of GO and doxorubicin hydrochloride (DXR) via non-covalent interactions. The link between the two species was made through π-π stacking, as well as hydrophobic interactions between the quinone functionality of DXR and sp^2 networks of GO[150].

1.3.3. Application of GO

GOs can be utilized for various applications due to their large surface area, mechanical stability, tuneable electrical and optical properties. By varying the concentrations of surface hydroxyl, epoxy and carboxylic functional groups, it can used for tuning band gap[151,152] for catalysis in photocatalytic water splitting[153], reduction of harmful gases[154] or heavy metal ions[155], and degradation of organic compounds[156]. Insulating nature of GO can be altered through appropriate reductions. Reduced GO shows higher electrical conductivity while keeping the inherent merits of GO and thus can be used as electrode materials in lithium batteries[157] and supercapacitors[158]. The coordination of its functional groups to other active materials, such as carbon materials, metals, metal oxides, conducting polymers and organic species, GO materials

allows to improve the performance of this system in the energy storage devices[159]. GO-based composites can be used for purifying water as it shows strong affinity for the adsorption of heavy metal ion[160] and organic containments[156] and converts the toxic metal ions[161] and organic containments[162] into the harmless products being a chemical- and photo- catalysts. GO offers enough space and active sites (due to abundant functional groups) to allow the adsorption of many gas molecules and various species in solutions. GOs are very useful for hydrogen storage by modulating the interlayer distance[163] and pore size[164]. GO with metals exhibits sensor properties for gas capture and detection of harmful gases like CO_2, CO, NO_2, and NH_3. Few-layer GO sheets show superior adsorption behaviour in the presence of water[165] as water can reduce the CO_2 migration by repulsive interaction between CO_2 and the oxygenated groups attached on the GO sheets[166]. Dispersion of 20%GO into chitosan matrix can drastically affect the aerogels morphological characteristics, enhancing the BET area and leading to higher CO_2 adsorption performance[167]. Similarly, in Cu-MOFs, GO can provide more active sites for CO_2 adsorption thus leading to high CO_2 adsorption capacity[168]. GOs can also act as catalysts for the conversion of CO_2 into propylene oxide[169].

The properties of GOs have also been explored for several applications by DFT and force field-based MC and MD simulations in the past. Vovusha et al[170] performed DFT calculations to study the interaction of nucleobases and several amino acids with GOs and its atomic stability for targeted drug delivery and biosensor applications. Further MD simulations were achieved by Shih et al.[138] to study pH dependent aggregation of GO and protonation of its functional groups providing fundamental insights into GO preparation for electronic, optical, and biological applications. Unusual mechanical properties of GOs were also predicted by MD simulations[171]. Their optical and electronic properties were explored by Jiang et. al. through DFT studies[172]. Simulated optical absorption spectra on GO with 50% coverage and OH:O (1:1) ratio revealed an enhancement of the solar light efficiency[173]. DFT calculations demonstrated chemisorption through strong interaction of harmful gases like NOx (x=1, 2, 3) by hydroxyl and carbonyl functional groups and nearby carbon atoms of the GO[174,175]. In terms of capture of greenhouse gases, MD simulations demonstrated that CO_2 can be efficiently intercalated into the GO while its functional groups can enhance the CO_2 affinity[176].

1.4. MOF/GO composites

MOFs are one of the state-of-the-art crystalline materials with various applications as discussed above. Nevertheless, there are some points which may hinder their full potential for diverse applications. Indeed, MOFs can be unstable against particular chemical environment and relatively high temperature while they are electrically non-conductive[96,177]. Moreover, some MOFs show poor mechanical resilience and this scenario is not optimal for subsequent processability[178,179]. In addition, MOFs with small pore sizes do not allow an efficient diffusion process once the molecules are captured in their pores[180]. In order to circumvent the above-mentioned limitations, the elaboration of MOF-based composites has been shown very promising[181]. This approach is relatively easy to handle and could add the advantageous properties of both materials while diminishing the disadvantages of the individual components. Various composites of MOF have been successfully constructed like MOF–metal nanoparticles[182], MOF–silica[183], MOF–organic polymers[1], MOF– polyoxometalates[184] and MOF–carbon[185]. Carbon-based composites can be of different types with the consideration of several allotropes (active carbon, nanotubes, fullerene, graphite etc.), existing forms (powder, fibre, monolith etc.), and multiple micro-textures with different dimensionalities and degrees of graphitization[186,187]. Hence, MOF have been combined mostly with PC (porous carbon), CNTs (carbon nanotubes), G/GO (graphite or graphene oxide), CF (carbon fibre), CQDs (carbon quantum dots) and fullerene. Here, I will focus on mostly MOF/GO composites that was the topic of my research within the frame of EU H2020 GRAMOFON. Integrating both components would amalgamate research interests of both their properties leading to good stabilities, electrical conductivities, templating effects in the resulting composites.

1.4.1. Main strategies to prepare MOF/GO composites

There are many ways of preparing MOF/GO composites using *in situ* (one-pot and stepwise synthesis) or *ex situ* approaches as well as other specific methods that are briefly discussed below.

1.4.1.1. One pot synthesis

In one pot synthesis, all reactants are added, and they chemically react subsequently in the same reactor. This avoids long separation and purification processes and it usually allows the synthesis of all kind of carbon/MOF composites (shown in Figure 1.11). Typically, MOF-5, MIL-100(Fe) and HKUST-1 with graphitic compounds were prepared using this approach[188]. In *in situ* process, the functional groups as well as the defects of the carbon components, can serve as nucleation sites for MOF growth.

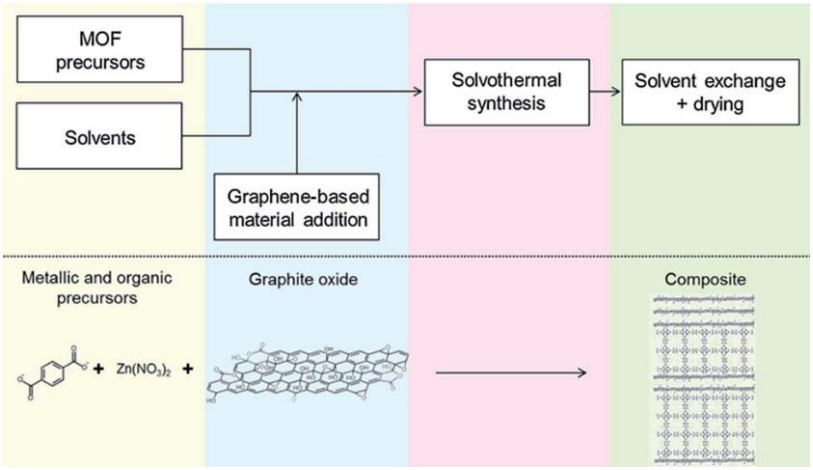

Figure 1.11 Schematic representation of one pot synthesis of MOFs/ graphene-based composites. Adapted from Ref.[188]

1.4.1.2. Stepwise synthesis

There are many types of stepwise synthesis approach (seeded, metal oxides/carbon-based materials or layered).

- *Seeded growth* is a type of secondary growth method widely followed to create MOF/carbon composites. This approach is quite efficient to produce robust, continuous and defect-free membranes. The MOF is pre-synthesized and deposited on seed supports as shown in Figure 1.12. Here the seed support has graphite which can act as a binding agent to stabilize and anchor the MOF seeds thus promoting MOF crystallization. Typically, this method was used to prepare compact ZIF-8 layer using graphite support by Kong et al[189]. Seeded layer is of vital importance and can be generated by rubbing, dip coating, wiping, spin coating and heating[190].

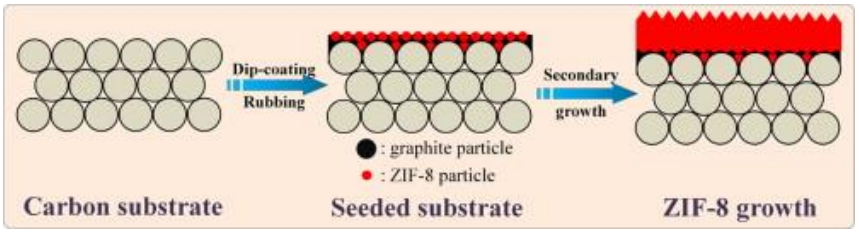

Figure 1.12 Schematic of seeded growth of ZIF-8 on graphite particles. Adapted from Ref. [189]

- *Transfer from metal oxides/carbon-based materials*: In this method, the metal oxide like ZnO act as precursors on the entangled Multi Wall Carbon Nanotube (MWCNT) or other carbon materials to synthesize MOF/carbon composites like ZIF-8/MWCNT. ZIF-8 is crystallized *in-situ* and nucleated around the MWCNT as shown in Figure 1.13[191]. In this method the metal oxide are incorporated at the carbon surface via the use of methods like ALD and ligands are further connected to the adsorbed nanoparticles to grow MOFs.

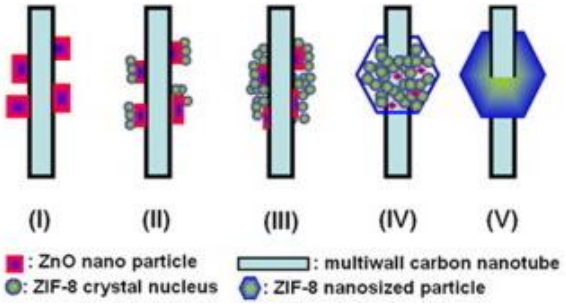

Figure 1.13 Scheme for composite preparation by metal oxide. Adapted from Ref.[191]

- *Layer by layer* method involves the use of Atomic Layer Deposition (ALD) for the MOF nucleation on fibre mats[192]. By this method, GO suspension was for instance deposited on a semi-continuous ZIF-8 layer through capillary forces and covalent bonds to create a bi-continuous ZIF-8/GO membrane as depicted in Figure 1.14[193]. Here the MOF precursor reactions are facilitated on a polydopamine (PDA)-modified alumina disk.

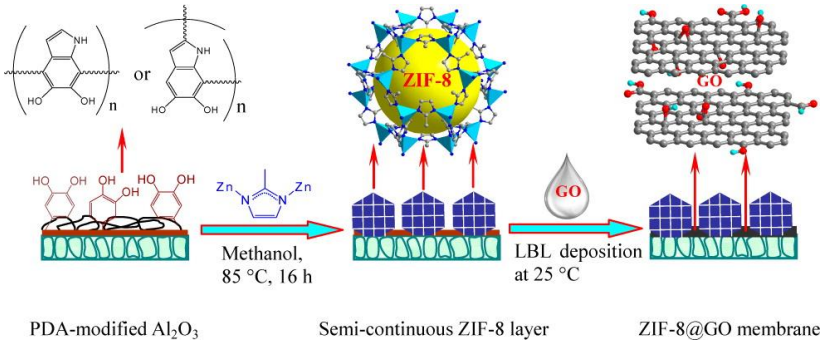

Figure 1.14 Layer by layer growth of ZIF-8/GO membrane. Adapted from Ref.[193]

1.4.1.3. Ex-situ methods

Ex-situ methods are mostly used when the methods mentioned above are not able to achieve a membrane of good quality. Some of the alternative methods employed are depicted below:

- *Direct mixing method* is mostly used in the field of super-capacitors electrodes. This approach was first explored by Yaghi's group who incorporated MOF nanocrystals in a graphene dispersion and then coated it on Ti substrate[194]. A supercapacitor electrode made of 10 wt.% rGO/HKUST-1 composite incorporating S-atom was also fabricated by liquid phase infiltration as shown in Figure 1.15[195].

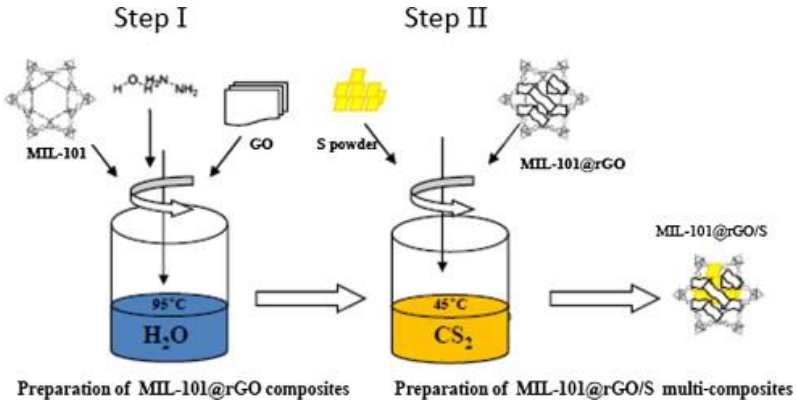

Figure 1.15 Direct mixing method used to prepare MIL-101(Cr)@rGO composite and MIL-101(Cr)@rGO/S multi-composites. Adapted from Ref.[195]

Other MOF/GO composites were prepared by ball milling, compression etc[196]. Such a mechanical treatment affects the textural (surface area and pore volume) and structural

properties of the resulting composite[197]. As an illustration IRMOF-1 and a 5% Pt/AC catalyst were crushed together and then melted sucrose was used to fill the space between the incorporated Pt particles and MOF leading to a carbon bridge[196](Figure 1.16a). This carbon bridge allows to improve the contact between the components of the composite.

- *Self-assembly method* is driven by electrostatic interactions, π-π stacking, hydrogen bonding and other forces acting between the two components. Typically, NH_2-mediated UiO-66/rGO was fabricated by electrostatic self-assembly process employing UiO-66(NH_2) with a positively charged surface and GO with a negatively charged surface[198]. In a similar way, ZIF-67/GO nanocomposites were prepared (Figure 1.16b)[199].

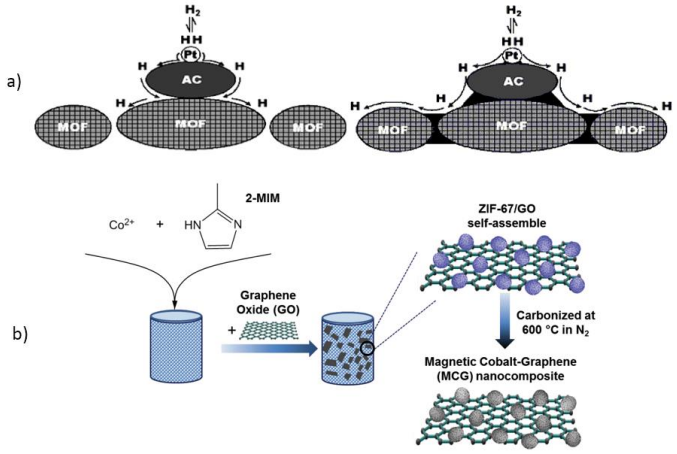

Figure 1.16 a) Schematic of the IRMOF-1 and 5% Pt/AC catalyst without and with a carbon bridge. Adapted from Ref.[196] and b) formation of magnetic cobalt–graphene (MCG) nanocomposites using self-assembly method. Adapted from Ref. [199]

1.4.1.4. Other preparation methods

- *Pickering emulsion* was proposed by Ramsden[200,201]. In this method, GOs act as productive stabilizers for producing the Pickering emulsion that was used to fabricate a series of different composites such as HKUST-1/GO reported in Figure 1.17[202]. This method is a promising strategy for designing and fabricating nanocomposites.

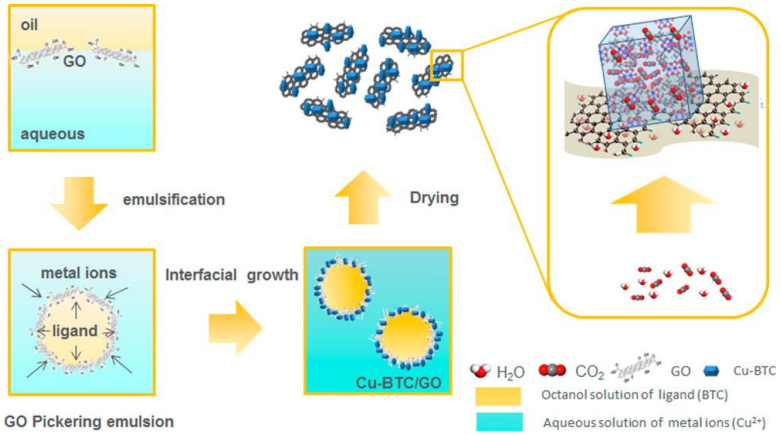

Figure 1.17 Schematic of HKUST-1/GO composites via the Pickering emulsion-induced growth. Adapted from Ref.[202]

1.4.2. Properties of MOF/GO composites

The most common functionalities of the MOF/GO composites arising from the incorporation of GO into MOFs are listed below.

1.4.2.1. Enhanced properties

- Chemical stability

  As discussed earlier, carbon-based materials inherently possess excellent stabilities towards water/vapor, high temperature, mechanical strength etc. When combined with MOFs, carbon materials break off the contacts between MOFs and water molecules. Usually GOs are relatively hydrophilic in nature due to its polar functional groups, but it still contains distorted graphene-like layers with a relatively high level of aromaticity which makes it more hydrophobic than pure MOFs and possess the ability to expulse water[203]. Typically MOF-5/amine-GO[204] and HKUST-1/GO[205] composites demonstrated good stability under humid conditions. In some other cases where pickering emulsion-induced interfacial growth method was used to develop HKUST-1/GO composite[202], the resulting highly dispersed GO sheets surrounding the surface of the composites hamper the entrance of water molecules onto the inner core which remarkably improved the surface water-resistance and hydrothermal stability of the composites.

- Thermal stability and electron-beam resistance

  Carbon based materials show good thermal stability and conductivity[206]. When MOFs are incorporated into GO, their thermal stability are considerably improved. Typically, a core–shell structure of USTA-16/GO film showed that the composite has much higher decomposition and collapse temperatures than their pristine components[207]. The composites also have enhanced electron beam resistance than pure MOFs since carbonaceous materials effectively dissipate electrostatic charges and thus protect the structure of the whole composite[207].

- Electrical conductivity

  Pure MOFs has insulating organic ligands and metal ions with overlapping p and d orbitals which makes them usually poor electrical conductors[208]. Ni-doped MOF-5/ reduced GO[209] and HKUST-1/graphene-like composites[210] showed enhanced electrical conductivity since GO can chemically bind them or even act as a building block during their assembly, which will generate new pathways in the composite for conducting electrical charges, thus leading to an increase of the electrical conductivity.

1.4.2.2. Templating effect

- Crystal morphology change

  Introduction of carbon-based material influences the morphology of the composite. Bandosz's group developed MOF-5/GO composite where they presented a sandwich-like structure with alternate MOF layers and GO sheets under appropriate GO loadings[211]. Such an arrangement is due to the formation of chemical bonds between the metal centres of MOFs and the epoxy groups of GO. At high GO loading, a wormlike structure was observed resulting from the interactions between ZnO_4 tetrahedra and carboxylic groups mainly at the edges of GO [211]. The La MOF reported by Wang et al contains La^{3+} ions that are nine coordinated forming a tricapped trigonal prismatic geometry[212]. Its structure is like a spindly rectangular rod (parallel-ribbon structure) extending along one axis and stacking along another axis via phenyl groups of organic linkers by strong π-π interactions. When loaded with GO, the morphology of this

MOF changes from spindly rectangular rods to irregular thick blocks as illustrated in Figure 1.18 [212,213].

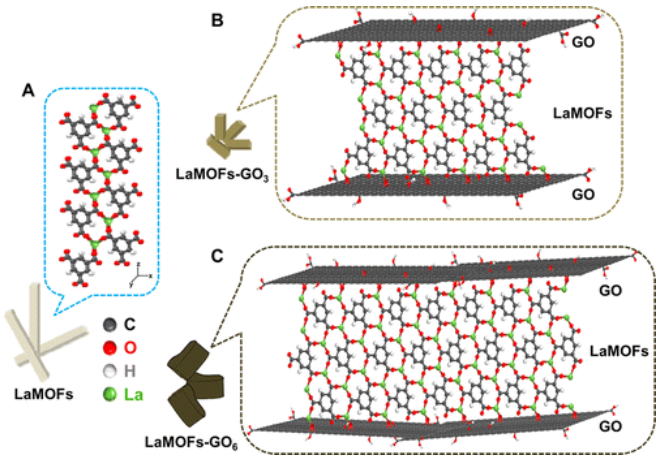

Figure 1.18 Schematic of the formation mechanism for a) LaMOFs, b) LaMOF–GO composites percentage of GO < 5% and c) LaMOF–GO composites percentage of GO > 5%. Adapted from Ref. [212]

- Crystal size change

  The MOF crystal usually becomes smaller when combined with GO. Indeed, metal ions first bind to the functional groups of the carbon materials, thus reducing the amount of free metallic ions to form further extended MOF crystals of large sizes[212]. With gradual increasing loading up to 20 wt.% GO in GO/ZIF-8, ZIF-8 crystals gradually change from a hexagonal shape with a size of 100–150 nm to uniform nanospheres with a diameter of ~4 nm[214]. Same behaviour was also observed for other composites such as 9 wt.% GO/HKUST-1[168].

- Synthesis acceleration

  Considerable importance is given for fast synthesis of MOFs using methodologies including microwave-assisted synthesis[215], ultrasound-assisted synthesis[5] etc. This fast synthesis is promoted with the help of functionalized self-assembled monolayers (SAMs). This was well accomplished by Jhung's group[216] where introduction of GO during MIL-101 synthesis, accelerated the reaction. The synthesis is faster owing to the chemical affinity between functional groups grafted to GO and the metal centres of MOFs which initiate the fast coordination reactions.[216]

- Creation of additional porosity

  When higher amounts of GO materials are introduced, additional micro- and/or mesopores are created not only between the MOF/GO interface but also between the

GO/GO interface. This is because of the number of functional groups on GO exceeds the accessible sites of MOFs[217]. These additional new pores can be regarded as favourable for the enhancement of gas storage capacity. The same was observed in HKUST-1/GO. The reaction of the HKUST-1 units with the functionalities of GO (up to 20%) leads to the creation of new pores responsible for the enhancement in the hydrogen uptake[217].

1.4.3. Main potential applications of MOF/GO composites

The most common applications of the MOF/GO based composites are briefly discussed below.

1.4.3.1. Sensors

In environmental and biological systems, selective detection of heavy metal ions in liquids, organic toxicants and hazardous gas analytes are of interest to monitor product quality, facilitate medical diagnostics and guarantee occupational safety[218]. The devices used in this method first require the adsorption of analyte molecules onto the surface of the sensors which then react to generate a signal for detection of diverse natures including electrochemistry and photoluminescence principles. Some MOFs exhibit attractive sensor properties because of their electrochemically active metal sites, inorganic clusters (especially lanthanides for photoluminescent components) or organic linkers containing aromatic or conjugated π moieties (for photoluminescent sensors)[11,218]. However, these MOFs show poor conductivity and electrocatalytic abilities as well as relatively low luminescence quantum yield because of the weak metal–ligand charge transfer. This later point can be overcome by adding carbon to the composite which can lead to increased conductivity or/and high luminescence[219]. In this context, a number of MOF–carbon composites, including Cu-MOF/GO, Zn-MOF/GO and Stilbene-MOF/GO were prepared to fabricate different sensors for the detection of organic hazardous compounds (dopamine, acetaminophen[220], di or tri-nitrotoluene[221]), heavy metal ions(Cu^{2+})[222] etc.

1.4.3.2. Batteries and supercapacitors

Energy storage devices like batteries and supercapacitors are of great importance for high energy and power delivery for electric vehicles and auxiliary power sources etc. However, the current rechargeable batteries have low power density and high energy density while vice versa for electrochemical capacitors[223]. Lithium sulphur batteries (LiS) have a higher theoretical specific capacity and energy density compared to highly studied Lithium ion batteries which show low electrical conductivity and a large volume expansion during insertion–extraction of Li[224]. The main challenge in operational LiS batteries lies in the insulation characteristics of sulphur element and its shuttle effect[224]. Carbon-based materials could provide extra Li ion diffusion pathways and can cushion the volume change in long-term cycling and host sulphur species by introducing them into the pores and restricting the shuttle effect[224,225]. Typically, this was studied by Zhang's group in MIL-101/rGO/S[195] composite. This composite displays a higher discharge capacity (650 mA h/g) with capacity retention rate of 66.6% at current density of 335mA/g after 50 cycles compared to MIL-101(Cr)/S composite. Also, supercapacitors involving MOF/carbon composites electrodes show outstanding physical and chemical charge storage properties. Here carbon-based materials increase the capacitance via electrostatic effects and also enhance the interactions between electrolytes and pseudocapacitive materials due to their high-surface-area. MOFs supply active sites to further increase the capacitance through Faradaic reactions. MOFs also act as a porous framework which eases fast ion diffusion of the composite electrodes. Ni-doped MOF-5/rGO composite electrodes developed by Majumder et al, demonstrated high energy storage properties[209]. In this case, Ni doping stabilizes the fragile structure of MOF-5 and promotes the reversible redox reactions in alkaline electrolytes. The resulting composite exhibits a maximum capacitance of 758 F/ g and a high energy density of 37.8 W h/kg at a power density of 227 W/kg.

1.4.3.3. Catalysis

MOF/carbon-based composites can be efficient for electrocatalysis, photocatalysis or heterocatalysis among others. These systems can be used as electrocatalysts due to the presence of electrochemically active metal sites, thus leading to an increase of the conductivity owing to the presence of the carbonaceous material. The $Cu_2(BDC)_2(dabco)$/rGO composite has been shown to be useful for oxygen reduction reaction (ORR), oxygen evolution reaction (OER), and

hydrogen evolution reaction (HER) applications[226]. Cu-bipy-BTC/GO (Cu-bipy-BTC= $[Cu_2(OH)(2,2'\text{-bipy})_2(BTC)2H_2O]_n$) was also prepared and applied in the electro-oxidative carbonylation synthesis of dimethyl carbonate using methanol and monoxide[227].

MOF–carbon composites as hetero-catalysts are quite useful since carbon materials make the metal sites of MOF more hydrophobic thus, not only protecting the material against water but also increasing the affinity of active sites towards organic reactants. Typically, HKUST-1/GO (8.7 wt.%) allowed a high conversion (74.1%) of styrene oxide in the ring-opening reaction compared to pure MOF (10.7%) [205]. ZIF-8/SO_3H–GO shows catalytic performance twice higher than that of the pristine ZIF-8 for the cyclo-addition reactions leading to the preparation of pyranyl heterocycles[228]. Zhang's group synthesized a ZIF-8/Pt–rGO composite[229] which exhibits a conversion efficiency of 21% and 4.8% for *n*-hexene and cis- cyclooctene, respectively. Besides, the MOF/GO composite catalysts usually show a good reusability[205].

1.4.3.4. Adsorption

- Liquid-phase adsorption

  Typically, HKUST-1/GO have been used for water purification, in particular for the removal of methylene blue (MB)[230]. The incorporation of 10 wt.% GO into HKUST-1 resulted in a maximum adsorption of 183.49 mg/g for MB in water. MIL-101/GO composite was also shown to be a highly effective adsorbent for the removal of nitrogen-containing compounds in model fuels[216]. Likewise, changing the Zn/imidazole ratio and the fraction of GO in the ZIF-8/GO composites led to unusually high surface area allowing a control of the methylene chloride adsorption performances from aqueous solutions[231].

- Gas-phase adsorption and storage

  There are many reports showing gas-phase adsorption employing MOF–carbon composites[181]. The surface modification of GO with diverse functional groups has been widely explored for such applications. Integration of MOFs with GO materials not only leads to the formation of new pores at the interface (50% increased porosity)[232] but also improve the non-specific dispersive force, and also reduce the pore size to an appropriate level for trapping molecules leading to high adsorption efficiency. Amine and other

groups attached to the GO can increase the number of adsorption sites in MOF. This was observed in Urea-modified GO with HKUST-1 showing an adsorbed amount of CO_2 at 30°C in dynamic conditions (4.23 mmol/g) twice higher than the performance of the pure MOF[232]. Cu-MOF (MOF-505) was combined with varying amount of GO (2-10%) showing that the incorporation of 5% GO leads to a drastic enhancement of CO_2 adsorption performance (3.9 mmol/g of CO_2 at 25 °C and 1 bar) corresponding to a 38 % increase compared to the pure MOF[233]. The MIL-101-Cr/GO composite demonstrated very attractive adsorption performances with CO_2 uptakes up to 22.4 mmol/g at 25 °C and 25 bar[234]. ZIF-8/GO revealed also relatively high CO_2 adsorption capacity of 16.3 mmol/g with 20% GO at -78°C [214]. HKUST-1/GO showed enhanced storage capacity with 30% increase in H_2 storage capacity (2.81 wt.% to 3.58 wt.% at 77 K and 42 bar) and CO_2 storage capacity (6.39 mmol/g to 8.26 mmol/g at 273 K and 1 atm)[168] Modified graphene oxide integrated with metal can significantly improve the performances of the pristine MOF. Typically a La-MOF with 11 wt.% Pt-decorated GO showed an enhancement of its CO_2 adsorption capacity at 0°C by 36%[235]. The adsorption of water (vapor), organic gases (e.g. acetone, n-alkanes) and harmful gases (NH_3, NO_2, H_2S) have also been explored using diverse MOF/composites like MIL- 101/GO, HKUST-1/GO, MOF-5/GO among others[203,236,237].

- Molecular separation

The incorporation of rGO in HKUST-1 was shown to increase the selectivity for CO_2/CH_4 from 5.3 to 14 (from pristine HKUST-1 to 1 wt.% rGO/HKUST-1) at 273 K and 1 bar[238]. The enhancement was associated to a stronger interaction of CO_2 with the oxygen atoms of the diverse functions present in GO. Similarly, the combination of MIL-101 with GO leads to an increase of the CO_2/CH_4 selectivity from 10 to 32 for the pure MIL-101 to MIL-101/GO composite respectively at 298 K and 1.5 bar[234]. ZIF-8/GO was also shown to be highly attractive for such applications since the resulting channels are highly favourable for gas permeation resulting in 35% increment of CO_2 permeance in CO_2/CH_4 separation without reducing the selectivity[239]. Similar study on ultrathin ZIF-8/GO showed high CO_2/N_2 selectivity of 7.0[240]. ZIF-8/GO is also very useful in improving hydrogen selectivity[241] generated through a facile strategy of selective nucleation and controlled growth of ZIF-8 crystals primarily at the defects of GO membranes. This introduces narrow nanochannels and non-selective defects in

GO. Notably, the oxygen-containing groups of GO especially the hydroxyl and carboxyl groups anchors with MOF atoms to reduce its non-selective pores. Such intergrown ZIF-8 crystals on ultrathin GO membranes can lead to high gas selectivity for hydrogen.

1.5. Atomistic models for MOF/GO composites

Even though MOF/GO composites have been intensively explored in the literature[230,242–245], a detailed description of their arrangements at the microscopic scale as well as the understanding of their properties are far to be achieved as attested by only two computational studies reported so far on this challenging topic. Sui et. al.[246] combined experimental and MD simulations to provide insights into the water transport behaviour of MOF/GO composite membranes. Using LAMMPS MD package, they carried out water transport simulations in nano-channels of MOFs and between GO nanosheets with different interlayer spacing. Two parallel GO layers were constructed with only carboxyl, carbonyl, and hydroxyl groups, noting that the presence of epoxy was missing. To simplify their simulation models, they assumed all the membrane atoms to be rigid. Here GO was combined with water stable MIL-140A(Zr) and UiO-66(Zr) MOF wherein increasing the weight ratio of MOF (up to 0.5) enhanced the water permeability up to 92%. This increase was driven by larger interlayer spacing and additional channel pathways generated by the presence of MOF nanoparticles.

In another study, Lin et. al.[247] performed DFT and reactive force field-based molecular calculations for the study of CO_2 adsorption on MOF-5/GO composite. They provided insights on the gas adsorbed at the interface region of the composite. Here a simplified GO model was used, which accounts only for the presence of epoxy and hydroxyl groups randomly placed on both sides of the pristine graphene sheet with a ratio of 1:1. The MOF-5 surface was constructed by eliminating 1,4-benzenedicarboxylate linkers from the surface of the unit cell followed by saturation of its dangling bonds, thus providing a rough estimation of the MOF surface. Except for the construction of the interface, the study presents a basic representation of the MOF-5 model as well as GO without any significant detail on interfacial structural characterization or site-to-site interactions between MOF and GO.

1.6. Conclusion

This litterature review emphasizes that the incorporation of GO into a MOF/GO composite can improve a wide range of properties in MOFs and in particular their gas adsorption and separation performances, a topic of interest within the EU H2020 GRAMOFON project. Hence, gaining insights into the microstructural properties of these composites at the interface can help fine tune their properties as well as facilitating their fabrication with a better control of association between two components. This latter crucial point is extremely poorly documented in the literature and this observation motivated my work that is exposed in chapters 3, 4 and 5 by considering the interactions between the MOFs ZIF-8, MIL-69, MIL-91 and pristine and functionalized GOs in order to gain an unprecedented fundamental knowledge of these composites at the atomistic scale.

REFERENCES

(1) Kitagawa, S.; Kitaura, R.; Noro, S. I. Functional Porous Coordination Polymers. *Angew. Chemie - Int. Ed.* **2004**, *43* (18), 2334–2375.

(2) Song, L.; Zhang, J.; Sun, L.; Xu, F.; Li, F.; Zhang, H.; Si, X.; Jiao, C.; Li, Z.; Liu, S.; Liu, Y.; Zhou, H.; Sun, D.; Du, Y.; Cao, Z.; Gabelica, Z. Mesoporous Metal-Organic Frameworks: Design and Applications. *Energy Environ. Sci.* **2012**, *5* (6), 7508–7520.

(3) Sumida, K.; Rogow, D. L.; Mason, J. A.; McDonald, T. M.; Bloch, E. D.; Herm, Z. R.; Bae, T. H.; Long, J. R. Carbon Dioxide Capture in Metal-Organic Frameworks. *Chem. Rev.* **2012**, *112* (2), 724–781.

(4) Li, J. R.; Kuppler, R. J.; Zhou, H. C. Selective Gas Adsorption and Separation in Metal-Organic Frameworks. *Chem. Soc. Rev.* **2009**, *38* (5), 1477–1504.

(5) Kuppler, R. J.; Timmons, D. J.; Fang, Q. R.; Li, J. R.; Makal, T. A.; Young, M. D.; Yuan, D.; Zhao, D.; Zhuang, W.; Zhou, H. C. Potential Applications of Metal-Organic Frameworks. *Coordination Chemistry Reviews*. **2009**, pp 3042–3066.

(6) Zhao, X.; Wang, Y.; Li, D. S.; Bu, X.; Feng, P. Metal–Organic Frameworks for Separation. *Adv. Mater.* **2018**, *30* (37), 1–34.

(7) Kishan, M. R.; Tian, J.; Thallapally, P. K.; Fernandez, C. A.; Dalgarno, S. J.; Warren, J. E.; McGrail, B. P.; Atwood, J. L. Flexible Metal-Organic Supramolecular Isomers for Gas Separation. *Chem. Commun.* **2010**, *46* (4), 538–540.

(8) Bedia, J.; Muelas-Ramos, V.; Peñas-Garzón, M.; Gómez-Avilés, A.; Rodríguez, J. J.; Belver, C. A Review on the Synthesis and Characterization of Metal Organic Frameworks for Photocatalytic Water Purification. *Catalysts* **2019**, *9* (1).

(9) Lee, J.; Farha, O. K.; Roberts, J.; Scheidt, K. A.; Nguyen, S. T.; Hupp, J. T. Metal-Organic Framework Materials as Catalysts. *Chem. Soc. Rev.* **2009**, *38* (5), 1450–1459.

(10) Hasegawa, S.; Horike, S.; Matsuda, R.; Furukawa, S.; Mochizuki, K.; Kinoshita, Y.; Kitagawa, S. Three-Dimensional Porous Coordination Polymer Functionalized with Amide Groups Based on Tridentate Ligand: Selective Sorption and Catalysis. *J. Am. Chem. Soc.* **2007**, *129* (9), 2607–2614.

(11) Cui, Y.; Yue, Y.; Qian, G.; Chen, B. Luminescent Functional Metal-Organic Frameworks. *Chem. Rev.* **2012**, *112* (2), 1126–1162.

(12) Chen, B.; Xiang, S.; Qian, G. Metal-Organic Frameworks with Functional Pores for Recognition of Small Molecules. *Acc. Chem. Res.* **2010**, *43* (8), 1115–1124.

(13) Suresh, V. M.; George, S. J.; Maji, T. K. MOF Nano-Vesicles and Toroids: Self-Assembled Porous Soft-Hybrids for Light Harvesting. *Adv. Funct. Mater.* **2013**, *23* (45), 5585–5590.

(14) Falcaro, P.; Buso, D.; Hill, A. J.; Doherty, C. M. Patterning Techniques for Metal Organic Frameworks. *Adv. Mater.* **2012**, *24* (24), 3153–3168.

(15) Muschi, M.; Serre, C. Progress and Challenges of Graphene Oxide/Metal-Organic Composites. *Coord. Chem. Rev.* **2019**, *387*, 262–272.

(16) Cychosz, K. A.; Matzger, A. J. Water Stability of Microporous Coordination Polymers and the Adsorption of Pharmaceuticals from Water. *Langmuir* **2010**, *26* (22), 17198–17202.

(17) Dan-Hardi, M.; Serre, C.; Frot, T.; Rozes, L.; Maurin, G.; Sanchez, C.; Férey, G. A New Photoactive Crystalline Highly Porous

Titanium(IV) Dicarboxylate. *J. Am. Chem. Soc.* **2009**, *131* (31), 10857–10859.

(18) Yang, R. . Activated Carbon. In Adsorbents: Fundamentals and Applications. *John Wiley Sons, Inc.,* **2003**, 79–130.

(19) Choi, S.; Drese, J. H.; Jones, C. W. Adsorbent Materials for Carbon Dioxide Capture from Large Anthropogenic Point Sources. *ChemSusChem* **2009**, *2* (9), 796–854.

(20) Goursot, A.; Vasilyev, V.; Arbuznikov, A. Modeling of Adsorption Properties of Zeolites: Correlation with the Structure. *J. Phys. Chem. B* **1997**, *101* (33), 6420–6428.

(21) Hoffmann, F.; Cornelius, M.; Morell, J.; Fröba, M. Silica-Based Mesoporous Organic-Inorganic Hybrid Materials. *Angew. Chemie - Int. Ed.* **2006**, *45* (20), 3216–3251.

(22) Batten, S. R.; Champness, N. R.; Chen, X. M.; Garcia-Martinez, J.; Kitagawa, S.; Öhrström, L.; O'Keeffe, M.; Suh, M. P.; Reedijk, J. Coordination Polymers, Metal-Organic Frameworks and the Need for Terminology Guidelines. *CrystEngComm* **2012**, *14* (9), 3001–3004.

(23) Kim, J.; Lin, L. C.; Swisher, J. A.; Haranczyk, M.; Smit, B. Predicting Large CO2 Adsorption in Aluminosilicate Zeolites for Postcombustion Carbon Dioxide Capture. *J. Am. Chem. Soc.* **2012**, *134* (46), 18940–18943.

(24) Díaz, E.; Muñoz, E.; Vega, A.; Ordóñez, S. Enhancement of the CO2 Retention Capacity of X Zeolites by Na- and Cs-Treatments. *Chemosphere* **2008**, *70* (8), 1375–1382.

(25) Chue, K. T.; Kim, J. N.; Yoo, Y. J.; Cho, S. H.; Yang, R. T. Comparison of Activated Carbon and Zeolite 13X for CO2 Recovery from Flue Gas by Pressure Swing Adsorption. *Ind. Eng. Chem. Res.* **1995**, *34* (2), 591–598.

(26) Jiang, J. X.; Su, F.; Trewin, A.; Wood, C. D.; Niu, H.; Jones, J. T. A.; Khimyak, Y. Z.; Cooper, A. I. Synthetic Control of the Pore Dimension and Surface Area in Conjugated Microporous Polymer and Copolymer Networks. *J. Am. Chem. Soc.* **2008**, *130* (24), 7710–7720.

(27) Liu, J.; Thallapally, P. K.; McGrail, B. P.; Brown, D. R.; Liu, J. Progress in Adsorption-Based CO2 Capture by Metal-Organic Frameworks. *Chem. Soc. Rev.* **2012**, *41* (6), 2308–2322.

(28) Gibson, L. T. Mesosilica Materials and Organic Pollutant Adsorption: Part A Removal from Air. *Chem. Soc. Rev.* **2014**, *43* (15), 5163–5172.

(29) Furukawa, H.; Cordova, K. E.; O'Keeffe, M.; Yaghi, O. M. The Chemistry and Applications of Metal-Organic Frameworks. *Science* **2013**, *341* (6149), 1230444–1230444.

(30) Li, H.; Li, L.; Lin, R.-B.; Zhou, W.; Zhang, Z.; Xiang, S.; Chen, B. Porous Metal-Organic Frameworks for Gas Storage and Separation: Status and Challenges. *EnergyChem* **2019**, *1* (1), 100006.

(31) Ma, S.; Zhou, H. C. Gas Storage in Porous Metal-Organic Frameworks for Clean Energy Applications. *Chem. Commun.* **2010**, *46* (1), 44–53.

(32) Latroche, M.; Surblé, S.; Serre, C.; Mellot-Draznieks, C.; Llewellyn, P. L.; Lee, J. H.; Chang, J. S.; Sung, H. J.; Férey, G. Hydrogen Storage in the Giant-Pore Metal-Organic Frameworks MIL-100 and MIL-101. *Angew. Chemie - Int. Ed.* **2006**, *45* (48), 8227–8231.

(33) Furukawa, S.; Reboul, J.; Diring, S.; Sumida, K.; Kitagawa, S. Structuring of Metal-Organic Frameworks at the Mesoscopic/Macroscopic Scale. *Chem. Soc. Rev.* **2014**, *43* (16), 5700–5734.

(34) Devic, T.; Serre, C. High Valence 3p and Transition Metal Based MOFs. *Chem. Soc. Rev.* **2014**, *43* (16), 6097–6115.

(35) Zarekarizi, F.; Joharian, M.; Morsali, A. Pillar-Layered MOFs: Functionality, Interpenetration, Flexibility and Applications. *J. Mater. Chem. A* **2018**, *6* (40), 19288–19329.

(36) Rouquerol, F.; Rouquerol, J.; Sing, K. S. .; Llewellyn, P.; Maurin, G. *Adsorption by Powders and Porous Solids*; **2014**.

(37) Deria, P.; Mondloch, J. E.; Karagiaridi, O.; Bury, W.; Hupp, J. T.; Farha, O. K. Beyond Post-Synthesis Modification: Evolution of Metal-Organic Frameworks via Building Block Replacement. *Chem. Soc. Rev.* **2014**, *43* (16), 5896–5912.

(38) Yaghi, O. M.; O'Keeffe, M.; Chae, H. K.; Eddaoudi, M.; Kim, J. Reticular Synthesis and the Design of New Materials. *Nature* **2003**, *423*.

(39) Eddaoudi, M.; Sava, D. F.; Eubank, J. F.; Adil, K.; Guillerm, V. Zeolite-like Metal-Organic Frameworks (ZMOFs): Design, Synthesis, and Properties. *Chem. Soc. Rev.* **2015**, *44* (1), 228–249.

(40) Cook, T. R.; Zheng, Y. R.; Stang, P. J. Metal-Organic Frameworks and Self-Assembled Supramolecular Coordination Complexes: Comparing and Contrasting the Design, Synthesis, and Functionality of Metal-Organic Materials. *Chem. Rev.* **2013**, *113* (1), 734–777.

(41) Dhakshinamoorthy, A.; Asiri, A. M.; Garcia, H. Mixed-Metal or Mixed-Linker Metal Organic Frameworks as Heterogeneous Catalysts. *Catal. Sci. Technol.* **2016**, *6* (14), 5238–5261.

(42) Lu, W.; Wei, Z.; Gu, Z. Y.; Liu, T. F.; Park, J.; Park, J.; Tian, J.; Zhang, M.; Zhang, Q.; Gentle, T.; Bosch, M.; Zhou, H. C. Tuning the Structure and Function of Metal-Organic Frameworks via Linker Design. *Chem. Soc. Rev.* **2014**, *43* (16), 5561–5593.

(43) Janiak, C. Functional Organic Analogues of Zeolites Based on Metal-Organic Coordination Frameworks. *Angew. Chemie (International Ed. English)* **1997**, *36* (13–14), 1431–1434.

(44) Li, H.; Eddaoudi, M.; O'Keeffe, M.; Yaghi, O. M. Design and synthesis of an exceptionally stable and highly porous metal-organic framework. *Nature* **1999**, *402*, 276–279.

(45) Fan, J.; Zhu, H. F.; Okamura, T. A.; Sun, W. Y.; Tang, W. X.; Ueyama, N. Novel One-Dimensional Tubelike and Two-Dimensional Polycatenated Metal-Organic Frameworks. *Inorg. Chem.* **2003**, *42* (1), 158–162.

(46) Huh, S.; Jung, S.; Kim, Y.; Kim, S. J.; Park, S. Two-Dimensional Metal-Organic Frameworks with Blue Luminescence. *Dalt. Trans.* **2010**, *39* (5), 1261–1265.

(47) Lu, W. G.; Jiang, L.; Feng, X. L.; Lu, T. B. Three-Dimensional Lanthanide Anionic Metal - Organic Frameworks with Tunable Luminescent Properties Induced by Cation Exchange. *Inorg. Chem.* **2009**, *48* (15), 6997–6999.

(48) Férey, G. Hybrid Porous Solids: Past, Present, Future. *Chem. Soc. Rev.* **2008**, *37* (1), 191–214.

(49) Moghadam, P. Z.; Li, A.; Wiggin, S. B.; Tao, A.; Maloney, A. G. P.; Wood, P. A.; Ward, S. C.; Fairen-Jimenez, D. Development of a Cambridge Structural Database Subset: A Collection of Metal-Organic Frameworks for Past, Present, and Future. *Chem. Mater.* **2017**, *29* (7), 2618–2625.

(50) Wilmer, C. E.; Leaf, M.; Lee, C. Y.; Farha, O. K.; Hauser, B. G.; Hupp, J. T.; Snurr, R. Q. Large-Scale Screening of Hypothetical Metal-Organic Frameworks. *Nat. Chem.* **2012**, *4* (2), 83–89.

(51) Dai, B.; Sholl, D. S.; Johnson, J. K. First-Principles Study of Experimental and Hypothetical Mg(BH4)2 Crystal Structures. *J. Phys. Chem. C* **2008**, *112* (11), 4391–4395.

(52) Witman, M.; Ling, S.; Anderson, S.; Tong, L.; Stylianou, K. C.; Slater, B.; Smit, B.; Haranczyk, M. In Silico Design and Screening of Hypothetical MOF-74 Analogs and Their Experimental Synthesis. *Chem. Sci.* **2016**, *7* (9), 6263–6272.

(53) Park, K. S.; Ni, Z.; Cote, A. P.; Choi, J. Y.; Huang, R.; Uribe-Romo, F. J.; Chae, H. K.; O'Keeffe, M.; Yaghi, O. M. Exceptional Chemical and Thermal Stability of Zeolitic Imidazolate Frameworks. *Proc. Natl. Acad. Sci.* **2006**, *103* (27), 10186–10191.

(54) Huang, X.; Zhang, J.; Chen, X. [Zn(Bim)2] · (H2O)1.67: A Metal-Organic Open-Framework with Sodalite Topology. *Chinese Sci. Bull.* **2003**, *48* (15), 1531–1534.

(55) Tian, Y. Q.; Cai, C. X.; Ji, Y.; You, X. Z.; Peng, S. M.; Lee, G. H. [Co5(Im)10·2MB]∞: A Metal-Organic Open-Framework with Zeolite-like Topology. *Angew. Chemie - Int. Ed.* **2002**, *41* (8), 1384–1386.

(56) Tian, Y. Q.; Cai, C. X.; Ren, X. M.; Duan, C. Y.; Xu, Y.; Gao, S.; You, X. Z. The Silica-Like Extended Polymorphism of Cobalt(II) Imidazolate Three-Dimensional Frameworks: X-Ray Single-Crystal Structures and Magnetic Properties. *Chem. - A Eur. J.* **2003**, *9* (22), 5673–5685.

(57) Noh, K.; Lee, J.; Kim, J. Compositions and Structures of Zeolitic Imidazolate Frameworks. *Isr. J. Chem.* **2018**, *58* (9), 1075–1088.

(58) Lian, X.; Xu, L.; Chen, M.; Wu, C.; Li, W.; Huang, B.; Cui, Y. Carbon Dioxide Captured by Metal Organic Frameworks and Its Subsequent Resource Utilization Strategy: A Review and Prospect. *J. Nanosci. Nanotechnol.* **2019**, *19* (6), 3059–3078.

(59) Gong, X.; Wang, Y.; Kuang, T. ZIF-8-Based Membranes for Carbon Dioxide Capture and Separation. *ACS Sustain. Chem. Eng.* **2017**, *5* (12), 11204–11214.

(60) Kaneti, Y. V.; Dutta, S.; Hossain, M. S. A.; Shiddiky, M. J. A.; Tung, K. L.; Shieh, F. K.; Tsung, C. K.; Wu, K. C. W.; Yamauchi, Y. Strategies for Improving the Functionality of Zeolitic Imidazolate Frameworks: Tailoring Nanoarchitectures for Functional Applications. *Adv. Mater.* **2017**, *29* (38).

(61) Fairen-Jimenez, D.; Moggach, S. A.; Wharmby, M. T.; Wright, P. A.; Parsons, S.; Düren, T. Opening the Gate: Framework Flexibility in ZIF-8 Explored by Experiments and Simulations. *J. Am. Chem. Soc.* **2011**, *133* (23), 8900–8902.

(62) Coudert, F. X. Molecular Mechanism of Swing Effect in Zeolitic Imidazolate Framework ZIF-8: Continuous Deformation upon Adsorption. *ChemPhysChem* **2017**, *18* (19), 2732–2738.

(63) Zheng, B.; Wang, L. L.; Du, L.; Huang, K. W.; Du, H. ZIF-8 Gate Tuning via Terminal Group Modification: A Computational Study. *Chem. Phys. Lett.* **2016**, *658*, 270–275.

(64) Wu, H.; Zhou, W.; Yildirim, T. Hydrogen Storage in a Prototypical Zeolitic Imidazolate Framework-8. *J. Am. Chem. Soc.* **2007**, *129* (17), 5314–5315.

(65) Wang, S.; Serre, C. Toward Green Production of Water-Stable Metal-Organic Frameworks Based on High-Valence Metals with Low Toxicities. *ACS Sustain. Chem. Eng.* **2019**, *7*, 11911–11927.

(66) Férey, G.; Serre, C. Large Breathing Effects in Three-Dimensional Porous Hybrid Matter: Facts, Analyses, Rules and Consequences. *Chem. Soc. Rev.* **2009**, *38* (5), 1380–1399.

(67) Lenzen, D.; Bendix, P.; Reinsch, H.; Fröhlich, D.; Kummer, H.; Möllers, M.; Hügenell, P. P. C.; Gläser, R.; Henninger, S.; Stock, N. Scalable Green Synthesis and Full-Scale Test of the Metal–Organic Framework CAU-10-H for Use in Adsorption-Driven Chillers. *Adv. Mater.* **2018**, *30* (6), 1–6.

(68) Permyakova, A.; Skrylnyk, O.; Courbon, E.; Affram, M.; Wang, S.; Lee, U. H.; Valekar, A. H.; Nouar, F.; Mouchaham, G.; Devic, T.; De Weireld, G.; Chang, J. S.; Steunou, N.; Frère, M.; Serre, C. Synthesis Optimization, Shaping, and Heat Reallocation Evaluation of the Hydrophilic Metal–Organic Framework MIL-160(Al). *ChemSusChem* **2017**, *10* (7), 1419–1426.

(69) Lenzen, D.; Zhao, J.; Ernst, S. J.; Wahiduzzaman, M.; Ken Inge, A.; Fröhlich, D.; Xu, H.; Bart, H. J.; Janiak, C.; Henninger, S.; Maurin, G.; Zou, X.; Stock, N. A Metal–Organic Framework for Efficient Water-Based Ultra-Low-Temperature-Driven Cooling. *Nat. Commun.* **2019**, *10* (1), 1–9.

(70) Fathieh, F.; Kalmutzki, M. J.; Kapustin, E. A.; Waller, P. J.; Yang, J.; Yaghi, O. M. Practical Water Production from Desert Air. *Sci. Adv.* **2018**, *4* (6), 1–10.

(71) Loiseau, T.; Mellot-Draznieks, C.; Muguerra, H.; Férey, G.; Haouas, M.; Taulelle, F. Hydrothermal Synthesis and Crystal Structure of a New Three-Dimensional Aluminum-Organic Framework MIL-69 with 2,6-Naphthalenedicarboxylate (Ndc), Al(OH)(Ndc)·H2O. *Comptes Rendus Chim.* **2005**, *8* (3–4), 765–772.

(72) Sabetghadam, A.; Liu, X.; Benzaqui, M.; Gkaniatsou, E.; Orsi, A.; Lozinska, M. M.; Sicard, C.; Johnson, T.; Steunou, N.; Wright, P. A.; Serre, C.; Gascon, J.; Kapteijn, F. Influence of Filler Pore Structure and Polymer on the Performance of MOF-Based Mixed-Matrix Membranes for CO 2 Capture. *Chem. - A Eur. J.* **2018**, *24* (31), 7949–7956.

(73) Assi, H.; Mouchaham, G.; Steunou, N.; Devic, T.; Serre, C. Titanium Coordination Compounds: From Discrete Metal Complexes to Metal-Organic Frameworks. *Chem. Soc. Rev.* **2017**, *46* (11), 3431–3452.

(74) Serre, C.; Groves, J. A.; Lightfoot, P.; Slawin, A. M. Z.; Wright, P. A.; Stock, N.; Bein, T.; Haouas, M.; Taulelle, F.; Férey, G. Synthesis, Structure and Properties of Related Microporous N,N'-Piperazinebismethylenephosphonates of Aluminum and Titanium. *Chem. Mater.* **2006**, *18* (6), 1451–1457.

(75) Gao, J.; Miao, J.; Li, P. Z.; Teng, W. Y.; Yang, L.;

Zhao, Y.; Liu, B.; Zhang, Q. A P-Type Ti(Iv)-Based Metal-Organic Framework with Visible-Light Photo-Response. *Chem. Commun.* **2014**, *50* (29), 3786–3788.

(76) Mason, J. A.; Darago, L. E.; Lukens, W. W.; Long, J. R. Synthesis and O2 Reactivity of a Titanium(III) Metal-Organic Framework. *Inorg. Chem.* **2015**, *54* (20), 10096–10104.

(77) Bueken, B.; Vermoortele, F.; Vanpoucke, D. E. P.; Reinsch, H.; Tsou, C. C.; Valvekens, P.; De Baerdemaeker, T.; Ameloot, R.; Kirschhock, C. E. A.; Van Speybroeck, V.; Mayer, J. M.; De Vos, D. A Flexible Photoactive Titanium Metal-Organic Framework Based on a [TiIV3(M3-O)(O)2(COO)6] Cluster. *Angew. Chemie - Int. Ed.* **2015**, *54* (47), 13912–13917.

(78) Nguyen, N. T. T.; Furukawa, H.; Gándara, F.; Trickett, C. A.; Jeong, H. M.; Cordova, K. E.; Yaghi, O. M. Three-Dimensional Metal-Catecholate Frameworks and Their Ultrahigh Proton Conductivity. *J. Am. Chem. Soc.* **2015**, *137* (49), 15394–15397.

(79) Assi, H.; Pardo Pérez, L. C.; Mouchaham, G.; Ragon, F.; Nasalevich, M.; Guillou, N.; Martineau, C.; Chevreau, H.; Kapteijn, F.; Gascon, J.; Fertey, P.; Elkaim, E.; Serre, C.; Devic, T. Investigating the Case of Titanium(IV) Carboxyphenolate Photoactive Coordination Polymers. *Inorg. Chem.* **2016**, *55* (15), 7192–7199.

(80) Serre, C.; Férey, G. Hydrothermal Synthesis and Structure Determination from Powder Data of New Three-Dimensional Titanium(IV) Diphosphonates Ti(O3P-(CH2)n-PO3) or MIL-25n (N=2, 3). *Inorg. Chem.* **2001**, *40* (21), 5350–5353.

(81) Wang, S.; Kitao, T.; Guillou, N.; Wahiduzzaman, M.; Martineau-Corcos, C.; Nouar, F.; Tissot, A.; Binet, L.; Ramsahye, N.; Devautour-Vinot, S.; Kitagawa, S.; Seki, S.; Tsutsui, Y.; Briois, V.; Steunou, N.; Maurin, G.; Uemura, T.; Serre, C. A Phase Transformable Ultrastable Titanium-Carboxylate Framework for Photoconduction. *Nat. Commun.* **2018**, *9* (1), 1–9.

(82) Castells-Gil, J.; M. Padial, N.; Almora-Barrios, N.; Da Silva, I.; Mateo, D.; Albero, J.; García, H.; Martí-Gastaldo, C. De Novo Synthesis of Mesoporous Photoactive Titanium(Iv)-Organic Frameworks with MIL-100 Topology. *Chem. Sci.* **2019**, *10* (15), 4313–4321.

(83) Lan, G.; Ni, K.; Veroneau, S. S.; Feng, X.; Nash, G. T.; Luo, T.; Xu, Z.; Lin, W. Titanium-Based Nanoscale Metal-Organic Framework for Type i Photodynamic Therapy. *J. Am. Chem. Soc.* **2019**, *141* (10), 4204–4208.

(84) Li, C.; Xu, H.; Gao, J.; Du, W.; Shangguan, L.; Zhang, X.; Lin, R. B.; Wu, H.; Zhou, W.; Liu, X.; Yao, J.; Chen, B. Tunable Titanium Metal-Organic Frameworks with Infinite 1D Ti-O Rods for Efficient Visible-Light-Driven Photocatalytic H2 Evolution. *J. Mater. Chem. A* **2019**, *7* (19), 11928–11933.

(85) Kim, M.; Cahill, J. F.; Fei, H.; Prather, K. A.; Cohen, S. M. Postsynthetic Ligand and Cation Exchange in Robust Metal-Organic Frameworks. *J. Am. Chem. Soc.* **2012**, *134* (43), 18082–18088.

(86) Brozek, Carl, K.; Dincă, M. Ti3+-, V2+/3+-, Cr2+/3+-, Mn2+-, and Fe2+-Subsituted MOF-5 and Redox Reactivity in Cr and Fe-MOF-5. *J. Am. Chem. Soc.* **2013**, *135*, 12886–12891.

(87) Zou, L.; Feng, D.; Liu, T. F.; Chen, Y. P.; Yuan, S.; Wang, K.; Wang, X.; Fordham, S.; Zhou, H. C. A Versatile Synthetic Route for the Preparation of Titanium Metal-Organic Frameworks. *Chem. Sci.* **2016**, *7* (2), 1063–1069.

(88) Benoit, V.; Pillai, R. S.; Orsi, A.; Normand, P.; Jobic, H.; Nouar, F.; Billemont, P.; Bloch, E.; Bourrelly, S.; Devic, T.; Wright, P. A.; De Weireld, G.; Serre, C.; Maurin, G.; Llewellyn, P. L. MIL-91(Ti), a Small Pore Metal-Organic Framework Which Fulfils Several Criteria: An Upscaled Green Synthesis, Excellent Water Stability, High CO2 Selectivity and Fast CO2 Transport. *J. Mater. Chem. A* **2016**, *4* (4), 1383–1389.

(89) Pillai, R. S.; Jobic, H.; Koza, M.; Nouar, F. Diffusion of Carbon Dioxide and Nitrogen in the Small- Pore Titanium Bis (Phosphonate) Metal – Organic Framework MIL-91 (Ti): A Combination of Quasielastic Neutron Scattering Measurements and Molecular Dynamics Simulations. **2017**, *91*, 1–9.

(90) Hobday, C. L.; Woodall, C. H.; Lennox, M. J.; Frost, M.; Kamenev, K.; Düren, T.; Morrison, C. A.; Moggach, S. A. Understanding the Adsorption Process in ZIF-8 Using High Pressure Crystallography and Computational Modelling. *Nat. Commun.* **2018**, *9* (1), 1–9.

(91) Stock, N.; Biswas, S. Synthesis of Metal-Organic Frameworks (MOFs): Routes to Various MOF Topologies, Morphologies, and Composites. *Chemical Reviews*. **2012**, pp 933–969.

(92) Thomas-Hillman, I.; Laybourn, A.; Dodds, C.; Kingman, S. W. Realising the Environmental Benefits of Metal-Organic Frameworks: Recent Advances in Microwave Synthesis. *J. Mater. Chem. A* **2018**, *6* (25), 11564–11581.

(93) Dey, C.; Kundu, T.; Biswal, B. P.; Mallick, A.; Banerjee, R. Crystalline Metal-Organic Frameworks (MOFs): Synthesis, Structure and Function. *Acta Crystallogr. Sect. B Struct. Sci. Cryst. Eng. Mater.* **2014**, *70* (1), 3–10.

(94) Ni, Z.; Masel, R. I. Rapid Production of Metal-Organic Frameworks via Microwave-Assisted Solvothermal Synthesis. *J. Am. Chem. Soc.* **2006**, *128* (38), 12394–12395.

(95) Abednatanzi, S.; Gohari Derakhshandeh, P.; Depauw, H.; Coudert, F. X.; Vrielinck, H.; Van Der Voort, P.; Leus, K. Mixed-Metal Metal-Organic Frameworks. *Chem. Soc. Rev.* **2019**, *48* (9), 2535–2565.

(96) Mueller, U.; Schubert, M.; Teich, F.; Puetter, H.; Schierle-Arndt, K.; Pastré, J. Metal-Organic Frameworks - Prospective Industrial Applications. *J. Mater. Chem.* **2006**, *16* (7), 626–636.

(97) Silva, C. G.; Luz, I.; Llabrés I Xamena, F. X.; Corma, A.; García, H. Water Stable Zr-Benzenedicarboxylate Metal-Organic Frameworks as Photocatalysts for Hydrogen Generation. *Chem. - A Eur. J.* **2010**, *16* (36), 11133–11138.

(98) Sosa, J. D.; Bennett, T. F.; Nelms, K. J.; Liu, B. M.; Tovar, R. C.; Liu, Y. Metal–Organic Framework Hybrid Materials and Their Applications. *Crystals* **2018**, *8* (8), 1–23.

(99) Mondloch, J. E.; Bury, W.; Fairen-Jimenez, D.; Kwon, S.; Demarco, E. J.; Weston, M. H.; Sarjeant,

A. A.; Nguyen, S. T.; Stair, P. C.; Snurr, R. Q.; Farha, O. K.; Hupp, J. T. Vapor-Phase Metalation by Atomic Layer Deposition in a Metal-Organic Framework. *J. Am. Chem. Soc.* **2013**, *135* (28), 10294–10297.

(100) Adil, K.; Belmabkhout, Y.; Pillai, R. S.; Cadiau, A.; Bhatt, P. M.; Assen, A. H.; Maurin, G.; Eddaoudi, M. Gas/Vapour Separation Using Ultra-Microporous Metal-Organic Frameworks: Insights into the Structure/Separation Relationship. *Chem. Soc. Rev.* **2017**, *46* (11), 3402–3430.

(101) Hon Lau, C.; Babarao, R.; Hill, M. R. A Route to Drastic Increase of CO2 Uptake in Zr Metal Organic Framework UiO-66. *Chem. Commun.* **2013**, *49* (35), 3634–3636.

(102) Nugent, P.; Giannopoulou, E. G.; Burd, S. D.; Elemento, O.; Giannopoulou, E. G.; Forrest, K.; Pham, T.; Ma, S.; Space, B.; Wojtas, L.; Eddaoudi, M.; Zaworotko, M. J. Porous Materials with Optimal Adsorption Thermodynamics and Kinetics for Co2 Separation. *Nature* **2013**, *495* (7439), 80–84.

(103) Skarmoutsos, I.; Eddaoudi, M.; Maurin, G. Highly Tunable Sulfur Hexafluoride Separation by Interpenetration Control in Metal Organic Frameworks. *Microporous Mesoporous Mater.* **2019**, 44–49.

(104) Liu, G.; Cadiau, A.; Liu, Y.; Adil, K.; Chernikova, V.; Carja, I. D.; Belmabkhout, Y.; Karunakaran, M.; Shekhah, O.; Zhang, C.; Itta, A. K.; Yi, S.; Eddaoudi, M.; Koros, W. J. Enabling Fluorinated MOF-Based Membranes for Simultaneous Removal of H2S and CO2 from Natural Gas. *Angew. Chemie - Int. Ed.* **2018**, *57* (45), 14811–14816.

(105) Senkovska, I.; Hoffmann, F.; Fröba, M.; Getzschmann, J.; Böhlmann, W.; Kaskel, S. New Highly Porous Aluminium Based Metal-Organic Frameworks: Al(OH)(Ndc) (Ndc = 2,6-Naphthalene Dicarboxylate) and Al(OH)(Bpdc) (Bpdc = 4,4'-Biphenyl Dicarboxylate). *Microporous Mesoporous Mater.* **2009**, *122* (1–3), 93–98.

(106) Zhou, C.; Cao, L.; Wei, S.; Zhang, Q.; Chen, L. A First Principles Study of Gas Adsorption on Charged Cu-BTC. *Comput. Theor. Chem.* **2011**, *976* (1–3), 153–160.

(107) Llewellyn, P. L.; Bourrelly, S.; Serre, C.; Vimont, A.; Daturi, M.; Hamon, L.; Weireld, G. De; Chang, J.; Hong, D.; Hwang, Y. K.; Jhung, S. H. High Uptakes of CO2 and CH4 in Mesoporous Metal s Organic Frameworks MIL-100 and MIL-101. *Langmuir* **2008**, *24*, 7245–7250.

(108) Yang, Q.; Guillerm, V.; Ragon, F.; Wiersum, A. D.; Llewellyn, P. L.; Zhong, C.; Devic, T.; Serre, C.; Maurin, G. CH4 Storage and CO2 Capture in Highly Porous Zirconium Oxide Based Metal-Organic Frameworks. *Chem. Commun.* **2012**, *48* (79), 9831–9833.

(109) Kong, L.; Zou, R.; Bi, W.; Zhong, R.; Mu, W.; Liu, J.; Han, R. P. S.; Zou, R. Selective Adsorption of CO2/CH4 and CO2/N2 within a Charged Metal-Organic Framework. *J. Mater. Chem. A* **2014**, *2* (42), 17771–17778.

(110) Gascon, J.; Aktay, U.; Hernandez-Alonso, M. D.; van Klink, G. P. M.; Kapteijn, F. Amino-Based Metal-Organic Frameworks as Stable, Highly Active Basic Catalysts. *J. Catal.* **2009**, *261* (1), 75–87.

(111) Kim, J.; Kim, W. Y.; Ahn, W. S. Amine-Functionalized MIL-53(Al) for CO 2/N 2 Separation: Effect of Textural Properties. *Fuel* **2012**, *102*, 574–579.

(112) Bourrelly, S.; Llewellyn, P. L.; Serre, C.; Millange, F.; Loiseau, T.; Férey, G. Different Adsorption Behaviors of Methane and Carbon Dioxide in the Isotypic Nanoporous Metal Terephthalates MIL-53 and MIL-47. *J. Am. Chem. Soc.* **2005**, *127* (39), 13519–13521.

(113) Couck, S.; Denayer, J. F. M.; Baron, G. V.; Re´my, T.; Gascon, J.; Kapteijn, F. An Amine-Functionalized MIL-53 Metal-Organic Framework with Large Separation Power for CO2 and CH4. *J. Am. Chem. SOC* **2009**, *131* (18), 6326–6327.

(114) Benoit, V.; Chanut, N.; Pillai, R. S.; Benzaqui, M.; Beurroies, I.; Devautour-Vinot, S.; Serre, C.; Steunou, N.; Maurin, G.; Llewellyn, P. L. A Promising Metal-Organic Framework (MOF), MIL-96(Al), for CO2 Separation under Humid Conditions. *J. Mater. Chem. A* **2018**, *6* (5), 2081–2090.

(115) Shekhah, O.; Belmabkhout, Y.; Chen, Z.; Guillerm, V.; Cairns, A.; Adil, K.; Eddaoudi, M. Made-to-Order Metal-Organic Frameworks for Trace Carbon Dioxide Removal and Air Capture. *Nat. Commun.* **2014**, *5* (May), 1–7.

(116) Voort, P. Van Der; Leus, K.; Canck, E. De. *Introduction of Porous Materials*; **2019**.

(117) Schafhaeutl, C. On the Combinations of Carbon with Silicon and Iron, and Other Metals, Forming the Different Species of Cast Iron, Steel, and Malleable Iron. *London, Edinburgh, Dublin Philos. Mag. J. Sci.* **1840**, *16* (106).

(118) Brodie, B. C. On the Atomic Weight of Graphit. *R. Soc. London* **1858**, *149*, 423–429.

(119) Hummers, W. S.; Offeman, R. E. Preparation of Graphitic Oxide. *J. Am. Chem. Soc.* **1958**, *80* (6), 1339–1339.

(120) Zhao, J.; Pei, S.; Ren, W.; Gao, L.; Cheng, H. M. Efficient Preparation of Large-Area Graphene Oxide Sheets for Transparent Conductive Films. *ACS Nano* **2010**, *4* (9), 5245–5252.

(121) Shuai Wu, Z.; Ren, W.; Gao, L.; Liu, B.; Jiang, C.; Cheng, H.-M. Synthesis of High-Quality Graphene with a Pre-Determined Number of Layers. *Carbon N. Y.* **2009**, *47* (2), 493–499.

(122) Szabó, T.; Berkesi, O.; Forgó, P.; Josepovits, K.; Sanakis, Y.; Petridis, D.; Dékány, I. Evolution of Surface Functional Groups in a Series of Progressively Oxidized Graphite Oxides Evolution of Surface Functional Groups in a Series of Progressively Oxidized Graphite Oxides. *Chem. Mater.* **2006**, *18* (11), 2740–2749.

(123) Lerf, A.; He, H.; Forster, M.; Klinowski, J. Structure of Graphite Oxide Revisited. *J. Phys. Chem. B* **1998**, *102* (23), 4477–4482.

(124) Singh, R. K.; Kumar, R.; Singh, D. P. Graphene Oxide: Strategies for Synthesis, Reduction and Frontier Applications. *RSC Adv.* **2016**, *6* (69), 64993–65011.

(125) Cervantes Amieva, E. J.; Barroso, J. L.; Hernández, Ana Laura Martínez Santos, C. V. *Graphene-Based Materials Functionalization with Natural Polymeric Biomolecules*; **2016**.

(126) Li, D.; Müller, M. B.; Gilje, S.; Kaner, R. B.;

Wallace, G. G. Processable Aqueous Dispersions of Graphene Nanosheets. *Nat. Nanotechnol.* **2008**, *3* (2), 101–105.

(127) Dreyer, D. R.; Park, S.; Bielawski, C. W.; Ruoff, R. S. The Chemistry of Graphene Oxide. *Chem. Soc. Rev.* **2010**, No. 39, 228–240.

(128) Gao, W.; Alemany, L. B.; Ci, L.; Ajayan, P. M. New Insights into the Structure and Reduction of Graphite Oxide. *Nat. Chem.* **2009**, *1* (5), 403–408.

(129) Schniepp, H. C.; Li, J. L.; McAllister, M. J.; Sai, H.; Herrera-Alonson, M.; Adamson, D. H.; Prud'homme, R. K.; Car, R.; Seville, D. A.; Aksay, I. A. Functionalized Single Graphene Sheets Derived from Splitting Graphite Oxide. *J. Phys. Chem. B* **2006**, *110* (17), 8535–8539.

(130) Mkhoyan, K. A.; Contryman, A. W.; Silcox, J.; Derek, A.; Eda, G.; Mattevi, C.; Miller, S.; Chhowalla, M.; Mkhoyan, K. A.; Contryman, A. W.; Silcox, J.; Stewart, D. A.; Eda, G.; Mattevi, C.; Miller, S.; Chhowalla, M. Atomic and Electronic Structure of Graphene-Oxide. *Nano Lett.* **2009**, *9* (3), 1058–1063.

(131) Pandey, D.; Reifenberger, R.; Piner, R. Scanning Probe Microscopy Study of Exfoliated Oxidized Graphene Sheets. *Surf. Sci.* **2008**, *602* (9), 1607–1613.

(132) Staudenmaier, L. No Title. *Ber. Dtsch. Chem. Rev.* **1898**, *31*, 1481–1487.

(133) Hofmann, U.; Koenig, E. No Title. *Z. Anorg. Allg. Chem.* **1937**, *234*, 311–336.

(134) Marcano, D. C.; Kosynkin, D. V.; Berlin, J. M.; Sinitskii, Z. S.; Slesarev, A.; Alemany, L. B.; Lu, W.; Tour, J. M. No Title. *ACS Nano* **2010**, *4*, 4806–4814.

(135) Dreyer, D. R.; Todd, A. D.; Bielawski, C. W. Harnessing the Chemistry of Graphene Oxide. *Chem. Soc. Rev.* **2014**, *43* (15), 5288.

(136) Liu, L.; Wang, L.; Gao, J.; Zhao, J.; Gao, X.; Chen, Z. Amorphous Structural Models for Graphene Oxides. *Carbon N. Y.* **2012**, *50* (4), 1690–1698.

(137) Hernández Rosas, J. J.; Ramírez Gutiérrez, R. E.; Escobedo-Morales, A.; Chigo Anota, E. First Principles Calculations of the Electronic and Chemical Properties of Graphene, Graphane, and Graphene Oxide. *J. Mol. Model.* **2011**, *17* (5), 1133–1139.

(138) Shih, C.-J.; Lin, S.; Sharma, R.; Strano, M. S.; Blankschtein, D. Understanding the PH-Dependent Behavior of Graphene Oxide Aqueous Solutions: A Comparative Experimental and Molecular Dynamics Simulation Study. *Langmuir* **2012**, *28* (1), 235–241.

(139) Ayrat M. Dimiev, S. E. *Graphene Oxide Fundamentals and Applications*; AYRAT M. DIMIEV, E. S., Ed.; **2017**.

(140) Zhang, X.; Huang, Y.; Wang, Y.; Ma, Y.; Liu, Z.; Chen, Y. Synthesis and Characterization of a Graphene-C60 Hybrid Material. *Carbon.* **2009**, pp 334–337.

(141) Mohanty, N.; Berry, V. Graphene-Based Single-Bacterium Resolution Biodevice and DNA Transistor: Interfacing Graphene Derivatives with Nanoscale and Microscale Biocomponents. *Nano Lett.* **2008**, *8* (12), 4469–4476.

(142) Liu, Z.; Robinson, J. T.; Sun, X.; Dai, H. PEGylated Nanographene Oxide for Delivery of Water-Insoluble Cancer Drugs. *J. Am. Chem. Soc.* **2008**, *130* (33), 10876–10877.

(143) Veca, L. M.; Lu, F.; Meziani, M. J.; Cao, L.; Zhang, P.; Qi, G.; Qu, L.; Shrestha, M.; Sun, Y. P. Polymer Functionalization and Solubilization of Carbon Nanosheets. *Chem. Commun.* **2009**, No. 18, 2565–2567.

(144) Xu, Y.; Liu, Z.; Zhang, X.; Wang, Y.; Tian, J.; Huang, Y.; Ma, Y.; Zhang, X.; Chen, Y. A Graphene Hybrid Material Covalently Functionalized with Porphyrin: Synthesis and Optical Limiting Property. *Adv. Mater.* **2009**, *21* (12), 1275–1279.

(145) Liu, Z. B.; Xu, Y. F.; Zhang, X. Y.; Zhang, X. L.; Chen, Y. S.; Tian, J. G. Porphyrin and Fullerene Covalently Functionalized Graphene Hybrid Materials with Large Nonlinear Optical Properties. *J. Phys. Chem. B* **2009**, *113* (29), 9681–9686.

(146) Lee, S. H.; Dreyer, D. R.; An, J.; Velamakanni, A.; Piner, R. D.; Park, S.; Zhu, Y.; Kim, S. O.; Bielawski, C. W.; Ruoff, R. S. Polymer Brushes via Controlled, Surface-Initiated Atom Transfer Radical Polymerization (ATRP) from Graphene Oxide. *Macromol. Rapid Commun.* **2010**, *31* (3), 281–288.

(147) Fang, M.; Wang, K.; Lu, H.; Yang, Y.; Nutt, S. Covalent Polymer Functionalization of Graphene Nanosheets and Mechanical Properties of Composites. *J. Mater. Chem.* **2009**, *19* (38), 7098–7105.

(148) Yang, H.; Li, F.; Shan, C.; Han, D.; Zhang, Q.; Niu, L.; Ivaska, A. Covalent Functionalization of Chemically Converted Graphene Sheets via Silane and Its Reinforcement. *J. Mater. Chem.* **2009**, *19* (26), 4632–4638.

(149) Zhang, B.; Chen, Y.; Xu, L.; Zeng, L.; He, Y.; Kang, E. T.; Zhang, J. Growing Poly(N-Vinylcarbazole) from the Surface of Graphene Oxide via RAFT Polymerization. *J. Polym. Sci. Part APolymer Chem.* **2011**, *49*, 2043–2050.

(150) Yang, X.; Zhang, X.; Liu, Z.; Ma, Y.; Huang, Y.; Chen, Y. High-Efficiency Loading and Controlled Release of Doxorubicin Hydrochloride on Graphene Oxide. *J. Phys. Chem. C* **2008**, *112* (45), 17554–17558.

(151) Lahaye, R. J. W. E.; Jeong, H. K.; Park, C. Y.; Lee, Y. H. Density Functional Theory Study of Graphite Oxide for Different Oxidation Levels. *Phys. Rev. B - Condens. Matter Mater. Phys.* **2009**, *79* (12), 1–8.

(152) Yan, J. A.; Xian, L.; Chou, M. Y. Structural and Electronic Properties of Oxidized Graphene. *Phys. Rev. Lett.* **2009**, *103* (8), 1–4.

(153) Yeh, T. F.; Chan, F. F.; Hsieh, C. Te; Teng, H. Graphite Oxide with Different Oxygenated Levels for Hydrogen and Oxygen Production from Water under Illumination: The Band Positions of Graphite Oxide. *J. Phys. Chem. C* **2011**, *115* (45), 22587–22597.

(154) Seredych, M.; Bandosz, T. J. Mechanism of Ammonia Retention on Graphite Oxides: Role of Surface Chemistry and Structure. *J. Phys. Chem. C* **2007**, *111* (43), 15596–15604.

(155) Ma, H. L.; Zhang, Y.; Hu, Q. H.; Yan, D.; Yu, Z. Z.; Zhai, M. Chemical Reduction and Removal of Cr(vi) from Acidic Aqueous Solution by Ethylenediamine-Reduced Graphene Oxide. *J. Mater. Chem.* **2012**, *22* (13), 5914–5916.

(156) Yang, S.-T.; Chen, S.; Chang, Y.; Cao, A.; Liu, Y.; Wang, H. Removal of Methylene Blue from Aqueous Solution by Graphene Oxide. *J. Colloid Interface Sci.* **2011**, *359* (1), 24–29.

(157) Channu, V. S.; Bobba, R.; Holze, R. Graphite and Graphene Oxide Electrodes for Lithium Ion Batteries. *Colloids Surfaces A Physicochem. Eng. Asp.* **2013**.

(158) Lin, Z.; Liu, Y.; Yao, Y.; Hildreth, O. J.; Li, Z.; Moon, K.; Wong, C. P. Superior Capacitance of Functionalized Graphene. *J. Phys. Chem. C* **2011**, *115* (14), 7120–7125.

(159) Zhang, J.; Cao, H.; Tang, X.; Fan, W.; Peng, G.; Qu, M. Graphite/Graphene Oxide Composite as High Capacity and Binder-Free Anode Material for Lithium Ion Batteries. *J. Power Sources* **2013**.

(160) Yang, S. T.; Chang, Y.; Wang, H.; Liu, G.; Chen, S.; Wang, Y.; Liu, Y.; Cao, A. Folding/Aggregation of Graphene Oxide and Its Application in Cu2+ Removal. *J. Colloid Interface Sci.* **2010**, *351* (1), 122–127.

(161) Pawar, R. C.; Lee, C. S. Sensitization of CdS Nanoparticles onto Reduced Graphene Oxide (RGO) Fabricated by Chemical Bath Deposition Method for Effective Removal of Cr(VI). *Mater. Chem. Phys.* **2013**.

(162) Ameen, S.; Shaheer Akhtar, M.; Seo, H. K.; Shik Shin, H. Advanced ZnO-Graphene Oxide Nanohybrid and Its Photocatalytic Applications. *Mater. Lett.* **2013**.

(163) Kim, B. H.; Hong, W. G.; Yu, H. Y.; Han, Y. K.; Lee, S. M.; Chang, S. J.; Moon, H. R.; Jun, Y.; Kim, H. J. Thermally Modulated Multilayered Graphene Oxide for Hydrogen Storage. *Phys. Chem. Chem. Phys.* **2012**, *14* (4), 1480–1484.

(164) Kim, J. M.; Hong, W. G.; Lee, S. M.; Chang, S. J.; Jun, Y.; Kim, B. H.; Kim, H. J. Energy Storage of Thermally Reduced Graphene Oxide. *Int. J. Hydrogen Energy* **2014**, *39* (8), 3799–3804.

(165) Kim, H. W.; Yoon, H. W.; Yoon, S.; Yoo, B. M.; Ahn, B. K.; Cho, Y. H.; Shin, H. J.; Yang, H.; Paik, U.; Kwon, S. Selective Gas Transport Through Few-Layered Graphene and Graphene Oxide Membranes. *Science (80-.).* **2013**, *342* (October), 91–95.

(166) Yumura, T.; Yamasaki, A. Roles of Water Molecules in Trapping Carbon Dioxide Molecules inside the Interlayer Space of Graphene Oxides. *Phys. Chem. Chem. Phys.* **2014**, *16* (20), 9656–9666.

(167) Alhwaige, A. A.; Agag, T.; Ishida, H.; Qutubuddin, S. Biobased Chitosan Hybrid Aerogels with Superior Adsorption: Role of Graphene Oxide in CO2 Capture. *RSC Adv.* **2013**, *3* (36), 16011–16020.

(168) Liu, S.; Sun, L.; Xu, F.; Zhang, J.; Jiao, C.; Li, F.; Li, Z.; Wang, S.; Wang, Z.; Jiang, X.; Zhou, H.; Yang, L.; Schick, C. Nanosized Cu-MOFs Induced by Graphene Oxide and Enhanced Gas Storage Capacity. *Energy Environ. Sci.* **2013**, *6* (3), 818.

(169) Lan, D. H.; Yang, F. M.; Luo, S. L.; Au, C. T.; Yin, S. F. Water-Tolerant Graphene Oxide as a High-Efficiency Catalyst for the Synthesis of Propylene Carbonate from Propylene Oxide and Carbon Dioxide. *Carbon N. Y.* **2014**.

(170) Vovusha, H.; Sanyal, S.; Sanyal, B. Interaction of Nucleobases and Aromatic Amino Acids with Graphene Oxide and Graphene Flakes. *J. Phys. Chem. Lett.* **2013**, *4* (21), 3710–3718.

(171) Zhang, J.; Jiang, D. Molecular Dynamics Simulation of Mechanical Performance of Graphene/Graphene Oxide Paper Based Polymer Composites. *Carbon N. Y.* **2014**, *67*, 784–791.

(172) Jiang, X.; Nisar, J.; Pathak, B.; Zhao, J.; Ahuja, R. Graphene Oxide as a Chemically Tunable 2-D Material for Visible-Light Photocatalyst Applications. *J. Catal.* **2013**, *299*, 204–209.

(173) Zhang, J.; Yu, J.; Jaroniec, M.; Gong, J. R. Noble Metal-Free Reduced Graphene Oxide-Zn x Cd 1-x S Nanocomposite with Enhanced Solar Photocatalytic H 2 -Production Performance. *Nano Lett.* **2012**, *12* (9), 4584–4589.

(174) Tang, S.; Cao, Z. Adsorption of Nitrogen Oxides on Graphene and Graphene Oxides: Insights from Density Functional Calculations. *J. Chem. Phys.* **2011**, *134* (4).

(175) Wang, L.; Zhao, J.; Wang, L.; Yan, T.; Sun, Y. Y.; Zhang, S. B. Titanium-Decorated Graphene Oxide for Carbon Monoxide Capture and Separation. *Phys. Chem. Chem. Phys.* **2011**, *13* (47), 21126–21131.

(176) Kim, D.; Kim, D. W.; Lim, H. K.; Jeon, J.; Kim, H.; Jung, H. T.; Lee, H. Intercalation of Gas Molecules in Graphene Oxide Interlayer: The Role of Water. *J. Phys. Chem. C* **2014**, *118* (20), 11142–11148.

(177) Küsgens, P.; Rose, M.; Senkovska, I.; Fröde, H.; Henschel, A.; Siegle, S.; Kaskel, S. Characterization of Metal-Organic Frameworks by Water Adsorption. *Microporous Mesoporous Mater.* **2009**, *120* (3), 325–330.

(178) Petit, C.; Mendoza, B.; O'Donnell, D.; Bandosz, T. J. Effect of Graphite Features on the Properties of Metal-Organic Framework/Graphite Hybrid Materials Prepared Using an in Situ Process. *Langmuir* **2011**, *27* (16), 10234–10242.

(179) Bradshaw, D.; Garai, A.; Huo, J. Metal-Organic Framework Growth at Functional Interfaces: Thin Films and Composites for Diverse Applications. *Chem. Soc. Rev.* **2012**, *41* (6), 2344–2381.

(180) Petit, C.; Bandosz, T. J. Engineering the Surface of a New Class of Adsorbents: Metal-Organic Framework/Graphite Oxide Composites. *J. Colloid Interface Sci.* **2015**, *447*, 139–151.

(181) Liu, X.-W.; Sun, T.-J.; Hu, J.-L.; Wang, S.-D. Composites of Metal-Organic Frameworks and Carbon-Based Materials: Preparations, Functionalities and Applications. *J. Mater. Chem. A* **2016**, *4* (10), 3584–3616.

(182) Moon, H. R.; Lim, D. W.; Suh, M. P. Fabrication of Metal Nanoparticles in Metal-Organic Frameworks. *Chem. Soc. Rev.* **2013**, *42* (4), 1807–1824.

(183) Górka, J.; Fulvio, P. F.; Pikus, S.; Jaroniec, M. Mesoporous Metal Organic Framework-Boehmite and Silica Composites. *Chem. Commun.* **2010**, *46* (36), 6798–6800.

(184) Juan-Alcañiz, J.; Gascon, J.; Kapteijn, F. Metal-Organic Frameworks as Scaffolds for the Encapsulation of Active Species: State of the Art and Future Perspectives. *J. Mater. Chem.* **2012**, *22* (20), 10102–10119.

(185) Zhang, Y.; Bo, X.; Nsabimana, A.; Han, C.; Li, M.; Guo, L. Electrocatalytically Active Cobalt-Based Metal-Organic Framework with Incorporated Macroporous Carbon Composite for

Electrochemical Applications. *J. Mater. Chem. A* **2015**, *3* (2), 732–738.

(186) Frackowiak, E.; Béguin, F. Carbon Materials for the Electrochemical Storage of Energy in Capacitors. *Carbon*. **2001**, pp 937–950.

(187) Zhu, Q. L.; Xu, Q. Metal-Organic Framework Composites. *Chem. Soc. Rev.* **2014**, *43* (16), 5468–5512.

(188) Petit, C.; Bandosz, T. J. Exploring the Coordination Chemistry of MOF-Graphite Oxide Composites and Their Applications as Adsorbents. *Dalt. Trans.* **2012**, *41* (14), 4027–4035.

(189) Kong, L.; Zhang, X.; Liu, H.; Wang, T.; Qiu, J. Preparation of ZIF-8 Membranes Supported on Macroporous Carbon Tubes via a Dipcoating-Rubbing Method. *J. Phys. Chem. Solids* **2015**, *77*, 23–29.

(190) Qiu, S.; Xue, M.; Zhu, G. Metal-Organic Framework Membranes: From Synthesis to Separation Application. *Chem. Soc. Rev.* **2014**, *43* (16), 6116–6140.

(191) Yue, Y.; Guo, B.; Qiao, Z. A.; Fulvio, P. F.; Chen, J.; Binder, A. J.; Tian, C.; Dai, S. Multi-Wall Carbon Nanotube@zeolite Imidazolate Framework Composite from a Nanoscale Zinc Oxide Precursor. *Microporous Mesoporous Mater.* **2014**.

(192) Zhao, J.; Gong, B.; Nunn, W. T.; Lemaire, P. C.; Stevens, E. C.; Sidi, F. I.; Williams, P. S.; Oldham, C. J.; Walls, H. J.; Shepherd, S. D.; Browe, M. A.; Peterson, G. W.; Losego, M. D.; Parsons, G. N. Conformal and Highly Adsorptive Metal-Organic Framework Thin Films via Layer-by-Layer Growth on ALD-Coated Fiber Mats. *J. Mater. Chem. A* **2015**, *3* (4), 1458–1464.

(193) Huang, A.; Liu, Q.; Wang, N.; Zhu, Y.; Caro, J. Bicontinuous Zeolitic Imidazolate Framework Zif-8@go Membrane with Enhanced Hydrogen Selectivity. *J. Am. Chem. Soc.* **2014**, *136* (42), 14686–14689.

(194) Choi, K. M.; Jeong, H. M.; Park, J. H.; Zhang, Y. B.; Kang, J. K.; Yaghi, O. M. Supercapacitors of Nanocrystalline Metal-Organic Frameworks. *ACS Nano* **2014**, *8* (7), 7451–7457.

(195) Bao, W.; Zhang, Z.; Qu, Y.; Zhou, C.; Wang, X.; Li, J. Confine Sulfur in Mesoporous Metal–Organic Framework @ Reduced Graphene Oxide for Lithium Sulfur Battery. *J. Alloys Compd.* **2014**, *582*, 334–340.

(196) Li, Y.; Yang, R. T.;. Hydrogen Storage in Metal-Organic Frameworks by Bridged Hydrogen Spillover. *J. Am. Chem.* **2006**, *128* (25), 8136–8137.

(197) Alcañiz-Monge, J.; Trautwein, G.; Pérez-Cadenas, M.; Román-Martínez, M. C. Effects of Compression on the Textural Properties of Porous Solids. *Microporous Mesoporous Mater.* **2009**.

(198) Shen, L.; Huang, L.; Liang, S.; Liang, R.; Qin, N.; Wu, L. Electrostatically Derived Self-Assembly of NH2-Mediated Zirconium MOFs with Graphene for Photocatalytic Reduction of Cr(Vi). *RSC Adv.* **2014**, *4* (5), 2546–2549.

(199) Andrew Lin, K. Y.; Hsu, F. K.; Lee, W. Der. Magnetic Cobalt-Graphene Nanocomposite Derived from Self-Assembly of MOFs with Graphene Oxide as an Activator for Peroxymonosulfate. *J. Mater. Chem. A* **2015**, *3* (18), 9480–9490.

(200) Ramsden, W. Separation of Solids in the Surface-Layers of Solutions and Suspensions. *Proc. R. Soc. London* **1903**, *72*, 156–164.

(201) Pickering, S. U. Pickering:Emulsions. *J. Chem. Soc., Trans.,* **1907**, *91*, 2001–2021.

(202) Bian, Z.; Xu, J.; Zhang, S.; Zhu, X.; Liu, H.; Hu, J. Interfacial Growth of Metal Organic Framework/Graphite Oxide Composites through Pickering Emulsion and Their CO<inf>2</Inf> Capture Performance in the Presence of Humidity. *Langmuir* **2015**, *31* (26), 7410–7417.

(203) Petit, C.; Levasseur, B.; Mendoza, B.; Bandosz, T. J. Reactive Adsorption of Acidic Gases on MOF/Graphite Oxide Composites. *Microporous Mesoporous Mater.* **2012**, *154*, 107–112.

(204) Zhao, Y.; Ding, H.; Zhong, Q. Synthesis and Characterization of MOF-Aminated Graphite Oxide Composites for CO2 Capture. *Appl. Surf. Sci.* **2013**, *284* (10), 138–144.

(205) Zu, D. D.; Lu, L.; Liu, X. Q.; Zhang, D. Y.; Sun, L. B. Improving Hydrothermal Stability and Catalytic Activity of Metal-Organic Frameworks by Graphite Oxide Incorporation. *J. Phys. Chem. C* **2014**, *118* (34), 19910–19917.

(206) Balandin, A. A. Thermal Properties of Graphene and Nanostructured Carbon Materials. *Nat. Mater.* **2011**, *10* (8), 569–581.

(207) Shen, Y.; Li, Z.; Wang, L.; Ye, Y.; Liu, Q.; Ma, X.; Chen, Q.; Zhang, Z.; Xiang, S. Cobalt-Citrate Framework Armored with Graphene Oxide Exhibiting Improved Thermal Stability and Selectivity for Biogas Decarburization. *J. Mater. Chem. A* **2015**, *3* (2), 593–599.

(208) Talin, A. A.; Centrone, A.; Ford, A. C.; Foster, M. E.; Stavila, V.; Haney, P.; Kinney, R. A.; Szalai, V.; El Gabaly, F.; Yoon, H. P.; Léonard, F.; Allendorf, M. D. Tunable Electrical Conductivity in Metal-Organic Framework Thin-Film Devices. *Science (80-.).* **2014**, *343* (6166), 66–69.

(209) Banerjee, P. C.; Lobo, D. E.; Middag, R.; Ng, W. K.; Shaibani, M. E.; Majumder, M. Electrochemical Capacitance of Ni-Doped Metal Organic Framework and Reduced Graphene Oxide Composites: More than the Sum of Its Parts. *ACS Appl. Mater. Interfaces* **2015**, *7* (6), 3655–3664.

(210) Alfè, M.; Gargiulo, V.; Lisi, L.; Di Capua, R. Synthesis and Characterization of Conductive Copper-Based Metal-Organic Framework/Graphene-like Composites. *Mater. Chem. Phys.* **2014**.

(211) Petit, C.; Bandosz, T. J. MOF-Graphite Oxide Composites: Combining the Uniqueness of Graphene Layers and Metal-Organic Frameworks. *Adv. Mater.* **2009**, *21* (46), 4753–4757.

(212) Liu, J. W.; Zhang, Y.; Chen, X. W.; Wang, J. H. Graphene Oxide-Rare Earth Metal-Organic Framework Composites for the Selective Isolation of Hemoglobin. *ACS Appl. Mater. Interfaces* **2014**, *6* (13), 10196–10204.

(213) Wen, Y. H.; Cheng, J. K.; Feng, Y. L.; Zhang, J. Synthesis and Crystal Structure of [La(BTC)(H2O) 6]N. *Chinese J. Struct. Chem.* **2005**, *24* (12), 1440–1444.

(214) Kumar, R.; Jayaramulu, K.; Maji, T. K.; Rao, C. N. R. R. Hybrid Nanocomposites of ZIF-8 with Graphene Oxide Exhibiting Tunable Morphology, Significant CO2 Uptake and Other Novel Properties. *Chem. Commun.* **2013**, *49* (43), 4947.

(215) Klinowski, J.; Almeida Paz, F. A.; Silva, P.; Rocha, J. Microwave-Assisted Synthesis of Metal-Organic Frameworks. *Dalt. Trans.* **2011**, *40* (2), 321–330.

(216) Ahmed, I.; Khan, N. A.; Jhung, S. H. Graphite Oxide/Metal-Organic Framework (MIL-101): Remarkable Performance in the Adsorptive Denitrogenation of Model Fuels. *Inorg. Chem.* **2013**, *52* (24), 14155–14161.

(217) Petit, C.; Burress, J.; Bandosz, T. J. The Synthesis and Characterization of Copper-Based Metal-Organic Framework/Graphite Oxide Composites. *Carbon N. Y.* **2011**, *49* (2), 563–572.

(218) Kreno, L. E.; Leong, K.; Farha, O. K.; Allendorf, M.; Van Richard P., D.; Hupp, J. T. Metal-Organic Framework Materials as Chemical Sensors. *Chem. Rev. (Washington, DC, United States)* **2012**, *112*, 1105–1125.

(219) Lin, X.; Gao, G.; Zheng, L.; Chi, Y.; Chen, G. Encapsulation of Strongly Fluorescent Carbon Quantum Dots in Metal-Organic Frameworks for Enhancing Chemical Sensing. *Anal. Chem.* **2014**, *86* (2), 1223–1228.

(220) Wang, X.; Wang, Q.; Wang, Q.; Gao, F.; Gao, F.; Yang, Y.; Guo, H. Highly Dispersible and Stable Copper Terephthalate Metal-Organic Framework-Graphene Oxide Nanocomposite for an Electrochemical Sensing Application. *ACS Appl. Mater. Interfaces* **2014**, *6* (14), 11573–11580.

(221) Lee, J. H.; Kang, S.; Jaworski, J.; Kwon, K. Y.; Seo, M. L.; Lee, J. Y.; Jung, J. H. Fluorescent Composite Hydrogels of Metal-Organic Frameworks and Functionalized Graphene Oxide. *Chem. - A Eur. J.* **2012**, *18* (3), 765–769.

(222) Hao, L.; Song, H.; Su, Y.; Lv, Y. A Cubic Luminescent Graphene Oxide Functionalized Zn-Based Metal-Organic Framework Composite for Fast and Highly Selective Detection of Cu2+ Ions in Aqueous Solution. *Analyst* **2014**, *139* (4), 764–770.

(223) Kötz, R.; Carlen, M. Principles and Applications of Electrochemical Capacitors. *Electrochim. Acta* **2000**.

(224) Chen, R.; Zhao, T.; Tian, T.; Cao, S.; Coxon, P. R.; Xi, K.; Fairen-Jimenez, D.; Vasant Kumar, R.; Cheetham, A. K. Graphene-Wrapped Sulfur/Metal Organic Framework-Derived Microporous Carbon Composite for Lithium Sulfur Batteries. *APL Mater.* **2014**, *2* (12).

(225) Zhao, Z.; Wang, S.; Liang, R.; Li, Z.; Shi, Z.; Chen, G. Graphene-Wrapped Chromium-MOF(MIL-101)/Sulfur Composite for Performance Improvement of High-Rate Rechargeable Li-S Batteries. *J. Mater. Chem. A* **2014**, *2* (33), 13509–13512.

(226) Jahan, M.; Liu, Z.; Loh, K. P. A Graphene Oxide and Copper-Centered Metal Organic Framework Composite as a Tri-Functional Catalyst for HER, OER, and ORR. *Adv. Funct. Mater.* **2013**, *23* (43), 5363–5372.

(227) Jia, G.; Zhang, W.; Jin, Z.; An, W.; Gao, Y.; Zhang, X.; Liu, J. Electrocatalytically Active MOF/Graphite Oxide Hybrid for Electrosynthesis of Dimethyl Carbonate. *Electrochim. Acta* **2014**.

(228) Wei, Y.; Hao, Z.; Zhang, F.; Li, H. A Functionalized Graphene Oxide and Nano-Zeolitic Imidazolate Framework Composite as a Highly Active and Reusable Catalyst for [3 + 3] Formal Cycloaddition Reactions. *J. Mater. Chem. A* **2015**, *3* (28), 14779–14785.

(229) Huang, X.; Zheng, B.; Liu, Z.; Tan, C.; Liu, J.; Chen, B.; Li, H.; Chen, J.; Zhang, X.; Fan, Z.; Zhang, W.; Guo, Z.; Huo, F.; Yang, Y.; Xie, L. H.; Huang, W.; Zhang, H. Coating Two-Dimensional Nanomaterials with Metal-Organic Frameworks. *ACS Nano* **2014**, *8* (8), 8695–8701.

(230) Li, L.; Liu, X. L.; Geng, H. Y.; Hu, B.; Song, G. W.; Xu, Z. S. A MOF/Graphite Oxide Hybrid (MOF: HKUST-1) Material for the Adsorption of Methylene Blue from Aqueous Solution. *J. Mater. Chem. A* **2013**, *1* (35), 10292–10299.

(231) Zhou, Y.; Zhou, L.; Zhang, X.; Chen, Y. Preparation of Zeolitic Imidazolate Framework-8 /Graphene Oxide Composites with Enhanced VOCs Adsorption Capacity. *Microporous Mesoporous Mater.* **2016**, *225*, 488–493.

(232) Zhao, Y.; Seredych, M.; Zhong, Q.; Bandosz, T. J. Aminated Graphite Oxides and Their Composites with Copper-Based Metal–Organic Framework: In Search for Efficient Media for CO2 Sequestration. *RSC Adv.* **2013**, *3* (25), 9932.

(233) Chen, Y.; Lv, D.; Wu, J.; Xiao, J.; Xi, H.; Xia, Q.; Li, Z. A New MOF-505@GO Composite with High Selectivity for CO2/CH4 and CO2/N2 Separation. *Chem. Eng. J.* **2017**, *308*, 1065–1072.

(234) Zhou, X.; Huang, W.; Miao, J.; Xia, Q.; Zhang, Z.; Wang, H.; Li, Z. Enhanced Separation Performance of a Novel Composite Material GrO@MIL-101 for CO2/CH4 Binary Mixture. *Chem. Eng. J.* **2015**, *266* (April), 339–344.

(235) Su, L.; Hu, J.; Wang, K.; Wang, Y.; Zhang, W.; Cao, Y.; Zhao, N. Facile Synthesis and Enhanced Adsorption Ability of Pt-GO/MOF Nanomaterials. *Mater. Manuf. Process.* **2016**, *31* (2), 141–145.

(236) Yan, J.; Yu, Y.; Ma, C.; Xiao, J.; Xia, Q.; Li, Y.; Li, Z. Adsorption Isotherms and Kinetics of Water Vapor on Novel Adsorbents MIL-101(Cr)@GO with Super-High Capacity. *Appl. Therm. Eng.* **2015**, *84*, 118–125.

(237) Zhou, X.; Huang, W.; Shi, J.; Zhao, Z.; Xia, Q.; Li, Y.; Wang, H.; Li, Z. A Novel MOF/Graphene Oxide Composite GrO@MIL-101 with High Adsorption Capacity for Acetone. *J. Mater. Chem. A* **2014**, *2* (13), 4722–4730.

(238) Huang, W.; Zhou, X.; Xia, Q.; Peng, J.; Wang, H.; Li, Z. Preparation and Adsorption Performance of GrO @ Cu-BTC for Separation of CO 2 / CH 4. **2014**, *101*.

(239) Nordin, N. A. H. M.; Ismail, A. F.; Yahya, N. Zeolitic Imidazole Framework 8 Decorated Graphene Oxide (ZIF-8/GO) Mixed Matrix Membrane (MMM) for CO2/CH4separation. *J. Teknol.* **2017**, *79* (1–2), 59–63.

(240) Hu, Y.; Wei, J.; Liang, Y.; Zhang, H.; Zhang, X.; Shen, W.; Wang, H. Zeolitic Imidazolate Framework/Graphene Oxide Hybrid Nanosheets as Seeds for the Growth of Ultrathin Molecular Sieving Membranes. *Angew. Chemie - Int. Ed.* **2016**, *55* (6), 2048–2052.

(241) Wang, X.; Chi, C.; Tao, J.; Peng, Y.; Ying, S.; Qian, Y.; Dong, J.; Hu, Z.; Gu, Y.; Zhao, D. Improving the Hydrogen Selectivity of Graphene Oxide Membranes by Reducing Non-Selective Pores with Intergrown ZIF-8 Crystals. *Chem. Commun.* **2016**, *52* (52), 8087–8090.

(242) Zheng, Y.; Zheng, S.; Xue, H.; Pang, H. Metal-Organic Frameworks/Graphene-Based Materials: Preparations and Applications. *Adv. Funct. Mater.* **2018**, *28* (47), 1–28.

(243) Li, W.; Zhang, Y.; Su, P.; Xu, Z.; Zhang, G.; Shen, C.; Meng, Q. Metal-Organic Framework Channelled Graphene Composite Membranes for H2/CO2 Separation. *J. Mater. Chem. A* **2016**, *4* (48), 18747–18752.

(244) Szczęśniak, B.; Choma, J.; Jaroniec, M. Gas Adsorption Properties of Hybrid Graphene-MOF Materials. *J. Colloid Interface Sci.* **2018**, *514*, 801–813.

(245) Dong, L.; Chen, M.; Li, J.; Shi, D.; Dong, W.; Li, X.; Bai, Y. Metal-Organic Framework-Graphene Oxide Composites: A Facile Method to Highly Improve the CO2 Separation Performance of Mixed Matrix Membranes. *J. Memb. Sci.* **2016**, *520*, 801–811.

(246) Sui, X.; Ding, H.; Yuan, Z.; Leong, C. F.; Goh, K.; Li, W.; Yang, N.; D'Alessandro, D. M.; Chen, Y. The Roles of Metal-Organic Frameworks in Modulating Water Permeability of Graphene Oxide-Based Carbon Membranes. *Carbon N. Y.* **2019**, *148*, 277–289.

(247) Lin, L.-C.; Paik, D.; Kim, J. Understanding Gas Adsorption in MOF-5/Graphene Oxide Composite Materials. *Phys. Chem. Chem. Phys.* **2017**, *19* (18), 11639–11644.

CHAPTER 2 – MOLECULAR SIMULATION METHODOLOGY

2.1. Introduction

Molecular modelling is a powerful tool for constructing realistic molecular models and helps in predicting several experimental observations or mechanisms in a convincing manner that cannot be readily accessible in any other way i.e., by theory, or in experiments individually. It bridges a range of time and length scales i.e., quantum, atomistic (all-atom), coarse-grained and mesoscale at different resolutions that can be used to predict various phenomena as shown in Figure 2.1. In my PhD, I mostly focused on the combination of quantum methods and atomistic-based simulations (also called force field-based simulations) to build microscopic models for both MOF and GO and further analyse the interactions between these two solids once assembled in binary composite systems prior to explore their adsorption behaviours with respect to different adsorbates.

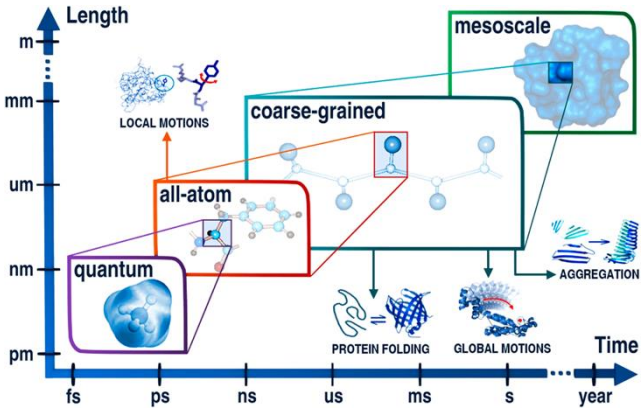

Figure 2.1 Molecular modelling schemes with length scales and time in y and x axis. Adapted from Ref.[1]

In this chapter, I introduce a short overview of the theoretical methods that have been used to model the individual MOFs and GO as well as their adsorption properties. The chapter is divided into three sections, starting off with the input required to run an atomistic simulation, i.e. the microscopic descriptions of MOF, GOs and adsorbates as well as the interatomic potentials (called force field along the manuscript) to describe the interactions between all these components. The next section introduces basic concepts of atomistic molecular simulations including Monte Carlo and Molecular dynamics methods while the third part is dedicated to the description of the main aspects involved in quantum calculations.

2.2. Force Field Molecular Simulations

2.2.1. Microscopic description of the adsorbents and adsorbates

- Adsorbents

To model any porous solids, first requirement is to have a realistic atomistic representation of the framework which can be obtained from the experimentally known crystallographic coordinates. The next major complexity lies on whether the structures are crystalline or non-crystalline, if their morphology/topology are controlled or not, if they are characterized by a chemical disorder or the positions of each atom type are well-defined, and if the structure contains chemical/structural defects[2]. Here, I have provided a small brief on types of adsorbents found in the literature.

MOFs, **GOs** and **Zeolites** can be usually classified under **Crystalline solids** (Figure 2.2) like other porous materials.

MOFs are formed by the assembly of inorganic nodes and organic linkers which usually leads to relatively uniform atom distributions and thus well-defined pore architectures. The positions of all atoms of these frameworks are generally experimentally resolved by X-ray diffraction and if needed this experimental effort can be assisted by molecular simulations tools for the most complex solids (large unit cell, low symmetry, poor crystallinity). On the other hand, defects in such structures can arise due to missing ligands or inorganic nodes. These latter features can be characterized by a combination of experimental techniques like Nuclear-Magnetic Resonance (NMR), Infra-red (IR), etc. It is to be noticed that some of the MOF frameworks undergo structural changes under diverse stimuli (adsorption, temperature, mechanical pressure). This behaviour is called as breathing (space group and large magnitude volume changes), swelling (continuous volume change without change of symmetry) or flexibility (local structural distortion associated with a low magnitude of volume change). Capturing such complex structural behaviours usually requires accurate force-field parameters to describe the bond-stretching, bond-bending, and torsional intra-molecular motions of the MOF framework (see section 2.2.2).

GOs are usually synthesized following the recipe described by Brodie, Staudenmaier and Hummers' methods[3], which involves the oxidation of graphite to various level as quantified by

the carbon/oxygen ratio that depends on the experimental condition as well as the length of reaction. Furthermore functionalization of GOs is experimentally widely investigated as a plausible strategy to enhance their adsorption performances[4], however, without a clear picture how these functional groups (mostly amine) are distributed in the GO layers. This makes highly challenging the definition of a microscopic model for this family of materials that can also show a swelling behaviour upon adsorption associated with a significant change of the interlayer distance. Indeed computational methods are increasingly used to understand the structure of GOs based on the experimental data gained from infrared absorption spectroscopy and X-ray photoelectron spectroscopy (XPS)[5]. One of the well elaborated initial model was developed by Lerf and Klinowski et al[6]. This model suggested that alcohol and epoxy groups are distributed randomly on the basal plane while the carboxyl groups are located on the edges. However, I will demonstrate in this thesis that this model needs to be improved to accurately describe the locations of the different oxo-groups as well as the amine-functions that are incorporated during the functionalization of the materials.

Zeolites are natural or synthetic crystalline solids. This 3D framework is created by linking corner sharing hydrated aluminosilicates made of Aluminium (III) or Silicon (IV) tetrahedra forming low density material with varied size and shape of void volumes. They have uniform pore size of 0.5-1.2 nm[7] and their crystal structures can be downloaded from the International Zeolite Association Structure Database. The complexity of these structures lies in the exact distribution of Si, Al atoms over the available T-sites and the location of the extra-framework cations in the pores in the case of Alumino-silicate zeolites. The complexity arises when we deal with more complex chemical composition of zeolite architectures including the Silico-alumino phosphate or Silico-germanate zeolites among others which involve the distribution of several types of atoms in the framework leading to a chemical disorder of the 3D structure architecture. Although bulk zeolites are well characterized using tools like NMR, crystallography but techniques like atomistic simulations are viable tools not only for modelling the structure, stability and coordination of atoms and have proven to be potent for investigating the reactivity within the porous host.

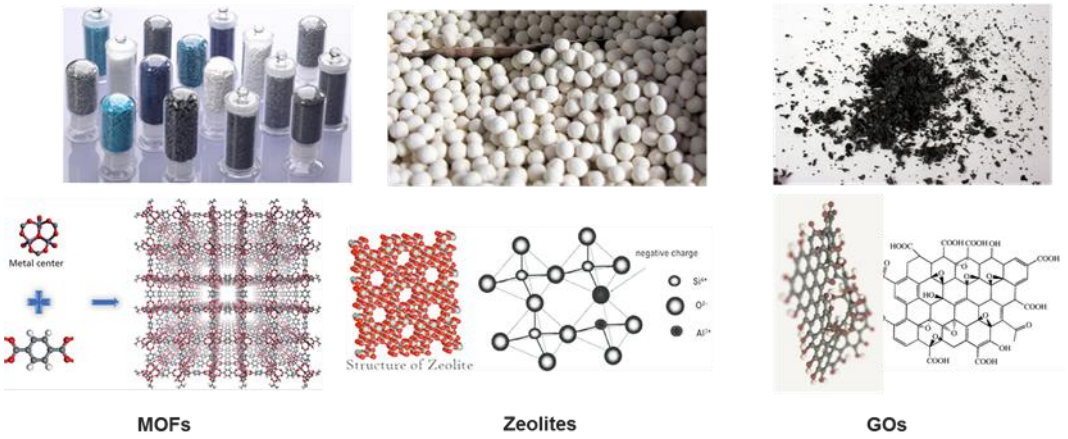

Figure 2.2 Illustration of the porous crystalline solids in real world and its microscopic structural description, a) MOFs, Adapted from Ref.[8,9], b) Zeolites, Adapted from Ref.[10] and c) Graphene oxide (GO). Adapted from Ref.[11]

Silica, **polymers**, **activated carbons** etc. are classified under **Non-crystalline porous materials** (Figure 2.3). Silica mesoporous solids have a wide range of existing topologies/morphologies. Every sample has its own surface complexities in terms of roughness, defects (constriction and tortuosity) etc. leading to drastic change in its diverse properties. Microscopic models for such porous solids are usually built individually being tailored for each sample to reproduce their structural features. Indeed, on-lattice MC simulation of surfactant–solvent–silica systems[12] that mimic the synthesis conditions are usually employed to generate realistic pore models for these solids. Another family of non-crystalline material is **polymer**. Different computational tools[13] can be used to attain *in silico* stepwise polymerization of the monomers based on tuneable distance and orientation criteria for the acceptance of the bonds. The so-constructed models are usually validated by a good agreement between their resulting density and the experimental data. Another class of non-crystalline material is the family of **activated carbons** which are ordered graphite-like layers that can be represented by sophisticated slit-pore models[14].

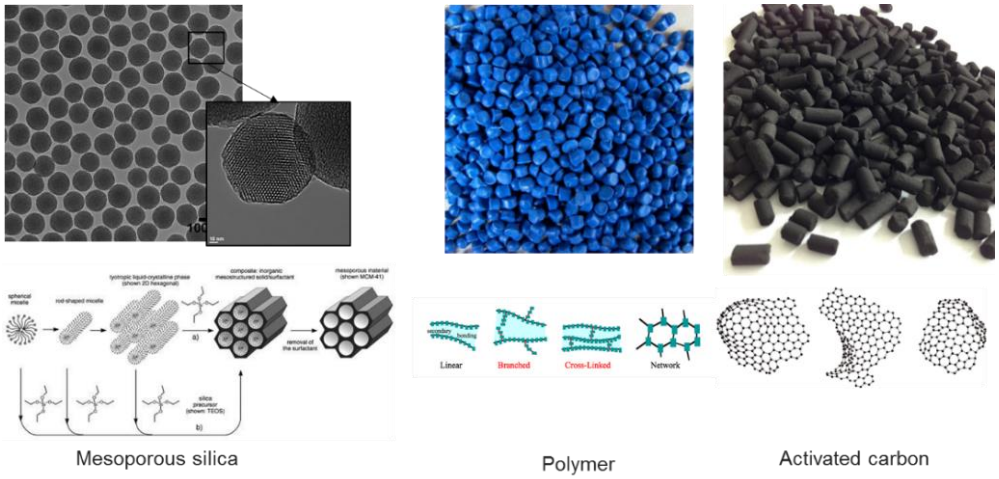

Figure 2.3 Illustration of the microscopic structural description of porous non-crystalline solids, a) Mesoporous silica, Adapted from Ref.[15–17], b) Polymer, Adapted from Ref.[18] and c) Activated carbon, Adapted from Ref.[19]

I have mostly confined my study to the crystalline MOFs and GOs solids. Regarding MOFs, I have considered one flexible architectures (ZIF-8[20]) and two rigid architectures {MIL-69(Al)[21] and MIL-91(Ti)[22]} with their atoms maintained fixed to the positions obtained experimentally. Each atom of the MOF was treated by a single charged Lennard-Jones (LJ) centre as it is usually operated in the field of porous materials. The LJ parameters in MOFs are generally taken from generic force fields available in the literature, in particular the OPLS-AA[23], Universal force field (UFF)[24], DREIDING[25] force fields. These force fields contain LJ parameters for most of the atoms of the periodic table that are transferable for different types of materials, although the UFF is more usually applied for the modelling of the inorganic node of the MOF while the DREIDING and OPLS force fields are more often used to describe the organic molecules. The charges assigned to all atoms of the MOF frameworks can be calculated by several methods including the charge equilibration or quantum calculation (e.g. Mulliken, ESP and ChelpG) approaches (see Section 2.3)

I have also developed two GO models i.e., pristine and it amino-pyridine functionalized versions. In this respect, an atomistic representation of the GO model was first derived integrating the nature and concentration of functional groups, i.e., epoxy, hydroxyl, carboxylic, and amine functions, as deduced from the experimental XPS data collected by our H2020 EU GRAMOFON partners. The monolayer structure was treated at the DFT level to energy minimize the initial structure. Later the structure was expanded at the force field level using a flexible description of the structure and all atoms of the GO were treated as charged LJ sites

with LJ parameters taken from OPLS-AA[23] force field while the partial charges were calculated at the quantum-level using the electrostatic potential scheme using CHELPG[26,27].

➢ Adsorbates

The microscopic models (interatomic potential parameters, charges, geometries) of the fluids are usually validated by a good agreement between their simulated and experimental intrinsic properties such as compressibility, density, dipole, and liquid vapor equilibrium (LVE) data. This latter data is one of the most reliable bases for the validation of a fluid model, even though experimental LVE data are often scarce for many systems. I have considered different adsorbates in my work including water and adsorbed gases (CO_2, N_2 and CH_4) whose microscopic models have been detailed as follows:

- Many models are available to describe the rigid non-polarizable **H_2O** potentials. I have considered the SPC/E model for this molecule since it satisfactorily define and explore the aggregation process of GO layers in water[28]. This model was effective in modelling the water contact angle on graphite surface experimentally. SPC/E is three-sited model, the partial charges are assigned to the centre of the oxygen and hydrogen atoms while a single LJ interacting centre is assigned to the oxygen atoms. The molecule is considered as rigid with a HOH angle of 109.5° and an O–H distance of 0.957 Å.
- Regarding the gases, **CO_2** was treated as a rigid linear triatomic model, with three charged LJ interaction sites (C-O bond length of 1.149 Å) located on each atom taken from the EPM2 force field as previously derived by Harris and Yung[29]. **N_2** was described by a three charged sites model taken from the TraPPE force field with two LJ sites located at the N atoms while a third site present at its centre of mass and only involves electrostatic interactions as previously described in the TraPPE potential mode[30] and from the paper of Straub et al[31] respectively. Finally, **CH_4** was described by the TraPPE uncharged single LJ interacting site model[32].

2.2.2. Interatomic potentials

The total potential energy of an adsorbate-adsorbent system can be analytically described as a sum of bonded and non-bonded energy terms:

$$U = U_{bonded} + U_{non\text{-}bonded} \quad (1)$$

The bonded energy term describes the intra-molecular interactions of the adsorbent and/or adsorbate and is most commonly described by the sum of bond (two-body), bond angle (three-body) and dihedral angle (four-body) potentials (equation (2))

$$U_{bonded} = \sum_{bonds} U_b(r_{ij}) + \sum_{angles} U_a(\theta_{ijk}) + \sum_{dihedrals} U_d(\emptyset_{ijkl}) + \sum_{imp-dihedrals} U_{id}(\xi_{ijkl}) \quad (2)$$

In my PhD, I used this analytical form to describe the flexibility of the MOF ZIF-8 as well as the GOs. However, the adsorbate molecules were treated as rigid molecules. I have not included a full flexibility of the other two MOFs, MIL-69 and MIL-91, since no reliable force field parameters were available. Also, in a first approximation, it is known that these materials do not show large flexibility upon adsorption[22,33], hence in these models we considered atoms fixed in their initial positions.

The non-bonded term is usually expressed by two terms to account for the electrostatic and the van der Waals interactions which are pair-additive. For each atom pair i and j with separation distance r_{ij}., the non-bonded term is expressed by equation (3)

$$U_{non-bonded}(r_{ij}) = U_{coulomb}(r_{ij}) + U_{vdw}(r_{ij}) \quad (3)$$

The electrostatic interactions are most often described by a classical Coulombic potential, as given in the equation below

$$U_{ij}^{coulomb} = \sum_i \sum_j \frac{1}{4\pi\varepsilon_0} \frac{q_i q_j}{r_{ij}} \quad (4)$$

where q_i and q_j are the charges associated with interacting atoms *i* and *j*, and ε_0 is the vacuum permittivity.

The van der Waals interactions (U_{vdw}) can be decomposed into two contributions i.e., attractive and repulsive part. In the former, the atoms are separated causing mutual attraction due to the formation of permanent or induced dipoles, above a long separation distance, the intermolecular potential becomes negative and approaches zero as the separation distance increases towards infinite. In the repulsive part, the intermolecular potential becomes increasingly positive. The large potential energy is energetically unfavourable, which is due to

atoms coming very close to each other leading to an overlap of their electronic clouds causing a strong repulsion between the atoms (as shown in Figure 2.4). This attractive potential is also called as dispersive potential and can be modelled by different functions r^{-6}, r^{-8} or r^{-10} accounting for dipole-dipole, dipole-quadrupole and quadrupole-quadrupole interactions. Furthermore, the repulsive contribution are commonly expressed by r^{-12} or by the Born-Mayer function $(A.e^{-Br})^2$.

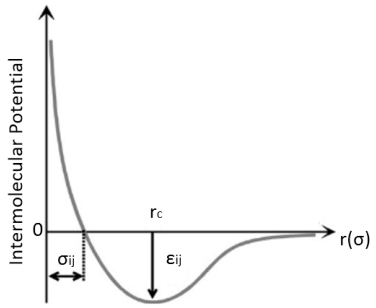

Figure 2.4 Plot of the Lennard–Jones potential function. Adapted from Ref.[2]

In this work, I have mostly used 12-6 Lennard Jones (12-6 LJ) potentials to describe the van der Waals interactions as defined by equation (5). The $(\sigma/r)^{12}$ describes the repulsive forces between the atoms while $(\sigma/r)^6$ describes the attraction forces.

$$U_{ij}^{vdw} = \sum_i \sum_{j>i} 4\varepsilon_{ij} \left[\left(\frac{\sigma_{ij}}{r_{ij}} \right)^{12} - \left(\frac{\sigma_{ij}}{r_{ij}} \right)^{6} \right] \qquad (5)$$

Here the ε is the Lennard-Jones energy well depth and measures how strongly the two atoms interact with each other, the deeper the ε the stronger the interaction. σ is the vdw radius which defines how close two non-bonding atoms can get which is always equal to half of internuclear distance between two atoms; r is the separation distance between the atoms measured from the centre of the atom and r_c is the critical distance from where the repulsion begins to occur.

The cross LJ parameters for the unlike pair of atoms are calculated by Lorentz-Berthelot mixing rule[34] obtained from the individual ε_i and σ_i parameters assigned to each atom or pseudo-atom which are related to their polarizability and size respectively using mixing rules. In the case of the Lorentz-Berthelot mixing rule[34] these parameters are obtained by using arithmetic and geometric averages for σ and ε respectively as follows:

$$\sigma_{ij} = \frac{\sigma_i + \sigma_j}{2} \text{ and } \varepsilon_{ij} = \sqrt{\varepsilon_i \varepsilon_j}$$

Usually the system with N atoms is simulated surrounded by vacuum but in most cases where we must simulate the bulk properties (liquids or solids), certain boundary conditions are required. ***Periodic boundary condition (PBC)*** is formed by an infinite replica of itself as shown in Figure 2.5. Typically, the selected molecule in the primary cell has eight replicas in red. In a simulation trajectory, if an atom moves in the original box, its periodic image moves in the same way in each of the neighbouring boxes. As an atom leaves the primary box, one of its images will appear through the opposite face. The primary box has no boundary walls or surface atoms and forms a suitable axis system for measuring the coordinates of the N atoms. The number density of the primary box is conserved as well as for the entire system of eight replicas. The coordinates of the atoms in the central box are stored but not of its images. PBC cell can be of any shape i.e., cubic, hexagonal, dodecahedron etc. In PBC, the atoms can interact with all periodic images including itself. This can sometimes generate artificial correlation effect and make the calculation very expensive. Hence PBC are combined with the minimum image convention such that only the nearest image (white square) of each particle is considered for short-range interaction as shown in Figure 2.5. The white square has the same number of molecules as that of the primary box. The interactions can be neglected above this range. The red circle represents the potential cut-off. The potential cut-off is applied so that we don't ignore important interactions usually termed as $r_{cut.}$

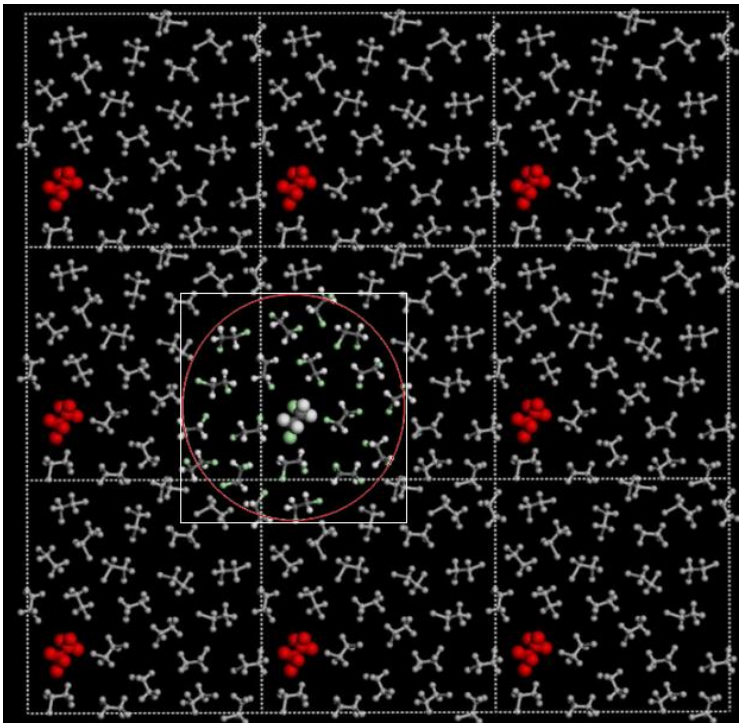

Figure 2.5 Schematic representation of periodic boundary condition. Adapted from Ref.[35]

Treatment of non-bonded interactions.

The most time-consuming part of an atomistic simulation is the calculation of the non-bonded interactions. An atom in a large system surrounded by many atoms leads to calculation of its non-bonded interactions very expensive. Therefore, the assessment of pairwise interactions, $U(r_{ij})$ is often restricted to a local area within a cut-off radius (r_{cut}). LJ or vdw interactions are usually treated with a cut-off distance of at least 10.0 to 12.0 Å. Over the years, these interactions are cut using many ways as shown in Figure 2.6. For problems associated with truncated (discontinuous) potential, the LJ potential is often modified by a switch/shift function that ensures that the energy goes to zero smoothly when approaching the cut-off distance.

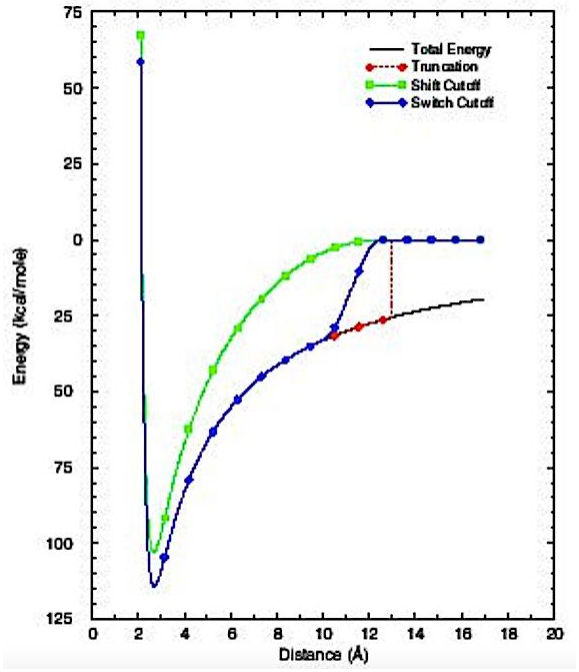

Figure 2.6 The graph showing the different ways to cut-off the interaction between two atoms: truncated, shift, switch. Adapted from Ref.[36]

Electrostatic interactions are of long ranged-type and do not decay to zero within interaction cut-off distances usually employed in atomistic simulations. Here ***Ewald summation method*** is usually preferred for the correct treatment for long-range electrostatic interactions. Variations of the Ewald method for periodic systems include the Smooth particle-mesh Ewald method (SPME) which I have used in my simulations. This method separates the electrostatic interactions into two contributions, a short-range and a long-range one. The short-range part is evaluated in real space while the long-range part in Fourier space and includes the interactions of their respective charges with all its period images.

The Coulombic interactions (equation (6)) in a periodic system using PBC consider all contribution from replicated cell. Here, R represents the vector connecting the primary cell to each of its replicas.

$$U_{ij}^{coulomb} = \sum_i \sum_j \frac{1}{4\pi\varepsilon_0} \frac{q_i q_j}{|r_{ij}+R|} \quad (6)$$

This sum is conditionally convergent hence Ewald suggested adding to each point charge a charge distribution of opposite sign through gaussian distribution (equation (7)), such that the electrostatic potential caused by the screened charges becomes short-ranged and can then be treated in real space.

$$\rho(r) = -q_i \left(\frac{\alpha}{\pi}\right)^{3/2} exp(-\alpha r^2) \quad (7)$$

The subsequent real space contribution is

$$U_{real,r}^{coulomb} = \frac{1}{2} \sum_{ij} \frac{q_i q_j \, erfc(\sqrt{\alpha} r_{ij})}{r_{ij}} \quad (8)$$

Here parameter α makes this potential enough small at the chosen cut-off to be safely truncated. Now to regain the original system, a compensating Gaussian distribution is added to equation (7) of opposite sign, which can be treated in reciprocal space to give equation:

$$U_{fourier,K}^{coulomb} = \frac{1}{2V} \sum_{k \neq 0} \frac{4\pi}{k^2} |\rho(k)|^2 \exp\left(-\frac{k^2}{4\alpha}\right) \quad (9)$$

with

$$\rho(K) = \sum_i q_i \ \exp(\mathrm{i}k r_i) \quad (10)$$

the self-interaction emerging from the unphysical interaction between the point charge and its compensating cloud needs to be corrected as follows:

$$U_{self}^{coulomb} = \left(\frac{\alpha}{\pi}\right)^{1/2} \sum_i q_i^2 \quad (11)$$

The sum in reciprocal space must be implemented up to a large k vector, $k_{max} = \frac{2\pi}{L} n_{max}$, which depends on the chosen value for α. Three parameters: the cut-off R_c, α and n_{max} are needed to converge the Ewald sum. R_c is normally taken as the same cut-off employed for the LJ potential for computational convenience. These values can be refined to optimize the computing

time without losing accuracy. The general concept of the Ewald summation method is shown in Figure 2.7.

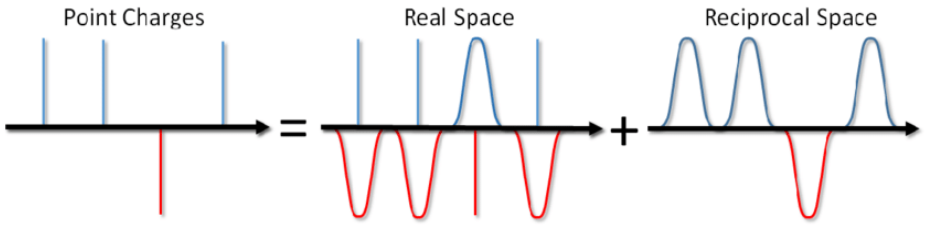

Figure 2.7 The illustration showing Ewald summation method which considers a set of point charges as a sum of screened charges in real space minus the sum of the screening background in reciprocal space. Adapted from Ref.[37]

2.2.3. Monte Carlo simulations

2.2.3.1. Basic principles

Monte Carlo (MC) is a stochastic method, i.e., non-time dependent, able to calculate the equilibrium properties of porous solids. A large sequence of random configurations comes from the desired Boltzmann distribution each being accepted or rejected according to a certain probability. Such a sampling method further allows the computation of average properties that can be directly compared to those experimentally observed. In my thesis, I have used MC simulations mostly in the grand canonical ensemble to explore the adsorption of gases for the MOF/GO composite systems.

In Grand Canonical Monte Carlo (GCMC) ensemble, the calculations are performed at constant μVT ensemble, where μ, V and T are chemical potential, volume and temperature, respectively. From here an adsorption isotherm can be obtained, where at any temperature, the average number of molecules adsorbed can be determined as a function of pressure. The experimental understanding of such thermodynamic ensemble consists of placing the adsorbent and adsorbate in a reservoir in equilibrium with each other at a given chemical potential and temperature. The number of particles can fluctuate, executing possible estimation of the number of adsorbed molecules averaged over the course of the simulation. These calculations can then be directly compared to the experimental data (gravimetry/volumetric/manometry) measurements mimicking the grand canonical ensemble. The chemical potential equation (12) is usually

calculated from an equation of state that represents the ideal or non-ideal behaviour of the gas at the gas-phase temperature and pressure and alternatively using the Gibbs ensemble formulation.

$$\mu = \frac{1}{\beta}\ln(\Lambda^3 \beta P) \qquad (12)$$

here μ is chemical potential, β is $1/kT$, Λ is the thermal deBroglie wavelength and P is the reservoir pressure.

At very low densities, a gas can be considered as a system of non-interacting point particles which is called an ideal gas. As the pressure increases, gas molecules come close together and start interacting with each other. In these situations, ideal gas model fails. As a result, the fugacity is introduced which is defined as the "corrected pressure" for real gases and this should be used to describe the reservoir gas. Equation (12) thus becomes equation (13) which includes the fugacity correction.

$$\mu = \frac{1}{\beta}\ln(\Lambda^3 \beta \emptyset P) \qquad (13)$$

here $\emptyset = \frac{f}{P}$ is the fugacity coefficient, f is fugacity of non-ideal gas and P is the ideal gas pressure, μ is chemical potential, β is $1/kT$, Λ is the thermal deBroglie wavelength.

The fugacity's for each adsorbed species used in the work (CO_2, N_2 and CH_4) at the investigated thermodynamic conditions were calculated using the Peng-Robinson equation of state[38] as shown in equation (14)

$$p = \frac{RT}{V_m - b} - \frac{a\alpha}{V_m^2 + 2bV_m - b^2} \qquad (14)$$

Here the constants a, b and α can be computed from critical temperature and pressure, T_c and p_c, and the reduced temperature T_r $(=T/T_c)$ by means of:

$$a = 0.45724\frac{R^2 T_c^2}{p_c}\ , b = 0.07780\frac{RT_c}{p_c}$$

$$\alpha = \left[1 + (0.37464 + 1.54226\omega - 0.26992\omega^2)(1 - \sqrt{T_r})\right]^2$$

where ω is the acentric factor, obtained from reference[39] for each gas.

The MC simulations applied to the adsorption of guest molecules in confined porous solids starts off with a randomly generated initial configuration of the molecules in the confined porous

solids and later generating several millions of random moves through translation and rotational displacements of the molecules, while also attempting to insert and to remove molecule that allow an efficient sampling of the selected ensemble. A translation/rotational displacement is accepted with the below probability,

$$P = min\{1, exp(-\beta\Delta U)\} \quad (15)$$

where ΔU is change in potential energy and β is $1/kT$.

The probability is based on Metropolis algorithm and is accepted if ΔU is negative or the magnitude of the potential energy change is lower than a random number ranging between 0 and 1.

The probability of an acceptance of the new configuration placed in a random position and orientation is given by,

$$P = min\left\{1, \frac{\beta f V}{N+1} exp(-\beta\Delta U)\right\} \quad (16)$$

where f is the fugacity of the gas-phase adsorptive.

Similarly, for a deletion step where a molecule is randomly removed, the new configuration is accepted with the probability given by

$$P = min\left\{1, \frac{N}{\beta f V} exp(-\beta\Delta U)\right\} \quad (17)$$

In the case of gas mixtures, an identity change, commonly called swap, trial is also employed to obtain a faster convergence. This move that consists of converting one randomly selected molecule of type A to type B, with A and B being two different components of the mixture, is accepted with the criteria fixed by,

$$P = min\left\{1, \frac{f_B N_A}{f_A(N_B+1)} exp(-\beta\Delta U)\right\} \quad (18)$$

where f_A and f_B are the fugacity of the components A and B in the gas-phase adsorptive, respectively, and N_A and N_B are the number of molecules. Using this methodology, a set of configurations that converge towards the specified chemical potential and temperature is generated.

Several million MC steps are needed to equilibrate from its original random starting point. The evolution of the total energy must be evaluated to control the equilibrium conditions. Acceptance rates for each possible trial is adjusted in order to approach the equilibrium and is usually fixed at about 0.4–0.5.

2.2.3.2. Applications of Monte Carlo in my work

This method is very much accepted in treating the adsorption of simple molecules like CO_2, CH_4, N_2, H_2 etc in a porous solid which does not have any significant guest-induced structural change, since all atoms are maintained in their initial positions. The details of microscopic models of gases have been presented in section 2.2.1. These GCMC simulations allow to predict the single gas component or mixtures adsorption isotherms by running a series of calculations at different pressure or fugacity.

GCMC simulations were also used in my work to determine the separation ability or selectivity (equation (19)) of the MOF material for gas A relative to gas B via the estimation of the corresponding selectivity from the binary mixture adsorption isotherms.

$$S_{A/B} = \frac{x_A}{x_B}.\frac{y_B}{y_A} \qquad (19)$$

where x_A and y_A correspond to the mole fractions of component A in the adsorbed and bulk gas phases, respectively.

When comparing the adsorbed molecules in simulated and experimental setup, there can be several possible reasons for mismatch: i) the porous material is modelled assuming the absence of defects and ii) the full porosity of the materials is assumed to be accessible. These two hypotheses are not always valid from an experimental standpoint particularly for porous materials that are not fully evacuated prior to the adsorption measurements. In addition, the standard Monte Carlo scheme assumes that there is no flexibility of the adsorbents which is a crude approximation sometimes.

GCMC is also used to calculate the enthalpy of adsorption ($\measuredangle H_{ads}$), which evaluates the fluctuation in the number of molecules (N) and the potential energy(U) in a system as described by equation (20). It measures the strength of the adsorbate–adsorbent and adsorbate–adsorbate interaction.

$$\Delta H_{ads} = RT - \frac{\langle U.N\rangle - \langle U\rangle\langle N\rangle}{\langle N^2\rangle - \langle\langle N\rangle\rangle^2} \quad (20)$$

This method assumes an ideal behaviour of gas phase and it depends considerably on large number of steps to achieve reliable results. Hence a recent strategy of canonical ensemble Widom's insertion[40] move can circumvent this limitation. The simulated adsorption enthalpy profile is then comparable with the experimental adsorption enthalpy profiles issued from microcalorimetry measurements.

2.2.4. Molecular Dynamics simulations

2.2.4.1. Basic principles

Molecular Dynamics (MD) simulations allow the exploration of the properties of the system from a dynamic standpoint. Basically, a distribution of the adsorbates within the porosity of the solid is usually produced by preliminary MC simulations and each atom of the system is randomly assigned an initial velocity following a Boltzmann distribution. The time-dependent trajectory of the system consisting of a sequence of atomic positions for the diffusive molecules with respect to time is then generated by integrating the Newton's equations of motion numerically over short-time steps via appropriate algorithms. N particles of a system are defined by their position (R_i) and Momenta ($P_i = m_i V_i$)[41]. The Hamiltonian of this system can be described as,

$$H(P^N, R^N) = \sum_{i=1}^{N} \frac{P_i^2}{2m_i} + U(R^N) \quad (21)$$

where R^N and P^N are positions and momenta of n particles whereas U is the potential energy which is a function of the positions. The forces acting on the all the particles are derived from their potential as,

$$F_i(R^N) = \frac{\partial U(R^N)}{\partial R_i} \quad (22)$$

The equations of motion are defined according to the Hamiltonian's equation

$$\dot{R}_i = \frac{\partial H}{\partial P_i} = \frac{P_i}{m_i} \quad (23)$$

$$\dot{P}_i = -\frac{\partial H}{\partial R_i} = -\frac{\partial U}{\partial R_i} = F_i(R^N) \qquad (24)$$

Integration of equation of motion

To integrate the equations of motion various algorithms have been introduced. Verlet algorithm used in my work is time reversible, conserves the phase space volume and it is efficient in expensive force calculations since the integration is only implemented once per time step in contrast to other algorithms[41]. Taylor expansion was used to derive this algorithm of the coordinate *Ri* of a particle at time *t*+ Δ*t*

$$R_i(t+\Delta t) = R_i(t) + V_i(t)\Delta t + \frac{F_i(t)}{2m_i}\Delta t^2 + \frac{\Delta t^3}{3!}\ddot{R}_i + O(\Delta t^4) \qquad (25)$$

similarly,

$$R_i(t-\Delta t) = R_i(t) - V_i(t)\Delta t + \frac{F_i(t)}{2m_i}\Delta t^2 - \frac{\Delta t^3}{3!}\ddot{R}_i + O(\Delta t^4) \qquad (26)$$

By summing above two (25) and (26), equation (27) is obtained

$$R_i(t+\Delta t) + R_i(t-\Delta t) = 2R_i(t) + \frac{F_i(t)}{m_i}\Delta t^2 + O(\Delta t^4) \qquad (27)$$

where Δ*t* is the time step and the estimated error in the new position is of order Δt^4. The Verlet algorithm does not use the velocity to compute the new position, although, the position of the particle at time *t* and *t* +Δ*t* can be used to calculate the velocity of the particle, using the following equation:

$$R_i(t+\Delta t) - R_i(t-\Delta t) = 2V_i(t)\Delta t + O(\Delta t^3) \qquad (28)$$

Or

$$V_i(t) = \frac{R_i(t+\Delta t) - R_i(t-\Delta t)}{2\Delta t} + O(\Delta t^2) \qquad (29)$$

Here the estimated error in the velocity is of order Δt^2. At each timestep, the temperature, potential energy and the total energy of the system is calculated. All through the MD simulations, total energy should be conserved. All the old positions and velocities at time $t - \Delta t$ can be discarded after all calculations are finished. The new positions and velocities become the next starting point leading to the process to be repeated in a given number of times such that the desired time frame is achieved

A MD simulation can be performed in the microcanonical (NVE) ensemble with constant number of particles N, volume V and energy E. However, in order to simulate experimental conditions, MD simulations with constant temperature are most of the time employed. Hence, the temperature of a simulated system needs to be regulated. For this purpose, the velocity rescaling thermostat are used to generate canonical (NVT) ensemble. The average kinetic energy(K)[41] is $\overline{K} = \frac{1}{2} N_f k_B T$ where N_f is the degree of freedom, k_B is the Boltzmann constant at given temperature T. All the particle velocities must be multiplied by the rescaling factor α to get the desired temperature,

$$\alpha = \sqrt{\frac{\overline{K}}{K}} \qquad (30)$$

In the above approach, the average kinetic energy is kept fixed and the canonical equilibrium distribution of the kinetic energy is not sampled. Bussi et al[42] have reworked the way the rescaling factor is calculated. Instead of forcing the kinetic energy to be exactly equal to $\overline{K}$, with a stochastic procedure a target value K_t have been selected intended to obtain the desired ensemble. Hence, the velocity-rescaling factor is evaluated as

$$\alpha = \sqrt{\frac{K_t}{K}} \qquad (31)$$

where K_t is derived from the canonical equilibrium distribution for the kinetic energy

$$\bar{p}(K_t)dK_t = K_t^{\left(\frac{N_f}{2}-1\right)} e^{-\beta K_t} dK_t \qquad (32)$$

The usual equations of motion are used to reproduce the rescaling. In this way, correct sampling of the canonical NVT ensembles is attained.

Most of the experiments are also temperature and pressure controlled. So, final production run is performed with the isothermal-isobaric (NPT) ensemble. In this ensemble, the average

pressure of the system, P_{int} is equal to an externally applied pressure P_{ext} so that the volume of the system varies. Hence, the volume is a dynamical variable in this ensemble. Here any instantaneous temperature and pressure fluctuations are monitored using a thermostat. For NPT ensemble, the equations of motion was proposed by Tuckerman and Martyna[43] for the positions and momenta:

$$\dot{R}_i = \frac{P_i}{m_i} + \frac{P_\epsilon}{W} R_i \quad (33)$$

$$\dot{P}_i = F_i - \left(1 - \frac{1}{N}\right)\frac{P_\epsilon}{W} P_i - \frac{P_\eta}{Q} P_i \quad (34)$$

$$\epsilon = ln\left(\frac{V}{V(0)}\right) \quad (35)$$

where $V(0)$ is the volume at $t = 0$, W is the mass parameter associated to ϵ, and P_ϵ is the momentum conjugate to the logarithm of the volume,

$$\dot{V}_i = \frac{dV_{P_\epsilon}}{W} \quad (36)$$

$$\dot{P}_\epsilon = (P_{int} - P_{ext}) + \frac{1}{N}\sum_{i=1}^{N} \frac{P_i^2}{2m_i} - \frac{P_\eta}{Q} P_\epsilon \quad (37)$$

$$\dot{\eta} = \frac{P_\eta}{Q} \quad (38)$$

$$\dot{P}_\eta = \sum_{i=1}^{N} \frac{P_i^2}{2m_i} + \frac{P_\epsilon^2}{W} - (dN + 1)kT \quad (39)$$

In these equations P_{ext} is the external imposed pressure while P_{int} is the internal pressure of the system given by

$$P_{int} = \frac{1}{dV}\left[\sum_{i=1}^{N} \frac{P_i^2}{m_i} + \sum_{i=1}^{N} R_i F_i - (dV)\frac{\partial U}{\partial V}\right] \quad (40)$$

The variable P_ϵ acts as a barostat which drives the system to the steady state $< P_{int} >= P_{ext}$.

Equation (39) defines the compressibility as

$$\kappa = -(dN + 1)\frac{P_\eta}{Q} = -(dN + 1)\dot{\eta} \quad (41)$$

$$H' = H(P^N, R^N) + \frac{P_\epsilon}{2W} + \frac{P_\eta}{W} + (dN + 1)kT\eta + P_{ext}V \quad (42)$$

Any system generally has vast molecular conformations in a configurational space which must be efficiently explored to attain a global low energy region in thermal equilibrium. This is a fundamental problem in simulation. For this, in MD simulation, an "ergodic hypothesis" is assumed. This hypothesis states that all the accessible states in the phase space are equiprobable if a simulation is run for a sufficiently long time. Over time the system would eventually pass through all the possible states and should generate enough number of representative configurations such that time average of a quantity of interest is equal to the ensemble average. Hence in many particle systems, MD simulation is used to study average properties through time evolution.

2.2.4.2. Applications of Molecular Dynamics in my work

MD is a valuable computational tool to probe the diffusivity of various guest molecules in porous solids. MC simulation generates a distribution of the adsorbates in the pores of a solid. Subsequently, each atom of the system is assigned an initial velocity using a Boltzmann distribution randomly, which can be used to determine a sequence of atomic positions for the diffusive molecules over time in MD simulation. Various type of molecular diffusion can be extracted from such equilibration like self-diffusivity[44], transport or Fickian diffusivity[45] which is of great interest in real applications. In my work, MD simulations were employed to construct and further characterize the structural, thermodynamics and dynamics features of MOF/GO interfaces[46,47]. As stated in chapter 3, 4 and 5, many average properties like RDF, atomic densities, pore sizes, dihedral distributions etc. were calculated to characterize the MOF/GO interfaces.

2.3. Quantum Calculations

2.3.1. Basic principles of Density Functional Theory

The quantum calculations aim is to provide a description of the behaviour of all the electrons of the system. This requires a Schrödinger equation to be solved for each electron which becomes quite expensive computationally. Hence quantum calculation relies on approximations which should be accurate enough for the system to be compared with experimental data. Such

approaches usually require an initial structure that can be either periodic or a small cluster that mimics the local environment of the system. Usually many quantum *ab initio* methods are available which are highly accurate but are limited by the number of atoms. Here, I have mostly focused on Density Functional Theory (DFT) method used for calculating the atomic partial charges of all systems and geometry optimization of both MOF and GO models.

DFT is developed based on two theorems of Hohenberg-Kohn. First theorem states the external potential $V_{ext}(r)$ is determined by the electron density $\rho(r)$. For each density has a single $V_{ext}(r)$. Thus, this theorem demonstrates that the electron density specifies uniquely the Hamiltonian operator. Hence, it states that any ground state expectation value corresponds to an observable $\hat{O}$ is a functional of density,

$$O[\rho] = \langle \psi[\rho] | \hat{O} | \psi[\rho] \rangle \qquad (43)$$

The second theorem states that the functional $F_{HK}[\rho]$ delivers the ground state energy if and only if input density is the true ground state density

$$E[\rho^0] = \rho^0(r) V_{ext}(r) dr + F_{HK}[\rho^0] \qquad (44)$$

where $E[\rho^0]$ is the energy functional.

According to Kohn Sham equations, a solid consists of heavy positively charged particles (nuclei) and lighter negatively charged particles (electrons). Nuclei is heavier and much slower than the electrons, hence mostly be fixed at fixed positions according to Born-Oppenheimer approximation and will act as an external potential to the electrons.

The solid is generally considered as a system of interacting electrons in the field of fixed ions (Born-Oppenheimer approximation) described by the Hamiltonian. We use atomic units i.e., e = m_e = ħ = 1; $4\pi\epsilon_o$=1.

$$\hat{H} = \sum_{i=1}^{N} -\frac{1}{2}\nabla_i^2 + \sum_{i=1}^{N} V_{ext}(r_i) + \sum_{i<j}^{N} \frac{1}{r_{ij}} \qquad (45)$$

Here $V_{ext}(r_i) = -\sum_{I=1}^{M} \frac{Z_I}{r_{iI}}$ is the external potential acting on i^{th} electron due to the M nuclei and r_{iI} is the separation of i^{th} electron and I^{th} nucleus while r_{ij} is the separation between i^{th} and j^{th} electrons.

A stationary electronic state is described by a wave function $\Psi(r_1, r_2 \ldots r_N)$ satisfying time-independent Schrödinger equation,

$$\hat{H}\psi = E\psi \quad (46)$$

$$i.e., [\hat{T} + \hat{V_{ext}} + \hat{V_{ee}}]\psi = E\psi \quad (47)$$

Hohenberg and Kohn demonstrated that the total energy of a system in the presence of the static external potential is a unique functional of the charge density (equation (48)).

$$E[\rho] = T[\rho] + V_{ee}[\rho] + V_{ext}[\rho] \quad (48)$$

$$E[\rho] = F_{HK}[\rho] + \int \rho(r)\, V_{ext}(r) d^3r \quad (49)$$

For all solids, the Hohenberg-Kohn functional $i.e,\ F_{HK}[\rho] = T[\rho] + V_{ee}[\rho]$ is same.

In the non-interacting system, where $V_{ee} = 0$, the ground state energy $E[\rho]$ has a kinetic and external potential contribution.

$$E[\rho] = T_o[\rho] + V_{ext}[\rho] = T_o[\rho] + \int \rho(r)\, V_{ext}(r) d^3r \quad (50)$$

Again, the ground state wave function of the non-interacting system can be written as a Slater determinant with the orbitals satisfying the single particle Schrodinger equation,

$$\left[-\frac{1}{2}\nabla^2 + V_{ext}(r)\right] \emptyset^0(r) = \varepsilon_m^0 \emptyset_m^0 \quad (51)$$

The ground state density is then given by a sum of occupied states,

$$\rho[r] = \sum_m^{occup} |\emptyset_m^0(r)|^2 \quad (52)$$

where the orbital $\emptyset_m^0$ are normalized so that the density satisfies the correct condition to the number of particles N.

Thus, we can write the ground state energy for this non-interacting case as,

$$\sum_m^{occup} \varepsilon_m^0 = T_o[\rho] + \int \rho(r)\, V_{ext}(r) d^3r \quad (53)$$

Now, for the interacting case, the energy functional $E[\rho]$ for a many electron system is,

$$E[\rho] = T_o[\rho] + \int \rho(r)\, V_{ext}(r) d^3r + \frac{1}{2}\iint \frac{\rho(r_1)\rho(r_2)}{|r_1 - r_2|} d^3r_1 d^3r_2 + E_{XC}[\rho(r)] \quad (54)$$

where $\frac{1}{2}\iint \frac{\rho(r_1)\rho(r_2)}{|r_1 - r_2|} d^3r_1 d^3r_2 = V_H[\rho]$ is the Hatree energy and $E_{XC}[\rho(r)]$ is the exchange correlation energy.

E_{xc} has all the contributions not taken into account for kinetic, the external and the Hatree energy.

Thus, we can write an equivalent equation for the interacting electron system like equation (51) as,

$$\left[-\frac{1}{2}\nabla^2 + V_{eff}(r)\right]\emptyset_m(r) = \varepsilon_m\emptyset_m \qquad (55)$$

where $\emptyset_m(r)$ is the single particle wave functions which are the N lowest energy solutions of Kohn Sham equation (55) and Kohn Sham orbital $\emptyset_m(r)$ that produce $\rho(r)$ of the original many-body problem.

$$V_{eff} = V_{ext}(r) + \int \frac{\rho(r')}{|r-r'|} d^3r' + \frac{\delta E_{XC}[\rho]}{\delta\rho(r)} \qquad (56)$$

i.e.,

$$V_{eff} = V_{ext}[r] + V_H[r] + V_{XC}[r] \rightarrow V_{ext} = V_{eff}[r] - V_H[r] - V_{XC}[r] \qquad (57)$$

Incorporating equation (57) in equation (54), we can write a final equation (58) for the ground state energy of the interacting system. This expression is used to determine the ground state energy in computational calculation.

$$E[\rho] = \sum_m^{occup} \varepsilon_m^o + \frac{1}{2}\iint \frac{\rho(r_1)\rho(r_2)}{|r_1-r_2|} d^3r_1 d^3r_2 - \int V_{XC}(r)\,\rho(r) d^3r + E_{XC}[\rho(r)] \qquad (58)$$

where E_{xc} are determined using several approaches such as Local Density Approximation (LDA)[48], the Generalized Gradient Approximation (GGA)[49], and Hybrid methods[50]. GGA is most popular and considers that the exchange-correlation energy depends not only on the electronic density but also on its gradient. Most popular GGA functionals employed in the literature is the PBE[49] functional(employed in our work), followed by PW91[51] and BLYP[52]. Although GGA is most popular in computational chemistry, when non-local approximations like dispersive interactions have large contributions to the total electronic energy, other methods are taken into account. The methods are vdW-DF, effective atom centred one-electron potential[53], the semi-empirical approach (DFT-D[54], DFT-D2[55], DFT-D3[56] and Tkatchenko-Scheffler[57]

approaches). To explicitly account for dispersion interactions, semiempirical dispersion correction of the form (equation (59)) have been proposed,

$$E_{disp} = -s \sum_{i<j} \int (R_{ij}) \frac{C_6^{ij}}{R_{ij}^6} \quad (59)$$

where *R* is the distance between each atom pair *i* and *j, C* is the dispersion coefficient between these atoms, *f(R)* is the parameterized damping function and *s* is an adjustable scaling parameter. The term C_6^{ij} is calculated empirically for any pair of atoms from same atom dispersion coefficients C_6^{ii} and atomic polarizability. DFT-D3 approach, used in my work is the latest version of DFT-D developed by Grimme which has C_8^{ij} two-body terms and C_9^{ij} three-body terms.

2.3.2. Applications of Density Functional Theory in my work

- Geometry optimization

A most common use of DFT calculations is to geometry optimize a system by a systematic evaluation of its electronic energy with the variation of geometric parameters such as the mutual distances, angles and dihedrals between its constitutive atoms. To find the global minimum, several algorithms have been implemented, of which Newton–Raphson algorithm and its derivative quasi-Newton methods are mostly used. This method is well adapted for molecular geometry optimization and leads to fast convergence. The most expensive part of Newton-Raphson method is the Hessian. It turns out that a good approximate Hessian may be extracted from the gradient history. The BFGS (Broyden-Fletcher-Goldfarb-Shanno) method[58] is particularly efficient. Quasi-Newton methods provide super-linear convergence at effectively the cost of the gradient descent method. The energy minimization can be a fast process depending on the initial configuration and number of atoms present. In order to better converge, other criterions are also employed other than minimizing the total energy such as minimization of average atom displacement and individual force on each atom. I have used this approach to minimize the periodic structures of MOF surfaces, GOs as well as cluster models representative of both systems using quantum Quickstep module of the CP2K software[59] and Gaussian 09 package[26].

- Charge calculations

Atomic partial charges can be derived by quantum calculations. Usually these charges are a useful simplification of the polarization of the electron distribution between bonded atoms. Under the framework of DFT calculations, atomic partial charges are obtained by the population analysis of wave functions e.g. Mulliken population analysis[60], natural population analysis[61], partitioning of electron density distributions (e.g. Bader[62], DDEC[63], CM5[64] and Hirshfield[65] charges). The most popular schemes are those based on the fitting of charges to mimic the electrostatic potential (ESP)[66] around the molecule such as CHelpG[27] or Merz-Kollman[67]. The ESP approach is based on iterative fitting of the atomic partial charges in a way that they generate an ESP grid as close as possible to a previously quantum-calculated ESP grid. This method is very useful for cluster based DFT calculations. I have used ChelpG for calculating charges for both GO and ZIF-8 surface models as implemented in Gaussian package 09[26] run using PBE functional, and the 6-31G(d,p) basis set as implemented in the package. A cluster of the crystal was cut from periodic structures and further saturated to avoid the presence of dangling bonds. Depending on the molecular coordinate system orientation and the choice of fitting points on the grid, the charges are obtained. The so-calculated charges are approximated as the global charges of the periodic system.

- Interaction energy

DFT method can be also used to determine the interaction energies between chemical species. Considering U_A and U_B are the respective energies of the isolated species A and B, and U_{AB} is the total energy of a system containing both species A and B. The interaction energy U_I would be

$$U_I = U_{AB} - (U_A + U_B) \qquad (60)$$

The interaction energy is calculated by considering U_{AB} as the total energy of the optimized (A, B) system while U_A and U_B are usually calculated using Single Point Energy calculation (SPE) with the geometries of the molecules A and B as observed in the binary system. The so-computed energy takes into account the electrostatic and repulsion energy contributions. For the adsorbate/adsorbent systems, this interaction energy is also called binding energy and has been widely employed to characterize the affinity of various adsorbates towards adsorbent and further compared to experimental data such as those extracted from Microcalorimetry. An alternative was also used in the calculation of this interaction energy as a function of the distance separating

the adsorbate and the preferential adsorption site of the adsorbent in order to further derive force field parameters to accurately describe the strength of interactions at the force field level using Monte Carlo/Molecular Dynamics simulations[68–72].

REFERENCES

(1) Kmiecik, S.; Gront, D.; Kolinski, M.; Wieteska, L.; Dawid, A. E.; Kolinski, A. Coarse-Grained Protein Models and Their Applications. *Chem. Rev.* **2016**, *116* (14), 7898–7936.

(2) Rouquerol, F.; Rouquerol, J.; Sing, K. S. .; Llewellyn, P.; Maurin, G. *Adsorption by Powders and Porous Solids*; **2014**.

(3) Compton, O. C.; Nguyen, S. T. Graphene Oxide, Highly Reduced Graphene Oxide, and Graphene: Versatile Building Blocks for Carbon-Based Materials. *Small* **2010**, *6* (6), 711–723.

(4) Zhao, Y.; Seredych, M.; Zhong, Q.; Bandosz, T. J. Aminated Graphite Oxides and Their Composites with Copper-Based Metal–Organic Framework: In Search for Efficient Media for CO2 Sequestration. *RSC Adv.* **2013**, *3* (25), 9932.

(5) Bagri, A.; Mattevi, C.; Acik, M.; Chabal, Y. J.; Chhowalla, M.; Shenoy, V. B. Structural Evolution during the Reduction of Chemically Derived Graphene Oxide. *Nat. Chem.* **2010**, *2* (7), 581–587.

(6) He, H.; Klinowski, J.; Forster, M.; Lerf, A. A New Structural Model for Graphite Oxide. **1998**, No. April, 53–56.

(7) Lee, S. Y.; Park, S. J. A Review on Solid Adsorbents for Carbon Dioxide Capture. *J. Ind. Eng. Chem.* **2015**, *23*, 1–11.

(8) S Bell, D. The Promise of Metal–Organic Frameworks for Use in Liquid Chromatography. **2018**.

(9) CHEMISTRY NEWS. http://www.societechimiquedefrance.fr/MOFs-a-fine-example-of-complementarity-between-academic-and-industrial-research-422?lang=fr.

(10) Zeolites and Usage Areas(https://steemit.com/science/@kedi/zeolites-and-usage-areas).

(11) Dimiev, A. M.; Eigler, S. *Graphene Oxide: Fundamentals and Applications*; John Wiley & Sons, Ltd., **2016**.

(12) Siperstein, F. R.; Gubbins, K. E. Phase Separation and Liquid Crystal Self-Assembly in Surfactant-Inorganic-Solvent Systems. *Langmuir* **2003**, *19* (6), 2049–2057.

(13) Abbott, L. J.; Hart, K. E.; Colina, C. M. Polymatic: A Generalized Simulated Polymerization Algorithm for Amorphous Polymers. *Theor. Chem. Acc.* **2013**, *132* (3), 1–19.

(14) Olivier, J. P. Improving the Models Used for Calculating the Size Distribution of Micropore Volume of Activated Carbons from Adsorption Data. *Carbon N. Y.* **1998**, *36* (10), 1469–1472.

(15) Akinjokun, A. I.; Ojuma, tunde V.; Ogunfowokan, A. O. Biomass, Abundant Resources for Synthesis of Mesoporous Silica Material. *Microporous Mesoporous Mater.* **2016**, 103–117.

(16) Nanocomposix. https://nanocomposix.eu/collections/material-silica/products/mesoporous-silica.

(17) https://en.wikipedia.org/wiki/Mesoporous_silica.

(18) Basic Polymer(https://www.e-education.psu.edu/matse81/node/2210).

(19) Harris, P. J. F.; Liu, Z.; Suenaga, K. Imaging the Atomic Structure of Activated Carbon. *J. Phys. Condens. Matter* **2008**, *20* (36), 1–5.

(20) Zheng, B.; Demontis, P.; Suffritti, G. B. Force Field for Molecular Dynamics Computations in Flexible ZIF-8 Framework.Pdf. *J. Phys. Chem. C* **2012**, *116*, 933–938.

(21) Muschi, M.; Lalitha, A.; Sene, S.; Aureau, D.; Devautour-Vinot, S.; Nouar, F.; Sicard, C.; Menguy, N.; Serre, C.; Maurin, G.; Steunou, N. Formation of Single Crystal Aluminium-Based MOF Nanowire with Graphene Oxide Nanoscolls as Structure-Directing Agent. *to be Publ.* **2019**.

(22) Benoit, V.; Pillai, R. S.; Orsi, A.; Normand, P.; Jobic, H.; Nouar, F.; Billemont, P.; Bloch, E.; Bourrelly, S.; Devic, T.; Wright, P. A.; De Weireld, G.; Serre, C.; Maurin, G.; Llewellyn, P. L. MIL-91(Ti), a Small Pore Metal-Organic Framework Which Fulfils Several Criteria: An Upscaled Green Synthesis, Excellent Water Stability, High CO2 Selectivity and Fast CO2 Transport. *J. Mater. Chem. A* **2016**, *4* (4), 1383–1389.

(23) Jorgensen, W. L.; Maxwell, D. S.; Tirado-Rives, J. Development and Testing of the OPLS All-Atom Force Field on Conformational Energetics and Properties of Organic Liquids. *J. Am. Chem. Soc.* **1996**, *118* (45), 11225–11236.

(24) A. K. Rappe, C. J. Casewit, K. S. Colwell, W. A. Goddard III, and W. M. S. UFF, a Full Periodic Table Force Field for Molecular Mechanics and

Molecular Dynamics Simulations. *J. Am. Chem. Soc* **1992**, *114*, 10024–10035.

(25) Mayo, S. L.; Olafson, B. D.; Goddard, W. A. DREIDING: A Generic Force Field for Molecular Simulations. *J. Phys. Chem.* **1990**, *94* (26), 8897–8909.

(26) Frisch, M. J.; Trucks, G. W.; Schlegel, H. B.; Scuseria, G. E.; Robb, M. A.; Cheeseman, J. R.; Scalmani, G.; Barone, V.; Mennucci, B.; Petersson, G. A.; Nakatsuji, H.; Caricato, M.; Li, X.; Hratchian, H. P.; Izmaylov, A. F.; Bloino, J.; Zheng, G.; Sonnenberg, J. L.; Hada, M.; Ehara, M.; Toyota, K.; Fukuda, R.; Hasegawa, J.; Ishida, M.; Nakajima, T.; Honda, Y.; Kitao, O.; Nakai, H.; Vreven, T.; Montgomery, J. A.; Peralta, J. E.; Ogliaro, F.; Bearpark, M.; Heyd, J. J.; Brothers, E.; Kudin, K. N.; Staroverov, V. N.; Kobayashi, R.; Normand, J.; Raghavachari, K.; Rendell, A.; Burant, J. C.; Iyengar, S. S.; Tomasi, J.; Cossi, M.; Rega, N.; Millam, J. M.; Klene, M.; Knox, J. E.; Cross, J. B.; Bakken, V.; Adamo, C.; Jaramillo, J.; Gomperts, R.; Stratmann, R. E.; Yazyev, O.; Austin, A. J.; Cammi, R.; Pomelli, C.; Ochterski, J. W.; Martin, R. L.; Morokuma, K.; Zakrzewski, V. G.; Voth, G. A.; Salvador, P.; Dannenberg, J. J.; Dapprich, S.; Daniels, A. D.; Farkas; Foresman, J. B.; Ortiz, J. V; Cioslowski, J.; Fox, D. J. Gaussian 09, Revision B.01. *Gaussian 09, Revision B.01, Gaussian, Inc., Wallingford CT*. Wallingford CT **2009**.

(27) Breneman, C. M.; Wiberg, K. B. Determining Atom-Centered Monopoles from Molecular Electrostatic Potentials. The Need for High Sampling Density in Formamide Conformational Analysis. *J. Comput. Chem.* **1990**, *11* (3), 361–373.

(28) Dai, H.; Xu, Z.; Yang, X. Water Permeation and Ion Rejection in Layer-by-Layer Stacked Graphene Oxide Nanochannels: A Molecular Dynamics Simulation. *J. Phys. Chem. C* **2016**, *120* (39), 22585–22596.

(29) Harris, J. G.; Yung, K. H. Carbon Dioxide's Liquid-Vapor Coexistence Curve and Critical Properties as Predicted by a Simple Molecular Model. *J. Phys. Chem.* **1995**, *99* (31), 12021–12024.

(30) Potoff, J. J.; Siepmann, J. I. Vapor-Liquid Equilibria of Mixtures Containing Alkanes, Carbon Dioxide, and Nitrogen. *AIChE J.* **2001**, *47* (7), 1676–1682.

(31) Straub, J. E.; Karplus, M. Molecular Dynamics Study of the Photodissociation of Carbon Monoxide from Myoglobin: Ligand Dynamics in the First 10 Ps. *Chem. Phys.* **1991**, *158* (2–3), 221–248.

(32) Martin, M. G.; Siepmann, J. I. Transferable Potentials for Phase Equilibria. 1. United-Atom Description of n-Alkanes. *J. Phys. Chem. B* **1998**, *102* (14), 2569–2577.

(33) Sabetghadam, A.; Liu, X.; Benzaqui, M.; Gkaniatsou, E.; Orsi, A.; Lozinska, M. M.; Sicard, C.; Johnson, T.; Steunou, N.; Wright, P. A.; Serre, C.; Gascon, J.; Kapteijn, F. Influence of Filler Pore Structure and Polymer on the Performance of MOF-Based Mixed-Matrix Membranes for CO 2 Capture. *Chem. - A Eur. J.* **2018**, *24* (31), 7949–7956.

(34) Lorentz, H. A. Ueber Die Anwendung Des Satzes Vom Virial in Der Kinetischen Theorie Der Gase. *Ann. Phys.* **1881**, *248* (1), 127–136.

(35) M.A. González. Force Fields and Molecular Dynamics Simulations. **1976**, *12*, 169–200.

(36) Https://www.ch.embnet.org/MD_tutorial/pages/MD.Part3.html. No Title.

(37) Frenkel, D.; Smit, B. *Understanding Molecular Simulation: From Algorithms to Applications (Computational Science)*; **2002**.

(38) Gasem, K. A. M.; Gao, W.; Pan, Z.; Robinson, R. L. A Modified Temperature Dependence for the Peng-Robinson Equation of State. *Fluid Phase Equilib.* **2001**, *181* (1–2), 113–125.

(39) Poling, B. E.; Prausnitz, J. M.; O'Connell, J. P. *The Properties of Gases and Liquids*; **2001**.

(40) Widom, B. Some Topics in the Theory of Fluids. *J. Chem. Phys.* **1963**, *39* (11), 2808–2812.

(41) Frenkel, D.; Smit, B. *Understanding Molecular Simulation: From Algorithms to Applications.*; Academic press: San Diego, California, **2002**.

(42) G. Bussi D. Donadio; Parrinello, M. Canonical Sampling through Velocity Rescaling. *J. Chem. Phys.* **2007**, *126(1)*, 14101.

(43) Tuckerman, M. E.; Martyna, G. J. Understanding Modern Molecular Dynamics: Techniques and Applications. *J. Phys. Chem. B* **2000**, *104* (2), 159–178.

(44) Nevin Gerek, Z.; Richard Elliott, J. Self-Diffusivity Estimation by Molecular Dynamics. *Ind. Eng. Chem. Res.* **2010**, *49* (7), 3411–3423.

(45) Tsige, M.; Grest, G. S. Molecular Dynamics Simulation of Solvent-Polymer Interdiffusion: Fickian Diffusion. *J. Chem. Phys.* **2004**, *120* (6), 2989–2995.

(46) Bonakala, S.; Lalitha, A.; Eun Shin, J.; Moghadam, F.; Semino, R.; Bum Park, H.; Maurin, G.; Shin, J. E.; Moghadam, F. Understanding of the Graphene Oxide / Metal-Organic Framework Interface at the Atomistic Scale. *ACS Appl. Mater. Interfaces* **2018**, *10*, 1–6.

(47) Lalitha, A.; Shin, J. E.; Bonakala, S.; Oh, J. Y.; Park, H. B.; Maurin, G. Unraveling the Enhancement of the Interfacial Compatibility Between Metal-Organic Framework and Functionalized Graphene Oxide. *J. Phys. Chem. C* **2019**, *123*, 4984–4993.

(48) Zunger, A.; J. P. Perdew. Self-Interaction Correction to Density-Functional Approximations for Many-Electron Systems. *Phys. Rev. B* **1981**, *23* (10), 5048–5079.

(49) Perdew, J. P.; Burke, K.; Ernzerhof, M.

Generalized Gradient Approximation Made Simple. *Phys. Rev. Lett.* **1996**, *77*, 3865–3868.

(50) Stephens, P. J.; Devlin, F. J.; Chabalowski, C. F.; Frisch, M. J. Ab Initio Calculation of Vibrational Absorption and Circular Dichroism Spectra Using Density Functional Force Fields. *J. Phys. Chem.* **1994**, *98* (45), 11623–11627.

(51) Perdew, J. P.; Chevary, J. A.; Vosko, S. H.; Koblar, A. J.; Pederson, M. R.; Singh, D. J.; Fiolhais, C. Atoms, Molecules, Solids and Surfaces: Applications of the GGA for Exchange Correlation. *Phys. Rev. B* **1992**, *46* (11), 6671–6687.

(52) Lee, C.; Hill, C.; Carolina, N. Development of the Colle-Salvetti Correlation-Energy Formula into a Functional of the Electron Density. *Chem. Phys. Lett.* **1989**, *162* (3), 165–169.

(53) Grimme, S. Density Functional Theory with London Dispersion Corrections. *Wiley Interdiscip. Rev. Comput. Mol. Sci.* **2011**, *1* (2), 211–228.

(54) Grimme, S. Accurate Description of van Der Waals Complexes by Density Functional Theory Including Empirical Corrections. *J. Comput. Chem.* **2004**, *25* (12), 1463–1473.

(55) Grimme, S. Semiempirical GGA-Type Density Functional Constructed with a Long-Range Dispersion Correction. *J Comput Chem* **2006**, *27*, 1787–1799.

(56) Grimme, S.; Antony, J.; Ehrlich, S.; Krieg, H. A Consistent and Accurate Ab Initio Parametrization of Density Functional Dispersion Correction (DFT-D) for the 94 Elements H-Pu. *J. Chem. Phys.* **2010**, *132* (15), 154104.

(57) Tkachenko, A. G.; Xie, H.; Coleman, D.; Glomm, W.; Ryan, J.; Anderson, M. F.; Franzen, S.; Feldheim, D. L. Multifunctional Gold Nanoparticle-Peptide Complexes for Nuclear Targeting. *J. Am. Chem. Soc.* **2003**, *125*, 4700–4701.

(58) Saputro, D. R. S.; Widyaningsih, P. Limited Memory Broyden-Fletcher-Goldfarb-Shanno (L-BFGS) Method for the Parameter Estimation on Geographically Weighted Ordinal Logistic Regression Model (GWOLR). *AIP Conf. Proc.* **2017**, *1868*.

(59) Vandevondele, J.; Krack, M.; Mohamed, F.; Parrinello, M.; Chassaing, T.; Hutter, J. Quickstep: Fast and Accurate Density Functional Calculations Using a Mixed Gaussian and Plane Waves Approach. *Comput. Phys. Commun.* **2005**, *167* (2), 103–128.

(60) R. S. Mulliken. Electronic Population Analysis on LCAO. *J. Chem. Phys* **1955**, *23* (January 1955), 1833.

(61) Reed, A. E.; Weinstock, R. B.; Weinhold, F. Natural Population Analysis. *J. Chem. Phys.* **1985**, *83* (2), 735–746.

(62) R. F. W. Bader. *Atoms in Molecules - A Quantum Theory*; **1990**.

(63) Manz, T. A.; Sholl, D. S. Improved Atoms-in-Molecule Charge Partitioning Functional for Simultaneously Reproducing the Electrostatic Potential and Chemical States in Periodic and Nonperiodic Materials. *J. Chem. Theory Comput.* **2012**, *8* (8), 2844–2867.

(64) Marenich, A. V.; Jerome, S. V.; Cramer, C. J.; Truhlar, D. G. Charge Model 5: An Extension of Hirshfeld Population Analysis for the Accurate Description of Molecular Interactions in Gaseous and Condensed Phases. *J. Chem. Theory Comput.* **2012**, *8* (2), 527–541.

(65) Hirshfeld, F. L. Bonded-Atom Fragments for Describing Molecular Charge Densities. *Theor. Chim. Acta* **1977**, *44* (2), 129–138.

(66) Sevillano, J. J. G.; Calero, S.; Ania, C. O.; Parra, J. B.; Kapteijn, F.; Gascon, J.; Hamad, S. Toward a Transferable Set of Charges to Model Zeolitic Imidazolate Frameworks: Combined Experimental-Theoretical Research. *J. Phys. Chem. C* **2013**, *117* (1), 466–471.

(67) Singh, U. C.; Kollman, P. A. An Approach to Computing Electrostatic Charges for Molecules. *J. Comput. Chem.* **1984**, *5* (2), 129–145.

(68) Lee, K.; Howe, J. D.; Lin, L. C.; Smit, B.; Neaton, J. B. Small-Molecule Adsorption in Open-Site Metal-Organic Frameworks: A Systematic Density Functional Theory Study for Rational Design. *Chem. Mater.* **2015**, *27* (3), 668–678.

(69) Becker, T. M.; Lin, L. C.; Dubbeldam, D.; Vlugt, T. J. H. Polarizable Force Field for CO2 in M-MOF-74 Derived from Quantum Mechanics. *J. Phys. Chem. C* **2018**, *122* (42), 24488–24498.

(70) Rudenko, A. N.; Bendt, S.; Keil, F. J. Multiscale Modeling of Water in Mg-MOF-74: From Electronic Structure Calculations to Adsorption Isotherms. *J. Phys. Chem. C* **2014**, *118* (29), 16218–16227.

(71) Fischer, M.; Gomes, J. R. B.; Fröba, M.; Jorge, M. Modeling Adsorption in Metal-Organic Frameworks with Open Metal Sites: Propane/Propylene Separations. *Langmuir* **2012**, *28* (22), 8537–8549.

(72) Bak, J. H.; Le, V. D.; Kang, J.; Wei, S. H.; Kim, Y. H. First-Principles Study of Electronic Structure and Hydrogen Adsorption of 3d Transition Metal Exposed Paddle Wheel Frameworks. *J. Phys. Chem. C* **2012**, *116* (13), 7386–7392.

CHAPTER 3 – CONSTRUCTION OF GO & ZIF-8 MODELS AND EXPLORATION OF ZIF-8/GO INTERFACES

3.1. Introduction

The MOF/GO composites have attracted extensive attention, as discussed in Chapter 1, however the interface formed between the two components is far from understood since its exploration is still challenging from both theoretical and experimental standpoints. Indeed, there is a critical need to combine molecular simulations based on a reliable atomistic description of the MOF/GO composites and advanced experimental techniques (HRTEM, NMR, XPS, etc.) to dramatically extend the knowledge of the corresponding solid/solid interface.

In the past couple of years, many DFT studies have been dedicated to construct microscopic illustrations of the MOF surface[1–7] and simplistic models of GO[8–15]. However effort to build more realistic GO structures especially in terms of nature, concentration, and spatial arrangement of the diverse oxygen functional groups (epoxy, hydroxyl, carboxylic, etc.) is still needed[16–18]. Furthermore, the literature only reports one study that recently attempted to model a MOF/GO interface[19]. However, this paper provides a rough representation of MOF-5 surface and GO layer. Indeed, a simplistic MOF model was obtained by considering the periodic unit cell of MOF-5 for which the 1,4-bdc linkers connected to the Zn_4O metal node were removed and the resulting dangling bonds were saturated by hydrogen atoms prior to being placed parallel to a GO layer. This previous work neither considered realistic MOF surface cleaved from crystallographic planes nor take into consideration the presence of a wide variety of chemical functions in GO except the epoxy and hydroxyl groups randomly distributed in the layer. Further this study did not report any characterization of the properties of the interface in terms of the structure and MOF/GO site-to-site interactions.

In my PhD, a computational toolbox has been extended to construct and characterize MOF/GO interface starting with the advances, the group has made recently on the MOF/Polymer interfaces[5,20–26]. This global approach integrates both quantum and force field-based simulations. As shown in Figure 3.1, a careful attention was first paid to derive realistic models for GO at the DFT level with a concentration of epoxy, hydroxyl, and carboxylic groups matching the X-ray photoelectron spectroscopy (XPS) data found experimentally. Next MOF slab models were cut from their 3D periodic structure along different crystallographic planes while the dangling bonds generated from the cut were saturated by terminal functional groups. Here the MOF model considered was the zinc-based zeolitic imidazole framework, ZIF-8 surface, which is a well-developed prototype to explore MOF/GO systems typically for CO_2

capture[27–29]. This MOF was considered as model system to train and validate our computational methodology. Force field-based molecular dynamics were performed to get a reliable description of the MOF/GO interface. Ultimately, properties of this interface such as the nature of the interactions, surface coverage, conformation, and rigidity of the MOF/GO systems were explored and further validated by a set of experimental data collected on the ZIF-8/GO. The scope of this chapter is to describe the different steps for the construction of the MOF/GO interfaces as well as the analysis of the main structural and interaction factors of the corresponding composite. The global strategy is described in Figure 3.1.

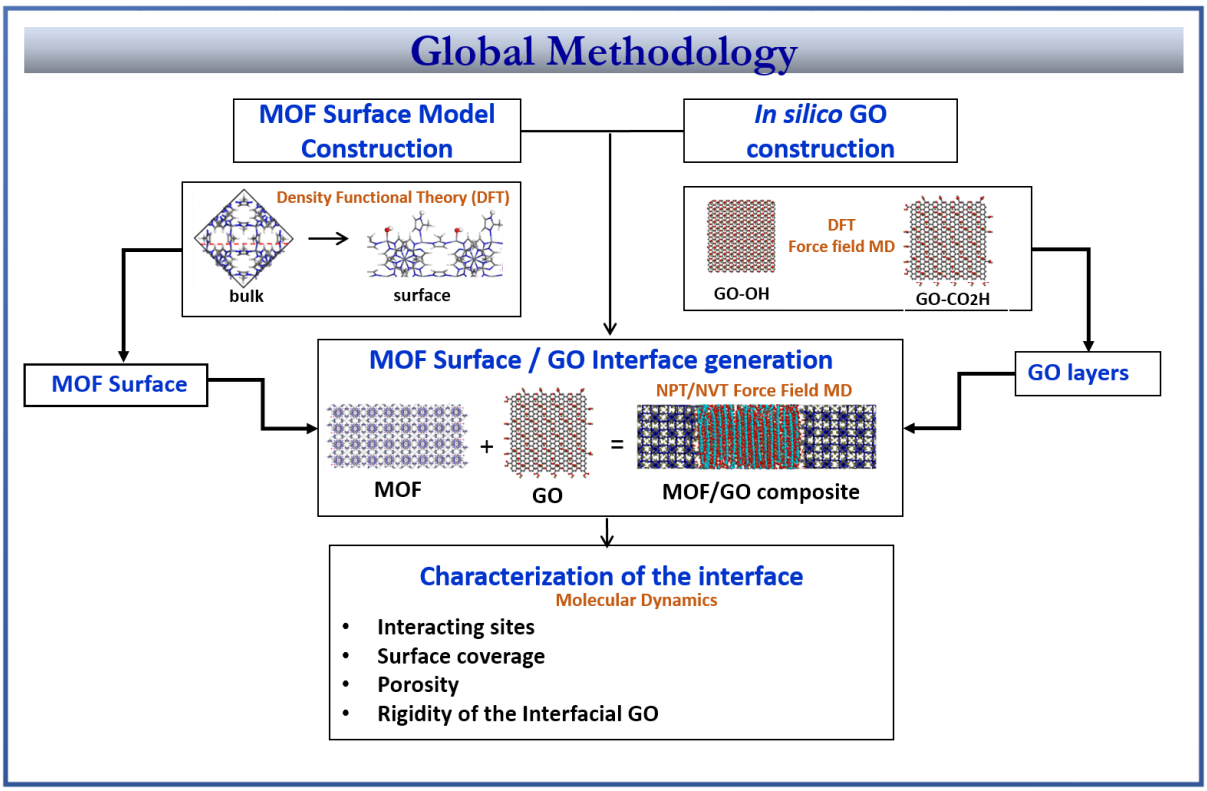

Figure 3.1 Workflow developed for the construction of MOF/GO interface and its characterization

3.2. Construction of GO Models

3.2.1. GO-OH Model

A simplified model of GO was first constructed corresponding to a periodic system along the x and y axis as shown in Figure 3.2a.

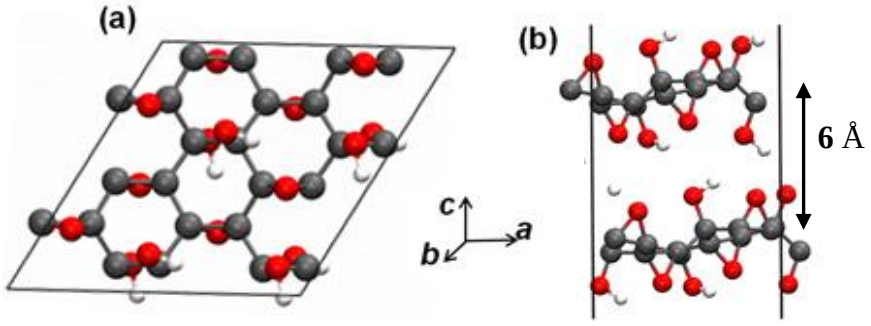

Figure 3.2 a) Initial configuration of GO-OH and b) DFT optimized geometry of the GO-OH model containing 2 layers leading to an interlayer distance of 6 Å. Colour scheme: C-grey, O-red and H-white

The initial geometry was constructed by incorporating functional groups consisting of epoxy (-O-) and hydroxyl (-OH) functions that are attached only to the basal plane. The constructed model was inspired by the widely accepted Lerf–Klinowski's structural model[30] which was derived through solid state NMR studies and first-principle calculations[31]. This GO-OH model has a chemical composition of C, O, and H of 52%, 43%, and 1%, respectively resulting in a C/O ratio of ~1.5.

i. The corresponding model was first geometry optimized at the DFT level using the Quickstep module of the CP2K software[32]. In these simulations, both the positions of the atoms of the framework and the unit cell parameters were fully relaxed. The resulting DFT-optimized cell parameters are reported in Table 3.1. We can see that they remain similar to the initial set of cell parameters (see Table 3.1). Here the valence electrons were treated on a mixed basis set with an energy cut-off of 280 Ry, while the short-range version of the double-zeta polarization basis set was used[33]. The effect of the core electrons and nuclei was considered by using pseudopotentials of Goedecker–Teter–Hutter[33], and the semiempirical dispersion corrections were included with the DFT-D3 method as developed by Grimme (PBE-D3)[34].

Table 3.1 . DFT- optimized cell dimensions of the GO-OH model

	a (Å)	b (Å)	c (Å)	α (°)	β (°)	γ (°)
DFT optimized	8.9	8.9	15.0	90.00	90.00	59.42
Initial Parameters[35]	9.0	9.0	15.0	90.00	90.00	60.00

ii. The DFT optimized periodic structure (with cell parameters mentioned in Table 3.1) was expanded in the z direction to create a two-layers model. The idea was to place the second layer varying the distance between each other from 5 to 11 Å. These corresponding structures were then geometry optimized at the DFT-level to obtain an energy minimization profile with respect to the interlayer distance. The minimum energy was obtained for an interlayer distance of 6 Å, which is in excellent agreement with the experimental data previously reported for dry GO sample[36]. The corresponding structure model is illustrated in Figure 3.2b.

iii. This periodic DFT optimized layer was enlarged in size for further force field-based molecular Dynamics (MD) simulations as implemented in DLPOLY[37]. The dimension of the layer was taken to be 35.6 Å × 35.6 Å corresponding to a 4x4 unit cell model. This corresponds to a system containing 768 atoms. The OPLS-AA[38] force field was used to describe the bonded (bond stretching, angle bending, and torsional and improper dihedral angles) and non-bonded parameters. The partial charges of the system were derived from the fragments cut from the periodic structures (Figure 3.3) using the electrostatic potential scheme[39] CHELPG with the PBE functional, and the 6-31G(d,p) basis set as implemented in the Gaussian 09 package[40]. The so-calculated partial charges are described in Table 3.2. The non-bonded interactions were described by a sum of Coulombic and LJ contributions. The LJ interactions were truncated at 10 Å and the cross-term potential parameters were computed by applying the Lorentz–Berthelot mixing rules, whereas long-range electrostatic interactions were calculated using the Ewald summation method[41].

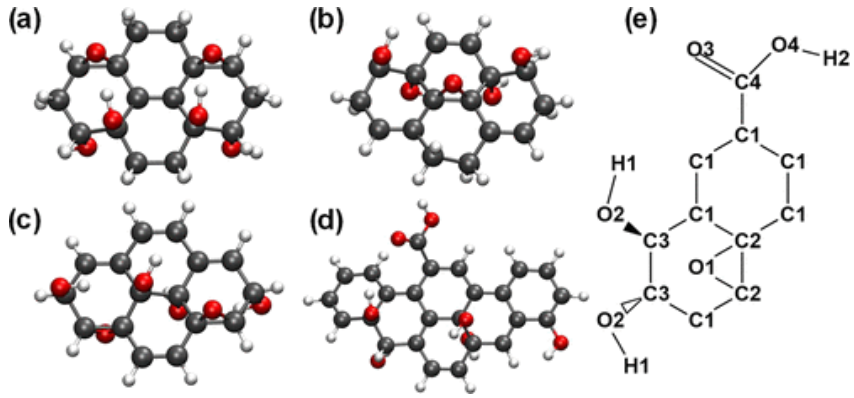

Figure 3.3 (a–c) and d) are the molecular fragments that were considered for charge calculations in the structural models of GO-OH and GO-CO_2H, respectively. e) Labels of the atoms present in the GO-OH and GO-CO_2H models

Table 3.2 DFT-Calculated Partial Charges for all atoms of GO-OH using the CHELPG approach

Atom	C1	C2	C3	C4	O1	O2	O3	O4	H1	H2
q (e units)	-0.169	0.430	0.223	0.642	-0.307	-0.550	-0.510	-0.568	0.387	0.404

iv. The force field MD was run in the NPT ensemble using a simulation box of 35.6 Å × 35.6 Å × 90 Å keeping enough vacuum gap along its z-axis. Berendsen thermostat and barostat was used to maintain the temperature and pressure with the barostat relaxation time of 0.1 and 0.5 ps respectively. Equations of motion were integrated using the velocity Verlet algorithm with a time step of 1 fs. The runs lasted for 2 ns and, later, a constant-NVT MD run of 5 ns was executed for analysis. Illustrations of the equilibrated GO-OH models obtained from MD simulations are reported in Figure 3.4a. For comparison, the same MD strategy was applied to a water loaded GO-OH system using the extended simple point charge model[42] (SPC/E) to describe the guest molecules. The SPC/E model used here as previously employed by Huan et al[43] to explore the aggregation of GO layers in water earlier. This model is a three site/atom water model which has partial charges assigned to oxygen and hydrogen atoms while LJ parameter assigned to oxygen atom. The hydrogen-oxygen-hydrogen angle is 109.47° while oxygen-hydrogen bond distance is 1.0 Å. Here the average polarization correction is included which results in a better density and diffusion properties of actual bulk water. We incorporated first 15 wt.% of water as determined experimentally for a hydrated GO sample which corresponds to 519 water molecules in the simulation box. The interlayer distances of the pristine and the water-loaded GO-OH models were found to be 5.5 and

7.0 Å, respectively (Figure 3.4a) and Figure 3.4b), in good agreement with the experimentally observed results of 6.0 and 7.8 Å[36]. This observation proves that the microscopic model of GO-OH is well described by the flexible force field defined above. The structure was later cleaved along the edges to make it square planar (43 Å × 43 Å) from its rhombic structure, such a cell size was selected to fit well with the dimension of the MOF model along x and y directions (discussed later in section 3.3).

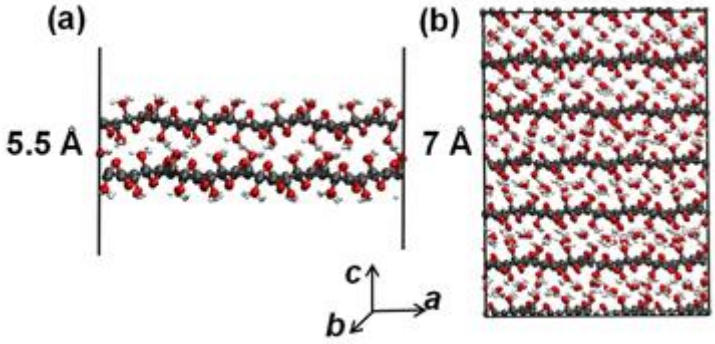

Figure 3.4 Force field optimized periodic models of GO-OH: (a) Dry model; (b) Solvated model containing 15 wt. % water. Colour scheme: C, grey; O, red; and H, white

3.2.2. GO-CO_2H Model

Even though a good representation of a simple GO-OH model was achieved, the target was to build a more realistic model including also carboxylic functions at the edges. The realistic model (labelled as GO-CO_2H) incorporates the chemical features of a real GO sample with the presence of –O– and -OH functional groups at the basal plane and -CO_2H at the edges. The model was constructed in order to reproduce as fairly as possible the experimental atomic concentrations and C/O ratio. The content of the functional groups was so adjusted to match a C/O ratio of ~2.8 corresponding to averaged carbon and oxygen concentrations currently reported for such a GO sample through NMR[16,17], Raman[14,18] and XPS[44,45] measurements as reported in Figure 3.5. The so-constructed GO-CO_2H model contains a concentration of sp^2 (41%) carbon, and sp^3 (34%) carbon, epoxy (12%), hydroxyl (11%), and carboxylic (3%) that fits well with the experimental findings[46]. To construct this model, the initial GO-OH model was considered, and two rows of atoms were chopped off the edges to add the carboxylic functions while maintaining the dimension like GO-OH model (43 Å × 43 Å). The GO-CO_2H layer was further equilibrated in force field MD using NPT ensemble which corresponds to 898 atoms.

Here the bonded and non-bonded parameters were taken from OPLS-AA force field for all atoms while atomic partial charges were derived using the same DFT approach as for GO-OH. Here again, Berendsen thermostat and barostat was used to maintain the temperature and pressure with the barostat relaxation times of 0.1 and 0.5 ps, respectively. Equations of motion were integrated using the velocity verlet algorithm with a time step of 1 fs for 10 ns production run.

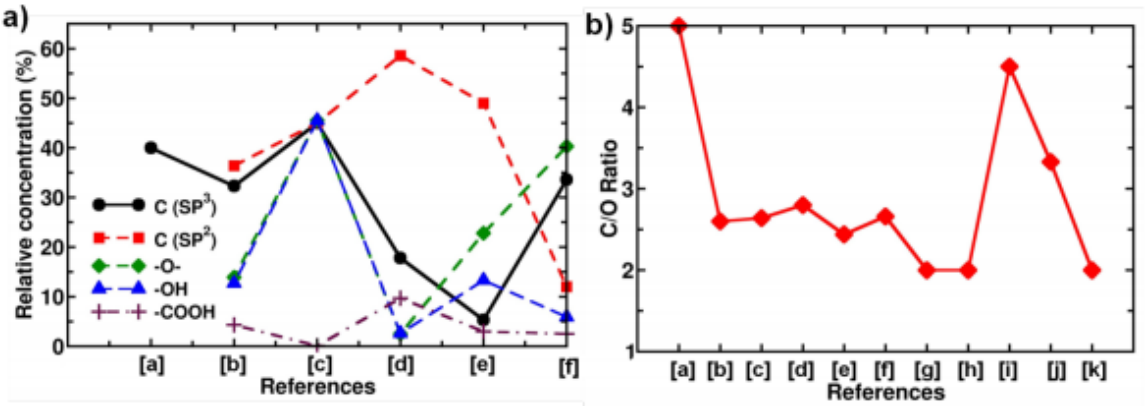

Figure 3.5 a) Relative concentration of various components reported in literature: [a] MKhoyan et al. (2009)[47]; [b] Felten et al. (2013)[46]; [c] Chen et al. (2017)[48]; [d] Lesiak et al. (2014)[45]; [e] Willems et al. (2017)[44] and [f] D' Angelo et al. (2017)[12]. b) Ratio of carbon to oxygen reported in literature: [a] MKhoyan et al. (2009)[47]; [b] SzabÓ et al. (2006)[49]; [c] Jeong et al. (2008)[16]; [d] Yang et al. (2009)[50]; [e] Gao et al. (2009)[51] ; [f] Saxena et al. (2010)[52]; [g] Kudin et al. (2008)[18]; [h] Wang et al. (2011)[14] ; [i] D' Angelo et al. (2017)[12]; [j] Shih et al. (2012)[53]; [k] Willems et al. (2017)[44]

3.3. Construction of ZIF-8 Surface Model

The ZIF-8 surface model was taken from a previous work performed in the group.[22] The construction of ZIF-8 surface was performed starting with the MOF bulk. The bulk ZIF-8 is first geometry optimized at the DFT level using the Quickstep module of the CP2K software. The PBE functional along with a combined Gaussian basis set and plane wave pseudopotential strategy was used. A triple-zeta Gaussian-type basis set (TZVP-MOLOPT) was considered for all atoms, except for the metal centres where double-zeta functions were employed (DZVP-MOLOPT). The pseudopotentials used for all the atoms were those obtained by Goedecker, Teter, and Hutter (GTH). The calculations included the semiempirical dispersion corrections as executed in the DFT-D3 method by Grimme. The resulting DFT optimized cell parameters are given in Table 3.3 showing a good accordance with the experimental data.

Table 3.3 Final DFT-optimized unit cell parameters of ZIF-8[22]

	a (Å)	b (Å)	c (Å)	α (°)	β (°)	γ (°)
DFT-optimized	17.116	17.116	17.110	90.00	90.00	90.00
Experiments	16.9932	16.9932	16.9932	90.00	90.00	90.00
% difference	0.72	0.72	0.68	0.00	0.00	0.00

The optimized structure was then cut along the most favourable crystal facets using Bravais–Friedel–Donnay–Harker (BFDH)[54–56] method. This method helps to identify and screen the sets of Miller indices to further focus on the most important material's crystal habit. Initially the slab models of the [100] and [011] surfaces were constructed considering 3D periodic boundary conditions. These models were eight-times the unit cell size with z length of 96.8 Å. When the energy calculation for different sized surface slabs was performed, the energy converged for the system built up with four-unit cells. The z-length of the surface slab also ensures that no interactions take place along z direction between the surfaces. For force field simulations, the system was doubled in size again and a vacuum gap of at least 15 Å was kept along the z-axis to avoid any interactions between the surface slab.

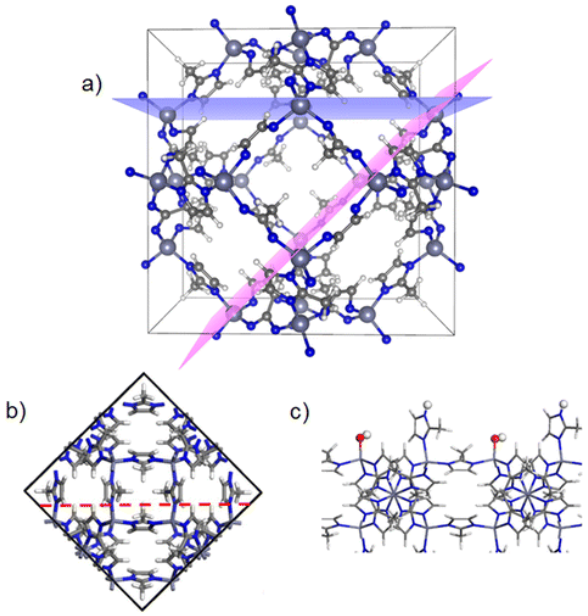

Figure 3.6 The cut from the bulk ZIF-8, exposing the [011] face of ZIF-8 a) the blue plane is that with Miller indices of [100], and the pink one corresponds to [011]. b) and c) show the cut plane (dashed line) and the [011] surface of ZIF-8, respectively. The atoms shown as spheres are those from the dissociative adsorption of water. The following colour code is used for the atoms: Zn, light blue; N, dark blue; C, grey; H, white; O, red. Adapted from Ref. [22]

Cleaving such a structure often leaves a net dipole along the z direction which is countered by "rebuilding" the surface. The net dipole across the vacuum gap can distort the surface. Hence the structure was restructured by moving certain atoms from the top to the bottom of the surface slab to attain a mirror plane of symmetry at the centre of the z-axis[57] while the exposed dangling bonds by the BFDH cut were capped by the attachment of an –OH group and a –H atom to the surface. On such under-coordinated sites(dangling areas), the dissociative adsorption of water was considered which is analogous to the surface terminations of ZIF-8 proposed by Tian et al.[58] and Chizallet et al.[2] in their experimental and computational studies respectively. These sites if untreated would be susceptible to reactions with solvents present in the synthesis medium. As seen in Figure 3.6, OH^- of water attaches itself to the undercoordinated surface Zn atoms, and the remaining H^+ ions compensate the imidazolate ligand for [011] surface. The so-rebuilt surface was again geometry-optimized using CP2K code using the same level of theory and parameters as the used for the optimization of the bulk ZIF-8 model.

Among the two surface cuts which was considered initially, the [011] surface was subsequently chosen as its surface energy was lower compared to [100] surface. The [011] surface had the energy of 3.31 J m^{-2} compared to 3.65 J m^{-2} for [100] surface. The surface energy was calculated based on the following expression(61):

$$E_{surface} = \frac{[E_{surfaceslab} - (n \cdot E_{bulk}) - E_{solvation}]}{A} \quad (61)$$

where $E_{surface}$ is the surface energy, $E_{surfaceslab}$ and E_{bulk} are the energies of the surface slab and bulk models, n is the number of bulk cells used to make the surface slab. $E_{solvation}$ is the energy of dissociative adsorption of solvent molecules on the surface.

MD simulations were further performed considering the ZIF-8 as flexible model. The dimension of the ZIF-8 surface model were 51 Å × 48 Å × 97 Å which correspond to 13320 atoms. The flexible force field parameters and the atomic partial charges of ZIF-8 are taken from Zheng et al[59,60]. In addition, the LJ parameters of the surface -OH and -H atoms were taken from the AMBER while atomic charges were calculated using a grid-based method (CHELPG) scheme[39] as implemented in the Gaussian[40] software with the consideration of the PBE functional[61] and the 6-31G(d,p) basis set[62]. The non-bonded parameters (charges and LJ parameters) are listed in Table 3.4.

Table 3.4 The atom types, LJ parameters (σ,ε) with their atomic partial charges(q) of ZIF-8 surface

Atom	σ (Å)	ε (kcal/mol)	Q
Zn	1.960	0.0125000	0.7362
Zs	1.960	0.0125000	0.7362
N	3.250	0.1700000	-0.3017
NH	3.250	0.1700000	-0.3017
NH	3.250	0.1700000	-0.3017
C1	3.400	0.0860000	0.4339
C2	3.400	0.0860000	-0.1924
C4	3.400	0.1094000	-0.6024
H1	2.511	0.0150000	0.1585
H2	2.650	0.0157000	0.2500
H3	2.511	0.0157000	0.2900
H4	2.650	0.0157000	0.1572
O	3.210	0.1700000	-0.5400

3.4. Construction of ZIF-8/GO Interfaces

The interface models of MOF/GO were constructed using both GO models i.e., GO-OH and GO-CO_2H with ZIF-8 surface model combining them together in a simulation box, the models has been shown in Figure 3.7. The choice of the dimension of ZIF-8 and GOs was made in order to ensure that GO layers fit the length of the ZIF-8 dimensions in both x and y directions. The simulation model for ZIF-8 shows a dimension of 51 Å × 48 Å × 97 Å, enough vacuum space was maintained along its z-axis so that initial configuration of GO layers can adjust well on its surface. The ZIF-8 surface was kept at the centre of the box while the GO layers were distributed at both the edge of the box along the z direction.

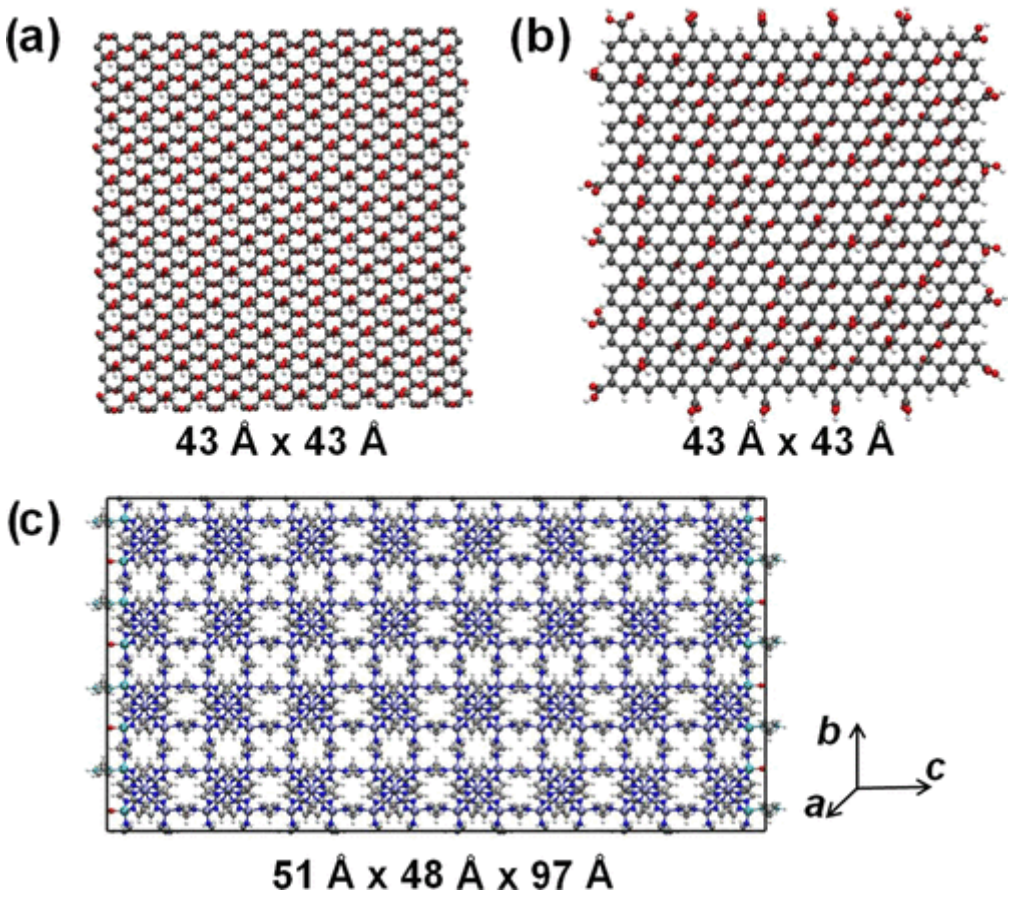

Figure 3.7 Models used to construct the ZIF-8/GOs interfaces: a) GO-OH, b) GO-CO_2H, and c) ZIF-8 surface. Colour scheme: GO layers: C, grey; O, red; H, white; ZIF-8: C, silver; N, blue; Zn, light blue (surface) and ice-blue (bulk); O, red; and H, white

Several GO layers were kept along the z direction to ensure no artificial interactions of MOF surface slabs occur along the z-axis.

- The first MD simulations were performed in the NP_zT ensemble with z being the direction perpendicular to the MOF surface. In this ensemble, the pressure is applied only along the z-axis while the other directions are relaxed. In this step the MOF atom coordinates are kept fixed while GOs are free to move. Since initially the MOF structure is at the centre of the box while the GOs are placed at both end of the box, this causes the GO layers to compress and expand just along the z direction. The interactions between the GO and the ZIF-8 were treated as a sum of Coulomb and LJ potentials, with cross-interaction parameters of GO and ZIF-8 computed using Lorentz–Berthelot mixing rules. This simulation was carried out at 1 kbar and 298 K using Berenson barostat with relaxation time of 0.5 ps. The system was run for a total time of 5 ns with a

time step of 1 fs using a modified version of DLPOLY code[63]. After this run, a packed set of GO layers in contact with ZIF-8 surface was obtained.

- The next run was achieved using the standard NPT ensemble again for a 5 ns with 1 bar pressure and 298 K where the whole system could relax. This ensemble enables to adjust the volume of the simulation box with constant pressure.
- Finally, the last run was realized in the NVT ensemble at 298 K for 5 ns maintaining the volume of the simulation box constant. The Nosé–Hoover thermostat[64] was used with a relaxation time of 0.1 ps. The final data was collected from 5 statistically independent simulations.

In all these calculations, 16 layers of GO was placed on the MOF associated with a separating distance of more than 75 Å in between ZIF-8 surfaces along the z direction. The models correspond to 14368 and 12288 number of GO atoms in GO-CO_2H and GO-OH respectively. The final relaxed structure for both ZIF-8/GO-OH and ZIF-8/GO-CO_2H interface which corresponds to a total number of atoms of 25608 and 27688 respectively, taking in account the 16 layers of GO, are shown in Figure 3.8.

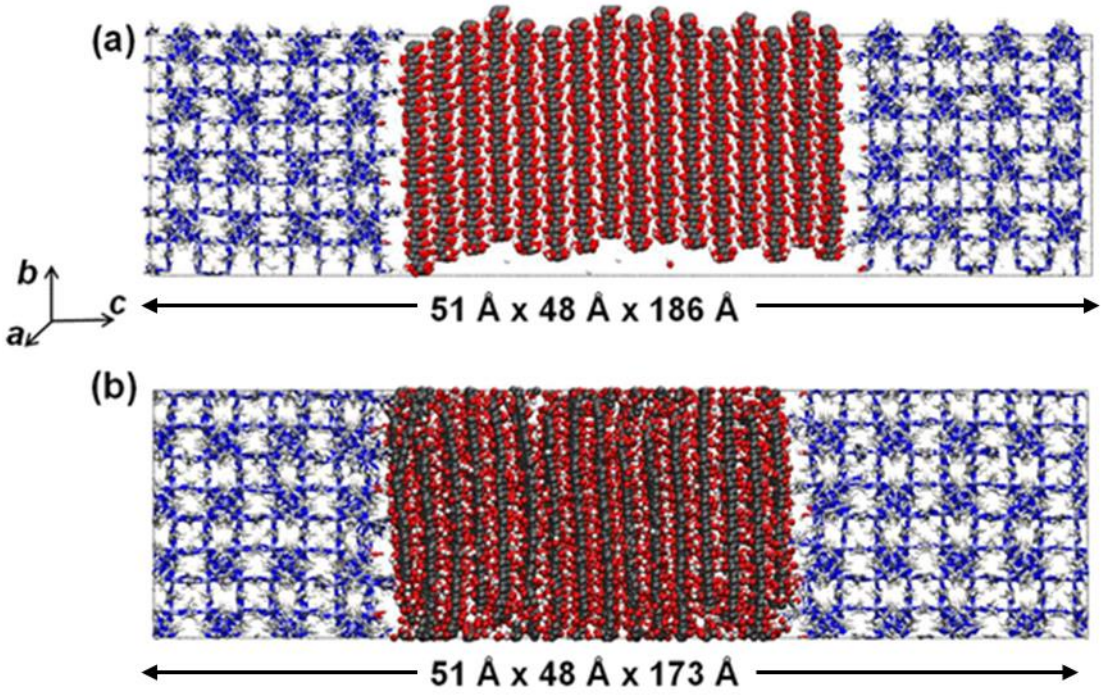

Figure 3.8 Models snapshots of one of the ZIF-8/GO interface configurations obtained from MD simulations consisting of 16 (a) GO-OH and (b) GO-CO2H layers. Atoms of ZIF-8 are in stick representation and GO layers in ball and stick representation. Colour scheme: GO layers: C, grey; O, red; H white; ZIF-8: C, grey; N, blue; Zn, ice-blue; O, red; and H, white

3.5. Analysis of ZIF-8/GO Interfaces

A preliminary step consisted of characterizing the preferential interactions between the GOs and the ZIF-8 surface. The radial distribution functions (RDFs) helps in understanding the short-range order in terms of number of neighbouring atoms as a function of distance from a reference particle. Here the RDFs were calculated and averaged over the MD trajectories between the terminations of the MOF surface, i.e. the –NH groups of the imidazole linker and the –OH groups bonded to the Zn atoms with that of potential interacting sites of GOs, i.e. the epoxy –O–, hydroxyl –OH and carboxylic –CO_2H groups. The corresponding data are plotted in Figure 3.9. The interactions encountered at the ZIF-8/GO-CO_2H interface are between the hydrogen atoms of the –NH (Figure 3.9a) and -OH (Figure 3.9b) groups of ZIF-8 with the oxygen atoms (epoxy, hydroxyl and carboxylic groups) in GO showing a relatively short interacting distances between 2.5 Å and 2.7 Å. One can notice than in the case of the interactions with the terminal carboxylic -CO_2H groups, this preferentially involves the oxygen of the carbonyl groups rather than the oxygen of the acidic functions. Regarding the MOF/GO-OH interface, similar interactions were evidenced between both –NH (Figure 3.9c) and –OH (Figure 3.9d) groups of the ZIF-8 surface and the epoxy and hydroxyl functions of GO-OH.

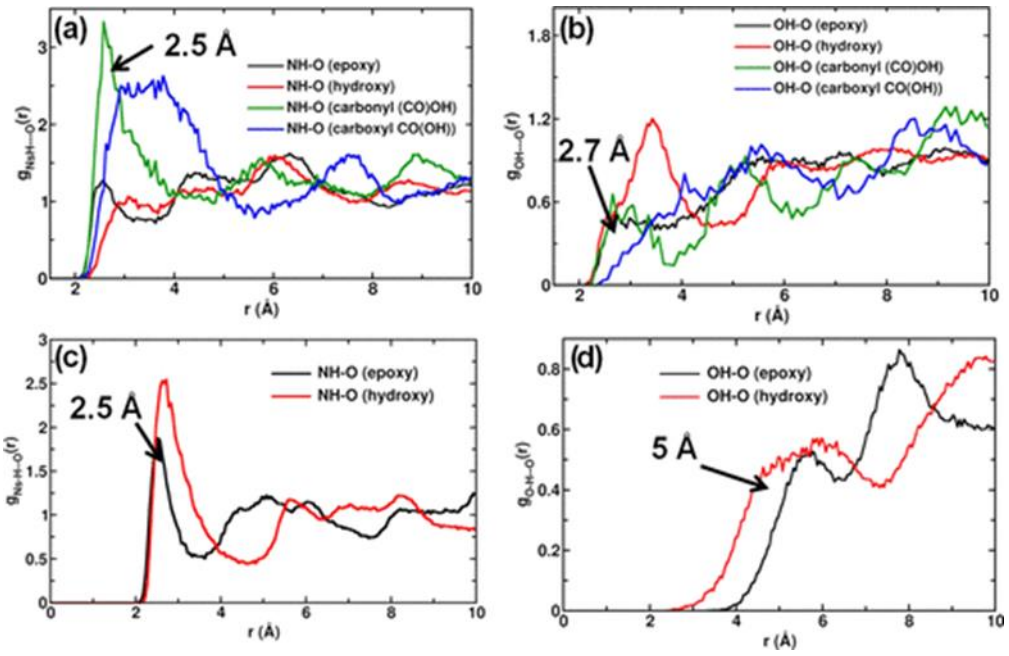

Figure 3.9 Radial distribution functions calculated between (a, c) H of the surface N-H and O atom of various molecular groups of GO layers and (b, d) H of the surface O-H and O of the GO layers in GO-CO_2H and GO-OH, respectively. Results are averaged over 5 different MD runs

An illustration of the resulting geometry of both components is provided in Figure 3.10 in the case of the ZIF-8/GO-CO_2H interface. Figure 3.10 a,b,c illustrate the interacting atom pairs of -NH with epoxy, -NH with hydroxyl and -NH with carboxyl functions of ZIF-8 and GO respectively. This observation suggests that both type of GOs i.e., GO-CO_2H and GO-OH are stabilized by a relatively homogeneous set of interactions.

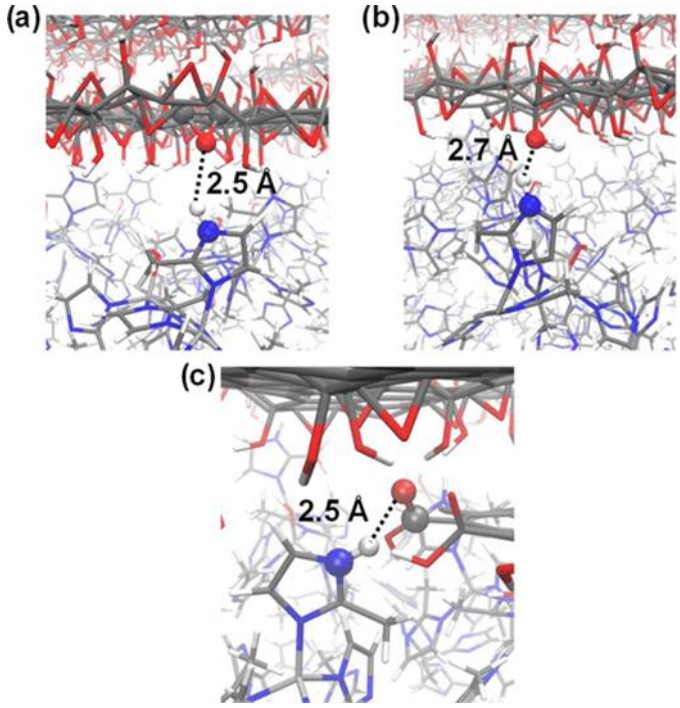

Figure 3.10 Preferential interactions between the H atom of the -NH group of ZIF-8 (below) and the O atom of the a) epoxy, b) hydroxyl, c) carbonyl function of the carboxylic groups present in the GO (above) in the case of the ZIF-8/GO-CO_2H interface. Colour codes are the same as Figure 3.8

As a following stage, the GOs coverage at the MOF surface was explored. Figure 3.11 shows a quantitative analysis of the density of the ZIF-8 and GOs atoms along the z-axis of the simulation box. The plots reported in Figure 3.11a and Figure 3.11b reveal that density profiles of both GO and MOF are fluctuating around a mean value along the z coordinate and decreases linearly at the interface of both. When one scans the z-interval [z = 0 Å to whole box length along the z-axis (173 Å for GO-CO_2H and 186 Å for GO-OH)], the first domain contains GOs with atomic density oscillating around an equilibrium value (see black line). This atomic density can be termed as bulk-like phase. Above z ≈ 25 Å (GO-CO_2H) and 40 Å (GO-OH), the atomic density of the GOs drops, reaching a region where only MOF is present until z ≈ 125 Å (GO-CO2H) and 140 Å (GO-OH) seen as the red curve. Here two distinct regions can be identified, first the interfacial region, **region A**, and a more "bulk-like" region, **region B.** When one

compares the plots of Figure 3.11a and Figure 3.11b for ZIF-8/GO-OH and ZIF-8/GO-CO_2H respectively, region A is larger for GO-CO_2H i.e., ~6 Å vs ~3 Å for GO-OH. Technically speaking, region A can be defined by the interval between a lower limit taken as the z value for the first non-zero atomic density of GOs and the upper limit, as that for which the atomic density of GO starts to oscillate. This difference in region A for the both GO-OH and GO-CO_2H can be explained by a pronounced distortion of the GO-CO_2H layer when brought into contact with the ZIF-8 surface which allows the atoms of the GO to populate in a larger extent this region. This structural behaviour is illustrated in the snapshots reported in Figure 3.11c and Figure 3.11d for the interfacial regions of both ZIF-8/GO-OH and ZIF-8/GO-CO_2H. These illustrations reveal that the GO-CO_2H and ZIF-8 can coexist together, GO-CO_2H penetrating the ZIF-8 surface in a zig-zag fashion similar to the scenario observed for MOF/polymer composites (UiO-66 coupled with PEG with z~5-6 Å)[65] suggesting an excellent compatibility.

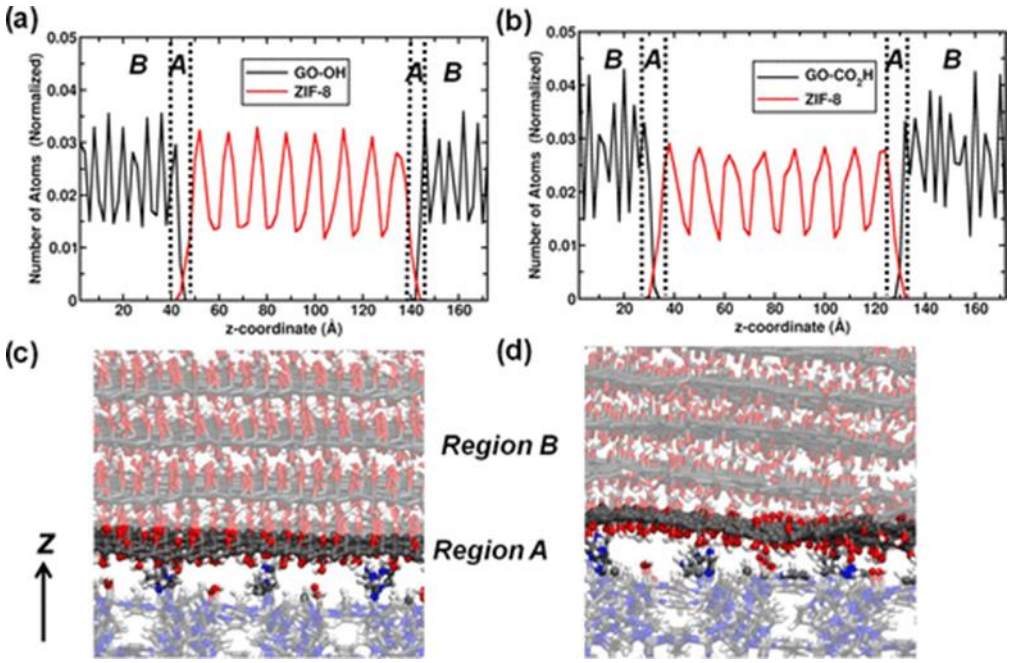

Figure 3.11 Atomic density of both ZIF-8 and GOs in the direction perpendicular to the surface slab (i.e. along the z direction) for a) ZIF-8/GO-OH and b) ZIF-8/GO-CO_2H interfaces. Snapshot of the ZIF-8/GO-CO_2H c) and ZIF-8/GO-OH d) interfaces, where the atoms that belong to region A are opaque, and the rest are transparent. The number of atoms in both MOF and GO phases are normalized with respect to the total number of atoms in each phase

In order to quantify the deformations of GOs in the vicinity of the ZIF-8 surface, the dihedral angles distribution was calculated for each GO layer distributed along the z-direction. As an illustration, the dihedral angles of the first two layers closest to the MOF surface (corresponding to region A) and a layer far away from the MOF surface (corresponding to region B), typically

the 8th layer are represented in Figure 3.12. One can first observe that region A of GO-CO_2H layers undergoes far higher degree of distortion as compared to its region B. The 1st and 2nd layer had prominent dihedral angles of the 120° and -40° as compared to a homogeneous distribution of dihedral angle for the 8th layer. In the case of GO-OH (figure below), both region A and region B layers show a planar conformation with a maximum probability distribution for the dihedral angles at -180° or 180. This analysis proves that the presence of the –CO_2H groups in GO enhances the distortion of the layer when brought into contact with the ZIF-8 surface and hence implies a significant shortening of the width of region A for GO-OH due to absence of it.

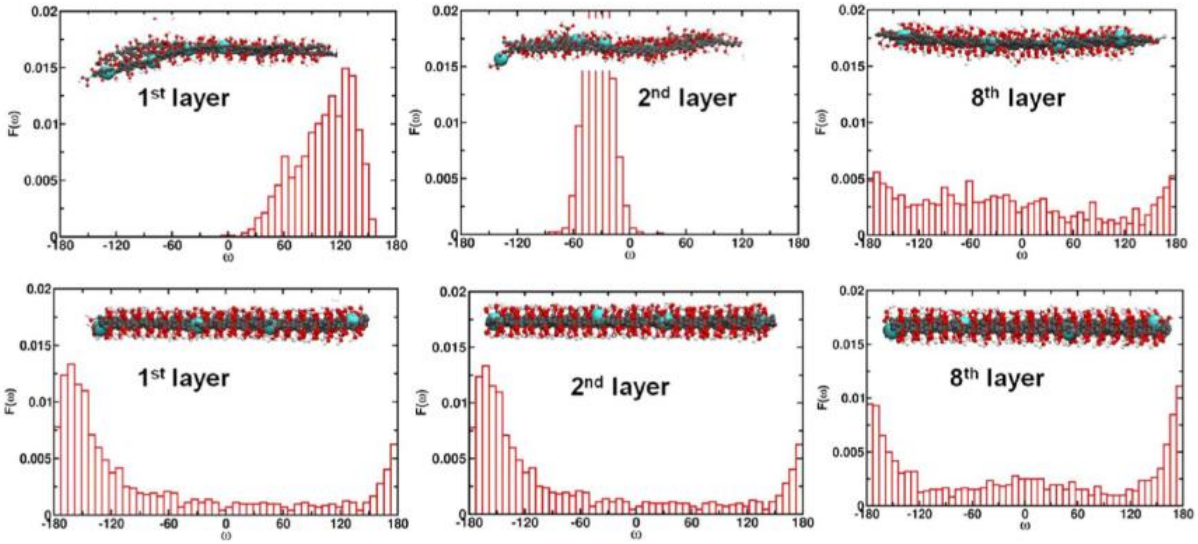

Figure 3.12 Dihedral angle distributions of the GO layers present in the ZIF-8/GO-CO_2H (top part) and ZIF-8/GO-OH (bottom part) interfaces. Atoms that are considered for dihedral angle calculations are represented with van der Waals spheres in cyan

3.6. Validation of Computational Findings by Experiments

The so-simulated ZIF-8/GO-CO_2H composite was further experimentally fabricated by dispersing GO and ZIF-8 in DMF solution followed by vacuum filtration to create a thick film. More details of the preparation of these membranes are found in the paper. The composite was further characterized the techniques mentioned below.

3.6.1. TEM Studies

The TEM studies carried out on TEM 2100F (JEOL, Tokyo, Japan) revealed possible morphological characteristics of both GO nanosheets and ZIF-8 nanoparticles. ZIF-8 nanocrystals have a particle size in the range of 50–70 nm forming an aggregated structure (Figure 3.13a). This is mainly due to drying process found common in ZIF-8 crystals. The TEM images of ZIF-8/GO (3:7 weight ratio) composites clearly revealed the interaction between ZIF-8 nanocrystals and GO sheets, as shown in Figure 3.13a and Figure 3.13b at different scales. Here the ZIF-8 nanocrystals are clearly in the vicinity of the GO nanosheets supporting again a good compatibility between the ZIF-8 and GO as predicted above.

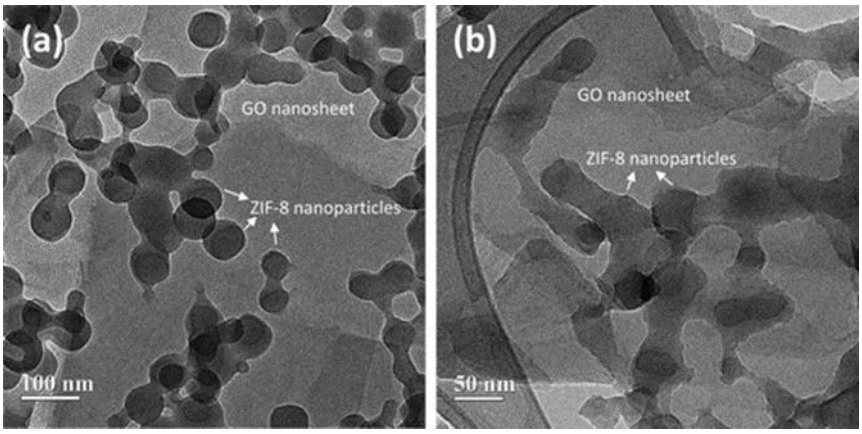

Figure 3.13 (a and b) TEM images of ZIF-8/GO composite with ZIF-8/GO ratio of 3:7 at different scales

3.6.2. Tensile Strength Measurements

The samples were prepared with height and width of 13 and 2 mm and strained in Instron universal testing system (AGS-J-500N, Norwood, MA) UTI at the strain rate of 1.0 mm/min. Figure 3.14 reveals the tensile stress/strain curves of GO and different concentration ratios of ZIF-8/GO samples. Here the ZIF-8/GO composite shows a lower mechanical strength when compared to that of the pristine GO (82 MPa). In general, a pristine GO membrane is composed of tightly packed two-dimensional flakes assembled in a laminar structure with high structural integrity. While the incorporation of ZIF-8 alters the layered organization of GO leading to lower mechanical strength. Mechanical strength was enhanced from 39.9 to 48.6 MPa when the concentration of the ZIF-8 filler was increased from 1:9 to 3:7 causing the MMMs to

become more rigid and indeed maintain an adequate mechanical stability to be handled. This improved stiffness is due to the relatively strong interactions between the ZIF-8 surface and the oxygen-based functional groups of GO nanosheets as revealed by the simulations. On the other hand, composite membranes consisting of low ZIF-8 content revealed higher strain, compared to high ZIF-8 content samples, demonstrating the more flexible structure of composite membranes induced by ZIF-8 nanoparticles. Hence an optimum composition of both can enhance the rigidity of the membrane.

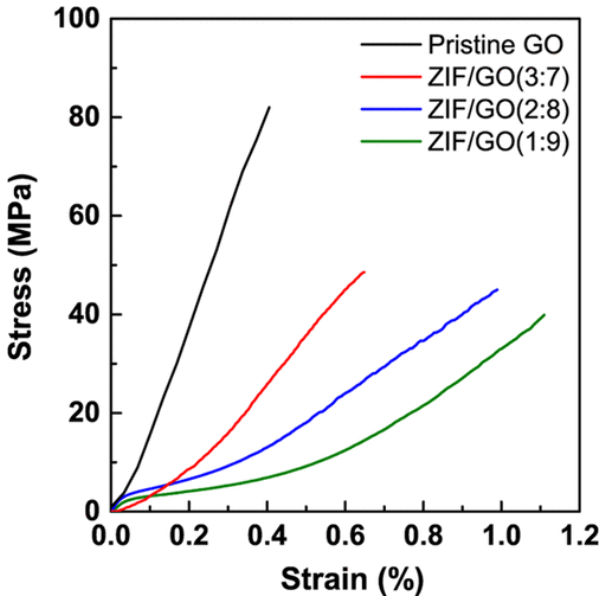

Figure 3.14 Tensile strength curves of ZIF-8/GO composite films with different contents of ZIF-8 and comparison with the pure GO

3.7. Conclusion

In conclusion, here for the first time, a computational methodology was deployed to construct and characterize a MOF/GO interface at the microscopic scale in tandem with experimental tools. The strong interplay with experimental data further allowed a validation of the computational methodology developed in this PhD. As a summary, two GO models were generated according to the experimental elemental composition and C/O ratio values (consistent with the FTIR and XPS analysis). Next, the structural models for two different ZIF-8/GO composites with sixteen GO layers were constructed and their interfacial properties, such as the main interactions between two components, the surface coverage and conformation of the GO

layers were carefully analysed. The interaction sites of the MOF surface are the terminal -NH groups of the imidazole and –OH molecules of the inorganic node which both interact strongly with all oxygen functional groups on the GO layers. In the case of GO-CO_2H composite with ZIF-8, the presence of –CO_2H groups at the edge leads to strong distortions at the interfacial region close to the MOF surface. Experimental results including TEM images and mechanical strength measurement (ZIF-8/GO: 3/7 weight ratio) confirmed the relatively strong interactions between GO nanosheets with ZIF-8 nanoparticles. Most importantly, the improved tensile strength of composite membranes with increasing the ZIF-8 content clearly demonstrated their mutual interactions between ZIF-8 nanoparticles and GO nanosheets.

The so-derived methodology opens the doors to study a wide range of MOF/GO systems provided that acceptable force field parameters exists, and it will be useful to scan the compatibility between different GOs and MOF surfaces. This preliminary work on the ZIF-8/GO system motivated further systematic work by changing the nature of the MOFs as well as the functionalization of the GO layers. This systematic exploration is described in the following two chapters.

REFERENCES

1. Amirjalayer, S., Tafipolsky, M. & Schmid, R. Surface termination of the metal-organic framework HKUST-1: A theoretical investigation. *J. Phys. Chem. Lett. 5*, 3206–3210 (**2014**).
2. Chizallet, C. *et al.* Catalysis of transesterification by a nonfunctionalized metal-organic framework: Acido-basicity at the external surface of ZIF-8 probed by FTIR and ab initio calculations. *J. Am. Chem. Soc. 132*, 12365–12377 (**2010**).
3. Chizallet, C. & Bats, N. External surface of zeolite imidazolate frameworks viewed ab initio: Multifunctionality at the organic-inorganic interface. *J. Phys. Chem. Lett. 1*, 349–353 (**2010**).
4. Tian, F. *et al.* Surface and stability characterization of a nanoporous ZIF-8 thin film. *J. Phys. Chem. C 118*, 14449–14456 (**2014**).
5. Semino, R., Moreton, J. C., Ramsahye, N. A., Cohen, S. M. & Maurin, G. Understanding the origins of metal–organic framework/polymer compatibility. *Chem. Sci. 9,* 315–324 (**2018**).
6. Yang, Q. *et al.* Probing the dynamics of CO2 and CH4 within the porous zirconium terephthalate UiO-66(Zr): A synergic combination of neutron scattering measurements and molecular simulations. *Chem. - A Eur. J. 17*, 8882–8889 (**2011**).
7. Lewis, D. W. *et al.* Zeolitic imidazole frameworks: Structural and energetics trends compared with their zeolite analogues. *CrystEngComm 11*, 2272–2276 (**2009**).
8. Yan, J. A., Xian, L. & Chou, M. Y. Structural and electronic properties of oxidized graphene. *Phys. Rev. Lett. 103*, 1–4 (**2009**).
9. Pykal, M. *et al.* Modelling of graphene functionalization. *Phys. Chem. Chem. Phys. 18,* 6351–6372 (**2016**).
10. Guilhon, I., Bechstedt, F., Botti, S., Marques, M. & Teles, L. K. Thermodynamic, electronic, and optical properties of graphene oxide: A statistical *ab initio* approach. *Phys. Rev. B 95*, 245427 (**2017**).
11. Hernández Rosas, J. J., Ramírez Gutiérrez, R. E., Escobedo-Morales, A. & Chigo Anota, E. First principles calculations of the electronic and chemical properties of graphene, graphane, and graphene oxide. *J. Mol. Model. 17*, 1133–1139 (**2011**).
12. D'Angelo, D. *et al.* Oxygen Functionalities Evolution in Thermally Treated Graphene Oxide Featured by EELS and DFT Calculations. *J. Phys. Chem. C 121*, 5408–5414 (**2017**).

13. Yin, D., Lu, N., Li, Z. & Yang, J. A computational infrared spectroscopic study of graphene oxide. *J. Chem. Phys. 139,* 084704 (**2013**).

14. Wang, L., Zhao, J., Sun, Y.-Y. Y. & Zhang, S. B. Characteristics of Raman spectra for graphene oxide from ab initio simulations. *J. Chem. Phys. 135*, 184503 (**2011**).

15. Zhou, S. & Bongiorno, A. Density functional theory modeling of multilayer 'epitaxial' graphene oxide. *Acc. Chem. Res. 47*, 3331–3339 (**2014**).

16. Jeong, H. K. *et al.* Evidence of graphitic AB stacking order of graphite oxides. *J. Am. Chem. Soc. 130*, 1362–1366 (**2008**).

17. Yang, D. *et al.* Chemical analysis of graphene oxide films after heat and chemical treatments by X-ray photoelectron and Micro-Raman spectroscopy. *Carbon N. Y. 47*, 145–152 (**2009**).

18. Kudin, K. N. *et al.* Raman spectra of graphite oxide and functionalized graphene sheets. *Nano Lett. 8*, 36–41 (**2008**).

19. Lin, L.-C., Paik, D. & Kim, J. Understanding gas adsorption in MOF-5/graphene oxide composite materials. *Phys. Chem. Chem. Phys. 19,* 11639–11644 (**2017**).

20. Benzaqui, M. *et al.* Toward an Understanding of the Microstructure and Interfacial Properties of PIMs/ZIF-8 Mixed Matrix Membranes. *ACS Appl. Mater. Interfaces 8,* 27311–27321 (**2016**).

21. Semino, R., Durholt, J. P., Schmid, R. & Marin, G. Multiscale modeling of the HKUST-1/polyvinyl alcohol) interface: From an atomistic to a coarse graining approach. *J. Phys. Chem. C 121,* 21491–21496 (**2017**).

22. Semino, R., Ramsahye, N. A., Ghoufi, A. & Maurin, G. Microscopic Model of the Metal-Organic Framework/Polymer Interface: A First Step toward Understanding the Compatibility in Mixed Matrix Membranes. *ACS Appl. Mater. Interfaces 8*, 809–819 (**2016**).

23. Duan, P. *et al.* Polymer Infiltration into Metal-Organic Frameworks in Mixed-Matrix Membranes Detected in Situ by NMR. *J. Am. Chem. Soc. 141*, 7589–7595 (**2019**).

24. Benzaqui, M. *et al.* Covalent and Selective Grafting of Polyethylene Glycol Brushes at the Surface of ZIF-8 for the Processing of Membranes for Pervaporation. *ACS Sustain. Chem. Eng. 7*, 6629–6639 (**2019**).

25. Ahmad, M. Z. *et al.* Enhanced gas separation performance of 6FDA-DAM based mixed matrix membranes by incorporating MOF UiO-66 and its derivatives. *J. Memb. Sci. 558*, 64–77 (**2018**).

26. Hwang, S. *et al.* Revealing Transient Concentration of CO2 in a Mixed Matrix Membrane by IR Microimaging and Molecular Modeling. *Angew. Chemie Int. Ed.* 4–9 (**2018**). doi:10.1002/anie.201713160

27. Cravillon, J. *et al.* Rapid room-temperature synthesis and characterization of nanocrystals of a prototypical zeolitic imidazolate framework. *Chem. Mater. 21,* 1410–1412 (**2009**).

28. Park, K. S. *et al.* Exceptional chemical and thermal stability of zeolitic imidazolate frameworks. *Proc. Natl. Acad. Sci. 103*, 10186–10191 (**2006**).

29. Huang, X. C., Lin, Y. Y., Zhang, J. P. & Chen, X. M. Ligand-directed strategy for zeolite-type metal-organic frameworks: Zinc(II) imidazolates with unusual zeolitic topologies. *Angew. Chemie - Int. Ed. 45*, 1557–1559 (**2006**).

30. Lerf, A., He, H., Forster, M. & Klinowski, J. Structure of Graphite Oxide Revisited. *J. Phys. Chem. B 102*, 4477–4482 (**1998**).

31. Wang, L. *et al.* Graphene oxide as an ideal substrate for hydrogen storage. *ACS Nano 3,* 2995–3000 (**2009**).

32. Vandevondele, J. *et al.* Quickstep: Fast and accurate density functional calculations using a mixed Gaussian and plane waves approach. *Comput. Phys. Commun. 167*, 103–128 (**2005**).

33. Elstner, M. *et al.* Self-consistent-charge density-functional tight-binding method for simulations of complex materials properties. *Phys. Rev. B 58,* 7260–7268 (**1998**).

34. Grimme, S., Antony, J., Ehrlich, S. & Krieg, H. A consistent and accurate ab initio parametrization of density functional dispersion correction (DFT-D) for the 94 elements H-Pu. *J. Chem. Phys. 132*, 154104 (**2010**).

35. Kukesh, J. S. & L. Pauling, L. The problem of the graphite structure. *Am. Mineral. 35:125*, (**1950**).

36. Dimiev, A. M. & Eigler, S. *Graphene Oxide: Fundamentals and Applications*. *Graphene Oxide: Fundamentals and Applications* (John Wiley & Sons, Ltd., **2016**). doi:10.1002/9781119069447

37. Todorov, I., Smith, W. & Cheshire, U. The DL POLY 4 user manual. *STFC, STFC Daresbury … 4.05.1*, (**2011**).

38. Jorgensen, W. L., Maxwell, D. S. & Tirado-Rives, J. Development and Testing of the OPLS All-Atom Force Field on Conformational Energetics and Properties of Organic Liquids. *J. Am. Chem. Soc. 118*, 11225–11236 (**1996**).

39. Breneman, C. M. & Wiberg, K. B. Determining atom-centered monopoles from molecular electrostatic potentials. The need for high sampling density in formamide conformational analysis. *J. Comput. Chem. 11*, 361–373 (**1990**).

40. Frisch, M. J. *et al.* Gaussian 09, Revision B.01. *Gaussian 09, Revision B.01, Gaussian, Inc., Wallingford CT* (**2009**).

41. Allen, M. P. & Tildesley, D. J. *Computer simulation of liquids*. doi:10.1016/j.cpc.2008.01.029

42. Dai, H., Xu, Z. & Yang, X. Water permeation and ion rejection in layer-by-layer stacked graphene oxide nanochannels: A molecular dynamics simulation. *J. Phys. Chem. C 120*, 22585–22596 (**2016**).

43. Berendsen, H. J. C., Grigera, J. R. & Straatsma, T. P. The missing term in effective pair potentials. *J. Phys. Chem. 91*, 6269–6271 (**1987**).

44. Willems, N. *et al.* Biomimetic Phospholipid Membrane Organization on Graphene and Graphene Oxide Surfaces: A Molecular Dynamics Simulation Study. *ACS Nano 11*, 1613–1625 (**2017**).

45. Lesiak, B. *et al.* Preparation of graphene oxide and characterisation using electron spectroscopy. *J. Electron Spectros. Relat. Phenomena 193*, 92–99 (**2014**).

46. Felten, A. *et al.* Single- and double-sided chemical functionalization of bilayer graphene. *Small 9*, 631–639 (**2013**).

47. Mkhoyan, K. A. *et al.* Atomic and Electronic Structure of Graphene-Oxide. *Nano Lett. 9,* 1058–1063 (**2009**).

48. Chen, C. H. *et al.* Effective Synthesis of Highly Oxidized Graphene Oxide That Enables Wafer-scale Nanopatterning: Preformed Acidic Oxidizing Medium Approach. *Sci. Rep. 7*, 3908 (**2017**).

49. Szabó, T. *et al.* Evolution of Surface Functional Groups in a Series of Progressively Oxidized Graphite Oxides Evolution of Surface Functional Groups in a Series of Progressively Oxidized Graphite Oxides. *Chem. Mater. 18*, 2740–2749 (**2006**).

50. Yang, H. *et al.* Covalent functionalization of chemically converted graphene sheets via silane and its reinforcement. *J. Mater. Chem. 19*, 4632–4638 (**2009**).

51. Gao, W., Alemany, L. B., Ci, L. & Ajayan, P. M. New insights into the structure and reduction of graphite oxide. *Nat. Chem. 1*, 403–408 (**2009**).

52. Saxena, S., Tyson, T. A. & Negusse, E. Investigation of the local structure of graphene oxide. *J. Phys. Chem. Lett. 1,* 3433–3437 (**2010**).

53. Shih, C.-J., Lin, S., Sharma, R., Strano, M. S. & Blankschtein, D. Understanding the pH-Dependent Behavior of Graphene Oxide Aqueous Solutions: A Comparative Experimental and Molecular Dynamics Simulation Study. *Langmuir 28*, 235–241 (**2012**).

54. Donnay, H., Harker, D. & Johns, T. A NEW LAW OF CRYSTAL MORPHOLOGY EXTENDING THE LAW OF BRAVAIS. *Am. Miner. 22*, 446−467. (**1937**).

55. Friedel, G. *Etudes sur la Loi de Bravais*. (Bull. Soc. Fr. Mineral., **1907**).

56. Bravais, A. *Etudes Cristallographiques*. (**1866**).

57. Catlow, C. R. A. *et al.* Computer modelling as a technique in solid state chemistry. *Faraday Discuss. 106*, 1–40 (**1997**).

58. Tian, F. *et al.* Surface and stability characterization of a nanoporous ZIF-8 thin film. *J. Phys. Chem. C 118*, 14449–14456 (**2014**).

59. Zheng, B., Demontis, P. & Suffritti, G. B. Force Field for Molecular Dynamics Computations in Flexible ZIF-8 Framework.pdf. *J. Phys. Chem. C 116*, 933–938 (**2012**).

60. Singh, U. C. & Kollman, P. A. An approach to computing electrostatic charges for molecules. *J. Comput. Chem. 5*, 129–145 (**1984**).

61. Perdew, J. P., Burke, K. & Ernzerhof, M. Generalized Gradient Approximation Made Simple. *Phys. Rev. Lett. 77*, 3865–3868 (**1996**).

62. Hehre, W. J., Ditchfield, R. & Pople, J. A. Self — Consistent Molecular Orbital Methods . XII . Further Extensions of Gaussian — Type Basis Sets for Use in Molecular Orbital Studies of Organic Molecules Published by the AIP Publishing Articles you may be interested in Self - consistent molecular or. *2257,* (**1977**).

63. Todorov, I. T., Smith, W., Trachenko, K. & Dove, M. T. DL_POLY_3: new dimensions in molecular dynamics simulations via massive parallelism. *J. Mater. Chem. 16,* 1911–1918 (**2006**).

64. Martyna, G. J., Klein, M. L. & Tuckerman, M. Nosé-Hoover chains: The canonical ensemble via continuous dynamics. *J. Chem. Phys. 97*, 2635–2643 (**1992**).

65. Semino, R., Moreton, J. C., Ramsahye, N. A., Cohen, S. M. & Maurin, G. Understanding the origins of metal-organic framework/polymer compatibility. *Chem. Sci. 9*, 315–324 (**2018**).

Article 1

ACS APPLIED MATERIALS & INTERFACES

Research Article

Cite This: *ACS Appl. Mater. Interfaces* 2018, 10, 33619−33629

www.acsami.org

Understanding of the Graphene Oxide/Metal-Organic Framework Interface at the Atomistic Scale

Satyanarayana Bonakala,[†,§] Anusha Lalitha,[†,§] Jae Eun Shin,[‡] Farhad Moghadam,[‡] Rocio Semino,[†] Ho Bum Park,[‡] and Guillaume Maurin*[,†]

[†]Institut Charles Gerhardt Montpellier UMR 5253 CNRS, Université de Montpellier, Place E. Bataillon, 34095 Montpellier Cedex 05, France

[‡]Department of Energy Engineering, Hanyang University, Seoul 04763, Republic of Korea

Supporting Information

ABSTRACT: An atomistic model of the metal-organic framework (MOF) ZIF-8/graphene oxide (GO) interface has been constructed using a combination of density functional theory calculations and force-field-based molecular dynamics simulations. Two microscopic models of GO were constructed integrating basal plane and both basal and edge plane functional groups, called GO-OH and GO-CO_2H, respectively. Analysis of the MOF/GO site-to-site interactions, surface coverage, and GO conformation/stiffness and a full characterization of the interfacial region is provided with a special emphasis on the influence of the chemical composition of GO. It was evidenced that the structure of the GO/ZIF-8 composite at the interface is stabilized by a relatively homogeneous set of interactions between the hydrogen atoms of the −NH and −OH terminal functions of ZIF-8 and the oxygen atoms of the epoxy, hydroxyl, and carboxylic groups of GO, leading to an optimal coverage of the MOF surface by GO. Such a scenario implies a significant distortion of the first GO layer brought into contact with the MOF surface, leading to an interfacial region with a relatively small width. This computational exploration strongly suggests that a very good compatibility between these two components would lead, in turn, to the preparation of defect-free ZIF-8/GO films. These predictions are correlated with an experimental effort that consists of successfully prepared homogeneous MOF/GO films that were further characterized by transmission electron microscopy and mechanical testing.

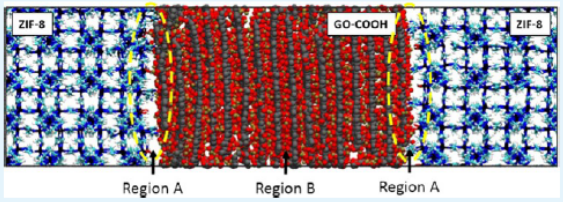

KEYWORDS: *density functional theory, force-field-based molecular dynamics, microscopic models, graphene oxide, metal-organic frameworks, mixed matrix membranes*

I. INTRODUCTION

Metal-organic framework (MOF)−graphene oxide (GO)-based composites have attracted considerable interest over the last decade owing to their promising performances in a wide range of applications including adsorption/separation,[1−8] catalysis,[9,10] supercapacitors,[11,12] and electrochemistry.[13−16] Although many studies have been reported on the preparation of MOF/GO composites by incorporating GO into a large variety of MOFs via diverse experimental strategies,[17−19] the microscopic structure of the interface formed by these two components is far from being understood. Unveiling the characteristics of the interfacial region is a challenging objective that requires first a detailed atomic description of the MOF surface as well as that of the GO. Recently, a few density functional theory (DFT) studies have been dedicated to construct microscopic models of the external surface of a series of MOFs including UiO-66(Zr),[20] ZIF-8,[21,22] and HKUST-1.[23] Although some atomistic representations of GO can be found in the literature,[24−27] more realistic models are still needed to account for the complexity of GO in terms of nature, concentration, and spatial arrangement of the diverse oxygen functional groups (epoxy, hydroxyl, carboxylic, etc.) that can be encountered experimentally.[28−31] A first attempt to build a MOF/GO interface has been recently reported by Lin et al.[32] This work considered a rough representation of the MOF-5 surface constructed by removing some organic linkers from the unit cell followed by a saturation of the dangling bonds prior to be placed parallel to a GO layer represented by a simplified model, which accounts only for the presence of epoxy and hydroxyl groups randomly distributed in the layer. Note that except for the construction of a MOF-5/GO model this previous study did not report any characterization of the properties of the interface in terms of the structure and MOF/GO site-to-site interactions in play.

Here, we report an extensive exploration of the properties of the MOF/GO interface that is expected to play a predominant role in explaining the compatibility of the two components and hence the stability/feasibility of the corresponding composite.

Received: June 13, 2018
Accepted: September 5, 2018
Published: September 5, 2018

DOI: 10.1021/acsami.8b09851
ACS Appl. Mater. Interfaces 2018, 10, 33619−33629

ACS Applied Materials & Interfaces Research Article

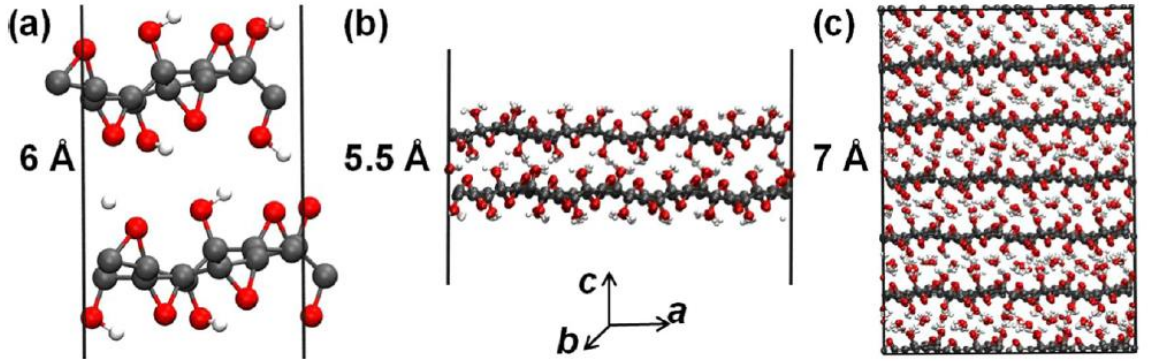

Figure 1. Optimized periodic models of GO-OH: (a) DFT simulations resulting in a desolvated model of 9 Å × 9 Å × 30 Å dimensions with an interlayer distance of 6 Å; (b) force-field-based molecular dynamics (MD) simulations resulting in a desolvated model of 36 Å × 36 Å × 90 Å dimensions (a higher value along the *c* axis is considered to exclude the interactions along this direction within the classical force field limit due to periodic boundary conditions with an interlayer distance of 5.5 Å); (c) force-field-based MD simulations resulting in a model containing 15 wt % water of 34 Å × 36 Å × 42 Å dimensions with an interlayer distance of 7.0 Å. Color scheme: C, gray; O, red; and H, white.

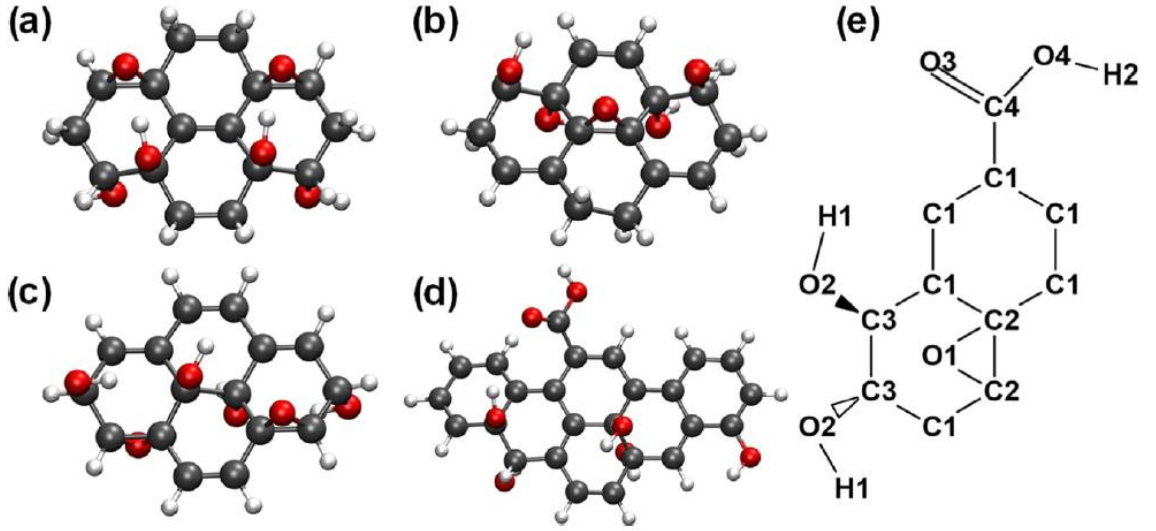

Figure 2. (a–c) and (d) are the molecular fragments that were considered for charge calculations in the structural models of GO-OH and GO-CO_2H, respectively. (e) Labels of the atoms present in the GO-OH and GO-CO_2H models.

As a first step, a careful attention has been paid to derive realistic models for GO at the DFT level, with a concentration of epoxy, hydroxyl, and carboxylic groups matching that experimentally found by X-ray photoelectron spectroscopy (XPS) analysis.[28] A special attention has been devoted to develop a first model called GO-OH containing only basal plan functional groups, i.e., epoxy and hydroxyl functions, and a more realistic model called GO-CO_2H integrating carboxylic functions in the edge plane. The zinc-based zeolite imidazole framework ZIF-8[33] has been further considered as a typical example to explore the MOF/GO interface because the ZIF-8/GO membranes have been proven to be promising for diverse applications including gas/liquid adsorption[34] and separation,[35−37] catalysts,[38,39] batteries,[40] etc. The corresponding ZIF-8/GO interface was thus constructed by adapting the computational toolbox we previously developed and validated for a series of MOF/polymer interfaces.[20−22,41,42] The so-modeled interface was further characterized in terms of the nature and strength of the interactions between the two components, the surface coverage, and the GO conformation with a special emphasis on the role of the carboxylic groups present in the edge plane of GO. The conclusions drawn from this computational effort were further supported by an in-depth characterization of the corresponding composite using advanced experimental tools including transmission electron microscopy (TEM) and mechanical strength measurement.

II. METHODS

II.I. Computational Construction of Graphene Oxide (GO) Models. A simplified GO model, labeled as GO-OH, was first constructed starting with the structure previously reported by Lerf–Klinowski's[43] containing functional groups distributed randomly over the carbon grid and characterized by an interlayer distance of 7.1 Å corresponding to a water content of 8–15%.[43] Our GO-OH model incorporates functional groups consisting of epoxy (−O−) and hydroxyl (−OH) functions that are attached only to the basal plane and positioned in close proximity to each other, possibly as nearest

DOI: 10.1021/acsami.8b09851
ACS Appl. Mater. Interfaces 2018, 10, 33619−33629

neighbors due to their stable orientation as suggested by Wang et al.[44] The so-generated model corresponds to a chemical composition for C, O, and H of 52, 43, and 1%, respectively, corresponding to a C/O ratio of 1.5.[45−47] The so-constructed periodic model was further fully geometry-optimized (atomic positions and cell parameters relaxed) at the density functional theory (DFT) level using a QUICKSTEP module in the CP2K package.[48] All valence electrons were treated on a mixed basis set with an energy cutoff of 280 Ry, while the short-range version of the double-ζ polarization basis set was used.[49] The effect of the core electrons and nuclei was considered by using pseudopotentials of Goedecker−Teter−Hutter,[49] and the semi-empirical dispersion corrections were included with the DFT-D3 method as developed by Grimme (PBE-D3).[50] The corresponding DFT-optimized cell parameters of the GO-OH model (Figure S1) are reported in Table S1. An extended GO-OH model containing two layers was further DFT-geometry-optimized. The resulting model reported in Figure 1 corresponds to an interlayer distance of 6 Å, which is in excellent agreement with that experimentally evidenced for a desolvated GO sample.[51]

This DFT-optimized two-layer GO-OH model was considered for further force-field-based molecular dynamics (MD) simulations. The nonbonded contributions were expressed as the sum of Coulombic and Lennard-Jones (LJ) 12-6 site−site potentials. To that purpose, the OPLS-AA[52] force field was used to describe the LJ potential parameters for each atom of GO-OH, whereas the partial charges were derived from the fragments cut from the periodic structures (Figure 2) using the electrostatic potential scheme[53] CHELPG with the PBE functional, and the 6-31G(d,p) basis set as implemented in the Gaussian 09 package.[54] The corresponding partial charges are described in Table 1. The LJ interactions were truncated at 10 Å with

Table 1. DFT-Calculated Partial Charges for All Atoms of O Calculated from CHELPG[a]

atom	C1	C2	C3	C4
q (e units)	−0.169	0.430	0.223	0.642
atom	O1	O2	O3	O4
q (e units)	−0.307	−0.550	−0.510	−0.568
atom		H1	H2	
q (e units)		0.387	0.404	

[a]Labels of the atoms are consistent with those in Figure 1.

the crossed-interactions computed by applying the Lorentz−Berthelot mixing rules, whereas the long-range electrostatic interactions were calculated using the Ewald summation method.[55] The flexibility of the GO-OH model was treated by considering intramolecular potentials including bond stretching, angle bending, and torsional and improper dihedral angles with parameters taken from the OPLS-AA force field.[52] MD simulations were further performed in the NPT ensemble using a simulation box consisting of (4, 4, 2) unit cells of GO-OH corresponding to system dimensions of 36 Å × 36 Å × 90 Å. The temperature and pressure were maintained through the use of a Berendsen thermostat and barostat with relaxation times of 0.1 and 0.5 ps, respectively. Equations of motion were integrated using the velocity Verlet algorithm with a time step of 1 fs. These constant-NPT MD simulations lasted 2 ns and, subsequently, a constant-NVT MD run of 5 ns was performed for analysis. Complementary calculations were performed considering the same GO-OH model loaded with 15 wt % water. Water was described by the extended simple point charge model,[56] which was successfully employed in the past by Huan et al.,[57] to explore the aggregation process of GO layers in water. This selected water loading was considered because this is the most common scenario encountered in the literature for a hydrated GO-OH sample.[51] This hydrated GO-OH model was subsequently investigated using the same MD approach described above for the pristine GO-OH model. Illustrations of the equilibrated models obtained from MD simulations are reported in Figure 1c with a slight relaxation of the cell parameters as compared to those in the pristine model. The interlayer distances of the pristine and the water-loaded GO-OH models were found to be 5.5 and 7.0 Å, respectively, in good agreement with the experimentally observed results of 6.0 and 7.8 Å.[51] This observation evidences that the microscopic model of GO-OH offers a reasonable description of the GO system.

As a complementary step, a more elaborated GO model, labeled as GO-CO_2H, made of a nonperiodic layered structure was built considering the presence of $-CO_2H$ motifs at the edges of the layer along with the presence of −O− and −OH functional groups to reproduce, as far as possible, the chemical features of a real GO sample. To that purpose, we have constructed a single-layer model by modifying the number of −O− and −OH groups randomly from the basal plane of the GO-OH model and placing $-CO_2H$ groups at the edges until the obtained C/O ratio matches well with the experimentally measured value of ∼2.8 corresponding to an average carbon and oxygen concentrations currently reported for such a GO sample through NMR,[24,25,58] Raman,[26,59,60] and XPS[28,61−63] measurements (see Figure S6). Moreover, the so-constructed model contains a concentration of sp^3 (41%) and sp^2 (41%) carbon, and sp^3 (34%) carbon, epoxy (12%), hydroxyl (11%), and carboxylic (3%) that fits well with the experimental content reported by Felton et al.[69] for a GO sample investigated using X-ray photoelectron spectroscopy that led to 37, 32, 14, 13, and 4% of sp^3 C, sp^2 C, −O−, −OH, and $-CO_2H$ species, respectively. This second model was further geometry-optimized at the force-field level using MD simulations in the NVT ensemble, all atoms of this GO-CO_2H model being described by the intramolecular and intermolecular potential parameters taken from the OPLS-AA force field,[52] whereas the atomic partial charges were derived using the same DFT approach as for GO-OH (Table 1).

II.II. Computational Construction of the ZIF-8 Surface Model. The most stable [011] ZIF-8 surface was taken from our previous work[22] where the undercoordinated atoms were saturated with two types of terminations: OH groups and imidazole moieties bonded to the Zn external atoms, in an alternate fashion. In this work,[22] two possible ZIF-8 surfaces ([100] and [011]) were considered in such a way so as to cut the bulk model where the least amount of bonds was severed and no aromatic ring was disrupted. Among these two, the [011] surface, which was found to be the surface with the lowest energy, was subsequently selected for the MOF/GO model. For MD simulations, all atoms of ZIF-8 were treated as charged LJ sites and the model was considered as flexible. A full list of force-field parameter charges can be found elsewhere.[22]

II.III. Computational Construction of the ZIF-8/GOs Interface. Both GO-OH and GO-CO_2H models were combined with the ZIF-8 surface to construct the ZIF-8/GO interfaces using a computational approach we previously developed, applied, and validated for diverse MOF/polymer interfaces.[20−22,41,42] The dimensions of the ZIF-8 surface model were 51 Å × 48 Å × 97 Å, and the GO-OH and GO-CO_2H models were cut from the models built in Section II.I to fit the lengths of ZIF-8 along the x, y directions, as illustrated in Figure 3a,b, with GO layers of 43 Å × 43 Å dimensions. These GO models were brought into contact with the ZIF-8 surface in the same simulation box of dimensions 51 Å × 48 Å × 200 Å (Figure 3c), the z direction of the ZIF-8 being perpendicular to the GO layer. The x and y directions are those corresponding to the ZIF-8 slab model, whereas the z direction was duplicated with respect to the slab not only to ensure that there will not be any artificial interactions between one end of the slab and the other but also to provide enough vacuum space to accommodate the initial configuration of GO layers. Several cycles of MD simulations were further performed as follows:

(i) The first simulation was carried out in the NP_nT ensemble at 1 kbar and 298 K with the use of a Berensen barostat (relaxation time of 0.5 ps), a time step of 1 fs, and a total run of 5 ns using a modified version of the DLPOLY code.[64] Pressure was applied along the z axis by fixing the MOF coordinates in such a way that the simulation box compresses/expands only in this direction. The interactions between GOs and ZIF-8 were described by the sum of Coulombic and LJ potential terms

DOI: 10.1021/acsami.8b09851
ACS Appl. Mater. Interfaces 2018, 10, 33619−33629

ACS Applied Materials & Interfaces Research Article

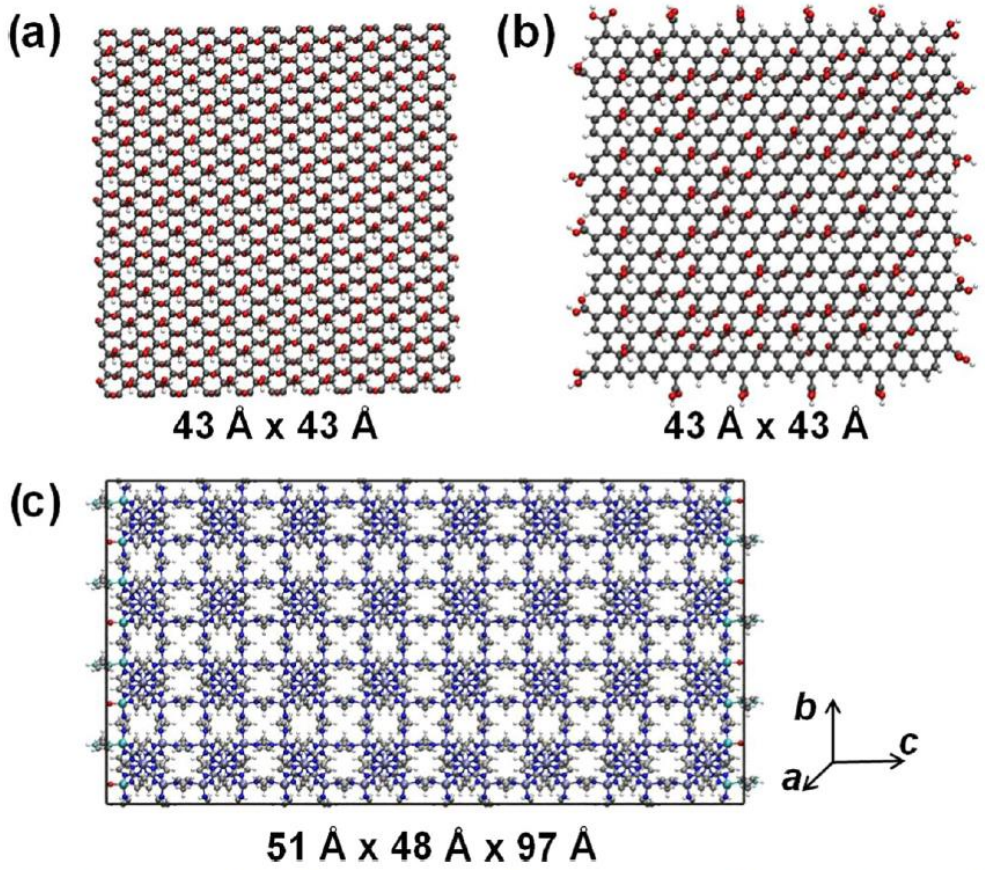

Figure 3. Models used to construct the ZIF-8/GOs interfaces: (a) GO-OH, (b) GO-CO_2H, and (c) ZIF-8 surface. Color scheme: GO layers: C, gray; O, red; H, white; ZIF-8: C, silver; N, blue; Zn, light blue (surface) and iceblue (bulk); O, red; and H, white.

with the crossed-interactions computed by applying the Lorentz–Berthelot mixing rules.[55]

(ii) This first step was followed by MD simulations in the NPT ensemble at 1 bar and 298 K for 5 ns, allowing the relaxation of both the ZIF-8 surface and GOs.

(iii) After these equilibration steps, data were collected from five statistically independent simulations, each considering a 5 ns MD run in the NVT ensemble using a Nosé–Hoover thermostat[65] with a relaxation time of 0.1 ps.

To exclude the mutual interactions between the ZIF-8 surfaces in all MOF/GOs models, these MD simulations were carried out again through varying the number of GO layers. The estimated MOF/GO interaction energy per GO layer was then calculated using the following equation: $E(\mathrm{MOF/GO}) = E(\mathrm{MOF + GO}) - E(\mathrm{MOF}) - n \times E(\mathrm{GO})$, where $E(\mathrm{MOF + GO})$, $E(\mathrm{MOF})$, and $E(\mathrm{GO})$ are the energies of the MOF + GO system, MOF, and GO while n corresponds to the number of GO layers present at the surface of the MOF. This corresponding MOF/GO interaction energy was further plotted as a function of the number of GO layers (see Figure S2). We evidenced that this value converges when one considers 16 layers of GOs, which corresponds to the case of a separating distance between MOF surfaces along the z direction of more than 75 Å. This distance is indeed large enough to exclude the interactions between MOF surfaces.

Figure 4 reports an illustration of the ZIF-8/GO interface generated for both GO-OH and GO-CO_2H considering 16 layers of each.

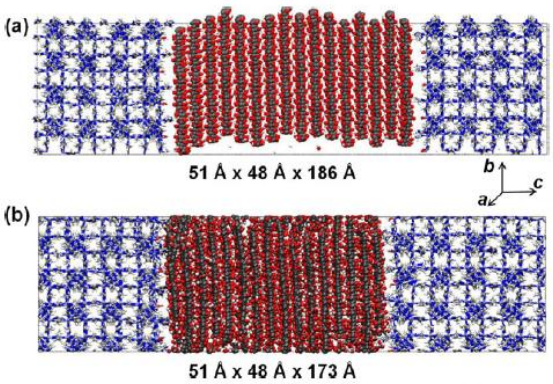

Figure 4. Snapshots of one of the ZIF-8/GO interface configurations obtained from MD simulations consisting of 16 (a) GO-OH and (b) GO-CO_2H layers. Atoms of ZIF-8 are in stick representation and GO layers in ball and stick representation. Color scheme: GO layers: C, gray; O, red; H white; ZIF-8: C, gray; N, blue; Zn, iceblue; O, red; and H, white.

II.IV. Experimental Section. *II.IV.I. Graphene Oxide Synthesis.* Graphene oxide (GO) was synthesized from natural graphite powder (SP-1, 100 Mesh was purchased from Bay Carbon) according to the following method. First, graphite powder and sulfuric acid (98%)

DOI: 10.1021/acsami.8b09851
ACS Appl. Mater. Interfaces 2018, 10, 33619–33629

ACS Applied Materials & Interfaces Research Article

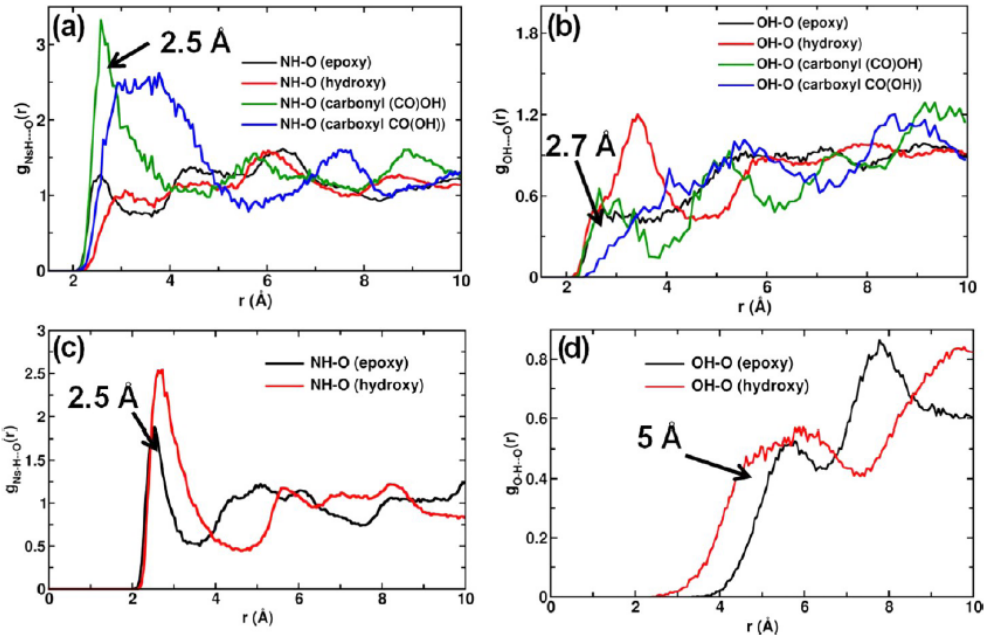

Figure 5. Radial distribution functions calculated between (a, c) H of the surface N−H and the O atom of various molecular groups of GO layers and (b, d) H of the surface −OH and O of the GO layers in GO-CO_2H and GO-OH, respectively. Results are averaged over the five different MD runs.

were mixed in a double-walled glass reactor at 5 °C and stirred for 10 min. Potassium permanganate was added to the solution, and the solution was stirred for 12 h at 35 °C. Then, 500 mL of deionized water (DI) water was gradually and stepwise added into the resulting GO solution in the glass reactor at the temperature below 5 °C. The so-obtained GO suspension was poured into a beaker and further diluted by two liters of DI water. To remove the remaining potassium permanganate, hydrogen peroxide (H_2O_2, 30%) was added into the GO solution until its color turned from brown to golden yellow. After stirring for 30 min, GO solution was vacuum-filtrated using a Whatman glass microfiber filter paper and the so-obtained GO layer was washed out via 10 wt % hydrochloric acid (HCl) aqueous solution. The GO layer was dried under vacuum conditions in a desiccator for 2 days and then washed in acetone (about 3 L) followed by filtration. Finally, the resultant GO was further dried in a desiccator under vacuum for 2−3 days.

II.IV.II. ZIF-8 Synthesis. Then, 0.366 g of zinc nitrate hexahydrate ($Zn(NO_3)_2{\cdot}6H_2O$) and 0.811 g of organic ligand (i.e., 2-methyl imidazole) were first dissolved in 15 and 20 mL of methanol, respectively, and then mixed together, followed by stirring for 5 h at room temperature to produce the ZIF-8 nanocrystals.[66] Zinc nitrate hexahydrate ($Zn(NO_3)_2{\cdot}6H_2O$, >99.0%), 2-methyl imidazole (>99%), and methanol (>99.8%) were supplied by Sigma-Aldrich. Finally, the so-obtained mixture was washed with methanol four times via centrifugation to remove any unreacted ligands and impurity, and nanocrystals were suspended in methanol again. These washing steps were performed four times.

II.IV.III. Fabrication of ZIF-8/GO Composite Membranes. To make ZIF-8/GO composite membranes with different compositions, GO powder was first dispersed in dimethylformamide (DMF) and sonicated for 30 min in a bath sonicator. Then, the GO suspension was tip-sonicated for 1 h to obtain well-dispersed GO flakes in the solvent. ZIF-8 nanocrystals in methanol were centrifuged for 15 min, and collected nanocrystals were dispersed in DMF, followed by stirring for 1 h to achieve a homogeneous dispersion. Different ZIF-8/GO composite membranes were fabricated by simply mixing GO and ZIF-8 dispersion followed by vacuum filtration on the anodic aluminum oxide support (Whatman, 0.2 micrometer pore size). Finally, the obtained ZIF-8/GO membrane was washed out with ethanol to remove all remaining DMF solvent. The self-standing ZIF-8/GO membrane was dried under vacuum at room temperature for 24 h before the mechanical strength test. The composition of ZIF-8 and GO in composite membranes was easily adjusted via the volume of ZIF-8 and GO dispersion used for membrane fabrication.

II.IV.IV. Characterization of the GO/ZIF-8 Composite Membrane. TEM 2100F (JEOL, Tokyo, Japan) was used to reveal the possible interfacial interactions between GO nanosheets and ZIF-8 nanoparticles. Tensile strength measurements were performed using an Instron universal testing system (AGS-J-500N, Norwood, MA). Samples with height and width of 13 and 2 mm, respectively, were held between two clamps, and the tensile stress was loaded at the strain rate of 1.0 mm/min.

III. RESULTS AND DISCUSSION

The first step of this study is the characterization of the preferential interactions between GO and the ZIF-8 surface. To that purpose, the radial distribution functions (RDFs) between the terminations of the MOF surface, i.e., the −NH groups of the imidazole linker and the −OH groups bonded to the Zn atoms, and the potential interacting sites of both GOs, i.e., the epoxy −O−, hydroxyl −OH, and carboxylic $-CO_2H$ groups, have been calculated and averaged over the MD trajectories. The corresponding data are plotted in Figure 5. Based on Figure 5a,b, interactions between the hydrogen atoms of the −NH and −OH groups and the oxygen atoms of the epoxy, hydroxyl, and carboxylic functions were found for the MOF/GO-CO_2H interface with relatively short interacting distances comprised between 2.5 and 2.7 Å. It can be noticed that the interaction with the terminal carboxylic $-CO_2H$ groups involves the oxygen of the carbonyl rather than the oxygen of the acidic function. Regarding the MOF/GO-OH interface, there are interactions between both −NH (Figure

DOI: 10.1021/acsami.8b09851
ACS Appl. Mater. Interfaces 2018, 10, 33619−33629

ACS Applied Materials & Interfaces Research Article

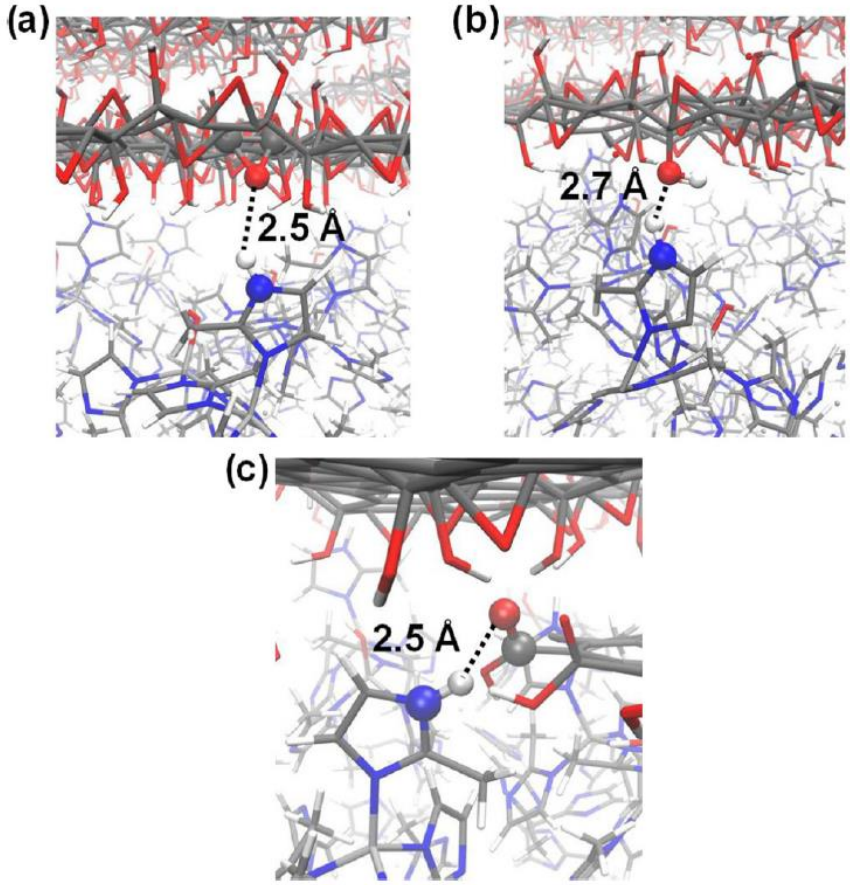

Figure 6. Preferential interactions between the H atom of the −NH group of ZIF-8 and the O atom of the (a) epoxy, (b) hydroxyl, and (c) carboxylic functions of the carboxylic groups present in the GO in the case of the ZIF-8/GO-CO_2H interface. Color scheme: GO layers: C, gray; O, red; H, white; ZIF-8: C, gray; N, blue; Zn, silver; O, red; and H, white.

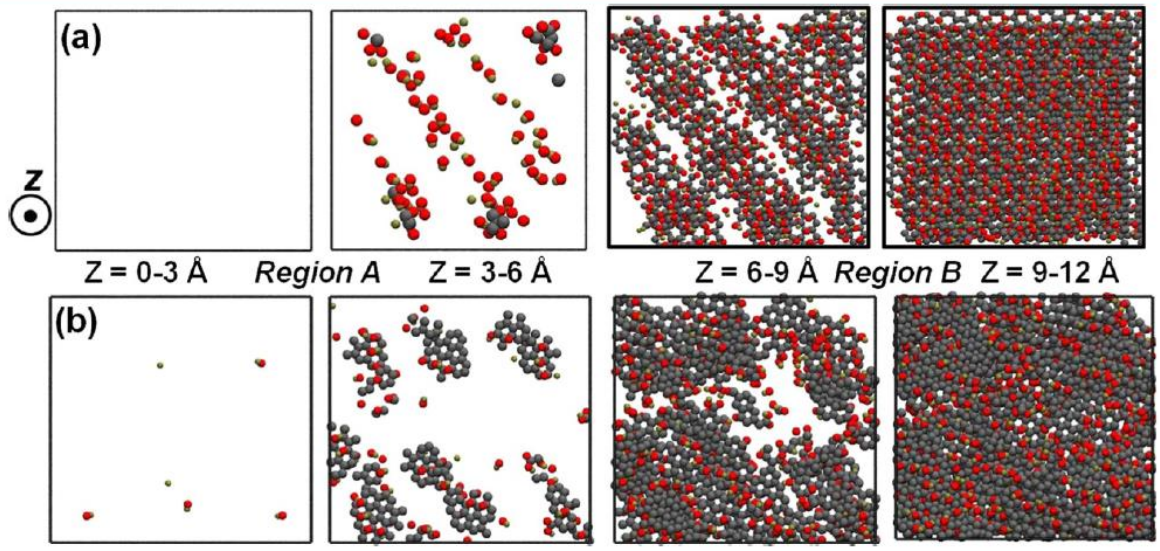

Figure 7. Snapshots of the slices of GOs of z = 3 Å width plotted as a function of the z distance away from the top of the MOF surface: (a) ZIF-8/GO-OH and (b) ZIF-8/GO-CO_2H. Zn atoms in the most external layers of ZIF-8 are considered as a reference for z = 0.

DOI: 10.1021/acsami.8b09851
ACS Appl. Mater. Interfaces 2018, 10, 33619−33629

ACS Applied Materials & Interfaces Research Article

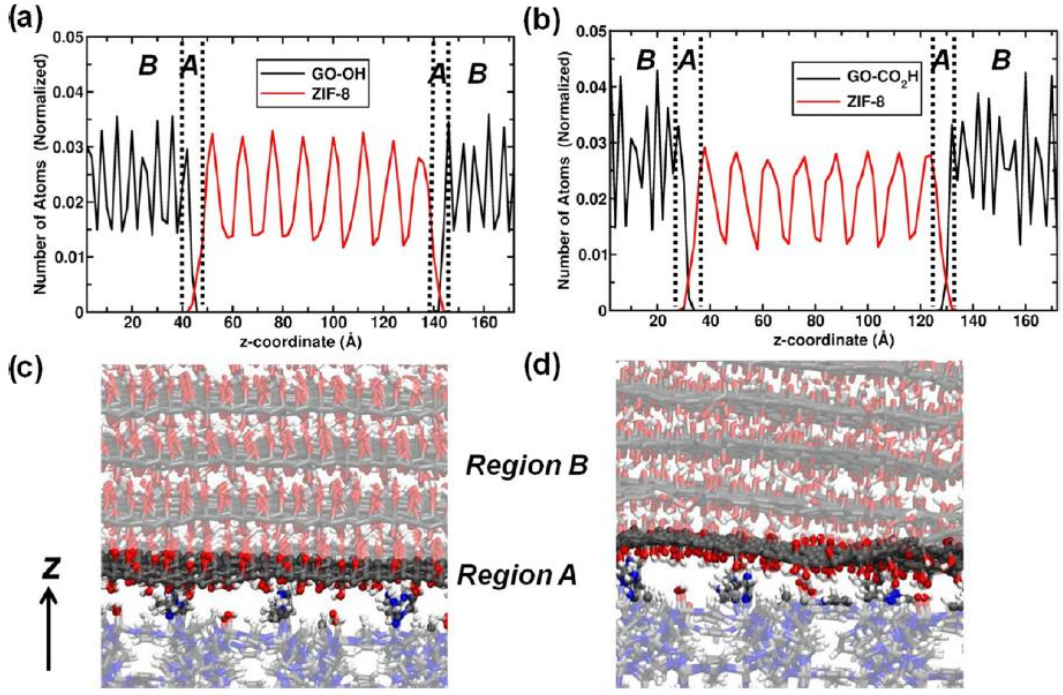

Figure 8. Normalized atomic density of both ZIF-8 and GOs in the direction perpendicular to the surface slab (i.e., along the z direction) for (a) ZIF-8/GO-OH and (b) ZIF-8/GO-CO_2H interfaces. Snapshots of the (c) ZIF-8/GO-OH and (d) ZIF-8/GO-CO_2H interfaces, where the atoms that belong to region A are opaque and the rest are transparent. The number of atoms in both MOF and GO phases is normalized with respect to the total number of atoms in each phase.

5c) and −OH (Figure 5d) groups of the ZIF-8 surface and the epoxy and hydroxyl functions of GO-OH.

An illustration of the resulting geometry for both components is provided in Figure 6 for the case of the ZIF-8/GO-CO_2H interface. The atomic distances between interacting moieties suggest that both types of GOs appear to be stabilized by a relatively homogeneous set of interactions.

As a further step, the atomic density of both ZIF-8 and GOs was analyzed along the direction normal to the MOF surface, i.e., the z-coordinate, for the two interfaces. The GO phase was cut at different z values to produce xy plane slices with a height of 3 Å along the z axis. Figure 7 reports a representation of these slices for both ZIF-8/GO-OH and ZIF-8/GO-CO_2H interfaces starting from the top part of the MOF surface (z = 0) until z = 12 Å away from the MOF surface. From these plots, it can be observed that the atomic density of GOs increases sequentially when one moves away from the ZIF-8 surface. Two distinct zones can be identified: (i) The first region is characterized by a low GO density near the ZIF-8 surface, labeled as region A, which is represented by the two first pictures. This region corresponds to the interfacial region of the MOF/GO system. (ii) The second region is labeled as region B, where the atomic density of GOs progressively increases up to its convergence toward an almost constant value. This region B is reminiscent of a bulk-like behavior of GOs. The comparison between Figure 7a and b evidences a significantly larger concentration of atoms in the interfacial zone in the case of ZIF-8/GO-CO_2H, suggesting a more optimal surface coverage of the ZIF-8 surface by GO-CO_2H.

To make a more quantitative analysis of the interfaces, we further computed the normalized atomic density of both GOs and ZIF-8 along the z axis. In this graph, consistent with the representation provided in Figure 4, the ZIF-8 surface is located at the center of the simulation box, whereas GOs are above and below the surface. The plots reported in Figure 8a,b reveal that when one scans the interval [z = 0 Å to z = whole box length along the z axis (173 Å for GO-CO_2H and 186 Å for GO-OH)], a first domain is defined, where only GOs are present and oscillate around an equilibrium value, region B (see the black line), which is consistent with the normalized atomic density of the bulk phase (see Figure S4). Above $z \approx 25$ Å (GO-CO_2H) and 40 Å (GO-OH), the normalized atomic density of GOs drops and then we enter a region where only the MOF is present, region A (see the red curve), until $z \approx 125$ Å (GO-CO_2H) and 140 Å (GO-OH). When one compares the plots of Figure 8a,b for ZIF-8/GO-CO_2H and ZIF-8/GO-OH, respectively, it can be clearly stated that extension of region A defined by the interval between the lower limit taken as the z value for the first nonzero normalized atomic density of GOs and the upper limit, as that for which the normalized atomic density of GO starts to oscillate, is larger in the case of GO-CO_2H (∼6 vs ∼3 Å), and this can be explained by a more-pronounced distortion of the GO-CO_2H layered structure when brought into contact with the ZIF-8 surface, which allows the atoms of GO to populate in a larger extent in region A. This structural behavior is illustrated in the snapshots reported in Figure 8c,d for the interfacial regions of both ZIF-8/GO-CO_2H and ZIF-8/GO-OH.

DOI: 10.1021/acsami.8b09851
ACS Appl. Mater. Interfaces 2018, 10, 33619−33629

ACS Applied Materials & Interfaces Research Article

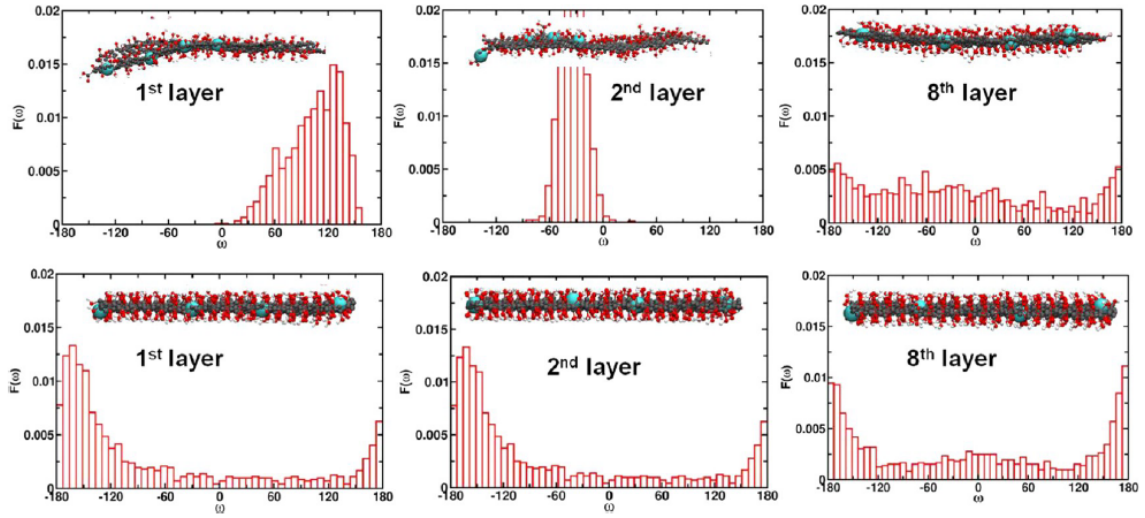

Figure 9. Dihedral angle distributions of the GO layers present in the ZIF-8/GO-CO_2H (top part) and ZIF-8/GO-OH (bottom part) interfaces. Atoms that are considered for dihedral angle calculations are represented with van der Waals spheres in cyan.

To quantify the distortions of the GO in the vicinity of the MOF surface, the dihedral angle distribution was calculated for each GO layer distributed along the z direction. As an illustration, the dihedral angles of the first two layers closest to the MOF surface (corresponding to region A) and a layer far away from the MOF surface (corresponding to region B), typically the eighth layer, are represented in Figure 9. One can first observe that the GO-CO_2H layers present in region A undergo a much higher degree of distortion as compared to that of those in region B, as shown by prominent dihedral angle peaks of the first and second GO-CO_2H layers at 120 and −40° as compared to a homogeneous distribution of dihedral angles for the eighth layer, which shows the same behavior as that of the bulk GO-CO_2H phase (see Figure S5). In the case of GO-OH, both region layers show a planar conformation with a maximum probability distribution for the dihedral angles at −180 or 180°. This analysis confirms that the presence of the −CO_2H groups favors the distortion of the layer when brought into contact with the MOF surface and hence implies a significant shortening of the width of region A (~6 vs ~3 Å for GO-OH).

Figure 8 further evidences that both GOs and ZIF-8 coexist throughout region A, which is consistent with the fact that GO terminations penetrate in the pockets formed by the zigzag shape of ZIF-8, and this is even more pronounced in the case of GO-CO_2H due to the higher degree of distortion of this layer as mentioned above. The affinity obtained between GOs and ZIF-8 surface is reminiscent of that we recently reported for flexible polymers such as poly(vinylidene difluoride) and poly(ethylene glycol) in interaction with the MOF surface of UiO-66(Zr), both characterized by a short z length of region A of 5−6 Å. This microscopic scenario that supports a good surface coverage of the ZIF-8 surface by GOs, even better in the case of GO-CO_2H, strongly suggests an excellent ZIF-8/GO compatibility.

Figure 10 shows the TEM image of ZIF-8 nanocrystals with the particle size in the range of 50−70 nm. The aggregation of ZIF-8 nanocrystals is a common behavior due to the drying process used for the preparation of the samples prior to TEM

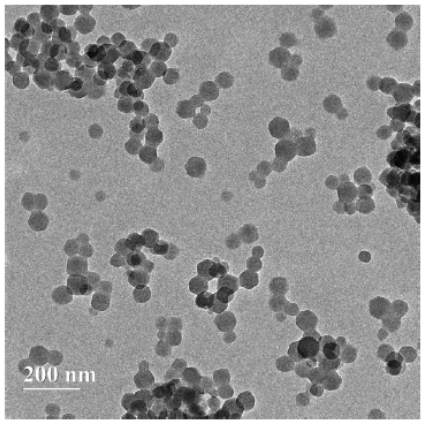

Figure 10. TEM image of ZIF-8 nanocrystals.

images. Similar structure/size of ZIF-8 nanocrystals was also observed in the case of the composite, and interestingly, they are located in the vicinity of the GO nanosheets (Figure 11). This observation supports a rather good compatibility between the two components as suggested by the molecular simulations presented above.

Referring to previous studies on polymer/MOF mixed matrix membranes (MMMs) that extracted information about the interactions between the two components based on the mechanical properties of the corresponding membranes,[20,67,68] tensile stress/strain curves of ZIF-8/GO composite samples were obtained using a universal testing system. Figure 12 first evidences that ZIF-8/GO MMM shows a lower mechanical strength than that of the pristine GO (82 MPa). This observation is consistent with the fact that the incorporation of ZIF-8 alters the layered organization of GO as evidenced by our computations with the presence of a significant distortion of the layer when brought into contact with the MOF surface (Figure 9). Interestingly, one observes that the mechanical strength is enhanced from 39.9 to 48.6 MPa when the

DOI: 10.1021/acsami.8b09851
ACS Appl. Mater. Interfaces 2018, 10, 33619−33629

ACS Applied Materials & Interfaces Research Article

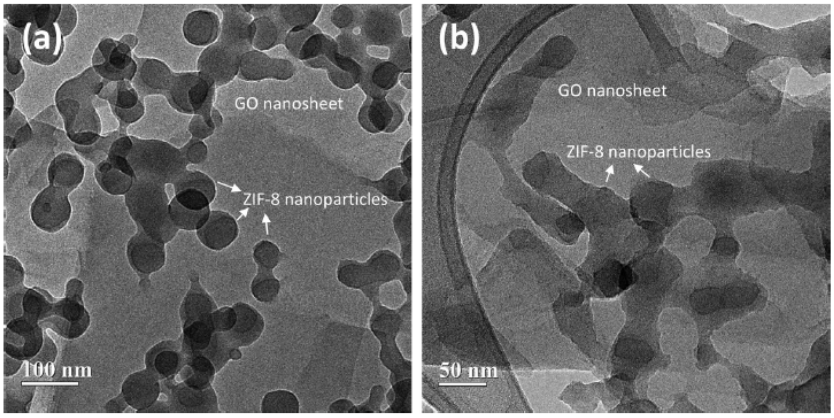

Figure 11. (a, b) TEM images of the ZIF-8/GO composite fabricated from a ZIF-8/GO ratio of 3/7 at different scales.

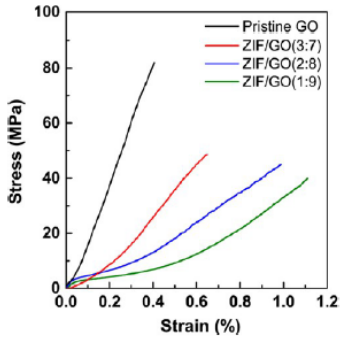

Figure 12. Tensile strength curves of ZIF-8/GO composite films with different contents of ZIF-8 and comparison with the pure GO.

concentration of the MOF filler increases, indicating that the MMMs become more rigid and indeed maintain a sufficient mechanical stability to be handled. This increased rigidity is attributed to the relatively strong interactions between the ZIF-8 surface and the oxygen-based functional groups of GO nanosheets revealed by the simulations and further supported by Fourier transform infrared (FTIR) spectra (Figure S7).

IV. CONCLUSIONS

This study integrates advanced computational and experimental tools to fully characterize the MOF ZIF-8/graphene oxide interface structure at the atomistic scale. This was achieved by preliminary modeling of the ZIF-8 surface and the GO. In this latter case, a special attention has been paid to build a realistic model of GO containing both basal plane functions, i.e., epoxy and hydroxyl groups, and edge plane functions, i.e., carboxylic groups, in concentration ratios consistent with experimental findings deduced from XPS analysis on GO. The computational work evidenced that the MOF/GO composite is characterized by two distinct regions: an interface part, region A, corresponding to a homogeneous coverage of the MOF surface by GO via relatively strong interactions between the NH− and OH− terminal functions of ZIF-8 and the functional groups of GO and a second region labeled as region B, which is reminiscent of a bulk-like behavior of GO. Such a predicted good affinity between the MOF surface and GO was made possible owing to a relatively high degree of distortion of the first layer of GO. This computational finding was further supported by a series of experimental results including TEM images and mechanical strength measurements that show a good dispersion of the filler into the GO matrix and an enhanced mechanical tensile strength of the composite with increasing ZIF-8 content, clearly demonstrating the good compatibility between the two components.

■ ASSOCIATED CONTENT

Supporting Information

The Supporting Information is available free of charge on the ACS Publications website at DOI: 10.1021/acsami.8b09851.

Additional figures and tables; optimized simulation cell parameters from DFT calculations, interaction energies with respect to the number of GO-CO_2H layers, snapshots of the interactions between GO-CO_2H and ZIF-8 at the interface region, atomic density of bulk GO layers, dihedral angle distributions of GO layers, literature summary of the relative concentration of the functional groups on the GO layers, FTIR spectra of ZIF-8/GO composites (PDF)

(PDF)

■ AUTHOR INFORMATION

Corresponding Author

*E-mail: guillaume.maurin@univ-montp2.fr.

ORCID

Ho Bum Park: 0000-0002-8003-9698

Guillaume Maurin: 0000-0002-2096-0450

Author Contributions

§S.B. and A.L. contributed equally to this work.

Notes

The authors declare no competing financial interest.

■ ACKNOWLEDGMENTS

The research leading to these results has received funding from the European Community H2020 (GRAMOFON GA 727619). G.M. thanks Institut Universitaire de France for its support. Authors are thankful for the support from the Korea CCS R&D Center (KCRC) grant funded by Ministry of

Science, ICT, & Future Planning from the Korean government (grant #2016910057).

REFERENCES

(1) Menzel, R.; Iruretagoyena, D.; Wang, Y.; Bawaked, S. M.; Mokhtar, M.; Al-Thabaiti, S. A.; Basahel, S. N.; Shaffer, M. S. P. Graphene Oxide/Mixed Metal Oxide Hybrid Materials for Enhanced Adsorption Desulfurization of Liquid Hydrocarbon Fuels. *Fuel* **2016**, *181*, 531−536.

(2) Dong, L.; Chen, M.; Li, J.; Shi, D.; Dong, W.; Li, X.; Bai, Y. Metal-Organic Framework-Graphene Oxide Composites: A Facile Method to Highly Improve the CO_2 Separation Performance of Mixed Matrix Membranes. *J. Membr. Sci.* **2016**, *520*, 801−811.

(3) Liu, Z.; Wang, Z.-M.; Yang, X.; Ooi, K. Intercalation of Organic Ammonium Ions into Layered Graphite Oxide. *Langmuir* **2002**, *18*, 4926−4932.

(4) Wei, N.; Peng, X.; Xu, Z. Understanding Water Permeation in Graphene Oxide Membranes. *ACS Appl. Mater. Interfaces* **2014**, *6*, 5877−5883.

(5) Wang, H.; Hao, Q.; Yang, X.; Lu, L.; Wang, X. Effect of Graphene Oxide on the Properties of Its Composite with Polyaniline. *ACS Appl. Mater. Interfaces* **2010**, *2*, 821−828.

(6) Yao, K.; Tan, P.; Luo, Y.; Feng, L.; Xu, L.; Liu, Z.; Li, Y.; Peng, R. Graphene Oxide Selectively Enhances Thermostability of Trypsin. *ACS Appl. Mater. Interfaces* **2015**, *7*, 12270−12277.

(7) Zhu, Q.-L.; Xu, Q. Metal-Organic Framework Composites. *Chem. Soc. Rev.* **2014**, *43*, 5468−5512.

(8) Anasthasiya, N. A.; Khaneja, M.; Jeyaprakash, B. G. Electronic Structure Calculations of Ammonia Adsorption on Graphene and Graphene Oxide with Epoxide and Hydroxyl Groups. *J. Electron. Mater.* **2017**, *46*, 5642−5656.

(9) Li, X.; Yu, J.; Wageh, S.; Al-Ghamdi, A. A.; Xie, J. Graphene in Photocatalysis: A Review. *Small* **2016**, *12*, 6640−6696.

(10) Low, J.; Yu, J.; Ho, W. Graphene-Based Photocatalysts for CO_2 Reduction to Solar Fuel. *J. Phys. Chem. Lett.* **2015**, *6*, 4244−4251.

(11) Ramachandran, R.; Xuan, W.; Zhao, C.; Leng, X.; Sun, D.; Luo, D.; Wang, F. Enhanced Electrochemical Properties of Cerium Metal−organic Framework Based Composite Electrodes for High-Performance Supercapacitor Application. *RSC Adv.* **2018**, *8*, 3462−3469.

(12) Ramachandran, R.; Zhao, C.; Luo, D.; Wang, K.; Wang, F. Morphology-Dependent Electrochemical Properties of Cobalt-Based Metal Organic Frameworks for Supercapacitor Electrode Materials. *Electrochim. Acta* **2018**, *267*, 170−180.

(13) Jin, Y.; Zhao, C.; Sun, Z.; Lin, Y.; Chen, L.; Wang, D.; Shen, C. Facile Synthesis of Fe-MOF/RGO and Its Application as a High Performance Anode in Lithium-Ion Batteries. *RSC Adv.* **2016**, *6*, 30763−30768.

(14) Wang, Z.; Gao, C.; Liu, Y.; Li, D.; Chen, W.; Ma, Y.; Wang, C.; Zhang, J. Electrochemical Performance and Transformation of Co-MOF/Reduced Graphene Oxide Composite. *Mater. Lett.* **2017**, *193*, 216−219.

(15) Wei, T.; Zhang, M.; Wu, P.; Tang, Y.-J.; Li, S.-L.; Shen, F.-C.; Wang, X.-L.; Zhou, X.-P.; Lan, Y.-Q. POM-Based Metal-Organic Framework/Reduced Graphene Oxide Nanocomposites with Hybrid Behavior of Battery-Supercapacitor for Superior Lithium Storage. *Nano Energy* **2017**, *34*, 205−214.

(16) Ramachandran, R.; Rajavel, K.; Xuan, W.; Lin, D.; Wang, F. Influence of $Ti_3C_2T_x$ (MXene) Intercalation Pseudocapacitance on Electrochemical Performance of Co-MOF Binder-Free Electrode. *Ceram. Int.* **2018**, *44*, 14425−14431.

(17) Huang, D.; Xin, Q.; Ni, Y.; Shuai, Y.; Wang, S.; Li, Y.; Ye, H.; Lin, L.; Ding, X.; Zhang, Y. Synergistic Effects of Zeolite Imidazole Framework@graphene Oxide Composites in Humidified Mixed Matrix Membranes on CO_2 Separation. *RSC Adv.* **2018**, *8*, 6099−6109.

(18) Yu, H.; Zhang, B.; Bulin, C.; Li, R.; Xing, R. High-Efficient Synthesis of Graphene Oxide Based on Improved Hummers Method. *Sci. Rep.* **2016**, *6*, No. 36143.

(19) Szczęśniak, B.; Choma, J.; Jaroniec, M. Gas Adsorption Properties of Hybrid Graphene-MOF Materials. *J. Colloid Interface Sci.* **2018**, *514*, 801−813.

(20) Semino, R.; Moreton, J. C.; Ramsahye, N. A.; Cohen, S. M.; Maurin, G. Understanding the Origins of Metal−organic Framework/Polymer Compatibility. *Chem. Sci.* **2018**, *9*, 315−324.

(21) Benzaqui, M.; Semino, R.; Menguy, N.; Carn, F.; Kundu, T.; Guigner, J.-M.; McKeown, N. B.; Msayib, K. J.; Carta, M.; Malpass-Evans, R.; Le Guillouzer, C.; Clet, G.; Ramsahye, N. A.; Serre, C.; Maurin, G.; Steunou, N. Toward an Understanding of the Microstructure and Interfacial Properties of PIMs/ZIF-8 Mixed Matrix Membranes. *ACS Appl. Mater. Interfaces* **2016**, *8*, 27311−27321.

(22) Semino, R.; Ramsahye, N. A.; Ghoufi, A.; Maurin, G. Microscopic Model of the Metal−Organic Framework/Polymer Interface: A First Step toward Understanding the Compatibility in Mixed Matrix Membranes. *ACS Appl. Mater. Interfaces* **2016**, *8*, 809−819.

(23) Amirjalayer, S.; Tafipolsky, M.; Schmid, R. Surface Termination of the Metal-Organic Framework HKUST-1: A Theoretical Investigation. *J. Phys. Chem. Lett.* **2014**, *5*, 3206−3210.

(24) Jeong, H.-K.; Lee, Y. P.; Lahaye, R. J. W. E.; Park, M.-H.; An, K. H.; Kim, I. J.; Yang, C.-W.; Park, C. Y.; Ruoff, R. S.; Lee, Y. H. Evidence of Graphitic AB Stacking Order of Graphite Oxides. *J. Am. Chem. Soc.* **2008**, *130*, 1362−1366.

(25) Yang, D.; Velamakanni, A.; Bozoklu, G.; Park, S.; Stoller, M.; Piner, R. D.; Stankovich, S.; Jung, I.; Field, D. A.; Ventrice, C. A.; Ruoff, R. S. Chemical Analysis of Graphene Oxide Films after Heat and Chemical Treatments by X-ray Photoelectron and Micro-Raman Spectroscopy. *Carbon* **2009**, *47*, 145−152.

(26) Kudin, K. N.; Ozbas, B.; Schniepp, H. C.; Prud'homme, R. K.; Aksay, I. A.; Car, R. Raman Spectra of Graphite Oxide and Functionalized Graphene Sheets. *Nano Lett.* **2008**, *8*, 36−41.

(27) Dave, S. H.; Gong, C.; Robertson, A. W.; Warner, J. H.; Grossman, J. C. Chemistry and Structure of Graphene Oxide via Direct Imaging. *ACS Nano* **2016**, *10*, 7515−7522.

(28) Willems, N.; Urtizberea, A.; Verre, A. F.; Iliut, M.; Lelimousin, M.; Hirtz, M.; Vijayaraghavan, A.; Sansom, M. S. P. Biomimetic Phospholipid Membrane Organization on Graphene and Graphene Oxide Surfaces: A Molecular Dynamics Simulation Study. *ACS Nano* **2017**, *11*, 1613−1625.

(29) Mkhoyan, K. A.; Contryman, A. W.; Silcox, J.; Stewart, D. A.; Eda, G.; Mattevi, C.; Miller, S.; Chhowalla, M. Atomic and Electronic Structure of Graphene-Oxide. *Nano Lett.* **2009**, *9*, 1058−1063.

(30) Saxena, S.; Tyson, T. A.; Negusse, E. Investigation of the Local Structure of Graphene Oxide. *J. Phys. Chem. Lett.* **2010**, *1*, 3433−3437.

(31) D'Angelo, D.; Bongiorno, C.; Amato, M.; Deretzis, I.; La Magna, A.; Fazio, E.; Scalese, S. Oxygen Functionalities Evolution in Thermally Treated Graphene Oxide Featured by EELS and DFT Calculations. *J. Phys. Chem. C* **2017**, *121*, 5408−5414.

(32) Lin, L.-C.; Paik, D.; Kim, J. Understanding Gas Adsorption in MOF-5/Graphene Oxide Composite Materials. *Phys. Chem. Chem. Phys.* **2017**, *19*, 11639−11644.

(33) Park, K. S.; Ni, Z.; Côté, A. P.; Choi, J. Y.; Huang, R.; Uribe-Romo, F. J.; Chae, H. K.; O'Keeffe, M.; Yaghi, O. M. Exceptional Chemical and Thermal Stability of Zeolitic Imidazolate Frameworks. *Proc. Natl. Acad. Sci. U.S.A.* **2006**, *103*, 10186−10191.

(34) Kim, D.; Kim, D. W.; Hong, W. G.; Coskun, A. Graphene/ZIF-8 Composites with Tunable Hierarchical Porosity and Electrical Conductivity. *J. Mater. Chem. A* **2016**, *4*, 7710−7717.

(35) Jayaramulu, K.; Datta, K. K. R.; Rösler, C.; Petr, M.; Otyepka, M.; Zboril, R.; Fischer, R. A. Biomimetic Superhydrophobic/Superoleophilic Highly Fluorinated Graphene Oxide and ZIF-8 Composites for Oil-Water Separation. *Angew. Chem., Int. Ed.* **2016**, *55*, 1178−1182.

(36) Huang, A.; Liu, Q.; Wang, N.; Zhu, Y.; Caro, J. Bicontinuous Zeolitic Imidazolate Framework Zif-8@go Membrane with Enhanced Hydrogen Selectivity. *J. Am. Chem. Soc.* **2014**, *136*, 14686−14689.

DOI: 10.1021/acsami.8b09851
ACS Appl. Mater. Interfaces 2018, 10, 33619−33629

(37) Hu, Y.; Wei, J.; Liang, Y.; Zhang, H.; Zhang, X.; Shen, W.; Wang, H. Zeolitic Imidazolate Framework/Graphene Oxide Hybrid Nanosheets as Seeds for the Growth of Ultrathin Molecular Sieving Membranes. *Angew. Chem., Int. Ed.* **2016**, *55*, 2048−2052.
(38) Thomas, M.; Illathvalappil, R.; Kurungot, S.; Nair, B. N.; Mohamed, A. A. P.; Anilkumar, G. M.; Yamaguchi, T.; Hareesh, U. S. Graphene Oxide Sheathed ZIF-8 Microcrystals: Engineered Precursors of Nitrogen-Doped Porous Carbon for Efficient Oxygen Reduction Reaction (ORR) Electrocatalysis. *ACS Appl. Mater. Interfaces* **2016**, *8*, 29373−29382.
(39) Zhong, H. X.; Wang, J.; Zhang, Y. W.; Xu, W. L.; Xing, W.; Xu, D.; Zhang, Y. F.; Zhang, X. B. ZIF-8 Derived Graphene-Based Nitrogen-Doped Porous Carbon Sheets as Highly Efficient and Durable Oxygen Reduction Electrocatalysts. *Angew. Chem., Int. Ed.* **2014**, *53*, 14235−14239.
(40) Xie, Z.; He, Z.; Feng, X.; Xu, W.; Cui, X.; Zhang, J.; Yan, C.; Carreon, M. A.; Liu, Z.; Wang, Y. Hierarchical Sandwich-Like Structure of Ultrafine N-Rich Porous Carbon Nanospheres Grown on Graphene Sheets as Superior Lithium-Ion Battery Anodes. *ACS Appl. Mater. Interfaces* **2016**, *8*, 10324−10333.
(41) Semino, R.; Durholt, J. P.; Schmid, R.; Marin, G. Multiscale Modeling of the HKUST-1/Polyvinyl Alcohol) Interface: From an Atomistic to a Coarse Graining Approach. *J. Phys. Chem. C* **2017**, *121*, 21491−21496.
(42) Semino, R.; Ramsahye, N. A.; Ghoufi, A.; Maurin, G. Role of MOF Surface Defects on the Microscopic Structure of MOF/Polymer Interfaces: A Computational Study of the ZIF-8/PIMs Systems. *Microporous Mesoporous Mater.* **2017**, *254*, 184−191.
(43) Lerf, A.; He, H.; Forster, M.; Klinowski, J. Structure of Graphite Oxide Revisited[II]. *J. Phys. Chem. B* **1998**, *102*, 4477−4482.
(44) Wang, L.; Lee, K.; Sun, Y.-Y.; Lucking, M.; Chen, Z.; Zhao, J. J.; Zhang, S. B. Graphene Oxide as an Ideal Substrate for Hydrogen Storage. *ACS Nano* **2009**, *3*, 2995−3000.
(45) Dehghanzad, B.; Razavi Aghjeh, M. K.; Rafeie, O.; Tavakoli, A.; Jameie Oskooie, A. Synthesis and Characterization of Graphene and Functionalized Graphene via Chemical and Thermal Treatment Methods. *RSC Adv.* **2016**, *6*, 3578−3585.
(46) Pendolino, F.; Armata, N. *Graphene Oxide in Environmental Remediation Process*; Springer Series Briefs in Applied Sciences and Technology;Springer International Publishing, 2017.
(47) Oh, W.-C.; Zhang, F.-J. Preparation and Characterization of Graphene Oxide Reduced From a Mild Chemical Method. *Asian J. Chem.* **2011**, *23*, 875−879.
(48) VandeVondele, J.; Krack, M.; Mohamed, F.; Parrinello, M.; Chassaing, T.; Hutter, J. Quickstep: Fast and Accurate Density Functional Calculations Using a Mixed Gaussian and Plane Waves Approach. *Comput. Phys. Commun.* **2005**, *167*, 103−128.
(49) Elstner, M.; Porezag, D.; Jungnickel, G.; Elsner, J.; Haugk, M.; Frauenheim, T.; Suhai, S.; Seifert, G. Self-Consistent-Charge Density-Functional Tight-Binding Method for Simulations of Complex Materials Properties. *Phys. Rev. B* **1998**, *58*, 7260−7268.
(50) Grimme, S.; Antony, J.; Ehrlich, S.; Krieg, H. A Consistent and Accurate Ab Initio Parametrization of Density Functional Dispersion Correction (DFT-D) for the 94 Elements H-Pu. *J. Chem. Phys.* **2010**, *132*, No. 154104.
(51) Dimiev, A. M.; Eigler, S. *Graphene Oxide: Fundamentals and Applications*; John Wiley & Sons, Ltd., 2016.
(52) Jorgensen, W. L.; Maxwell, D. S.; Tirado-Rives, J. Development and Testing of the OPLS All-Atom Force Field on Conformational Energetics and Properties of Organic Liquids. *J. Am. Chem. Soc.* **1996**, *118*, 11225−11236.
(53) Breneman, C. M.; Wiberg, K. B. Determining Atom-Centered Monopoles from Molecular Electrostatic Potentials. The Need for High Sampling Density in Formamide Conformational Analysis. *J. Comput. Chem.* **1990**, *11*, 361−373.
(54) Frisch, M. J.; Trucks, G. W.; Schlegel, H. B.; Scuseria, G. E.; Robb, M. A.; Cheeseman, J. R.; Scalmani, G.; Barone, V.; Mennucci, B.; Petersson, G. A.; Nakatsuji, H.; Caricato, M.; Li, X.; Hratchian, H. P.; Izmaylov, A. F.; Bloino, J.; Zheng, G.; Sonnenberg, J. L.; Hada, M.; Ehara, M.; Toyota, K.; Fukuda, R.; Hasegawa, J.; Ishida, M.; Nakajima, T.; Honda, Y.; Kitao, O.; Nakai, H.; Vreven, T.; Montgomery, J. A.; Peralta, J. E.; Ogliaro, F.; Bearpark, M.; Heyd, J. J.; Brothers, E.; Kudin, K. N.; Staroverov, V. N.; Kobayashi, R.; Normand, J.; Raghavachari, K.; Rendell, A.; Burant, J. C.; Iyengar, S. S.; Tomasi, J.; Cossi, M.; Rega, N.; Millam, J. M.; Klene, M.; Knox, J. E.; Cross, J. B.; Bakken, V.; Adamo, C.; Jaramillo, J.; Gomperts, R.; Stratmann, R. E.; Yazyev, O.; Austin, A. J.; Cammi, R.; Pomelli, C.; Ochterski, J. W.; Martin, R. L.; Morokuma, K.; Zakrzewski, V. G.; Voth, G. A.; Salvador, P.; Dannenberg, J. J.; Dapprich, S.; Daniels, A. D.; Farkas; Foresman, J. B.; Ortiz, J. V.; Cioslowski, J.; Fox, D. J. *Gaussian 09*, Revision B.01; Gaussian, Inc.: Wallingford, CT, 2009.
(55) Allen, M. P.; Tildesley, D. J. *Computer Simulation of Liquids*; Oxford Science Publications, 1987.
(56) Dai, H.; Xu, Z.; Yang, X. Water Permeation and Ion Rejection in Layer-by-Layer Stacked Graphene Oxide Nanochannels: A Molecular Dynamics Simulation. *J. Phys. Chem. C* **2016**, *120*, 22585−22596.
(57) Berendsen, H. J. C.; Grigera, J. R.; Straatsma, T. P. The Missing Term in Effective Pair Potentials. *J. Phys. Chem.* **1987**, *91*, 6269−6271.
(58) Szabó, T.; Berkesi, O.; Forgó, P.; Josepovits, K.; Sanakis, Y.; Petridis, D.; Dékány, I. Evolution of Surface Functional Groups in a Series of Progressively Oxidized Graphite Oxides. *Chem. Mater.* **2006**, *18*, 2740−2749.
(59) Wang, L.; Zhao, J.; Sun, Y.-Y.; Zhang, S. B. Characteristics of Raman Spectra for Graphene Oxide from Ab Initio Simulations. *J. Chem. Phys.* **2011**, *135*, No. 184503.
(60) Rogala, M.; Dabrowski, P.; Kowalczyk, P. J.; Wlasny, I.; Kozlowski, W.; Busiakiewicz, A.; Karaduman, I.; Lipinska, L.; Baranowski, J. M.; Klusek, Z. The Observer Effect in Graphene Oxide − How the Standard Measurements Affect the Chemical and Electronic Structure. *Carbon* **2016**, *103*, 235−241.
(61) Lesiak, B.; Stobinski, L.; Malolepszy, A.; Mazurkiewicz, M.; Kövér, L.; Tóth, J. Preparation of Graphene Oxide and Characterisation Using Electron Spectroscopy. *J. Electron Spectrosc. Relat. Phenom.* **2014**, *193*, 92−99.
(62) Gonçalves, G.; Vila, M.; Bdikin, I.; de Andrés, A.; Emami, N.; Ferreira, R. A. S.; Carlos, L. D.; Grácio, J.; Marques, P. A. A. P. Breakdown into Nanoscale of Graphene Oxide: Confined Hot Spot Atomic Reduction and Fragmentation. *Sci. Rep.* **2014**, *4*, No. 6735.
(63) Felten, A.; Flavel, B. S.; Britnell, L.; Eckmann, A.; Louette, P.; Pireaux, J.-J.; Hirtz, M.; Krupke, R.; Casiraghi, C. Single- and Double-Sided Chemical Functionalization of Bilayer Graphene. *Small* **2013**, *9*, 631−639.
(64) Todorov, I. T.; Smith, W.; Trachenko, K.; Dove, M. T. DL_POLY_3: New Dimensions in Molecular Dynamics Simulations via Massive Parallelism. *J. Mater. Chem.* **2006**, *16*, 1911−1918.
(65) Martyna, G. J.; Klein, M. L.; Tuckerman, M. Nosé−Hoover Chains: The Canonical Ensemble via Continuous Dynamics. *J. Chem. Phys.* **1992**, *97*, 2635−2643.
(66) Lee, H.; Park, S. C.; Roh, J. S.; Moon, G. H.; Shin, J. E.; Kang, Y. S.; Park, H. B. Metal-Organic Frameworks Grown on Porous Planar Template with Exceptionally High Surface Area: Promising Nanofiller Platforms for CO_2 Separation. *J. Mater. Chem. A* **2017**, *5*, 22500−22505.
(67) Venna, S. R.; Lartey, M.; Li, T.; Spore, A.; Kumar, S.; Nulwala, H. B.; Luebke, D. R.; Rosi, N. L.; Albenze, E. Fabrication of MMMs with Improved Gas Separation Properties Using Externally-Functionalized MOF Particles. *J. Mater. Chem. A* **2015**, *3*, 5014−5022.
(68) Ordoñez, M. J. C.; Balkus, K. J.; Ferraris, J. P.; Musselman, I. H. Molecular Sieving Realized with ZIF-8/Matrimid Mixed-Matrix Membranes. *J. Membr. Sci.* **2010**, *361*, 28−37.
(69) Felten, A. Single- and Double-Sided Chemical Functionalization of Bilayer Graphene. *Small* **2013**, *9*, 631−639.

DOI: 10.1021/acsami.8b09851
ACS Appl. Mater. Interfaces 2018, 10, 33619−33629

CHAPTER 4 – EFFECT OF THE NATURE OF MOFs ON MOF/GO INTERFACES

4.1. Introduction

The adhesion and spatial configurations of GOs can be likely influenced by the nature of MOFs, i.e. its chemical functional groups and surface shape/roughness, which can lead to different degree of MOF/GO compatibility. Here particular attention is paid to explore high valence cations (+III, +IV) ultra-microporous MOFs which are known to be chemically stable. More specifically, MIL-69(Al) and MIL-91(Ti) were combined with GO layers to create their respective composites owing to their highly attractive performances for CO_2 capture with respect to other gases including N_2 and CH_4 either by molecular sieving and thermodynamics effect respectively[1,2]. The resulting interfacial properties in terms of nature and strength of the interactions, the surface coverage and the GO conformation at the MOF surface were studied using the computational strategy that was preliminary developed and validated for ZIF-8/GO interface in Chapter 3. In MIL-69(Al)/GO, the interaction of two crystallographic facets (001) and (010) were examined to explore their facet specific compatibility with GO. The conclusions drawn from this computational effort were further validated by *in-depth* experimental exploration including a series of advanced characterization tools. At a later stage, the MIL-91(Ti)/GO composite has been theoretically investigated.

4.2. MIL-69(Al)/GO Interfaces Models

4.2.1. MIL-69(Al) Surfaces Construction

The surface models of MIL-69 were cut from the crystal structure following the same approach that was used in the previous chapter for ZIF-8[3]. Two surface models were cleaved along the (001) and (010) crystallographic planes using the Bravais−Friedel−Donnay−Harker (BFDH) method[4–6]. These models were of 57 Å and 40 Å in length along the z-axis. It was further ensured that no surface interactions take place along the z direction by maintaining gaps between periodic images large enough i.e. 22 Å and 13 Å for the (001) and (010) surface models respectively. Again to maintain the dipole neutrality of the system along z-axis, the model was reconstructed by creating a mirror plane symmetry at the centre of the z-axis moving certain atoms from the top to the bottom of the slab[7]. The under-coordinated sites, i.e. dangling bonds left after the BFDH method was applied, were capped considering the dissociative adsorption of

water[8,9] i.e., the exposed Aluminium centres were saturated by hydroxyl groups while the under-coordinated oxygen atoms were bonded to hydrogen atoms. These built models were fully optimized at the DFT level using the Quickstep module of the CP2K code[10]. PBE[11] GGA functional was used in combination with Gaussian basis set and plane wave pseudopotential strategy. A triple-zeta Gaussian-type basis set (TZVP-MOLOPT basis set) was considered for all atoms, except for the metal centres, where double-zeta functions were employed (DZVP-MOLOPT)[12]. The pseudopotentials used for all the atoms were those derived by Goedecker, Teter, and Hutter[12]. These calculations included the semi-empirical dispersion corrections as implemented in the DFT-D3 method, developed by Grimme[13].

The sizes of the final surface models were increased in size to perform the force-field based-simulations leading to models for (001) as 49 Å x 52 Å x 57 Å and for (010) as 53 Å x 47 Å x 40 Å respectively. Figure 4.1a,b shows an illustration of the surface models of MIL-69 (001) and MIL-69 (010). Interestingly, it can be observed that the surface cleaved along the (001) plane offers pore opening at the surface.

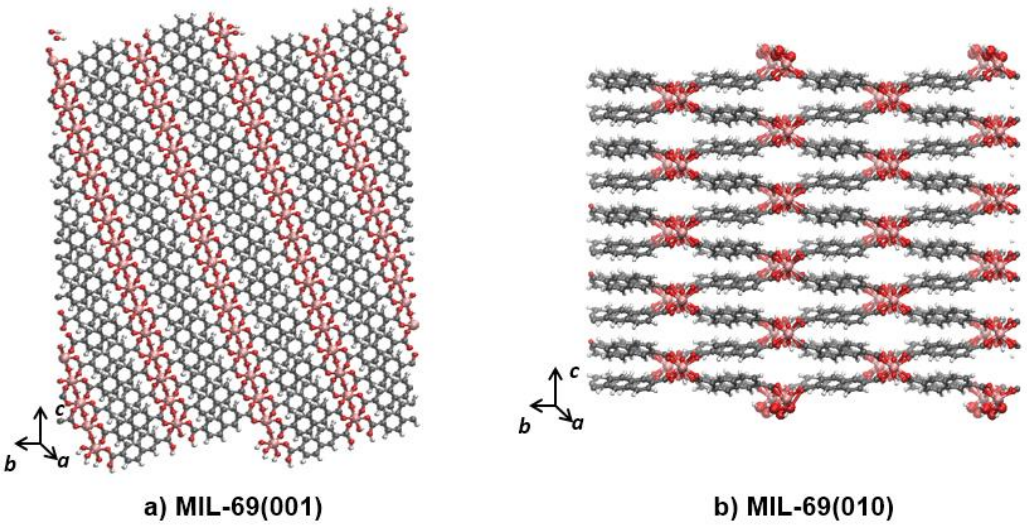

Figure 4.1 Microscopic surface models constructed for MIL-69 a) 001 crystallographic plane and b) 010 crystallographic plane. Colour scheme of MIL-69: C-grey, Al-pink, O-red and H-white

4.2.2. MIL-69(Al)/GO Interfaces construction

The surface models obtained for MIL-69 surfaces were combined to construct two different interfaces i.e., MIL-69(001)/GO-CO_2H and MIL-69(010)/GO-CO_2H using the same computational approach described earlier for ZIF-8 related composites. The GO-CO_2H model

was the same taken from the previous study and for simplicity GO-CO_2H will be termed as "pristine-GO" hereafter. The pristine-GO layers were placed along the z-axis of the MIL-69 surfaces in such a way that the cleaved MIL-69 surfaces face the basal plane of the GO. The pristine-GO model is of dimension 43 Å x 43 Å that fits well on both (001) and (010) MIL-69 surface slabs which have dimensions of 49 Å x 52 Å and 53 Å x 47 Å along x and y planes. Thereafter, 16 and 12 layers of GOs were placed on MIL-69(001) and MIL-69(010) slabs in order to exclude the mutual interactions between MOF surfaces[14]. Each atom of MIL-69 models was treated by a charged LJ site. The LJ parameters for the framework were taken from both Dreiding[15] and universal force field (UFF)[16] for the organic and inorganic nodes respectively. The charges for MIL-69 surfaces were obtained using the electrostatic potential scheme CHELPG[17] with the PBE functional and the 6-31G(d,p) basis set as implemented in the Gaussian 03 package. The interactions between pristine-GO and the MIL-69 surface slabs were described by the sum of a Coulombic and LJ potential terms with the crossed-interactions being computed by Lorentz−Berthelot mixing rules[18] The corresponding charges for the MIL-69 surfaces are reported in Table 4.1 while the labels of the atoms are provided in Figure 4.2. For aluminium atom, the attractive van der Waals force is not exerted as it is screened by its oxygen environment. The same attractive force has been ignored for mobile protons, H1/Hs, in the surrounding of aluminium atom.

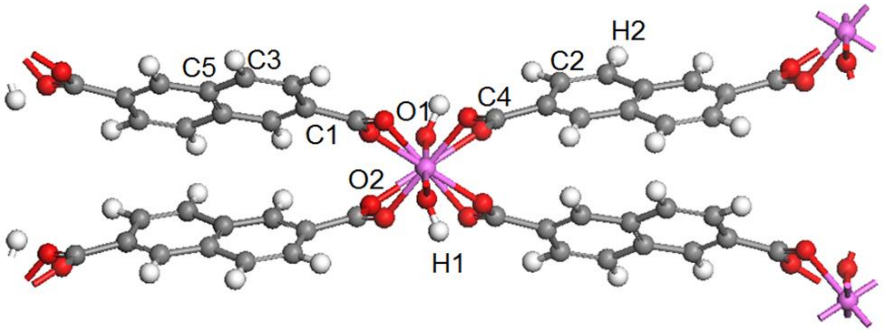

Figure 4.2 Atom types considered for the MIL-69 model. Colour codes for the atoms are the same as Figure 4.1. In addition, we have the terminal atoms as Os and Hs on the surface attached to Al atoms

Table 4.1 Atom types, LJ parameters and charges for the MIL-69 model

Atom type	ε_{ii} (kcal/mol)	σ_{ii} (Å)	q_i (e)
Al	0.0000*	4.009	+1.419
C1	0.0951	3.473	-0.069
C2	0.0951	3.473	-0.121
C3	0.0951	3.473	-0.155
C4	0.0951	3.473	+0.588
C5	0.0951	3.473	-0.014
O1	0.0600	3.118	-0.691
O2	0.0600	3.118	-0.556
H1	0.0000*	2.571	+0.300
H2	0.0152	2.846	+0.168
Os	0.1700	3.210	-0.6945
Hs	0.0000*	2.500	+0.301

The so-constructed composite models were geometry optimized with the consideration of a series of MD cycles. Here again, the pressure was applied along a single direction fixing the MOF coordinates so that the expansion and contraction happen only in one direction altering the GO positions, i.e. in our case along z-axis. These MD simulations were considered in the NP_zT ensemble at 100 bar and 1000 K with the use of a Berensen barostat and a relaxation time of 0.5 ps. This allowed to stack the GO layers at the surfaces of the MOF. The system was run with a time step of 1 fs for a total run of 1 ns. The so-obtained model was then considered for further MD simulations in the NPT ensemble at 1 bar and 298 K for 500 ps to relax the composite. After these equilibration steps, MD simulations were executed in the Nosé–Hoover[19] NVT ensemble at 1 bar and 298 K for 5 ns production run with a thermostat relaxation time of 0.5 ps. The resulting equilibrated MOF/GO models are illustrated in Figure 4.3.

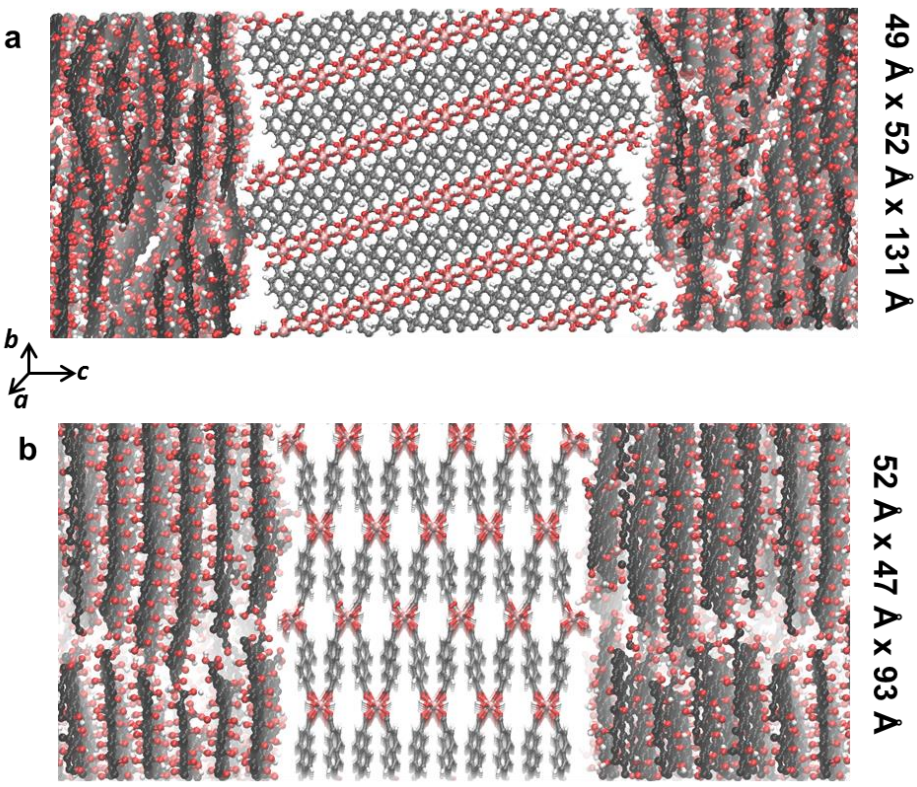

Figure 4.3 Illustration of a) MIL-69(001)/pristine-GO and b) MIL-69(010)/pristine-GO models. Colour scheme: GO layers: C-black; O-red, H-white; MIL-69: C-grey, Al-pink, O-red and H-white

4.2.3. Analysis of MIL-69(Al)/GO Interfaces

Figure 4.4a reports the normalized atomic density for the MIL-69(010)/pristine-GO models plotted along the z-axis of the simulation box. We can distinguish two regions defined as region A marked as "A" and region B marked as "B". Region B is reminiscent of a bulk-like behaviour of the GO where its density oscillates around a steady value i.e., till 44 Å (line in black). Above 44 Å, the GO density decreases, reaching the MOF region represented in red line that extends till 93 Å. Region A corresponds to the cross-section between GO and MOF which starts from the lower limit where the density of MOF atoms tends to zero i.e. 46 Å till 51 Å, where the GO density tends to zero. The region A corresponds to the interfacial zone between the two components which has a z-length value of ~5 Å. Figure 4.4b provides an illustrative snapshot of these two regions. The same conclusion holds true when MIL-69(001)/pristine-GO model is examined (Figure 4.4c) with a similar length of region A ~4 Å. Its illustrative snapshot is shown in (Figure 4.4d).

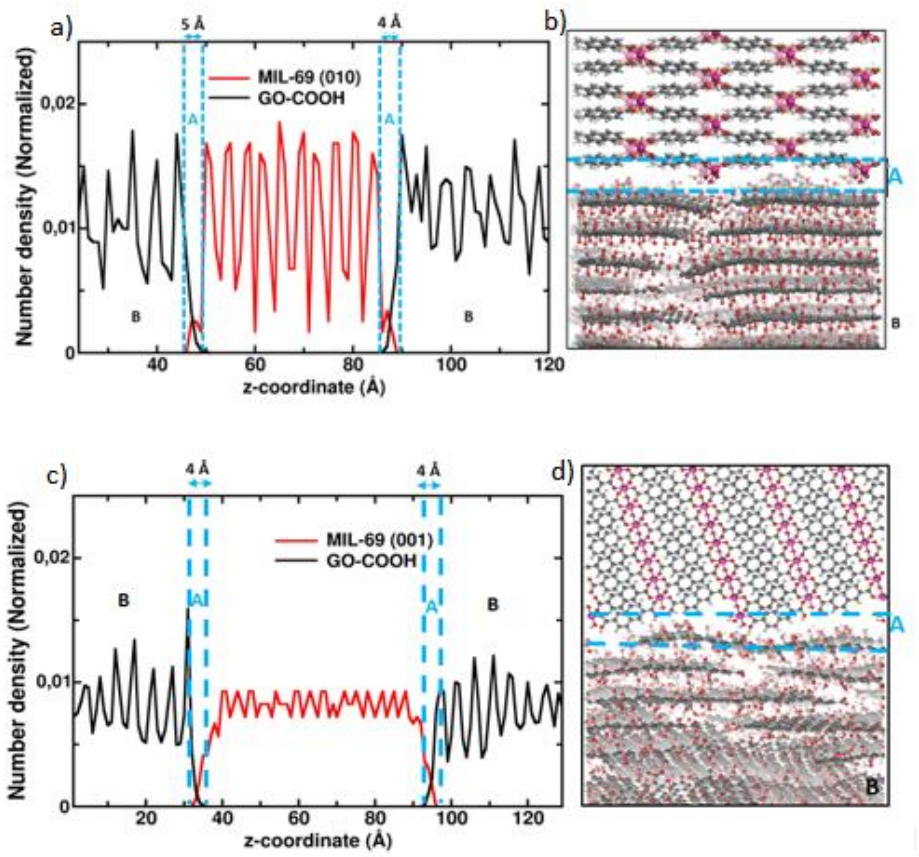

Figure 4.4 Representation of the normalized atomic density for the (a-b) MIL-69(010)/pristine-GO model and its Illustrative snapshot showing the interfacial (region A) and bulk (region B) regions. (c-d) MIL-69(001)/pristine-GO model and its illustrative snapshot showing region A and region B. Colour schemes are GO layers: C-grey; O-red, H-white; MIL-69(010): C-grey, Al-magenta, O-red and H-white

The next step was to illustrate the preferential interactions between the MOF and GO at the interfacial region. Figure 4.5a and Figure 4.5b shows the RDF plots between the hydrogen atom "Hs" (see Figure 4.2) of the -OH functional groups present at the MIL-69 surface and the diverse oxygen atoms of the GO. The shortest interacting distance is found to be about ~1.8 Å to 2 Å between Hs and the O atom of the hydroxyl function of GO for both MIL-69(010)/pristine-GO and MIL-69(001)/pristine-GO interfaces as shown in Figure 4.5. These RDF plots show that the most predominant interactions involve the H atom of the –OH groups of MIL-69 with the edged $–CO_2H$ functions for both models while the intensity of the corresponding peaks is four times higher for the MIL-69(010)/pristine-GO interface than MIL-69(001)/pristine-GO interface. This emphasizes that the MOF/GO interactions are significantly stronger in the former case.

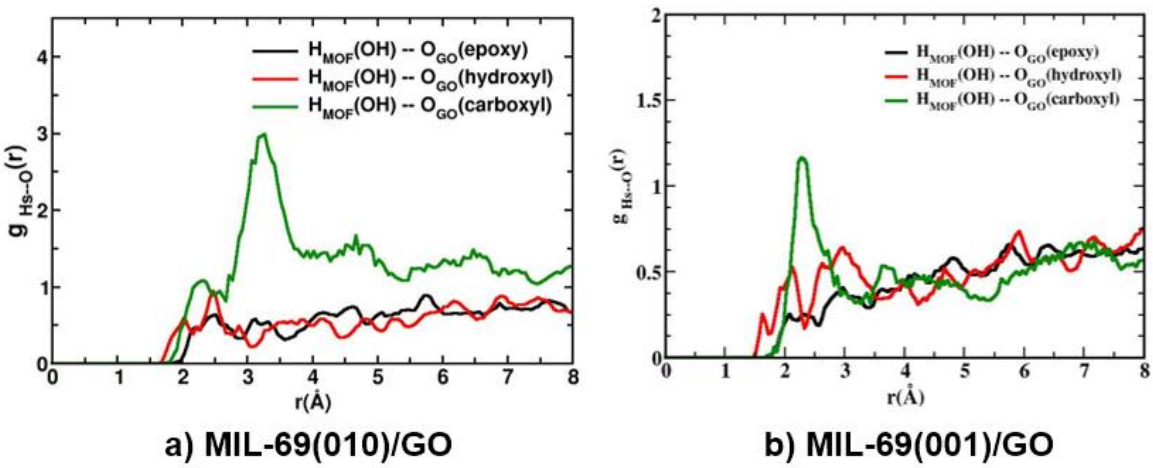

Figure 4.5 RDFs for a) MIL-69(010)/pristine-GO and b) MIL-69(001)/pristine-GO models calculated between the hydrogen atoms of the terminal -OH groups of MIL-69 and the different O functional groups of GO

The dihedral angle distribution of pristine-GO was calculated for both models along the z-axis in the vicinity of MOF. The GO layers closer to the MIL-69(010) surface (see Figure 4.6) surface were found by far more twisted or disoriented compared with the scenario encountered for the MIL-69(001) surface (see Figure 4.7). This distinct conformational behaviour is consistent with a stronger interaction between the MIL-69(010) surface and the $–CO_2H$ groups of the GO that tends to geometrically distort the conformation of the GO layer at the MOF surface.

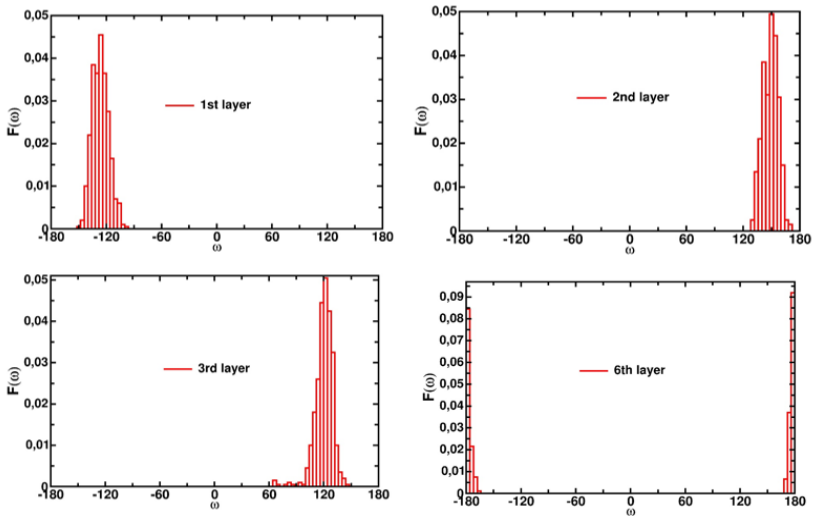

Figure 4.6 Dihedral angle distributions of the 1st, 2nd ,3rd layer and 6th layers of pristine-GO on MIL-69(010) surface

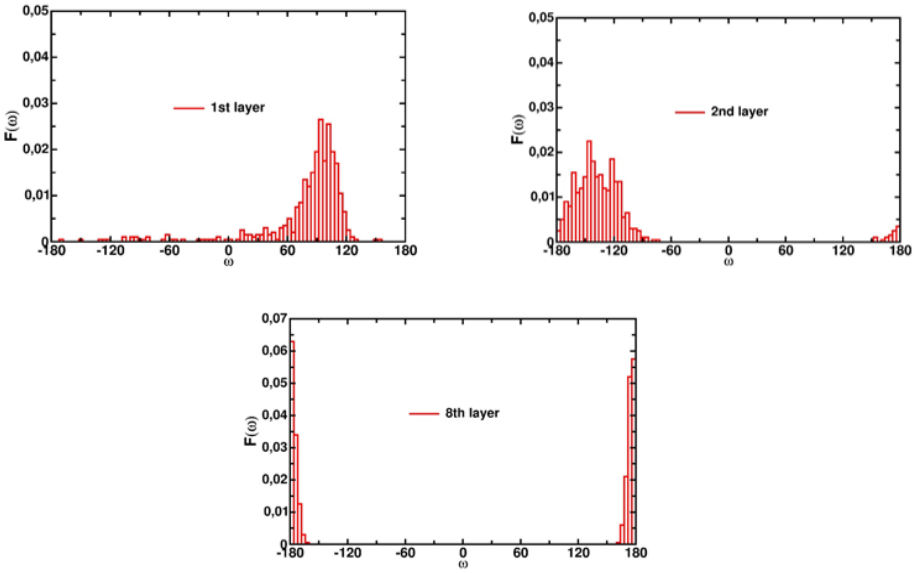

Figure 4.7 Dihedral angle distributions of the 1st, 2nd and 8th layers of pristine-GO on MIL-69(001) surface

GO layer was further revealed to arrange at the MOF surface in a such a way to establish π-π like-stacking interactions between the aromatic rings of MIL-69(010) and pristine-GO. Indeed, the RDF plots shown in Figure 4.8a show a significant interaction between the naphthalene linker of MIL-69 and the carboxylic group of GO with an associated separating carbon-carbon distance of ~3.0 Å. Such an interaction is much less probable in the case of the MIL-69(001) when one compares the intensity of the corresponding RDF peaks (see Figure 4.8b). An illustrative snapshot of such interactions are provided in Figure 4.8 (right side) leading to a geometry where the naphthalene linker lies parallel to the aromatic ring of GO in MIL-69(010) that significantly differs with the scenario observed for MIL-69(001) (see Figure 4.8a and Figure 4.8b). Besides reinforcing the compatibility between the two components, such a π-π like-stacking interaction tends to monopolize the MIL-69(010) surface hence it is not free anymore for further processing. This observation might suggest that the crystal growth preferentially proceeds via the (001) surface rather than (010) surface.

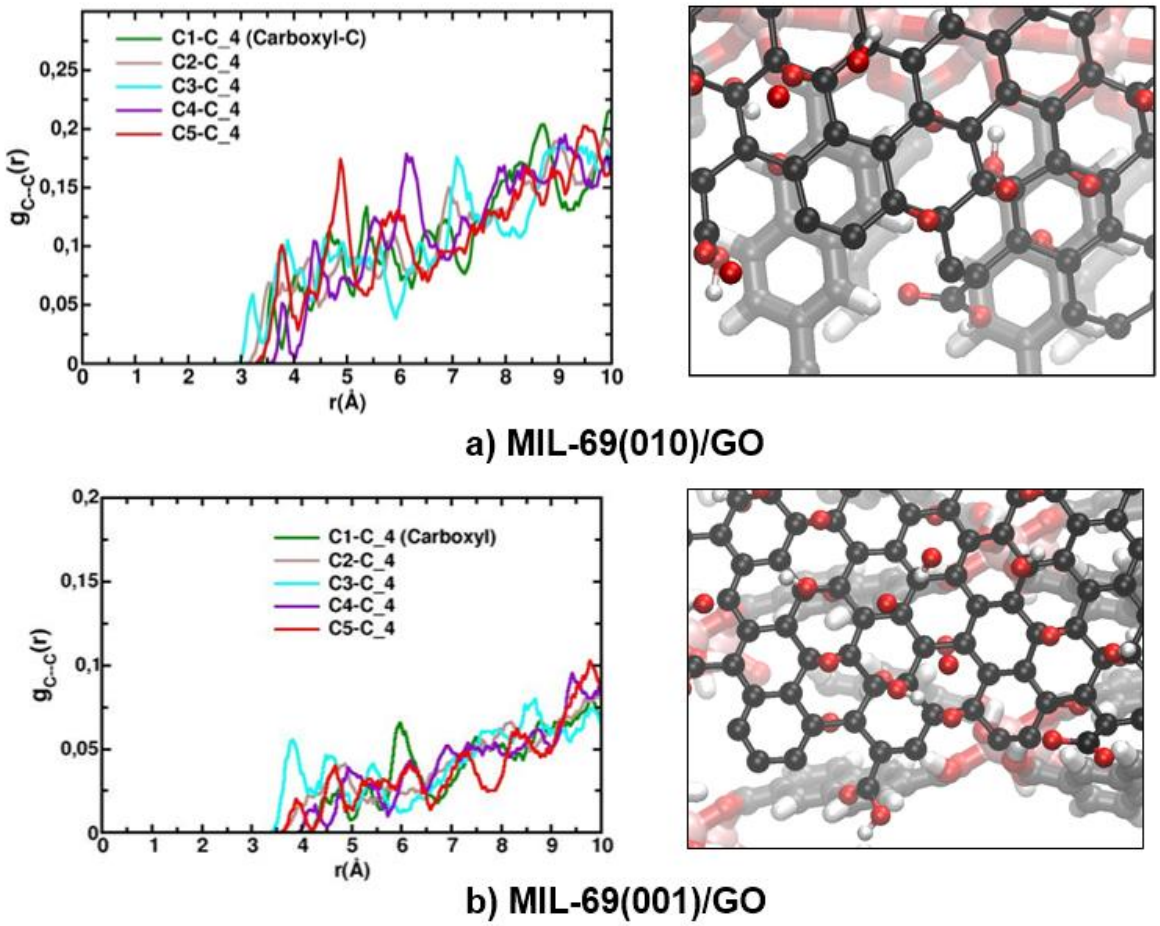

Figure 4.8. Preferential π--π like interactions for a) MIL-69(010)/pristine-GO and b) MIL-69(001)/pristine-GO composites. On the left side are the RDFs between the C atoms of MIL-69(010) and the C_4 atoms (carboxyl function) of the GOs while on the right side are its corresponding snapshot. The labels of the atoms are mentioned in Figure 4.2 and Table 4.1. Colour scheme of GO layers: C-black; O-red, H-white; MOF: C-grey, Al-pink, O-red and H-white

4.2.4. Correlation with Experimental Findings

The corresponding composite was further explored experimentally by our collaborators from the Institut Lavoisier Versailles and Institut de Minéralogie, de Physique des Matériaux et de Cosmochimie. The fabrication of the MIL-69(Al)/GO composites were performed through *in-situ* formation of the MOF in the presence of GO. The corresponding membrane was characterized using various advanced techniques (XRD, TEM, HAADF-STEM, EDX, XPS etc.). The full experimental characterization is described in detail in the paper included at the end of this chapter. As a summary, the presence of sharp and intense Bragg peaks in the PXRD pattern of MIL-69/GO is remarkable and suggested that the nucleation and growth of MIL-69(Al) does not lead to MIL-69(Al) nanoparticles (NPs) but to highly crystalline MIL-69(Al) crystals with a different morphology.

TEM Bright field (TEM-BF) and Scanning TEM using the High Angle Annular Dark Field mode (HAADF-STEM) images of the corresponding composite reported in Figure 4.9 evidenced intergrown MIL-69(Al) nanowires (NWs) and GO sheets. The MIL-69(Al) NWs present a uniform shape, an average diameter of 70 ± 20 nm, lengths up to 2 μm and aspect ratio up to 20, as evaluated from 50 NWs randomly selected from TEM images. Selected area electron diffraction (SAED) pattern clearly indicates that the nanowire is a single crystal of MIL-69(Al) (Figure 4.9f,e). A large majority of NWs are well-crystalline and are characterized by a uniform contrast in the HAADF-STEM images. The indexation of the regular diffraction spots revealed that the nanowire grows along the (001) direction. This is consistent with the results of simulations showing that MIL-69(010)/pristine-GO is characterized by higher intensity of interactions between GO and MOF compared to MIL-69(001)/pristine-GO thus proving that [001] is the growth direction of the MOF where it has more room to move around when combined with GO.

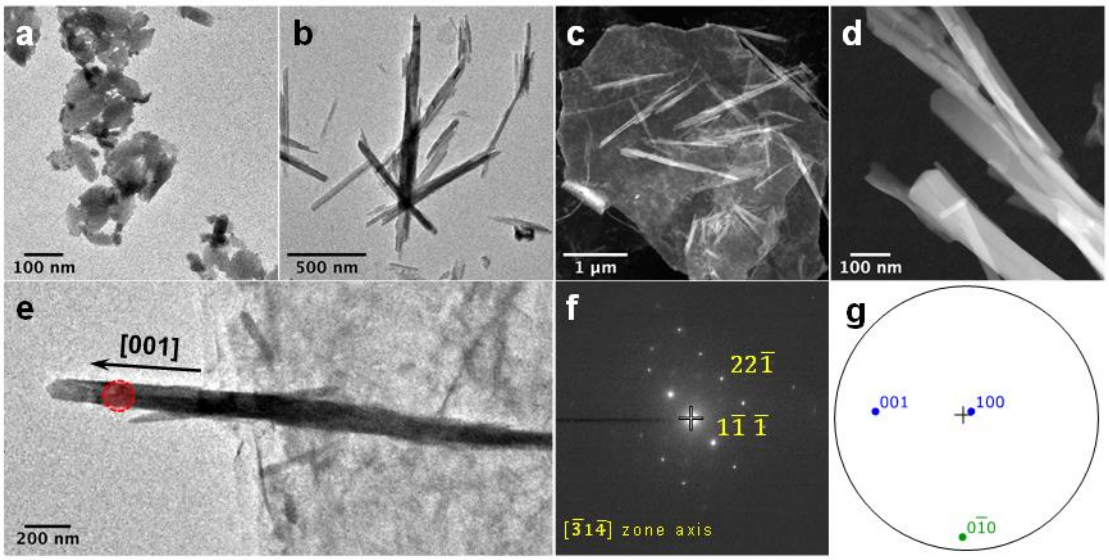

Figure 4.9 a) TEM-BF image of MIL-69 NPs; (b, e) TEM-BF, (c,d) STEM-HAADF images of MIL-69/GO-4.5-24 (f) SAED of the area high-lighted by the red circle in (e).The SAED indexation is given with respect to the MIL-69(Al) structure. The stereographic projection (g) - related to the crystallographic orientation deduced from (f) - indicates that the crystal growth proceeds along the [001] direction

HAADF-SAED images further evidenced the presence of bundles of MIL-69(Al) 1D tubular nanostructures interwoven with GO sheets (Figure 4.10). These observations are fully consistent with Archimedean-type nanoscrolls formed by rolling single rGO sheets from one side or from a corner. Analogous nanoscrolls were previously reported for composites obtained by assembling preformed maghemite nanoparticles and graphene sheets[20]. This can be also correlated to the

theoretical findings revealing (i) the preferential interactions of edged carboxyl groups of GO with the -OH functions of the MOF surface (see Figure 4.5), and (ii) the significant twisting of the GO-layer in direct contact with the MOF as suggested by the analysis of the dihedral angle distribution (see Figure 4.6 and 4.7), that act as a driving force for the scrolling of GO evidenced experimentally.

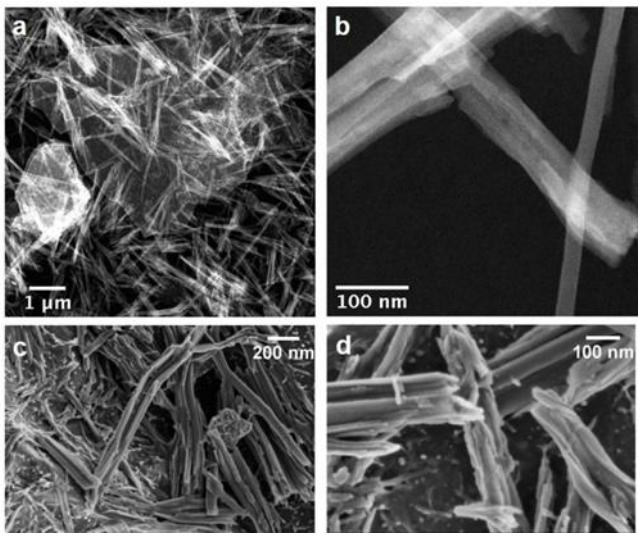

Figure 4.10 (a, b) HAADF-STEM images and (c, d) SEM observations of MIL-69/GO composites

In summary, when the two (001) and (010) surface MOF/GO composites were compared, predicted specific π-π interactions between the pristine-GO layers and the external surface of MIL-69(Al) at the MOF/GO interface were proposed to direct the anisotropic growth of MIL-69(Al) specially along the [001] direction. This was further supported experimentally with the formation of MIL-69(Al) NWs using GO nanoscrolls as structure-directing agent. By coupling multimodal characterization techniques and molecular simulation, a mechanism of their formation has been proposed. The self-scrolling of GO sheets is presumably induced by the covalent bonding between Al^{3+} centres and oxygen functions of GO (hydroxyl and carboxylate groups) and favourable π-π interactions between GO sheets and MIL-69(Al). This is followed by the nucleation and growth of MIL-69(Al) NPs at the surface of GO ribbons. Then, the growth of MIL-69(Al) NW is templated by the GO nanoscrolls as a result of the confinement of a high amount of MIL-69(Al) seeds in the inner cavity of GO nanoscrolls. This mechanism is summarized in Figure 4.11.

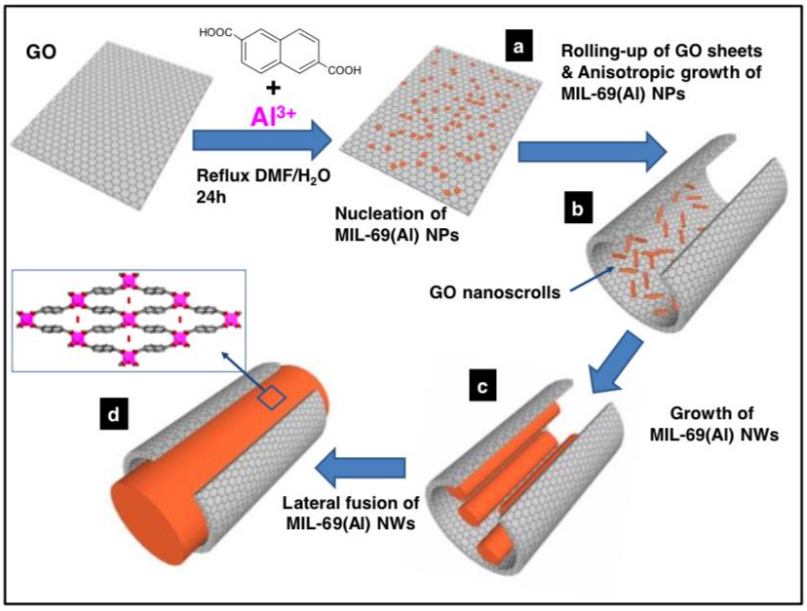

Figure 4.11 Mechanistic scheme summarizing the main stages of the MIL- 69(Al) NWs formation

4.3. MIL-91(Ti)/GO Interface Model

4.3.1. MIL-91(Ti) Surface Construction

The unit cell of the crystal structure was 19 Å x 14 Å x 11 Å in size. This model was enlarged in size and cleaved along the (100) crystallographic planes using the Bravais−Friedel−Donnay−Harker (BFDH) method[4–6]. The uncoordinated bonds left after cleaving were also capped using the dissociative adsorption of water[8,9] with the exposed phosphorus centres saturated with hydroxyl groups while the under-coordinated carbon atoms were bonded with hydrogen atoms. The model was reconstructed by creating a mirror plane symmetry at the centre of z-axis and moved certain atoms from top to bottom and vice versa[7] to make the system dipole neutral. This unit model was of size 14 x 11 Å along x and y plane. The MIL-91 surface model was fully optimized at the DFT level using CP2K code[10] using the same functional/basis set described above for MIL-69. Here again, it was ensured that no surface interaction is taking place along the z direction by maintaining vacuum gap between periodic images as large as possible. This DFT optimized model were later enlarged for force field-based MD simulations leading to the model size of 57 Å x 45 Å x 76 Å. Figure 4.12 shows an illustration of the surface models of MIL-91(100).

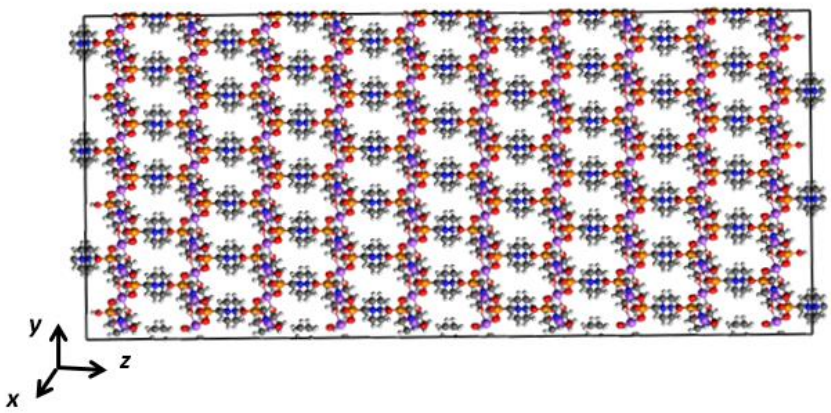

Figure 4.12 Microscopic models constructed for MIL-91 (100) surface. Colour scheme of MIL-91 model: C-grey, P-orange, O-red, N-blue, Ti-purple and H-white

4.3.2. MIL-91(Ti)/GO Interface Construction

The models of the MIL-91 and pristine-GO were combined together in a series of MD simulation to construct MIL-91(100)/pristine-GO interface, following the same strategy as described earlier[3,14,21,22]. The GO layers were placed along the z-axis of the MIL-91 surface so that the cleaved MIL-91 surfaces face the basal plane of the GO. The GO model fits well on MIL-91(100) slab. To exclude the mutual interactions between MOF surfaces, we placed 16 layers of GOs same as ZIF-8/GO system[14]. The LJ parameters of the MOF framework[23] were adopted from UFF[16]. For titanium atom, the attractive van der Waals force is not exerted as it is screened by its oxygen environment. The same has been ignored for mobile protons in the environment of piperazine-bis-methyl-phosphonate groups[24]. The charges for MIL-91 surfaces were obtained using the electrostatic potential scheme CHELPG[17] with the PBE[11] functional and the 6-31G(d,p) basis set as implemented in the Gaussian 03 package[25]. The corresponding charges used for the MIL-91 surface is reported in Table 4.2 while the labels of the atoms are provided in Figure 4.13. The so-constructed interface model was geometry optimized in a series of force field MD cycles as described for MIL-69. The final optimized MIL-91(100)/pristine-GO interface snapshot is illustrated in Figure 4.14.

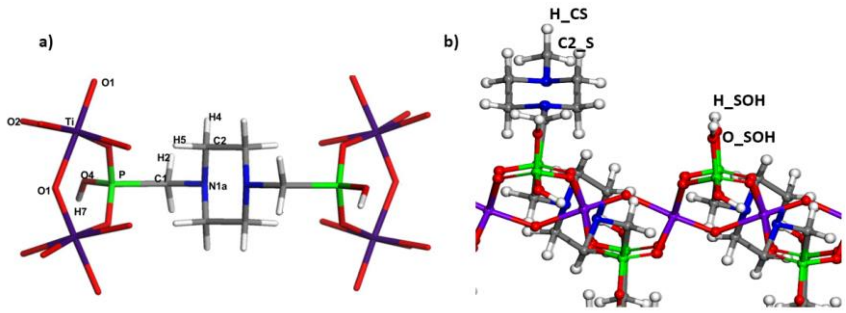

Figure 4.13 Atom types considered for the MIL-91 model a) bulk atoms and b) terminal surface atoms termed as H_CS, C2_S attached to N group and H_SOH and O_SOH attached to P group at the surface. Colour scheme of MIL-91 model: C-grey, P-green, O-red, N-blue, Ti-deep purple and H-white

Table 4.2 Atom types, LJ parameters and charges for the MIL-91 model

Atom type	ε_{ii} (kcal/mol)	σ_{ii} (Å)	q_i (e)
P	0.30500	3.695	1.4650
Ti	0.00000*	2.829	1.4040
N1b	0.06900	3.261	-0.4320
N1a	0.68900	3.261	-0.4320
O2	0.06000	3.118	-0.7480
O1	0.06000	3.118	-0.7340
O4	0.06000	3.118	-0.7940
C2	0.10500	3.431	-0.1150
C1	0.10500	3.431	-0.3710
H4	0.04400	2.571	0.2460
H5	0.04400	2.571	0.1540
H2	0.04400	2.571	0.1590
H7	0.00000*	2.571	0.4050
H_SOH	0.00000*	2.571	0.2830
O_SOH	0.06000	3.118	-0.5960
H_CS	0.04400	2.571	0.1110
C2_S	0.10500	3.431	-0.1630

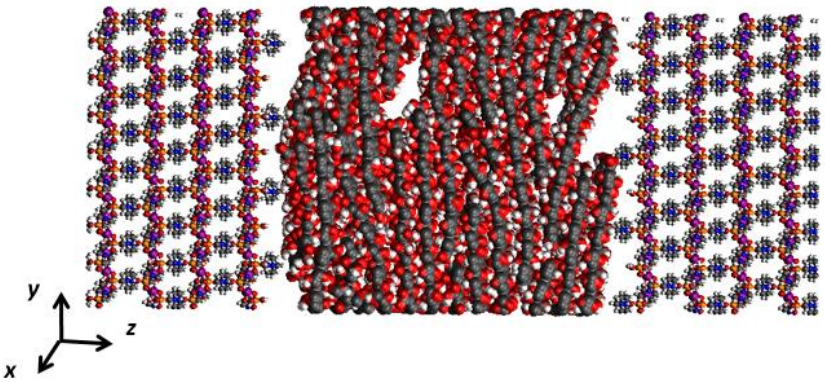

Figure 4.14 Representation of the final optimized MIL-91(100)/pristine-GO model

4.3.3. Analysis of the MIL-91(Ti)/GO Interface

Figure 4.15a illustrates the normalized atomic density of the composite model, plotted along the z-axis of the simulation box. Here again the model was separated into region A (interfacial region) and region B (bulk region). Figure 4.15a showed the GO layers located at the centre of the simulation box, while MOF is at both ends. As we scan from along the z-axis of the box i.e., from 0 Å till 145 Å, we first reach at the MIL-91 region. The MIL-91 density oscillates around a steady value till 36 Å (line in black) and then it drops. The crossover region starts from 39 Å, which has the atoms of both GO and MOF called as region A. After 39 Å, we enter the region where only GOs are present (line in red) until 102 Å. This is called as region B, where the density revolves around an equilibrium value which is consistent with the normalized atomic bulk density of GO. The length of region A is calculated from where the density of GO and MOF tends to zero. This z-length of region A was calculated to be ~3 Å.

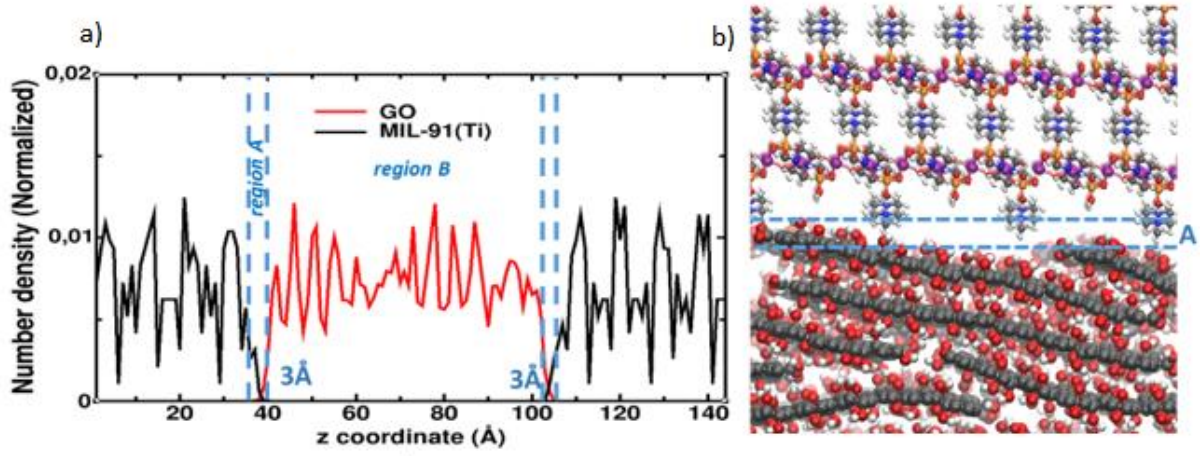

Figure 4.15 a) Representation of the normalized atomic density for the MIL-91(100)/pristine-GO model and b) Illustrative snapshot showing the interfacial (region A) and bulk (region B) regions. Colour schemes are GO layers: C-grey; O-red, H-white; MIL-91(100): C-grey, Ti-purple, O-red, P-orange, N-blue and H-white

The following step was to characterize the preferential interactions between the MOF and GO in the interfacial region. At the surface of MIL-91(Ti), there are two different terminal atoms. The hydrogen atom "H_CS" of -CH group bonded to nitrogen atom and "H_POH" atom of -OH group bonded to phosphorus. Figure 4.16 shows the RDF plots between the hydrogen atoms "H_CS" presents on the MIL-91 surface with different oxygen functional groups of GO. The shortest interacting distance was found to be about ~ 2.4 Å between H_CS and oxygen atom of epoxy group of GO. Here the most predominant interaction is between H_CS and oxygen atom of the carbonyl function of -CO_2H group of GO. The intensity of the interaction peak is stronger than others with interactive distance of 2.6 Å. This is followed by the H_CS and oxygen atom of the carboxyl function of -CO_2H group of GO with interacting distance of 2.8 Å. H_POH does not play a prominent role in such interactions with interactive distances above 3 Å hence the corresponding RDF data was not shown here.

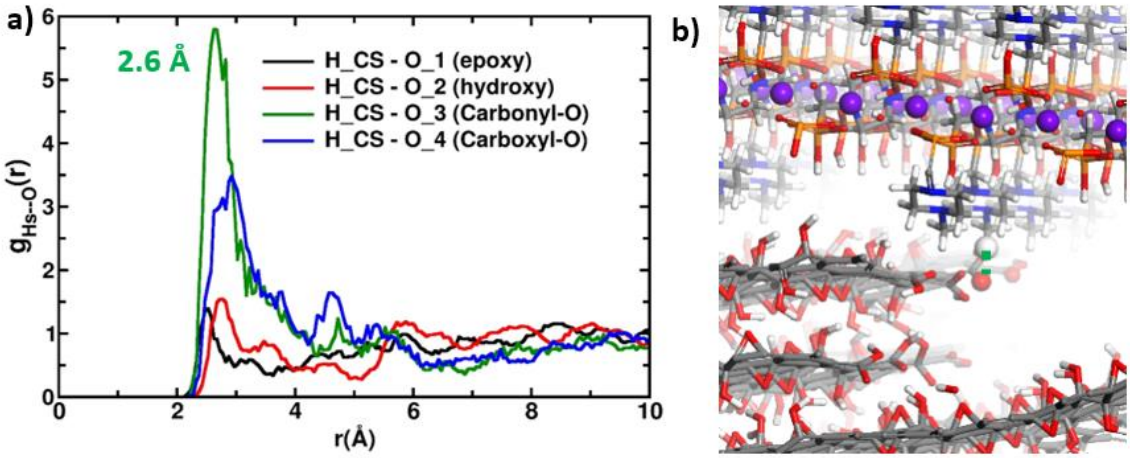

Figure 4.16 a) RDF calculated between the hydrogen atom "H_Cs" of the terminal surface atoms of MIL-91 and different O atoms of functional groups of pristine-GO and b) Corresponding snapshot of the main interaction between H_Cs and carbonyl function of GO

To go deeper, the conformation of GO layers was studied through dihedral angle distribution in the vicinity of MOF surface as shown in Figure 4.17. The first layer of GO layers closest to the MIL-91(100) surface was found by far more twisted or disoriented compared to the second and third layers. The distribution was oriented around 60°. This signifies that GO layer is trying hard to adapt to the geometry of MOF. The second layer also has a prominent distortion. These two layers are reminiscent of the interfacial region. The third layer until the eight layers has least distortion angles and reminiscent of a bulk like behaviour.

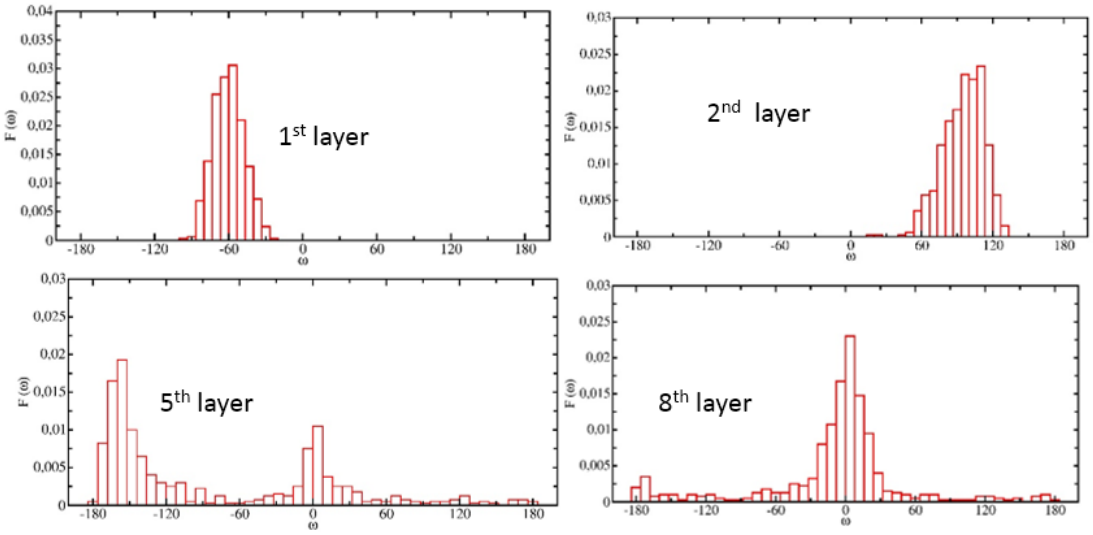

Figure 4.17 Dihedral angle distributions of the GO layers present at the MIL-91/pristine-GO interfaces

In summary, the computational methodology was deployed to construct and characterize the MIL-91(Ti)/pristine-GO interface at the microscopic scale. The corresponding composite models were characterized using various analysis tools like RDF, atomic density, dihedral distribution etc. The atomic density plot calculated for MIL-91(Ti)/pristine-GO interface showed an interface region of ~3 Å (region A). This region is smaller compared to the ZIF-8/pristine-GO and MIL-69/pristine-GO interface "region A" and can be linked to the corrugated surface terminal groups on the MIL-91(Ti) surface. The most important interaction sites on the surface of the MIL-91(Ti) was with H_CS atom linked to the -CH group bonded to nitrogen atom of the MOF surface which interact with all oxygen groups of GO layers. However, the most prominent interaction occurs between -CO_2H groups of GO with the H_CS atom of MOF and this leads to strong distortion of the GO layers present in the near vicinity of MOF. This preliminary work on MIL-91(Ti)/pristine-GO is expected to motivate further experimental work to fabricate the corresponding composite and test it for various applications especially in CO_2 capture and selectivity.

4.4. Conclusion

In summary, through computational methodology, several MOF/GO interfaces were constructed and analysed using the GO model developed in the previous chapter and two different MOFs. The basic idea was to explore the effect of different MOFs on MOF/GO

compatibility with the consideration of two MOFs, i.e. MIL-69(Al) and MIL-91(Ti). In MIL-69(Al)/pristine-GO study, two different facets of MOFs have been taken and combined with GO layers. Through the combination of experimental characterization techniques and molecular modelling, we have unravelled the formation of anisotropic 1D MIL-69(Al) owing to GO layer. In MIL-91(Ti)/pristine-GO composite, the predominant interactions occurring at the interface which lead to gain insight on its interfacial properties have been presented. Through forming hydrogen bonds and π−π like interactions, GOs interact with MOF surface populating its contacting area. The key role is played by the carboxyl groups of GOs in enhancing the compatibility of these composites. This work presented here provides a fundamental roadmap to study different MOF/GO interfaces in general using MD simulation techniques to scan the compatibility between GO layer and MOF surfaces. This study paves way for the development of several mixed matrix membranes in upcoming years.

REFERENCES

(1) Wang, S.; Serre, C. Toward Green Production of Water-Stable Metal-Organic Frameworks Based on High-Valence Metals with Low Toxicities. *ACS Sustain. Chem. Eng.* **2019**, *7*, 11911–11927.

(2) Devic, T.; Serre, C. High Valence 3p and Transition Metal Based MOFs. *Chem. Soc. Rev.* **2014**, *43* (16), 6097–6115.

(3) Semino, R.; Ramsahye, N. A.; Ghoufi, A.; Maurin, G. Microscopic Model of the Metal-Organic Framework/Polymer Interface: A First Step toward Understanding the Compatibility in Mixed Matrix Membranes. *ACS Appl. Mater. Interfaces* **2016**, *8* (1), 809–819.

(4) Donnay, H.; Harker, D.; Johns, T. A NEW LAW OF CRYSTAL MORPHOLOGY EXTENDING THE LAW OF BRAVAIS. *Am. Miner.* **1937**, *22*, 446−467.

(5) Friedel, G. *Etudes Sur La Loi de Bravais*, 30th ed.; Bull. Soc. Fr. Mineral., **1907**.

(6) Bravais, A. *Etudes Cristallographiques*; Gauthier-Villars: Paris, **1866**.

(7) Catlow, C. R. A.; Ackermann, L.; Bell, R. G.; Cora, F.; Gay, D. H.; Nygren, M. A.; Pereira, J. C.; Sastre, G.; Slater, B.; Sinclair, P. E. Computer Modelling as a Technique in Solid State Chemistry. *Faraday Discuss.* **1997**, *106*, 1–40.

(8) Tian, F.; Cerro, A. M.; Mosier, A. M.; Wayment-Steele, H. K.; Shine, R. S.; Park, A.; Webster, E. R.; Johnson, L. E.; Johal, M. S.; Benz, L. Surface and Stability Characterization of a Nanoporous ZIF-8 Thin Film. *J. Phys. Chem. C* **2014**, *118* (26), 14449–14456.

(9) Chizallet, C.; Lazare, S.; Bazer-Bachi, D.; Bonnier, F.; Lecocq, V.; Soyer, E.; Quoineaud, A. A.; Bats, N. Catalysis of Transesterification by a Nonfunctionalized Metal-Organic Framework: Acido-Basicity at the External Surface of ZIF-8 Probed by FTIR and Ab Initio Calculations. *J. Am. Chem. Soc.* **2010**, *132* (35), 12365–12377.

(10) Vandevondele, J.; Krack, M.; Mohamed, F.; Parrinello, M.; Chassaing, T.; Hutter, J. Quickstep: Fast and Accurate Density Functional Calculations Using a Mixed Gaussian and Plane Waves Approach. *Comput. Phys. Commun.* **2005**, *167* (2), 103–128.

(11) Perdew, J. P.; Burke, K.; Ernzerhof, M. Generalized Gradient Approximation Made Simple. *Phys. Rev. Lett.* **1996**, *77*, 3865–3868.

(12) Elstner, M.; Porezag, D.; Jungnickel, G.; Elsner, J.; Haugk, M.; Frauenheim, T.; Suhai, S.; Seifert, G. Self-Consistent-Charge Density-Functional Tight-Binding Method for Simulations of Complex Materials Properties. *Phys. Rev. B* **1998**, *58* (11), 7260–7268.

(13) Grimme, S.; Antony, J.; Ehrlich, S.; Krieg, H. A Consistent and Accurate Ab Initio Parametrization of Density Functional Dispersion Correction (DFT-D) for the 94 Elements H-Pu. *J. Chem. Phys.* **2010**, *132* (15), 154104.

(14) Bonakala, S.; Lalitha, A.; Eun Shin, J.; Moghadam, F.; Semino, R.; Bum Park, H.; Maurin, G.; Shin, J.

E.; Moghadam, F. Understanding of the Graphene Oxide / Metal-Organic Framework Interface at the Atomistic Scale. *ACS Appl. Mater. Interfaces* **2018**, *10*, 1–6.

(15) Mayo, S. L.; Olafson, B. D.; Goddard, W. A. DREIDING: A Generic Force Field for Molecular Simulations. *J. Phys. Chem.* **1990**, *94* (26), 8897–8909.

(16) A. K. Rappe, C. J. Casewit, K. S. Colwell, W. A. Goddard III, and W. M. S. UFF, a Full Periodic Table Force Field for Molecular Mechanics and Molecular Dynamics Simulations. *J. Am. Chem. Soc* **1992**, *114*, 10024–10035.

(17) Breneman, C. M.; Wiberg, K. B. Determining Atom-Centered Monopoles from Molecular Electrostatic Potentials. The Need for High Sampling Density in Formamide Conformational Analysis. *J. Comput. Chem.* **1990**, *11* (3), 361–373.

(18) Allen, M. P.; Tildesley, D. J. *Computer Simulation of Liquids*.

(19) Martyna, G. J.; Klein, M. L.; Tuckerman, M. Nosé-Hoover Chains: The Canonical Ensemble via Continuous Dynamics. *J. Chem. Phys.* **1992**, *97* (4), 2635–2643.

(20) Sharifi, T.; Gracia-Espino, E.; Reza Barzegar, H.; Jia, X.; Nitze, F.; Hu, G.; Nordblad, P.; Tai, C. W.; Wågberg, T. Formation of Nitrogen-Doped Graphene Nanoscrolls by Adsorption of Magnetic γ-Fe2O3 Nanoparticles. *Nat. Commun.* **2013**, *4*.

(21) Semino, R.; Durholt, J. P.; Schmid, R.; Marin, G. Multiscale Modeling of the HKUST-1/Polyvinyl Alcohol) Interface: From an Atomistic to a Coarse Graining Approach. *J. Phys. Chem. C* **2017**, *121* (39), 21491–21496.

(22) Benzaqui, M.; Semino, R.; Menguy, N.; Carn, F.; Kundu, T.; Guigner, J. M.; McKeown, N. B.; Msayib, K. J.; Carta, M.; Malpass-Evans, R.; Le Guillouzer, C.; Clet, G.; Ramsahye, N. A.; Serre, C.; Maurin, G.; Steunou, N. Toward an Understanding of the Microstructure and Interfacial Properties of PIMs/ZIF-8 Mixed Matrix Membranes. *ACS Appl. Mater. Interfaces* **2016**, *8* (40), 27311–27321.

(23) Pillai, R. S.; Jobic, H.; Koza, M.; Nouar, F. Diffusion of Carbon Dioxide and Nitrogen in the Small- Pore Titanium Bis (Phosphonate) Metal – Organic Framework MIL-91 (Ti): A Combination of Quasielastic Neutron Scattering Measurements and Molecular Dynamics Simulations. **2017**, *91*, 1–9.

(24) Llewellyn, P. L.; Garcia-Rates, M.; Gaberová, L.; Miller, S. R.; Devic, T.; Lavalley, J. C.; Bourrelly, S.; Bloch, E.; Filinchuk, Y.; Wright, P. A.; Serre, C.; Vimont, A.; Maurin, G. Structural Origin of Unusual CO2 Adsorption Behavior of a Small-Pore Aluminum Bisphosphonate MOF. *J. Phys. Chem. C* **2015**, *119* (8), 4208–4216.

(25) Frisch, M. J.; Trucks, G. W.; Schlegel, H. B.; Scuseria, G. E.; Robb, M. A.; Cheeseman, J. R.; Scalmani, G.; Barone, V.; Mennucci, B.; Petersson, G. A.; Nakatsuji, H.; Caricato, M.; Li, X.; Hratchian, H. P.; Izmaylov, A. F.; Bloino, J.; Zheng, G.; Sonnenberg, J. L.; Hada, M.; Ehara, M.; Toyota, K.; Fukuda, R.; Hasegawa, J.; Ishida, M.; Nakajima, T.; Honda, Y.; Kitao, O.; Nakai, H.; Vreven, T.; Montgomery, J. A.; Peralta, J. E.; Ogliaro, F.; Bearpark, M.; Heyd, J. J.; Brothers, E.; Kudin, K. N.; Staroverov, V. N.; Kobayashi, R.; Normand, J.; Raghavachari, K.; Rendell, A.; Burant, J. C.; Iyengar, S. S.; Tomasi, J.; Cossi, M.; Rega, N.; Millam, J. M.; Klene, M.; Knox, J. E.; Cross, J. B.; Bakken, V.; Adamo, C.; Jaramillo, J.; Gomperts, R.; Stratmann, R. E.; Yazyev, O.; Austin, A. J.; Cammi, R.; Pomelli, C.; Ochterski, J. W.; Martin, R. L.; Morokuma, K.; Zakrzewski, V. G.; Voth, G. A.; Salvador, P.; Dannenberg, J. J.; Dapprich, S.; Daniels, A. D.; Farkas; Foresman, J. B.; Ortiz, J. V; Cioslowski, J.; Fox, D. J. Gaussian 09, Revision B.01. *Gaussian 09, Revision B.01, Gaussian, Inc., Wallingford CT*. Wallingford CT **2009**.

Article 1

COMMUNICATION WILEY-VCH

Formation of Single Crystal Aluminum-based MOF Nanowire with Graphene Oxide Nanoscrolls as Structure-Directing Agents

Mégane Muschi,[a] Anusha Lalitha,[b] Saad Sene,[a] Damien Aureau,[c] Mathieu Fregnaux,[c] Imène Esteve[d] Lucie Rivier,[c] Olivier Beyssac,[d] Naseem Ramsahye,[b] Sabine Devautour-Vinot,[b] Clémence Sicard,[c] Nicolas Menguy,[d] Christian Serre,[a] Guillaume Maurin,[b] Nathalie Steunou.*[c] [a]*

Abstract: *Here we propose an innovative strategy to synthesize single-crystal nanowires (NWs) of the Al^{3+} dicarboxylate MIL-69(Al) MOF by using graphene oxide nanoscrolls as structure directing agents. MIL-69(Al) NWs with an average diameter of 70 ± 20 nm and lengths up to 2 μm were found to preferentially grow along the [001] crystallographic direction. Advanced characterization tools (electron diffraction, TEM, STEM-HAADF, SEM, XPS) and molecular modelling revealed the mechanism of formation of MIL-69(Al) NWs involving size-confinement and surface directing effects. The formation of MIL-69(Al) seeds and the self-scroll of GO sheets followed by the anisotropic growth of MIL-69(Al) crystals are mediated by specific GO sheets/MOF interactions. This study delivers an unprecedented approach to control the design of 1D MOF nanostructures and superstructures.*

MOFs have attracted a tremendous interest over the last decades in material science since this family of porous solids offers a unique opportunity to design a wide range of architectures with modulated porosities and chemical functionality.[1,2] These materials constructed through the assembly of metal ions and organic polydentate ligands present crystalline hybrid porous structures[3,4] of interest for a wide range of applications including gas storage/separation, catalysis, sensing, electronics, biomedicine etc.[1] To date, most of the works on MOFs have been devoted to the discovery of novel structures, properties testing and composites processing.[1-11]The control over the crystal size, morphology, and multi-scale porosity of MOFs as well as the shape of their crystal aggregates has been much less explored. Indeed, this was rarely achieved by using polymers, proteins, or metal oxides as additives.[12-16] In particular, low-symmetry nano-crystals (NCs), which exhibit high energy facets are of interest in the fields of catalysis, sensing and electronics.[17,18] However, only very few one-dimensional (1D) anisotropic MOF nanostructures has been discovered so far since MOF nanoparticles (NPs) are mostly obtained as polycrystalline powders or spherical NCs.[19-24] The rare existing 1D MOF architectures in the forms of nanowires (NW), nanotubes and nanorods were synthesized through a bottom-up solution route or hydrothermal process eventually templated by polymer or inorganic 1D nanostructures.[19-24] Note that the nucleation and growth processes of 1D MOFs are far to be understood similarly to a wide range of anisotropic oxides and metal nanostructures.[17,25,26,27] Furthermore, MOFs still present other shortcomings, which restrict their applications to a great extent. Above all, most MOFs are inherently electrically non-conductive and not robust against water/vapour or high temperature. To circumvent these drawbacks, MOF/graphene oxide (GO)-based materials[5-11] have attracted widespread attention in recent years since they can present an improved stability, enhanced electrical conductivity and processibility as a result of a synergistic effect of the two components. These composites have been explored in various applications including sensors, supercapacitors, batteries, gas storage, and catalysis.[5-11] However, the development of such MOF/GO composites suffer from a disordered spatial arrangement of GO sheets and MOF particles as well as a strong aggregation of MOFs NPs. Therefore, the engineering of MOF/GO composite with hierarchical architectures, such as core–shell structure and layer-by-layer, would be most desirable to further optimize the performance of such systems.

In this context herein, we report the synthesis of single-crystal Al^{3+} dicarboxylate MOF (i.e. MIL-69(Al) MIL, Material of Institut Lavoisier) NW by using graphene oxide. (GO) nanoscrolls as structure-directing agents. GO nanoscrolls are 1D carbon materials formed by rolling GO sheets from one side or from the corner into Archimedean-type spirals.[28] They present open structures at both ends and interlayer galleries that can be easily intercalated. Recently, the assembly of GO sheets with preformed oxide or metal NPs led to the formation of GO nanoscrolls decorated by NPs.[28,29,30,31] Inspired by these findings, we have exploited the potential rolling of GO to control the

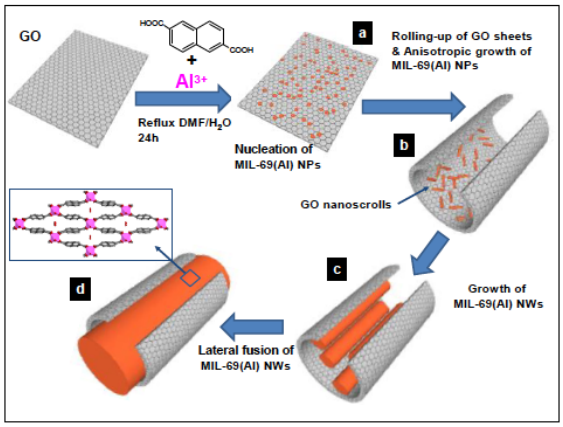

Scheme 1. Mechanistic scheme summarizing the main stages of the MIL-69(Al) NWs formation.

[a] Dr M. Muschi, Dr S. Sene, Dr C. Serre, Pr N. Steunou
Institut des Matériaux Poreux de Paris, UMR 8004 CNRS-ENS-ESPCI, PSL research university, Paris, France.
E-mail: nathalie.steunou@uvsq.fr
[b] A. Lalitha, Dr N. Ramsahye, Dr S. Devautour-Vinot, Pr G. Maurin
Institut Charles Gerhardt Montpellier, UMR 5253 CNRS, Université de Montpellier, Montpellier, France.
E-mail : Guillaume.Maurin@univ-montp2.fr
[c] Dr D. Aureau, Dr M. Fregnaux, Dr L. Rivier, Dr C. Sicard, Pr N. Steunou
Institut Lavoisier de Versailles, UMR CNRS 8180, Université de Versailles St Quentin en Yvelines, Université Paris Saclay, Versailles, France.
[d] Dr I. Esteve, Dr O. Beyssac, Pr N. Menguy
Sorbonne Université, UMR CNRS 7590, MNHN, IRD, Institut de Minéralogie, de Physique des Matériaux et de Cosmochimie, IMPMC, 75005 Paris, France.

Supporting information for this article is given via a link at the end of the document.

formation of single-crystal MOF NWs. The growth of these MOFs NWs were further scrutinized by combining multimodal *ex situ* advanced characterization techniques (electron diffraction,TEM, STEM-HAADF, SEM, XPS) and molecular modelling, thereby allowing us to propose a mechanism of formation as illustrated in scheme 1. To the best of our knowledge, this is the first study reporting the possible synthesis of single-crystal MOF NW directed by GO nanscrolls.

To that purpose, the microporous Al 2,6 naphtalene dicarboxylate (2,6 ndc) based MOF, denoted MIL-69(Al) was considered as a typical example.[32] This network which is structurally analogue to the terephtalate-based MIL-53, is built up from the connection of infinite chains of corner- sharing octahedral $AlO_4(OH)_2$ units with 2,6 ndc ligand. Its hydrated form presents one-dimensional narrow rhombic channels with a window size around 2.7 x 13.6 Å (see scheme 1).[33,34]

The synthesis of MIL-69(Al) NWs was conducted *in-situ* with GO as a co-reactant with a mixture of Al^{3+} salts, NaOH and 2,6 ndc in DMF/H_2O solution heated under reflux. Note that the same reactants without GO led to MIL-69(Al) NPs (see SI for details).[35] TEM images reveal that the pure MIL-69(Al) NPs are polydisperse in size and morphology with diameters ranging from 20 to 90 nm (Figures 1(a) and S1). Varying the GO content and the heating time led to different nanostructured composites. These materials are denoted MIL69/GO-X-Y with X and Y corresponding to the initial Al/GO weight ratio (calculated from the amount of $Al(NO_3)_3.9H_2O$ precursor) and the reflux time respectively. The powder X-ray diffraction (PXRD) pattern of MIL-69/GO-X-24 composites displays the characteristic Bragg peaks of MIL-69(Al) in its narrow pore form, however they are much sharper and intense for X=4.5 & 9 than for X= 18 and MIL-69(Al) NPs (see Figure S2). In comparison to micrometer scale MIL-69(Al) particles, (200) reflections are much more intense in the PXRD pattern of MIL-69/GO-X-24, suggesting a preferential orientation of such crystals with a possible shape anisotropy. MIL-69(Al) NWs were typically obtained for X= 4.5 and after a reflux of 24 hours. As shown by N_2 porosimetry (Figure S3), MIL-69/GO-4.5-24 presents a hierarchical porous structure that consists in an ordered array of micropores inherent of the MOF framework and mesoporous inter-particle voids. TGA, FT-IR, Raman and XPS spectroscopies (see SI for details), show that this composite results from the assembling of GO and MIL-69(Al) with a GO content of 30 wt% (Figures S4-S8). Both TEM Bright field (TEM-BF) and Scanning TEM using the High Angle Annular Dark Field mode (STEM-HAADF) images evidence that MIL-69/GO-4.5-24 is composed of inter-grown MIL-69(Al) NWs and GO sheets (Figure 1b-e). MIL-69(Al) NWs present an average diameter of 70 ± 20 nm, lengths up to 2 µm and aspect ratio up to 20, as evaluated from 50 NWs randomly selected from TEM images (Figures S9-S11). Note that the morphology of MIL-69(Al) NWs is completely different than nano- or micrometer sized MIL-69(Al) particles (see Figure S1). Selected area electron diffraction (SAED) analyses were performed at low voltage (60 kV) in order to reduce the irradiation damage on a series of isolated NWs, showing that each NW corresponds to a single crystal of MIL-69(Al) (Figures 1f, S9-S10). From the SAED indexation, it can be inferred that NW grows along the [001] direction which is parallel to the chain axis of the corner-sharing Al^{3+} octahedra in the structure of MIL-69(Al).[32]

MIL-69/GO composites were also prepared with a higher Al content. MIL-69/GO-9-24 consists of bundles of MIL-69(Al) 1D tubular nanostructures interwoven with GO sheets as shown by STEM-HAADF (Figures 2 and S12). TEM and SAED experiments evidence analogous single crystal NWs than those of MIL-69/GO-4.5-24 with a [001] growth direction. Remarkably, STEM-HAADF and SEM images show that MIL-69/GO-9-24 contains a high amount of GO nanoscrolls with a diameter ranging between 70 and 100 nm (Figures 2 and S12). Note that the diameter of GO nanoscrolls is close to that of MIL-69(Al) NW suggesting a templating effect of GO. Their archimedean-type nanoscrolls morphology is reminiscent to that previously reported for maghemite/graphene composites.[28] Upon increasing X to 18, both TEM and STEM-HAADF images reveal the co-existence of GO sheets and bundles of 1D GO nanoscrolls. (Figure S13) with only MIL-69(Al) as NPs. This observation emphasizes that Al/GO content needs to be critically controlled to ensure the formation of MIL-69(Al) NWs.

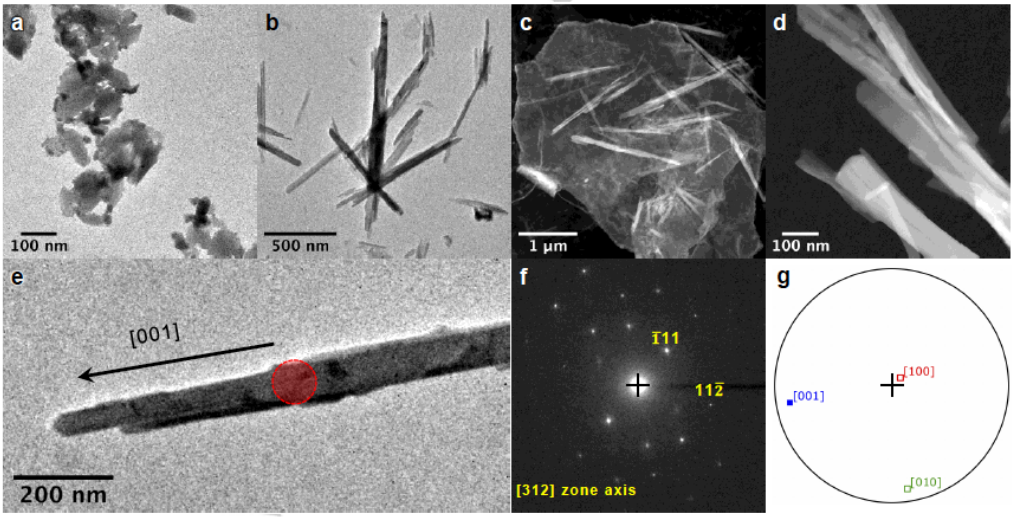

Figure 1. (a) TEM-BF image of MIL-69 NPs; (b, e) TEM-BF, (c,d) STEM-HAADF images of MIL-69/GO-4.5-24 (f) SAED of the area highlighted by the red circle in (e).The SAED indexation is given with respect to the MIL-69(Al) structure.[32] The stereographic projection (g) - related to the crystallographic orientation deduced from (f) – indicates unambiguously that the crystal growth proceeds along the [001] direction (see SI for details).

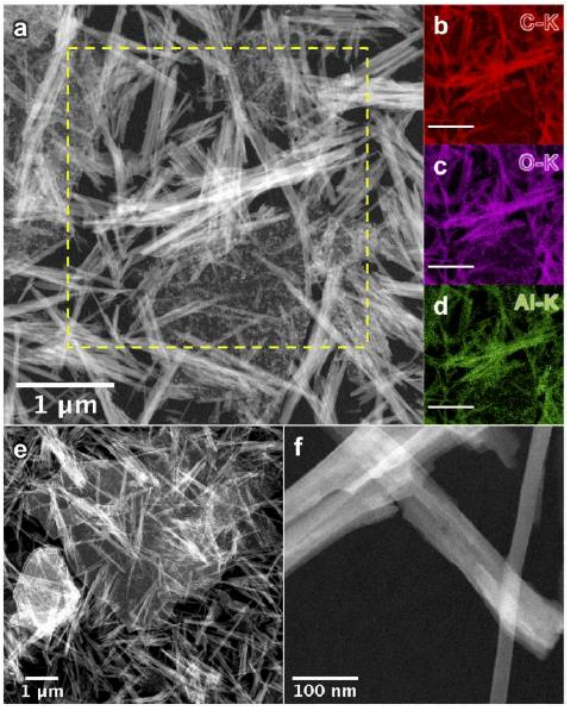

Figure 2. (a) STEM-HAADF, (b-d) STEM-XEDS elemental map for the rectangular yellow area indicated in (a), (e,f) SEM of MIL-69/GO-9-24.

A series of samples was collected at different stages of the reflux and further characterized by TEM, STEM-HAADF and PXRD (Figure 3 & Figures S14-S15) in order to follow the GO-assisted formation of MIL-69(Al) NWs. At this stage, MIL-69/GO-9 was considered as a model system to emphasize the interplay between the formation of GO nanoscrolls and of MIL-69(Al) NWs. After a reflux of 2 hours, the sample consists of individual GO sheets and aggregates of a few 100 nm in size (Figures 3 and S14). These aggregates result from the assembly of GO sheets and MIL-69(Al) nanoparticles as shown by PXRD and FT-IR (Figure S15). The progressive crystallization and growth of MIL-69(Al) NWs starts to be observed after a reflux of 4 hours. For a reflux of 12 hours, bundles of almost parallel GO nanoscrolls and MIL-69(Al) NWs emerge from the aggregates (Figures 3e and S14 d). This suggests that these aggregates act as anchors for the initial formation of MIL-69(Al) seeds, followed by their further outward growth, gradually forming the 1D GO nanoscrolls and MIL-69(Al) NWs.

An atomistic model of the interface formed between the GO sheet and the MIL-69(Al) surface was constructed and further analyzed by applying our recently developed computational strategy.[36,37] A GO model integrating both basal functions, i.e., epoxy and hydroxyl groups and edged carboxylic acid groups, was brought into contact with two distinct 3D MIL-69(Al) slab models that represent its crystallographic (010) and (001) surfaces and the resulting composites were geometry optimized by Molecular Dynamics (MD) simulations (see SI for details). The plot of the normalized atomic density along the z axis for the optimized MIL-69(010)/GO (Figure 4a) and MIL-69(001)/GO

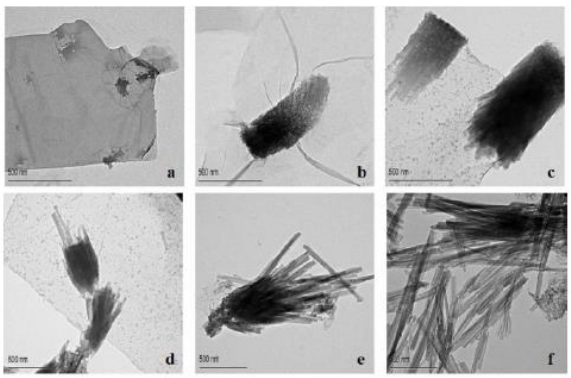

Figure 3. TEM images of MIL-69/GO-9-Y prepared with different duration Y of the reflux namely a) 1 h b) 2 h c) 4 h d) 8 h e) 12 h f) 24 h.

models (Figure S21a) respectively emphasizes the formation of an interfacial zone denoted A with a z-length of 4.5 Å where the GO terminations penetrate the pore pocket of the MIL-69(Al) surfaces. This observation confirms the good affinity observed experimentally between the two components. The radial distribution functions (RDFs) plotted for diverse MOF/GO pairs evidenced (Figure 4b and Figure S23a) that the MOF/GO interactions imply the OH groups present along the chain of MIL-69(Al). The most prominent interaction between the edged carboxylic acid functions and the OH groups of MIL-69(Al) (Figure 4c) leads to a significant twisting of the GO-layer in direct contact with the MOF as also suggested by the analysis of the dihedral angle distribution plotted for GO (Figure S22). Such predicted high degree of distortion for the first GO layers is expected to act as a driving force for the scrolling of GO evidenced experimentally. Interestingly, the intensity of the RDF peaks for all MOF/GO pairs is four times higher for MIL-69(010)/GO (Figure 4b) than for MIL-69(001)/GO (Figure S23a). This reveals that GO more strongly interacts with MIL-69(010) than MIL-69(001). We further disclosed that GO arranges at the MIL-69(Al) (010) surface in such a way to establish π--π like-stacking interactions where the naphthalene linker lies parallel to the aromatic ring of GO (Figure 4d). Besides reinforcing the affinity between the two components, such π-π like-stacking interactions may limit the relative crystal growth of the MIL-69(010) surface. This prediction is fully consistent with the experimental observation of an anisotropic growth of MIL-69(Al) NW along the [001] direction. The key role of the π--π stacking interactions through the naphthalene ring of MIL-69(Al) in the formation of NWs is also supported experimentally with the absence of NWs when we considered the *in situ* formation of the isostructural MIL-53(Al)-NH_2 in the presence of GO (see Figures S24 for more details).

The combination of *ex situ* experiments and molecular modelling not only revealed the GO-assisted formation of MIL-69(Al) NWs but also grasped a series of evidences that led us to propose the mechanism of formation summarized in Scheme 1. This mechanism involves a mutual recognition between GO and MIL-69(Al) :GO directs the formation of the MOF while conversely, the MOF surface may drive the structuring of GO. The first step implies a coordination of Al^{3+} cations to both the basal plane hydroxyl groups and edged carboxylate functions of GO which is

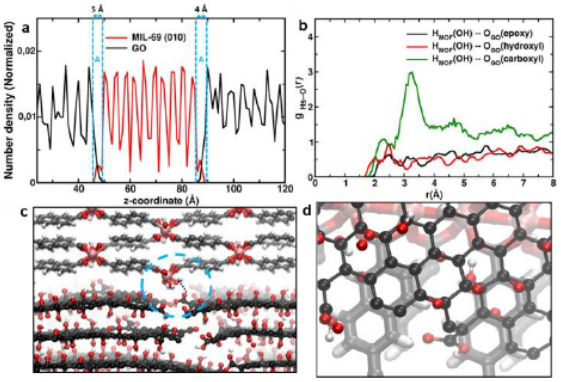

Figure 4. MIL-69(Al)(010)/GO model a) Representation of the normalized atomic density showing the interfacial region denoted A. (b) Radial Distribution Functions calculated between H_{OH} of MIL-69(Al) and the different O atoms of the functional groups of GO (c) Illustrative snapshot showing the main interactions between the edge carboxylic acid groups of GO and H_{OH} of MIL-69(Al). (d) Snapshot showing preferential π—π like interactions at the MIL-69(Al)(010)/GO interface. Color schemes are GO layers: C-black; O-red, H-white; MIL-69(010): C-gray, Al-pink, O-red and H-white.

favoured by the attractive electrostatic interactions between the negatively charged GO sheets (i.e., negative zeta potential of GO in aqueous solution) and Al^{3+} cations. This most probably initiates the assembly of GO sheets and the nucleation of MIL-69(Al) NPs (Scheme 1a), as previously mentioned for the MOF-253/GO composite.[38] Indeed for the three MIL-69/GO-X-24 composites, the surface of GO sheets is coated by MIL-69(Al) NPs with a diameter up to 50 nm as revealed by combining STEM-HAADF and STEM-XEDS elemental mapping (Figures 2a and S12). Moreover, MIL-69(Al) nanorods up to 100 nm in length were also observed at the surface of GO for X=4.5 (Figure S10d). Molecular modelling supports an anisotropic growth of MIL-69(Al) nanostructures along the [001] direction (Scheme1a). The following step is the rolling up of GO sheets into nanoscrolls (Scheme 1b) that is favoured by relative strong interactions between GO sheets and MIL-69(Al) surfaces. In particular, MIL-69(Al) NPs located at the edges of the bended part of GO sheets may be attracted by the inner part of GO. Moreover, the spontaneous scrolling of GO sheets can occur in the presence of DMF due to the inhomogeneous distribution of hydrophilic groups (hydroxy, epoxide and carboxylic acid) of GO and surface tension, as previously shown.[39] Finally, the growth of MIL-69(Al) NWs most probably occurs within a confined space, namely the inner part of the GO nanoscrolls (Scheme 1c) based on the electrical data recorded on the composites (see Figure S25). Indeed, despite the introduction of insulating MIL-69(Al), the semi-conducting behavior of GO is maintained for MIL69/GO-X-24. In contrast, an insulating behaviour was observed by mixing preformed MIL-69(Al) NPs with GO. These results show that the homogeneous distribution of the MOF inside the GO nanoscrolls in MIL69/GO-X-24 does not disrupt the carrier traveling through the extended conjugated network in the GO sheets and sheet-to-sheet junctions. Since the internal surface of GO nanoscrolls is decorated by numerous MIL-69(Al) nanorods and NPs, their further growth may proceed from the GO surface inward, gradually forming primary smaller aligned NWs (scheme 1c) whose lateral aggregation or crystallite fusion via Ostwald ripening can lead to one single crystalline NW (Scheme 1d) as previously reported for V_2O_5 nanobelts.[18,40] This last crystallization step could be explained by the spatial proximity of the primary NWs. Their constrained growth may proceed through coordination reactions with the MOF precursors or grain boundary consumption at the interfaces as previously reported for MOF-74-II tubular superstructures.[41]

In summary, GO nanoscrolls were demonstrated to act as structure-directing agents to form 1D MOF NWs. The interplay between multimodal characterization techniques and molecular modelling unravels their mechanism of formation. The self-scrolling of GO sheets and the subsequent anisotropic growth of MIL-69(Al) NWs in the inner cavity of GO nanoscrolls are driven by the covalent bonding between MIL-69(Al) NPs and the hydroxyl and carboxylic acid functions of GO that restrict the crystal growth on certain facets. This leads to the formation of MOF/GO composites that present a core-shell microstructure composed of highly dispersed MIL-69(Al) NWs. Considering the chemical tunability of MOFs and the possible functionalization of GO as well as the potential enhancement of their electron conductivity, this strategy opens up a new avenue for fabricating hierarchical and nanostructured MOF-GO composites that might be optimal systems for different applications including separation, energy storage (batteries and supercapacitors) and sensing.[42]

Acknowledgements

The authors would like to acknowledge the European Community Horizon 2020 Program (H2020/2014-2020) for funding the research presented in this article under Grant Agreement No. 727619 (project Gramofon). The authors would like to acknowledge B. Alonso, A. Ortega from Graphenea S. A. (www.graphenea.com) for providing the graphene oxide sample. N. Heymans and G. De Weireld (University of Mons) are acknowledged for useful discussions.

Keywords: metal-organic frameworks • graphene oxide • nanowire • self-assembly • template

[1] P. K. Bharadwaj, P. Feng, S. Kaskel, Q. Xu, *Chem. Asian J.* **2019**, *14*,3450–3451.
[2] D. Zhao, P. K. Thallapally, C. Petit, J. Gascon, *ACS Sustainable Chem. Eng.* **2019**, *7*, 7997-7998.
[3] M. O'Keeffe, O. M. Yaghi, *Chem. Rev.* **2012**, *112*, 675–702.
[4] J. Cepeda, S. Perez-Yanez, G. Beobide, O. Castillo, E. Goikolea, F. Aguesse, L. Garrido, A. Luque, P.A. Wright, P. A. *Chem. Mater.* **2016**, *28*, 2519–2528.
[5] A. Huang, Q. Liu, N. Wang, Y. Zhu, J. Caro, *J. Am. Chem. Soc.* **2014**, *136*, 42, 14686-14689.
[6] Y. Hu, J. Wei, Y. Liang, H. Zhang, X. Zhang, W. Shen, H. Wang, *Angew. Chem. Int. Ed.* **2016**, *55*, 2048-2052.
[7] D. Kim, D. Woo Kim, W. G. Hong, A. Coskun, *J. Mater. Chem. A* **2016**, *4*, 7710-7717.
[8] J. Wang, Y. Wang, Y. Zhang, A. Uliana, J. Zhu, J. Liu, B. Van der Bruggen, *ACS Appl. Mater. Interfaces* **2016**, *8*, 25508-25519.
[9] J. Wei, Y. Hu, Y. Liang, B. Kong, Z. Zheng, J. Zhang, S. Ping Jiang, Y. Zhao, H. Wang, *J. Mater. Chem. A* **2017**, *5*, 10182-10189.
[10] M. Muschi, C. Serre, *Coord. Chem. Rev.* **2019**, 387, 262-272.
[11] Y. Hu, Y. Wu, C. Devendran, J. Wei, Y. Liang, M. Matsukata, W. Shen, A. Neild, H. Huang, H. Wang, *J. Mater. Chem. A* **2017**, *5*, 16255-16262.
[12] M. Pang, A. J. Cairns, Y. Liu, Y. Belmabkhout, H. C. Zeng, M. Eddaoudi, *J. Am. Chem. Soc.* **2013**, *135*, 10234–10237.
[13] J. Huo, M. Marcello, A. Garai, D. Bradshaw, *Adv. Mater.* **2013**, *25*, 2717–2722.

[14] D. Bradshaw, S. El-Hankari, L. Lupica-Spagnolo, *Chem. Soc. Rev.* **2014**, *43*, 5431-5443.
[15] J. Hwang, T. Heil, M. Antonietti, B. V. K. J. Schmidt, *J. Am. Chem. Soc.* **2018**, *140*, 2947-2956.
[16]S. Jr. Ayala, K. C. Bentz, S. M. Cohen, *Chem. Sci.* **2019**, *10*, 1746–1753.
[17] L. Pan, P. Gao, E. Tervoort, A. M. Tartakovsky, M. Niederberger, *J. Mater. Chem. A* **2018**, *6*, 18551–18560.
[18] N. Steunou, J. Livage, *CrystEngComm.* **2015**, *17*, 6780–6795.
[19] M. Jahan, Q. Ban, J. –X.Yang, K. P. Loh, J. *Am. Chem. Soc.* **2010**, *132*, 14487-14495.
[20] X. Dao, Y. Ni, *Dalton Trans.* **2017**, *46*, 5373–5383.
[21] R. C. Arbulu, Y.-B. Jiang, E. J. Peterson, Y. Qin, *Angew. Chem. Int. Ed.* **2018**, *57*, 5813 –5817.
[22] L. Zou, C.-C. Hou, Z. Liu, H. Pang, Q. Xu, *J. Am. Chem. Soc.* **2018**, *140*, 15393–15401.
[23] T. He, S. Chen, B. Ni, Y. Gong, Z. Wu, L. Song, L. Gu, W. Hu, X. Wang, *Angew. Chem. Int. Ed.* **2018**, *57*, 3493 –3498.
[24] J. Shi, J. Zhang, D. Tan, X. Cheng, X. Tan, B. Zhang, B. Han, L. Liu, F. Zhang, M. Liu, J. Xiang, *ChemCatChem* **2019**, *11*, 2058-2062.
[25] G. T. Chandrappa, N. Steunou, S. Cassaignon, C. Bauvais, J. Livage, J. *Catal. Today* **2003**, *78*, 85–89.
[26] M. Jaber, F. Ribot, L. Binet, V. Briois, S. Cassaignon, K. J. Rao, J. Livage, N. Steunou, *J. Phys. Chem. C* **2012**, *116*, 25126-25136.
[27] R. Deshmukh, M. Niederberger, *Chem. Eur.J.* **2017**, *23*, 8542 -8570.
[28] T. Sharifi, E. Gracia-Espino, H. Reza Barzegar, X. Jia, F. Nitze, G. Hu, P. Nordblad, C.-W. Tai, T. Wågberg, *Nature Comm.* **2013**, *4*, 2319.
[29] H. Pang, Q. Lu, F. Gao, *Chem. Commun.* **2011**, *47*, 11772-11774.
[30] X. Wang, D.-P. Yang, G. Huang, P. Huang, G. Shen, S. Guo, Y. Mei, D. Cui. J. *Mater. Chem.* **2012**, *22*, 17441–17444.
[31] M. Yan, F. Wang, C. Han, X. Ma, X. Xu, Q. An, L. Xu, C. Niu, Y. Zhao, X. Tian, P. Hu, H. Wu, L. Mai, *J. Am. Chem. Soc.* **2013**, *135*, 18176–18182.
[32] T. Loiseau, C. Mellot-Draznieks, H. Muguerra, G. Férey, M. Haouas, F. Taulelle, *C. R. Chim.* **2005**, *8*, 765–772.
[33] I. Senkovska, F. Hoffmann, M. Fröba, J. Getzschmann, W. Böhlmann, S. Kaskel, *Micropor. Mesopor. Mater.* **2009**, *122*, 93–98.
[34] P. L. Feng, K. Leong, M. D. Allendorf, *Dalton Trans.* **2012**, *41*, 8869–8877.
[35] A. Sabetghadam, X. Liu, M. Benzaqui, E. Gkaniatsou, A. Orsi, M. M. Lozinska, C. Sicard, T. Johnson, N. Steunou, P. A. Wright, C. Serre, J. Gascon, F. Kapteijn, *Chem. Eur. J.* **2018**, *24*, 7949-7956.
[36] R. Semino, N. A. Ramsahye, A. Ghoufi, G. Maurin *ACS Appl. Mater. Interfaces* **2016**, *8*, 809-819.
[37] S. Bonakala, A. Lalitha, J. E. Shin, F. Moghadam, R. Semino, H. B. Park, G. Maurin, *ACS Appl. Mater. Interfaces* **2018**, *10*, 33619–33629.
[38] X. Qiu, X. Wang, Y. Li, *Chem. Commun.* **2015**, *51*, 3874-3877.
[39] B. Tang, Z. Xiong, X. Yun, X. Wang, *Nanoscale* **2018**, *10*, 4113-4122.
[40] M. Li, F. Kong, H. Wang, G. Li, *CrystEngComm.* **2011**, *13*, 5317-5320.
[41] L. Feng, J. –L. Li, G. S. Day, X. –L. Lv, H. –C. Zhou, *Chem*, **2019**, *5*, 1-10.
[42] a) Y Zheng, S. Zheng, H. Xue, H. Pang, *Adv. Funct. Mater.* **2018**, *28*, 1804950; b) H. Wu, W. Zhang,S. Kandambeth, O. Shekhah, M. Eddaoudi, H. N. Alshareef, *Adv. Energy Mater.* **2019**, *9*, 1900482.

CHAPTER 5 – IMPACT OF GRAFTING AMINE TO GO ON THE ZIF-8/GO INTERFACE AND ITS GAS ADSORPTION PROPERTIES

5.1 Introduction

To utilize the full potential of the MOF/GO composites, a chemical modification of GO can strengthen the MOF/GO interfacial interactions leading to an enhancement of the mechanical properties of the resulting composites[1] while it can also lead to an enhancement of the interactions with guest molecules[2,3]. Amine containing functional groups when attached to the GO have proven to interact with other functional groups of the MOF and enhance its micro-porosity[3–5] which is of interest especially in CO_2 adsorption[2,5–7] and catalysis[8]. In this chapter, I have applied the computational strategy validated in Chapter 3 to construct microscopic models of 4-aminopyridine functionalized GO, its interface with ZIF-8 to emphasize the role of the functionalization on the MOF/GO interface. 4-aminopyridine functionalized GO[9,10] has the presence of both amine function and aromatic ring which can synergistically favour high affinity with the incorporated MOF. The construction of the microscopic model for 4-aminopyridine functionalized GO (termed as FGO) was performed in strong interplay with the experimental data collected by our collaborators using X-ray photoelectron spectroscopy and Infrared spectroscopy. The resulting MOF/FGO composite is further carefully characterized in terms of nature and strength of MOF/GO interactions, surface coverage and GO conformation at the MOF surface. This scenario is compared with the result reported in chapter III on the pristine GO/ZIF-8 interface model. The predictions were further validated experimentally by Transmission Electron microscopy images and Mechanical testing on the corresponding composite.

The last part of the chapter is dedicated to study the adsorption of various gases including CO_2, CH_4 and N_2 in both the so-built ZIF-8/pristine-GO and ZIF-8/FGO microscopic models for the interfaces using Grand Canonical Monte Carlo simulations.

5.2 Construction of FGO

5.2.1. Synthesis and characterization of FGO

- **X-ray photoelectron Spectral (XPS) Analysis**

XPS with ESC system (XPS-theta probe, Thermo Fisher Scientific Co., USA) equipped with a monochromatic Al Kα source (C correction: 284.5 eV) was used for characterizing the synthesized 4-aminopyridine GO sample. For comparison, the pristine GO sample was also characterized. Through this characterization, the nature of the chemical bonding, the atomic ratios (C/O and C/N) and atomic compositions were deduced. The corresponding results are summarized in Figure 5.1.

The C1s XPS spectra for 4AmPy-GO, contains most of the characteristic peaks discussed for the pristine GO (see chapter 3) except that assigned to the carboxylic functions. This clearly indicates that the amine groups of 4AmPy are combined with the edge groups of the GO sheets. Further, the C/O ratio was found to be slightly higher than that for the pristine GO, i.e. 3.3 vs 2.5 (pristine), because of a partial reduction of the GO during the preparation of 4AmPy-GO. In addition, the N percentage was approximately 10% after functionalization leading to a C/N ratio of 6.2.

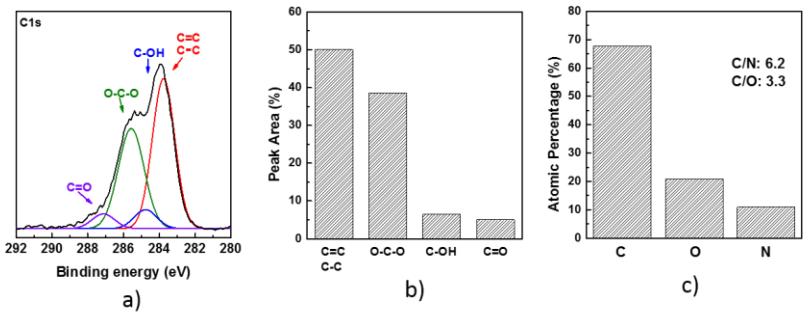

Figure 5.1 FGO with a) XPS spectra b) Peak areas of each oxygen functional groups deduced from the XPS spectral analysis and c) Atomic percentages of C, O, and N

- **Powder X-ray diffraction (PXRD)**

The PXRD pattern for 4AmPy-GO was recorded on a diffractometer (D8 Advance, Bruker, Germany) fitted with a monochromatic Al Kα source (λ =1.5406 Å) at 40 kV and 40 mA (1.6 Kw) in the range of 5-30°, and the scan rate of 1 degree/min to obtained PXRD patters (Figure 5.2). The interlayer distance for FGO was estimated through the main characteristic peak position. The interlayer spacing of 4AmPy-GO was found to be about 13.1 Å while for the pristine GO was 7.7 Å[11]. In Figure 5.2, the bump that appeared between 19-23° for 4AmPy-GO,

are associated with the reduction of the graphene oxide resulting from the activation process with the use of $SOCl_2$.

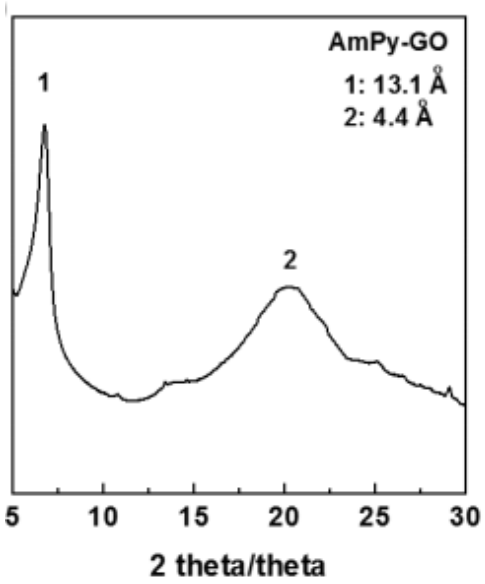

Figure 5.2 PXRD patterns of 4AmPy-GO nanoparticles. Inset numbers indicate the d-spacing values

- **Fourier Transform Infrared (FTIR) Spectroscopy**

The FTIR spectra for the synthesized 4AmPy-GO and 4-AmPy were collected using a Nicolet 6700 (Thermo electron scientific instruments, U.S) in the range from 4000 to 600 cm^{-1} and the corresponding data is reported in Figure 5.3. The distinct characteristic peaks observed for 4AmPy-GO is at 1400 and 1120 cm^{-1} associated with the C-N and C=N stretching modes of the pyridine group respectively[12] while the distinct peaks observed for the pristine GO is at 3450, 1710, 1230, and 1065 cm^{-1} are attributed to the stretching vibration of the CO-H, C=OOH, C-O-C, and C-OH groups, respectively[13]. Two additional peaks appear at 3130, and 1645 cm^{-1} characteristics of the N-H stretching mode respectively[10,14] in 4AmPy. The presence of these latter features indicates a successful chemical bonding of 4AmPy on the surface of the GO nanosheet.

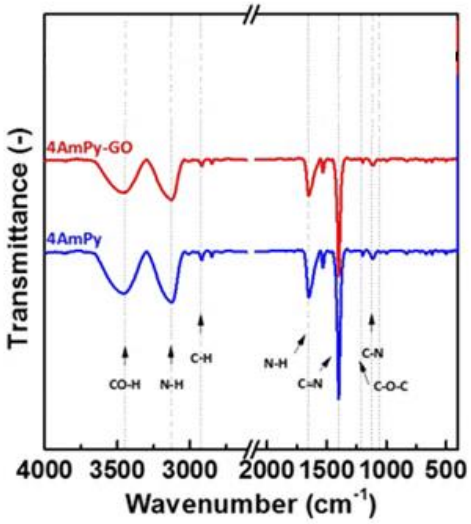

Figure 5.3 FT-IR spectra of 4AmPy-GO and 4AmPy.

5.2.2. Construction of FGO model

The initial model of periodic GO-OH[15] (discussed in detail in Chapter 3) was used for the construction of 4AmPy-GO. It already had epoxy (−O−), and hydroxyl (−OH) functional groups attached its basal plane. 4AmPy reacts with both edge and basal plane motifs as shown in Figure 5.4.

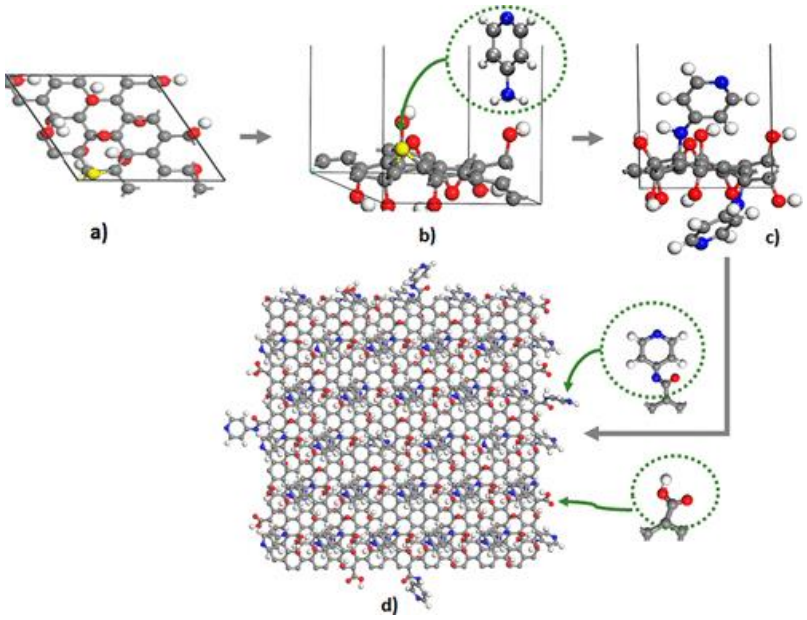

Figure 5.4 Schematic illustration of the stepwise construction of the atomistic model for 4AmPy-GO: a) initial periodic GO–OH model (top view, marked epoxy group in yellow), b) 4AmPy (encircled in green) and reactive epoxy motifs (highlighted in yellow), c) resulting 4AmPy grafting, and d) final nonperiodic model labelled as 4AmPy-GO, where $-CO_2H$ and 4AmPy are incorporated on the edges

- The first step was to attach 4AmPy to the epoxy motifs of the basal plane. The -NH_2 function of 4AmPy reacts with epoxy motifs on both sides of the layer breaking the C-O-C bridge leading to the formation of a C-OH group and a pyridine-NH complex, releasing H^+ following the proposed mechanism[16], as illustrated in Figure 5.4c. The C/N and C/O atomic ratios are 6 and 3 respectively as experimentally evidenced. This periodic model was then optimized at the DFT-level using QUICKSTEP module in CP2K package[17] to fully relax of both atomic position and cell dimension. The Gaussian and plane waves (GPW) dual basis set method was applied. The Grimme developed PBE functional[18] with D3[19] dispersion correction developed was used. A double zeta basis set[20] with pseudopotentials of Goedecker-Teter-Hutter (GTH)[20] describing core electrons were used for all elements. Charge density in plane waves were expanded up to an energy cut off 240 Ry. This DFT-optimized model and its resulting cell parameters are reported in Figure 5.5a and Table 5.1.

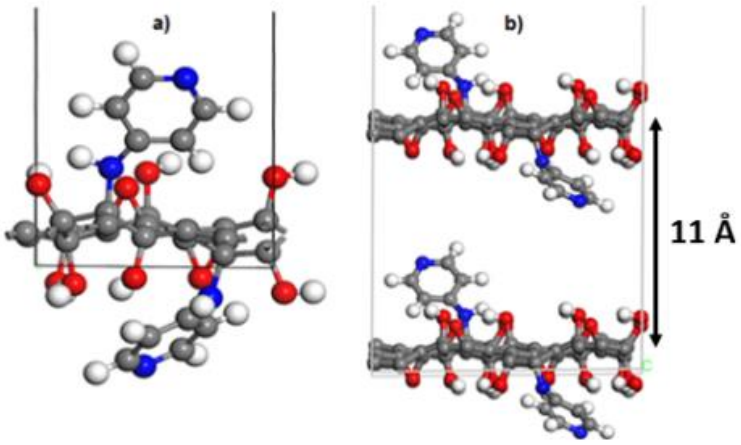

Figure 5.5 a) DFT optimized 4AmPy-GO model with cell parameters listed in Table 5.1. b) DFT optimized 2-layer models of (8 Å x 9 Å x 60 Å) dimension leading to an interlayer distance of 11 Å; Colour scheme: C, grey; N, blue; O, red; H, white

Table 5.1 DFT-optimized cell dimensions of the 4AmPy-GO model

a (Å)	b (Å)	c (Å)	α (°)	β (°)	γ (°)
8.475	8.547	30.699	91.776	90.535	60.169

- After the successful incorporation of 4AmPy to the basal function. The 2nd step consisted of creating the refined model (non-periodic) by incorporating -CO_2H functions

at the edges of the GO layer, which will subsequently react with 4AmPy (see Figure 5.4d) as verified by the experimental XPS analysis (detailed in Figure 5.1). Here the -NH_2 function of 4AmPy reacts with –CO_2H motifs releasing H_2O and subsequently forming of amide complexes[16]. The model was labelled as 4AmPy-GO which corresponds to the C/N and C/O ratios of ~6.26 and ~3.7 respectively in excellent agreement with the experimental findings. The dimension of the model was 40 Å x 40 Å in x and y directions. The model contains 1685 atoms. In terms of the atomic compositions, it corresponds to C, O and N as 70%, 19% and 11% respectively. These values matched well the experimentally obtained data of 66 %, 20 % and 10 % respectively.

The final model of 4AmPy-GO was fully optimized using MD simulations at the force field level. NVT ensemble was used at 298 K using the Hoover thermostat with a relaxation time of 0.5 ps. Velocity Verlet algorithm was used to compute the equation of motion with a time step of 1 fs. The force field parameters were taken from OPLS-2005[21] to describe the bonded and non-bonded potentials. The non-bonded interactions correspond to the sum of a 12-6 Lennard-Jones (LJ) contribution and a Coulombic contribution. The Lorentz-Berthelot mixing rules were used to compute crossed LJ parameters. The van der Waals interactions were truncated at 10 Å while the long-range electrostatic interactions were calculated using the Ewald summation method[22]. The atomic partial charges of the attached 4AmPy motifs were calculated through electrostatic potential scheme using CHELPG[23] approach applied to representative fragments with PBE functional 6-311g(d,p) basis set implemented in Gaussian package[24]. The clusters of 4AmPy used to calculate the charges are shown in Figure 5.6 while the charges of other functional groups were kept the same as in the initial GO-CO_2H model[15]. The full set of charges are listed in Table 3.4 with atom labels in Figure 5.7.

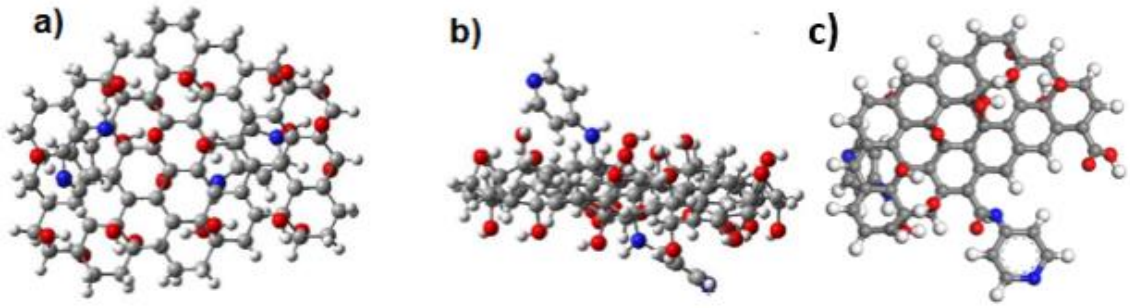

Figure 5.6 Clusters used for charge calculations of 4AmPy on GO a) basal structure (Top view), b) basal structure (Side view), and c) edge structure

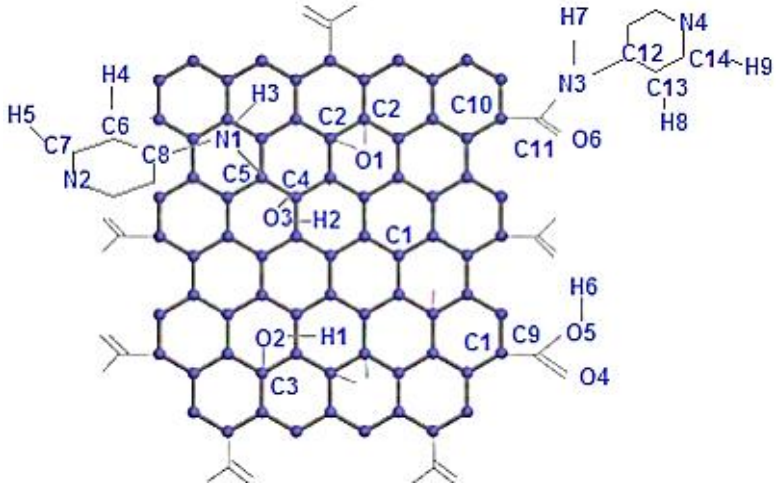

Figure 5.7 Labels of the atoms present in the 4AmPy-GO model

Table 5.2 The atom types, LJ parameters (σ,ε) with their atomic partial charges(q) of 4AmPy-GO model

Atom	Q	ε (kcal/mol)	σ (Å)
C1	0.088	0.070	3.550
C2	-0.5004	0.066	3.500
C3	0.2465	0.070	3.550
C4	0.2270	0.070	3.550
C5	0.9920	0.070	3.550
C6	-0.6430	0.070	3.905
C7	0.4298	0.070	3.905
C8	0.8405	0.070	3.905
C9	0.7370	0.1094	3.400
H1	0.3870	0.000	0.000
H2	0.4345	0.000	0.000
H3	0.3800	0.030	2.420
H4	0.1863	0.030	2.662
H5	0.0360	0.030	2.662
H6	0.3730	0.000	0.000
N1	-1.31225	0.170	3.575
N2	-1.0064	0.170	3.575
O1	-0.3070	0.140	2.900
O2	-0.5500	0.170	3.070
O3	-0.7010	0.170	3.120
O4	-0.5010	0.2100	2.960
O5	-0.5380	0.1700	3.000
C10	-0.4690	0.070	3.550
C11	0.8490	0.105	3.750
C12	0.8050	0.070	3.550

C13	- -0.6620	0.070	3.550
C14	0.4510	0.070	3.550
H7	0.3520	0.030	2.420
H8	0.2295	0.030	2.420
H9	0.0295	0.030	2.420
N3	-0.7960	0.170	3.250
N4	-0.6290	0.170	3.250
O6	-0.500	0.210	2.960

An illustration of the force field optimized 4AmPy-GO model is provided in Figure 5.8. The resulting interlayer distance of 10 Å is within the same range of value that was obtained for DFT-optimized model (11 Å) (see Figure 5.5b) also consistent with the experimental value obtained from the PXRD analysis (~13 Å). The slight deviation in the interlayer distance between experimental and simulated values can be attributed to the functional group distribution in the modelled layer and disordered partition in the real layer. Through these observations, selected force field parameters and charges which is used to describe the 4AmPy-GO atomistic model were validated.

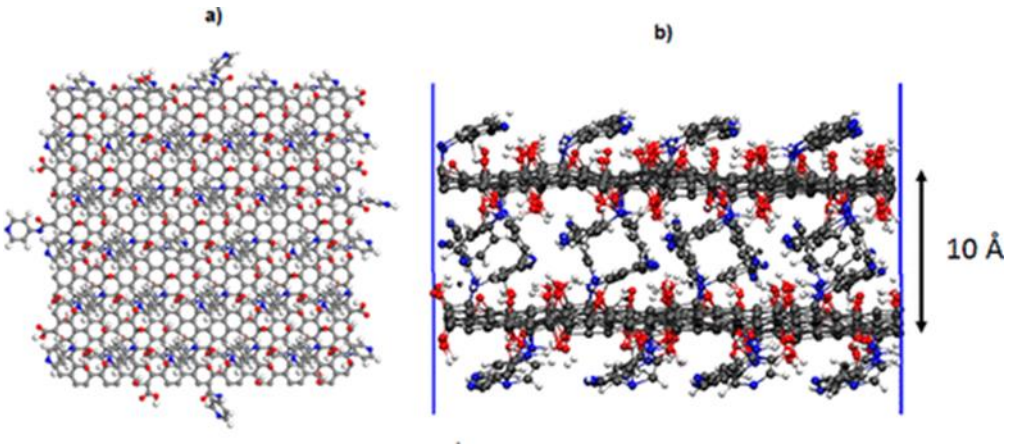

Figure 5.8 Geometry optimized model for 4AmPy-GO generated by the force field-based-MD simulations a) Top view and b) lateral view showing the interlayer distance of 10 Å. Colour scheme for GO layer: C, grey; O, red; H, white; N, blue

5.3 Construction of ZIF-8/FGO Interface

The interface model of 4AmPy-GO/ZIF-8 was constructed using the same strategy that was used for ZIF-8/pristine-GO[15]. 4AmPy-GO model being 40 Å × 40 Å, fits well along the lengths of ZIF-8 with 51 Å × 48 Å × 97 Å in dimensions. Here eight layers of 4AmPy-GO were stacked

on the top of the ZIF-8 to exclude mutual interactions between ZIF-8 to ZIF-8 surfaces along the z-axis. The consideration of eight layers of 4AmPy-GO corresponds to ~75 Å separating distance between MOF surfaces along the z direction[15]. In these calculations, all atoms of flexible ZIF-8 were treated as charged LJ sites as defined in ZIF-8/pristine-GO interface. The interactions between FGO and ZIF-8 were described by the sum of Coulombic and LJ potential terms with the crossed-interactions computed by applying the Lorentz−Berthelot mixing rules. Here several sets of MD simulations were performed for equilibration using NVT Hoover ensemble. NVT simulations with 0.5 ps thermostat relaxation time were run in a sequence of temperatures (30 K, 100 K and 298 K) each for 2ns, with a 1fs timestep to carefully equilibrate the system followed by a 5 ns production run. An illustration of the optimized ZIF-8/4AmPy-GO composite is presented in Figure 5.9. This composite model corresponds to 26800 atoms.

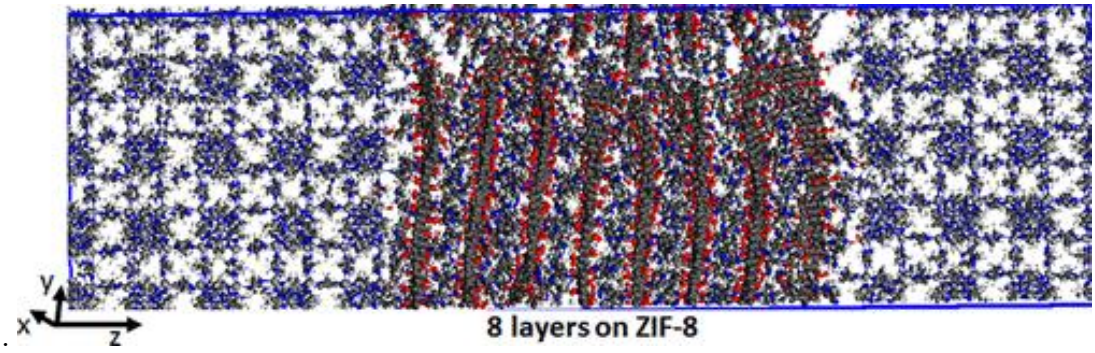

Figure 5.9 Illustration of the constructed ZIF-8/4AmPy-GO interface: Colour scheme for GO layers follows the same colour code as while ZIF-8: C, grey; N, blue; Zn, grey; O, red; H, white

5.4 Analysis of the ZIF-8/FGO Interface

Figure 5.10a showcases the normalized atomic density of the composite by scanning the system along the z-axis. The 4AmPy-GO and ZIF-8 are depicted in black and red lines respectively. The density profile is divided into three zones: (i) a bulk-like behaviour of 4AmPy-GO that extends till 34 Å, here the density wavers around an equilibrium value, (ii) the interface region that extends from 34 to 42 Å, where the equilibrated normalized density of 4AmPy-GO and ZIF-8 decreases and tends towards zero. This cross-sectional z-length of GO and MOF is marked with a dashed orange line and is also called penetration depth, which is ~8 Å. And (iii) ZIF-8 bulk phase, that extends from 43 to 130 Å. Figure 5.10b shows the illustration of the interfacial region

A with dashed line in orange. It can be clearly observed that FGO penetrates the deep pockets of ZIF-8 forming a mesh and even twisting the ZIF-8 surface. When compared to ZIF-8/pristine-GO, a partial penetration of the GO in the ZIF-8 with a corresponding depth of ~5 Å was observed. This observation clearly proves that the amine functionalization of the GO affects the interlocking between the two components at the interface.

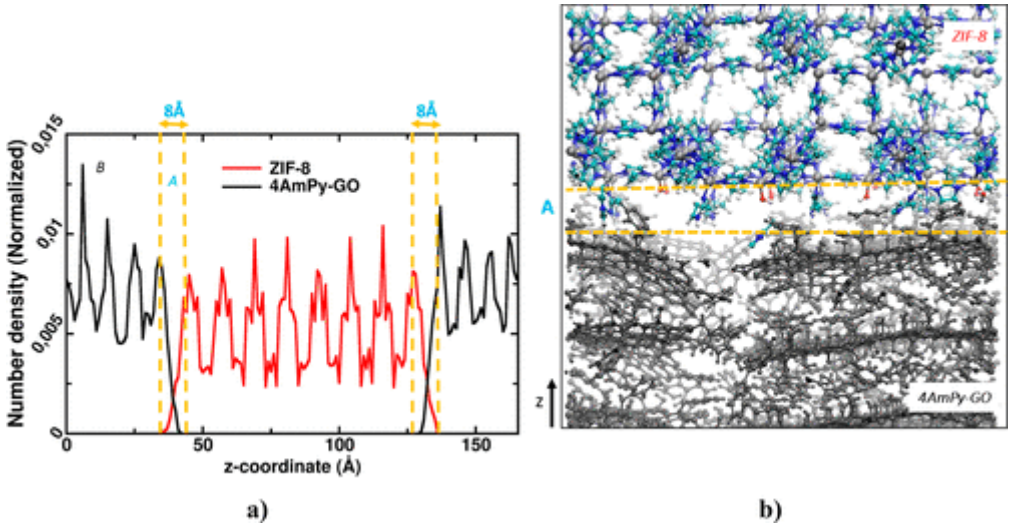

Figure 5.10 a) Normalized Atomic density profiles of GO and MOF at the interface. b) Corresponding snapshot of the interface depicting the strain induced by FGO

The higher penetration depth of 4AmPy-GO in the interfacial region is due to the preferential interactions between the two components of the composite. This was carefully assessed by plotting the RDFs for all corresponding ZIF-8/FGO atomic pairs. GO-4AmPy has epoxy, hydroxy at the basal plane, aminopyridine at both the basal plane and the edges and lastly carboxylic functional groups at the edges as potential interacting sites. The surface of ZIF-8(001) has (-OH) groups and imidazole moieties (-NH) bonded to the Zn external atoms, in an alternating manner, as potential interacting sites. The corresponding results are shown in Figure 5.11. The shortest interacting distances was observed for the H atoms of -NH functions of ZIF-8 and the O atom of the edged carbonyl function of 4AmPy with 2.5 Å interacting distance (See snapshot of Figure 5.11a). Similarly, H atoms of -OH in ZIF-8 and basal N atoms of the pyridine 4AmPy group implying interactions with 3.0 Å interacting distance (See snapshot Figure 5.11b). It is clearly evidenced that the preferential interactions of the amine function has shown higher intensity in both the RDF plots (Figure 5.11a,b). This proves that the origin of in-depth penetration at the interface is predominantly contributed by the strongly interacting amine functional groups.

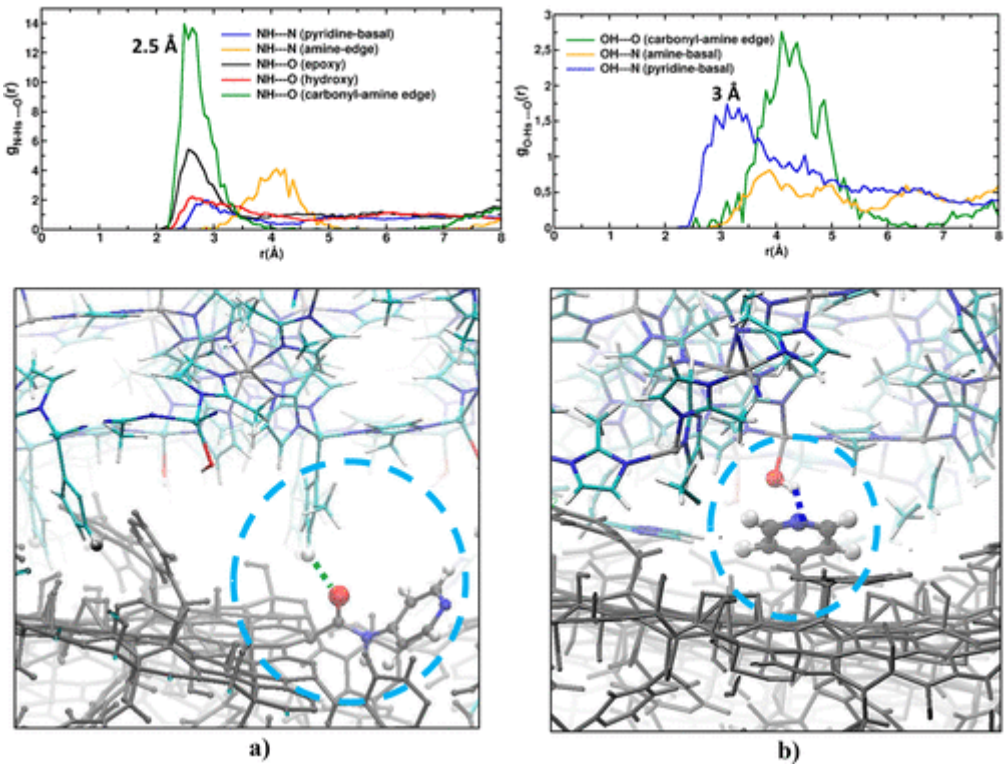

Figure 5.11 Radial Distribution Functions plotted for different ZIF-8/4AmPy-GO atom pairs a) –NH (ZIF-8) terminations and b) –OH (ZIF-8) terminations with all the oxygen and nitrogen containing groups of 4AmPy-GO. Subsequent snapshots are shown as illustrations. The colour scheme of ZIF-8 and GOs are kept the same as above figures

To quantify the local structural deformation of the FGO layers in the vicinity of the ZIF-8 surface, dihedral angle distribution for the FGO along the z-axis of the simulation box was calculated (Figure 5.12). A set of four carbon atoms was selected on the layer where we could see the maximum distortion of the layer, then a dihedral distribution through all the MD trajectory was calculated. The dihedral angles of the first, second layer closest to the MOF surface (corresponding to region A) and the eighth layer far away from the MOF surface (corresponding to region B) are illustrated in Figure 5.12. An angle distribution around 90° is found for the first layer. The geometry of first layer is quite distorted, this is attributed to the strong interactions between -NH atoms of ZIF-8 and amine functional groups in the GO layer. This interaction generates a meshed structure as illustrated in Figure 5.10b. For the eighth layer, a uniform distribution of angle was noticed consistent with a bulk like behaviour. This emphasizes that this layer is much less affected by the ZIF-8 surface.

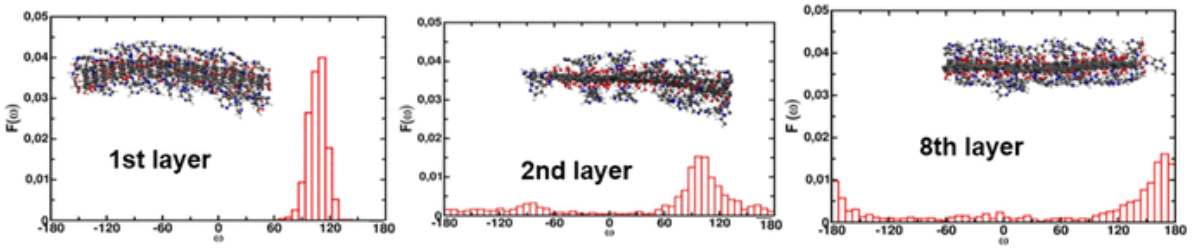

Figure 5.12 Dihedral angle distributions of the 1st, 2nd and 8th layers of FGO attached to the ZIF-8 surface averaged over the MD simulations

5.5 Validation of Computational Findings by Experiments

- **(FTIR) Spectroscopy**

FT-IR spectra of ZIF-8/FGO composites (see Figure 5.13) clearly indicated the interaction between the ZIF surface and the amine functional groups of AmPy-GO. FGO showed distinct peaks of N-H vibration at ~3200 cm^{-1}[112]. This peak height was slightly decreased with increasing ZIF concentration, indicating that the hydroxyl functional groups of ZIF surface combined with the N-H groups of AmPy-GO. This means that ZIF particles interact strongly with the 4AmPy functions of GO.

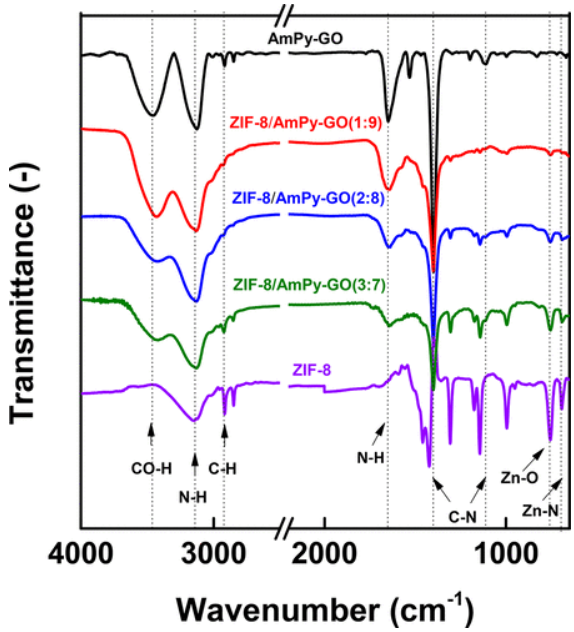

Figure 5.13 FT-IR spectra of the ZIF-8/4AmPy-GO composites corresponding to different contents of ZIF-8. Comparison with the data collected for the pure 4AmPy-GO

- **TEM Studies**

The structure and the morphology of ZIF-8/FGO composite observed by TEM is reported in Figure 5.14. The ZIF-8 nanoparticles were homogeneously attached on the surface of amine-functionalized GO nanosheet. This behaviour is very different from experimentally observed ZIF-8 nanocrystal composites with GO[25]. This means that the compatibility between ZIF-8 nanoparticles and amine-functional groups of GO is far better compared to ZIF-8/pristine-GO case. This observation clearly supports our predictions.

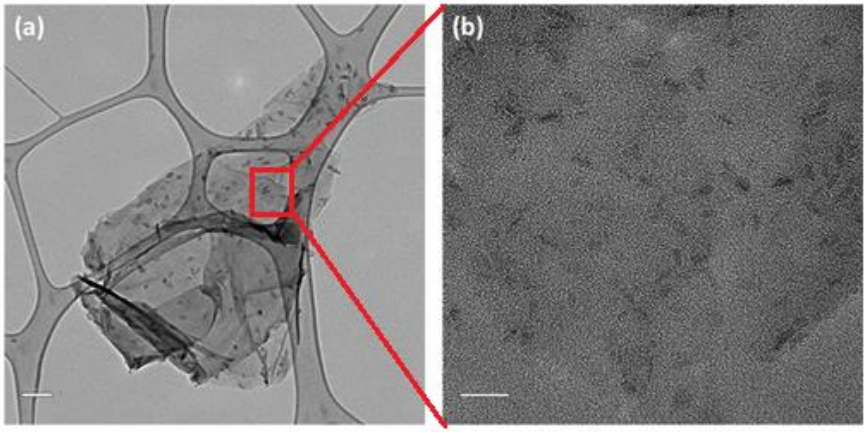

Figure 5.14 TEM images of ZIF-8/4AmPy-GO nanosheets. (ZIF-8: 4AmPy-GO ratio = 3:7) with scale bar a) 0.2 µm to b)50 nm

- **Tensile Strength Measurements**

Mechanical properties of the composites were probed using an Instron Universal Testing System (AGS-J-500N, Norwood, MA). The samples were of 13 mm and 2 mm in height and width respectively. The tensile test rate was 1.0 mm/min. Figure 5.15 shows that as the concentration of ZIF-8 fillers is increased in the FGO matrix, interestingly, it leads to an enhancement of the mechanical properties. Indeed, the tensile strength of the resulting composite is drastically improved (red line, Figure 5.15).

When comparing the tensile strength of ZIF-8/FGO with the ZIF-8/pristine-GO composites as a function of ZIF-8 concentration, it was observed that the tensile strength was increased up to ~15 MPa (65.3 to 80.9 MPa) for the former case while ~8 MPa (from 39.9 to 48.8 MPa) for the later. This clearly supports a relatively stronger interaction between the ZIF-8 surface and amine-functional groups on the GO nanosheets.

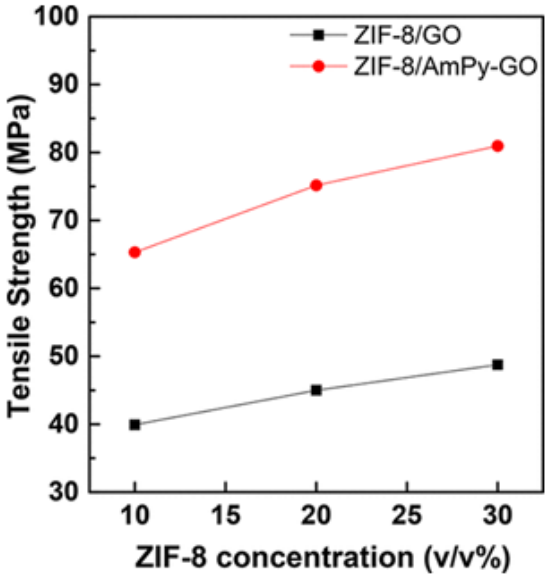

Figure 5.15 Tensile strength of ZIF-8/pristine-GO and ZIF-8/4AmPy-GO composites containing different concentrations (v/v%) of ZIF-8

5.6 Adsorption Study on ZIF-8/GO and ZIF-8/FGO

5.6.1. Simulation Methods

The adsorption isotherms of single components CO_2, N_2 and CH_4 and their binary mixtures CO_2/N_2 (molar gas composition, 15:85) and CO_2/CH_4 (molar gas composition, 50:50) were performed by GCMC simulations on the so-obtained ZIF-8/pristine-GO and ZIF-8/FGO composites.

The interaction between the composites and the guest molecules (CO_2, CH_4 and N_2) was modelled using the sum of a LJ contribution and a Coulombic term (for CO_2 and N_2), while for CH_4 only LJ contribution was considered. The LJ crossing parameters for guest/composite interactions were obtained using Lorentz–Berthelot mixing rules. The Ewald summation was used for the calculations of the electrostatic interactions, while the short-range contributions were computed with a cut-off distance of 12 Å. Gas-phase fugacity values were calculated with the Peng–Robinson equation of state[26]. These GCMC simulations were performed using CADSS (Complex Adsorption and Diffusion Simulation Suite)[27]. In these calculations, the atoms of the composites were maintained fixed at their initial equilibrated positions. For each state point, 9×10^7 Monte Carlo steps were used for both equilibration and production runs. And the adsorption

enthalpy at low coverage (ΔH) for each gas was calculated through configurational-bias Monte Carlo simulations performed in the μVT ensemble using the revised Widom's test particle insertion method[28]. The RDF for different guest/atoms of MOFs and GOs were also calculated at different pressures. The selectivity for CO_2 over other gases n, where n = N_2, CO_2, and CH_4, is quantified by calculating the separation factor, α, defined as $\alpha = (yCO_2/y_n)/(xCO_2/x_n)$, where y is the molar fractions in the adsorbed phase and x is the mole fractions in the gas phase, both at equilibrium.

5.6.2. Prediction of the Adsorption/Co-adsorption behaviours

- **Single component adsorption**

The simulated single component adsorption isotherms at 298 K for the three gases are provided in Figure 5.16 for ZIF-8/pristine-GO. All gases show a type I isotherm shape consistent with the behaviour of a microporous adsorbent. One observes that the saturation capacity increases following the sequence CO_2 > CH_4 > N_2. Interestingly the CO_2 uptake remains significantly higher than for the other gas molecules in the whole range of explored pressure. The simulated adsorption uptake of CO_2 at 50 bar and 298 K is ~5.06 mmol/g while for CH_4 is ~3.74 mmol/g and for N_2 is ~2.62 mmol/g.

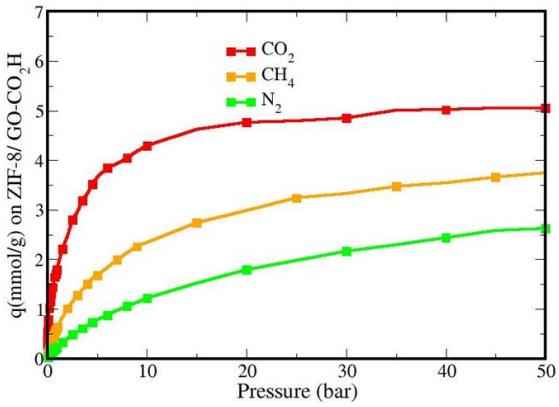

Figure 5.16 GCMC simulated single component adsorption isotherms of CO_2 (red), CH_4 (orange) and N_2 (green) in pristine GO/ZIF-8 at 298 K

The simulated adsorption enthalpies at low coverage follow the same sequence CO_2 > CH_4 > N_2 with 28.5 kJ/mol, 23.3 kJ/mol and 19.1 kJ/mol respectively. This evidences that ZIF-8/GO show a higher affinity for the polar CO_2 molecules compared to N_2 and CH_4.

The adsorption mechanism for CO_2, N_2 and CH_4 molecules when the pressure increases in ZIF-8/pristine-GO composites were illustrated in Figure 5.17. It can be observed that CO_2 molecules preferentially sit near the edges of GO which are the most energetic adsorption site and then next at the interface between the GO and MOF (Figure 5.17a). MOF sites are the least energetic adsorption sites. This scenario holds true for N_2 (Figure 5.17b) and CH_4 (Figure 5.17c) also.

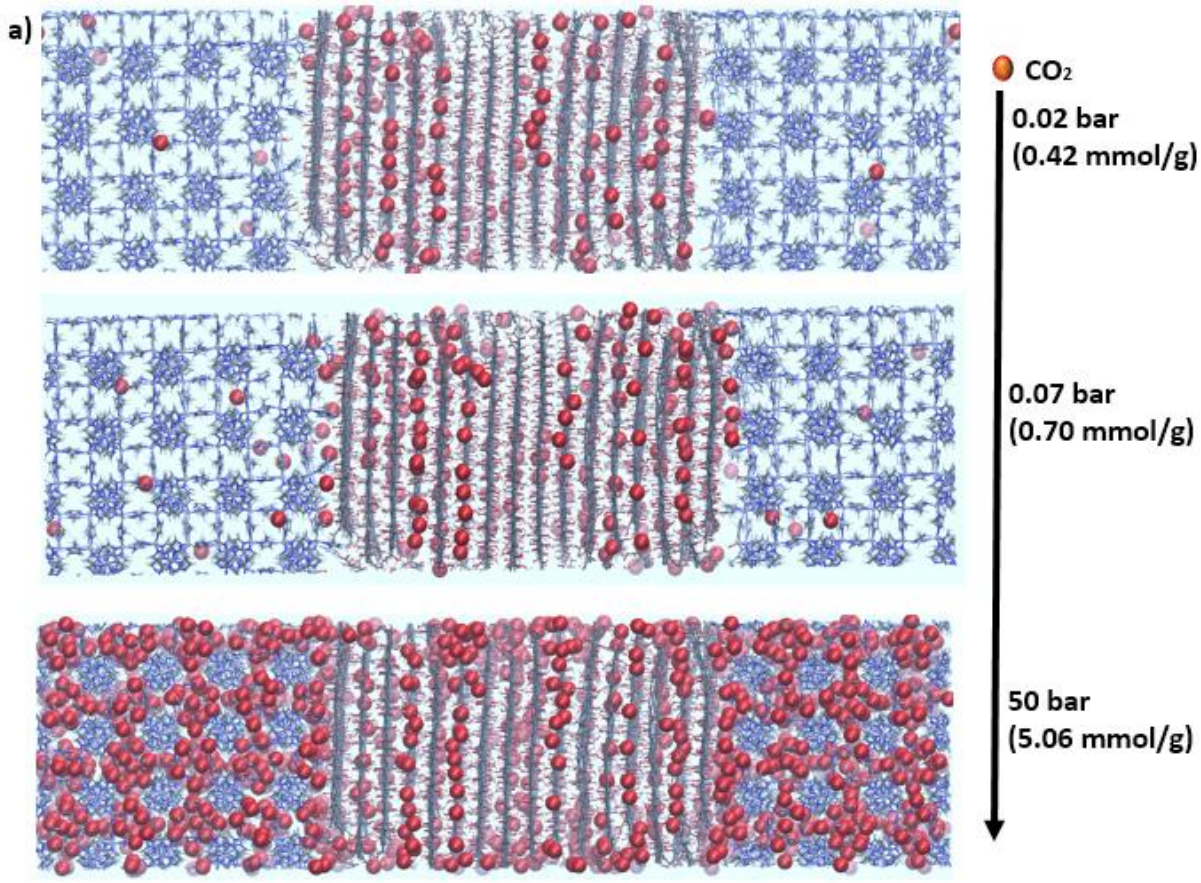

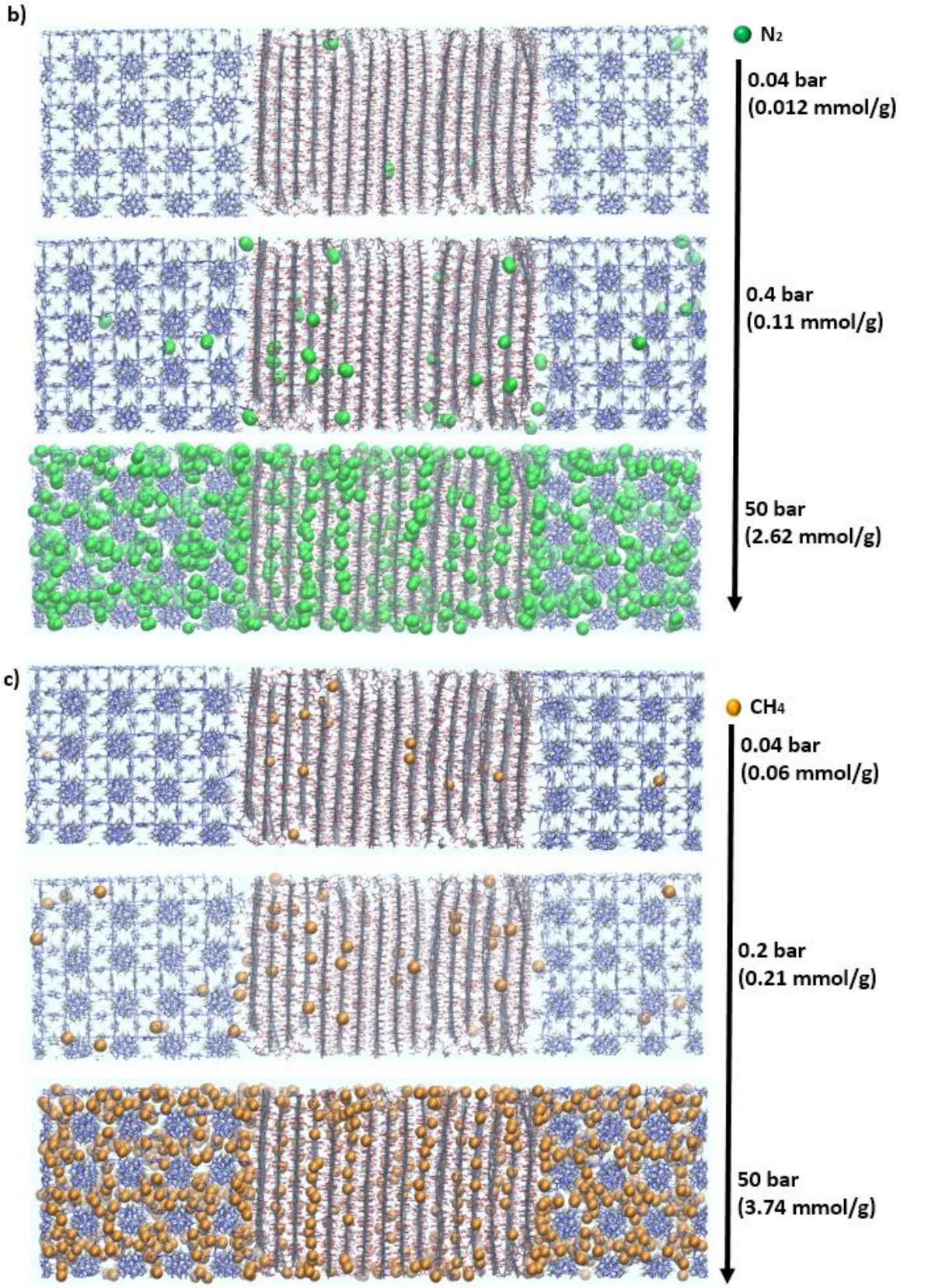

Figure 5.17 Ilustration of the single component adsorption on ZIF-8/pristine-GO composite from the GCMC simulations at 298 K and varying pressures. The colour codes for CO_2 (red), CH_4 (orange) and N_2 (green)

As a further step, when comparing the CO_2 uptake on ZIF-8/pristine-GO and ZIF-8/FGO, one observes that the saturation capacity in ZIF-8/FGO is higher than in GO/ZIF-8. The predicted adsorption uptakes of CO_2 at 298 K and 50 bar for ZIF-8/GO is ~5.06 mmol/g while for ZIF-8/FGO is ~6.25 mmol/g as exhibited in Figure 5.18. However at lower pressure, the uptake is higher for ZIF-8/pristine-GO (~0.70 mmol/g at 0.07 bar) than for ZIF-8/FGO (~0.66 mmol/g at 0.07 bar) as shown in Figure 5.19. This trend is consistent with a lowering of the adsorption enthalpy in ZIF-8/FGO (27.1 kJ/mol). This decrease is associated to a steric effect of the bulky amine functional groups that are not enough exposed to optimize the interactions with the guest molecules. At higher pressure, more and more CO_2 gas molecules are trapped at the edges of the FGO (which is a highly porous region due to the intercalation of amine groups) and this is responsible for higher uptake in FGO/ZIF-8 composite(Figure 5.19b). Like the scenario observed in single component adsorption in ZIF-8/pristine-GO(Figure 5.19a), CO_2 molecules have more affinity towards the edges of GOs and then next they accumulate at the interfacial region. And the least affinity is towards pore walls of ZIF-8 for FGO case (Figure 5.19b).

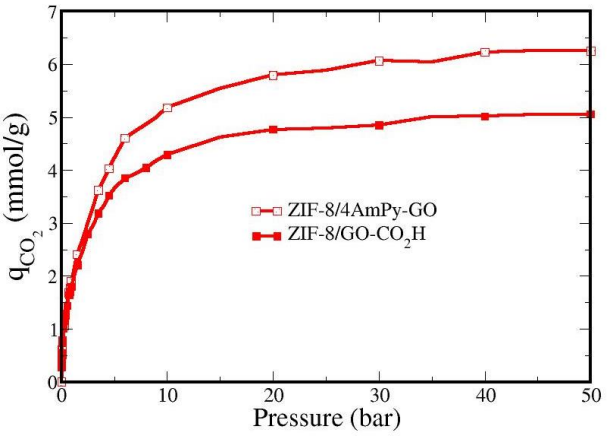

Figure 5.18 GCMC simulated single component adsorption isotherms of CO_2 in ZIF-8/pristine-GO (solid squares) and ZIF-8/FGO (open squares) at 298 K

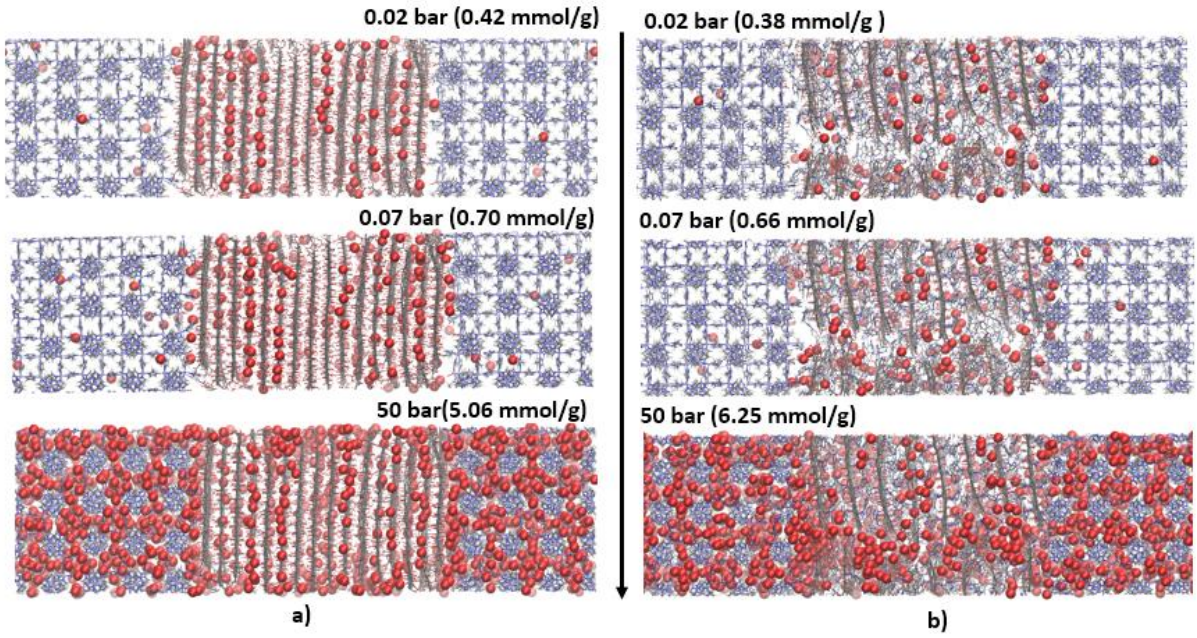

Figure 5.19 Ilustration of the CO_2 adsorption at 298 K and varying pressures in a) ZIF-8/pristine-GO and b) ZIF-8/FGO

To confirm the preferential interactions for CO_2 at the initial stage of adsorption in both ZIF-8/pristine-GO and ZIF-8/FGO, a series of RDFs were calculated and plotted in Figure 5.20 and Figure 5.21. Figure 5.20 shows the RDF plot of CO_2 molecules on the ZIF-8/pristine-GO and ZIF-8/FGO composites respectively. For ZIF-8/pristine-GO, CO_2 preferentially interact with the edge carboxylic motifs of GO (Figure 5.20a, left) with ~3.0 Å separating distance. In the interfacial region, CO_2 mostly interact with the MOF surface H atoms (Figure 5.20a, right). In the case of ZIF-8/FGO, CO_2 preferentially interact with epoxy and also with a higher intensity to the edge amine groups attached to 4AmPy motifs in the GO region, with separating distance of ~2.8 Å and ~3.2 Å respectively (Figure 5.20b, left). In the interfacial region, CO_2 mostly interact with the MOF surface H atoms same as in the pristine GO case (Figure 5.20b, right). Here the corresponding RDF intensity is higher for GO region compared to that of the interfacial MOF/GO region in both cases.

With increasing pressure (1 bar and 298 K), the trend remains the same with CO_2 preferentially interacting with the edge carboxylic motifs of GO with ~3.0 Å separating distance, for ZIF-8/pristine-GO case (Figure 5.21a, left). However for ZIF-8/FGO case, CO_2 predominantly interact with edge amine groups in the GO region, with separating distance of ~3.1 Å while the interaction with epoxy is reduced drastically (Figure 5.21b, left). When comparing the plots in the

interfacial region, the trend remain the same (Figure 5.21 with Figure 5.20, right) that is CO_2 mostly interact with the MOF surface atoms.

Figure 5.22 shows the preferential interactions for CH_4 and N_2 molecules in ZIF-8/pristine-GO case. Again, RDF plots of CH_4 molecules show that the preferential interaction is with the edge carboxylic motifs of GO region, with ~3.5 Å separating distance (Figure 5.22a, left). The same trend was observed for N_2 molecules (Figure 5.22b, left) but with a lower RDF intensity. This demonstrates that the CH_4 molecules has higher affinity with the GO than N_2 as confirmed by the adsorption enthalpy previously. A higher interaction for GO region than the interfacial MOF/GO region was demonstrated through all RDF plots (Figure 5.22 a and b, right).

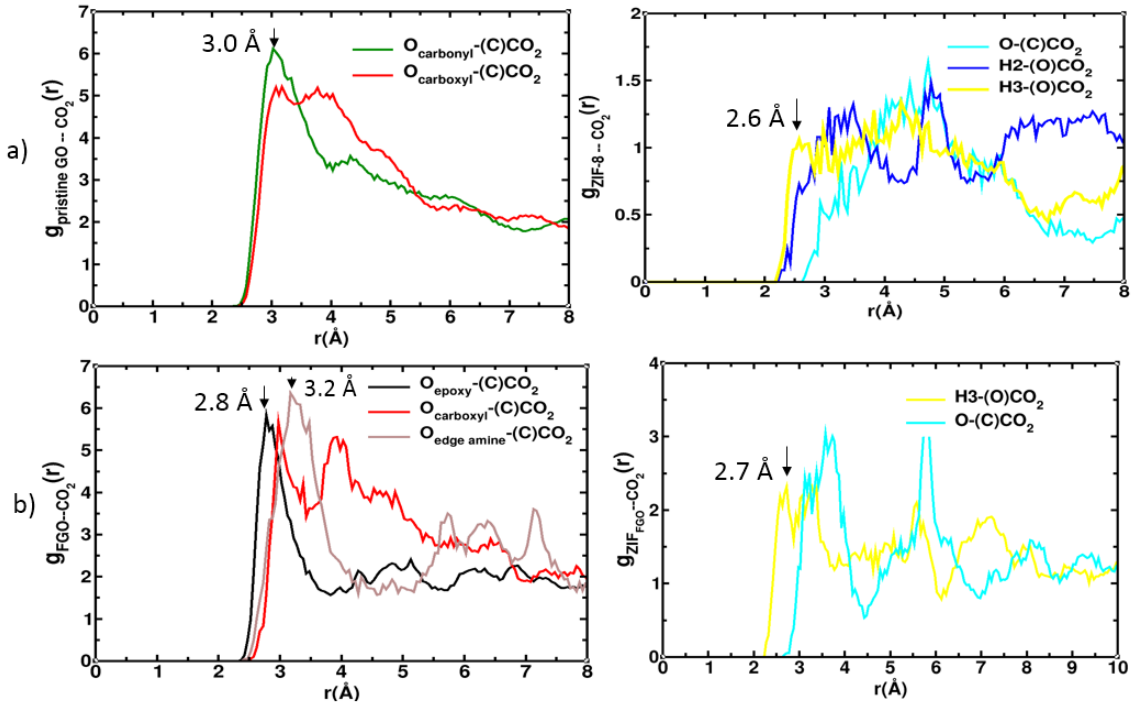

Figure 5.20 RDFs of CO_2 molecules with a) ZIF-8/pristine-GO and b) ZIF-8/FGO composites with respect to GO sites(left) and MOF sites (right) calculated from the GCMC simulations performed at **0.04 bar** and 298 K

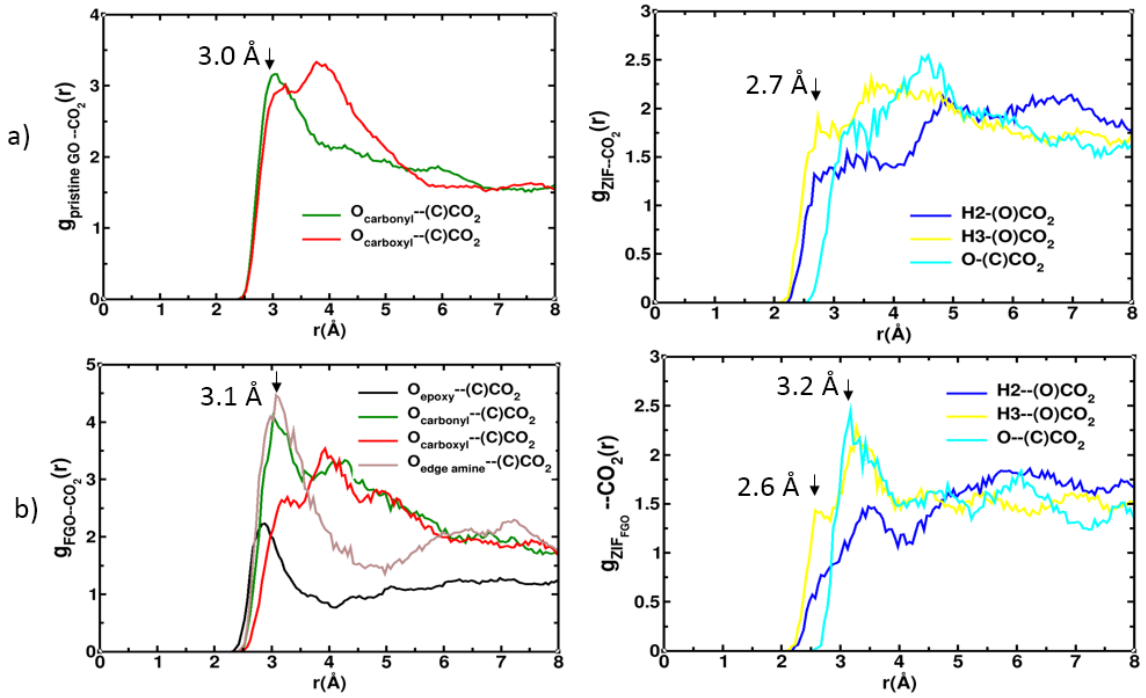

Figure 5.21 RDFs of CO_2 molecules with a) ZIF-8/pristine-GO and b) ZIF-8/FGO composites with respect to GO sites(left) and MOF sites (right) calculated from the GCMC simulations performed at **1 bar** and 298 K

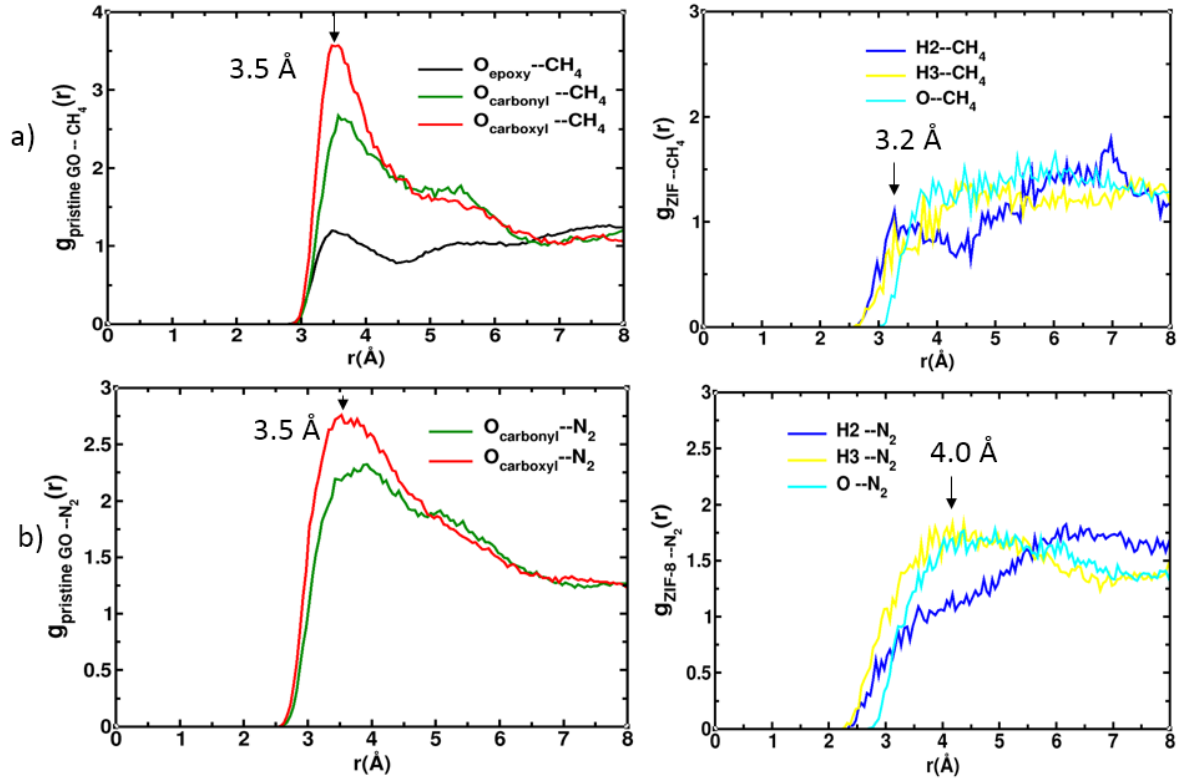

Figure 5.22 RDFs calculated for ZIF-8/pristine-GO a) CH_4 molecules performed at **1 bar** and 298 K and b) N_2 molecules performed at **5 bar** and 298 K with respect to GO sites(left) and MOF sites (right) calculated from the GCMC simulations

- **Binary mixture adsorption**

As a next step, GCMC simulations were performed to predict the separation performances in ZIF-8/GO and ZIF-8/FGO at 298 K for two binary mixtures: CO_2/N_2 (15:85) and CO_2/CH_4 (50:50). From the binary mixture adsorption isotherm plots, it can be confirmed that CO_2 adsorbs over the other two gases in both ZIF-8/pristine-GO (Figure 5.23a) and ZIF-8/FGO (Figure 5.23b) preferably as expected from the single component adsorption behaviour. The corresponding simulated selectivity for CO_2/N_2 (Figure 5.23c, left) and CO_2/CH_4 (Figure 5.23c, right) shows that the selectivity in pristine GO is slightly higher than the FGO case as expected from the adsorption enthalpy trend above.

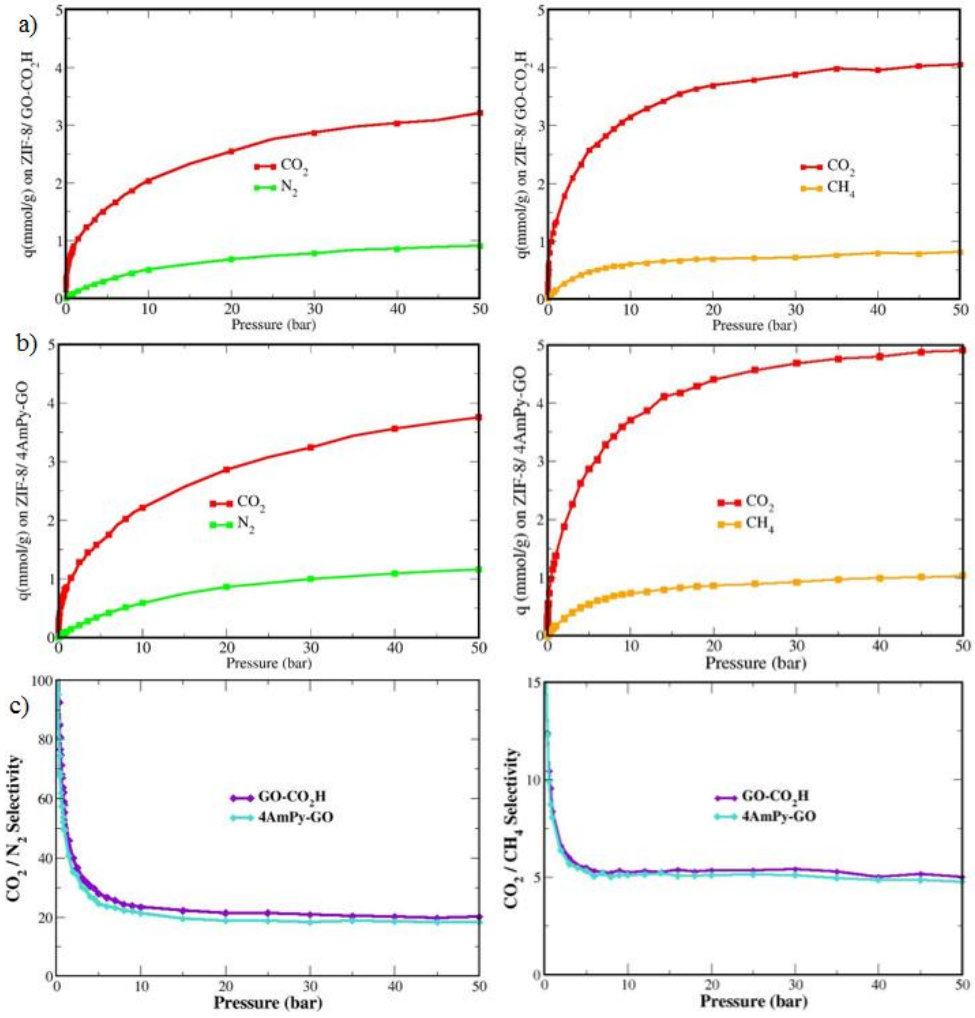

Figure 5.23 GCMC simulated co-adsorption isotherms at 298K for CO_2/N_2 (left) and CO_2/CH_4 (right) in a) ZIF-8/pristine-GO and b) ZIF-8/FGO composite respectively. And c) CO_2/N_2 selectivity (left) and CO_2/CH_4 selectivity (right) in both ZIF-8/pristine-GO and ZIF-8/FGO composites

The co-adsorption mechanism of CO_2/N_2 and CO_2/CH_4 molecules in ZIF-8/pristine-GO are illustrated in Figure 5.24a and b respectively at pressure values of increasing order. Similarly, the co-adsorption mechanism of CO_2/N_2 and CO_2/CH_4 molecules in case of ZIF-8/FGO is illustrated in Figure 5.25 a and b. Like the single component adsorption behaviour in both pristine and functionalized case, CO_2 preferentially sits near the edges of the GO than next at the interface and lastly fills the vicinity of the MOF bulk.

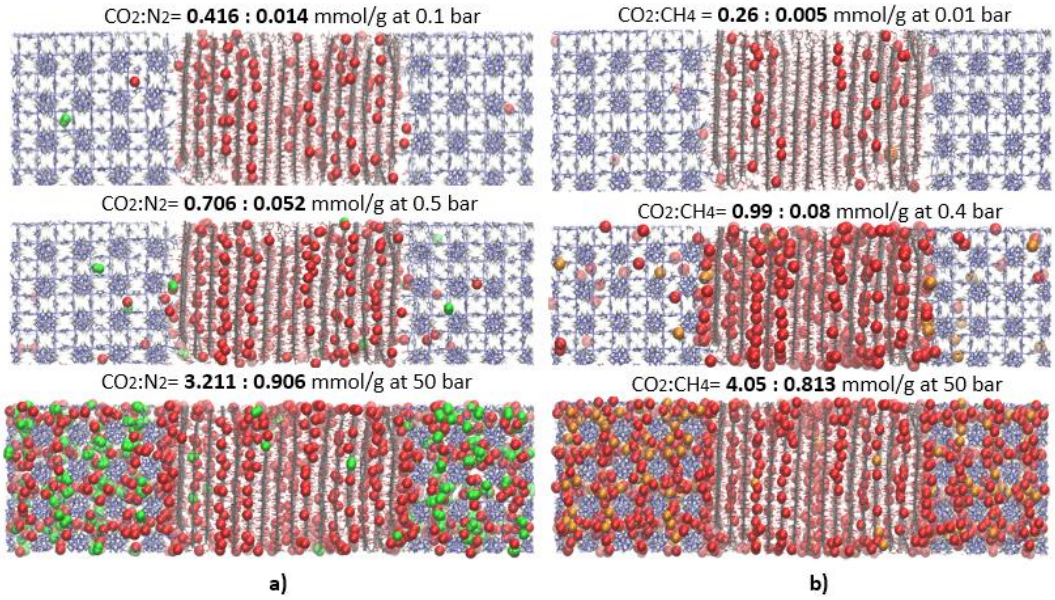

Figure 5.24 Snapshots of the simulated co-adsorption at varying pressures for ZIF-8/pristine-GO a) CO_2/N_2 and b) CO_2/CH_4. N_2 and CH_4 is represented by green and orange beads

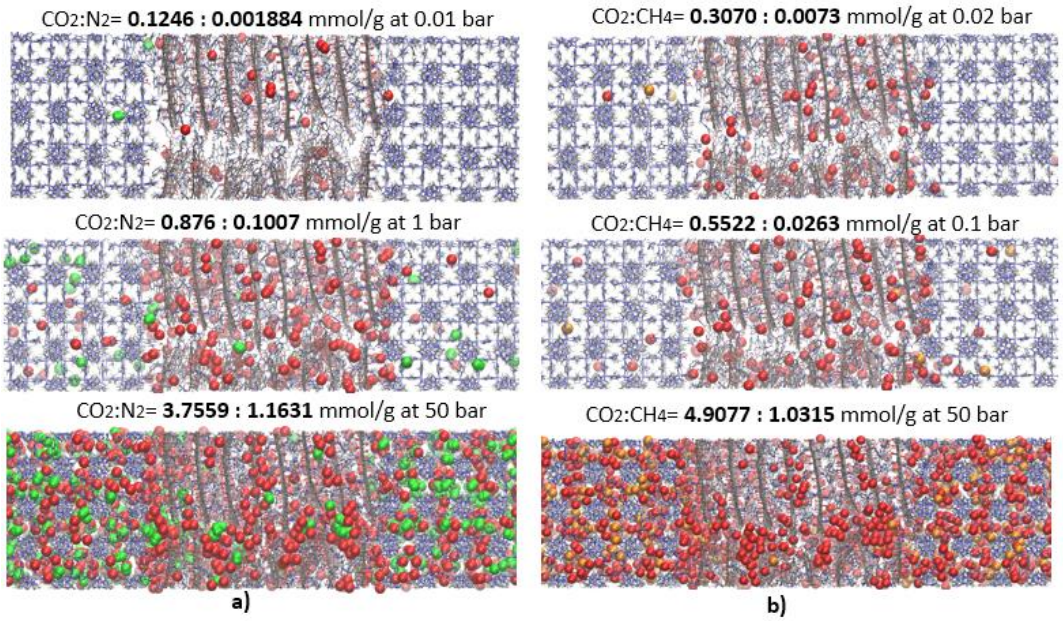

Figure 5.25 Snapshots of the simulated co-adsorption at varying pressures for ZIF-8/FGO a) CO_2/N_2 and b) CO_2/CH_4. Here N_2 and CH_4 is represented by green and orange beads

These predictions show that ZIF-8/GO composite shows moderate selectivity for CO_2 over the other gases. Further, amine functionalization of GO enhances the CO_2 uptake while maintaining a similar level of selectivity.

5.7 Conclusion

This chapter describes the computational approach that was applied to carefully construct FGO microscopic model incorporating all the experimental data gained on the corresponding system (elemental analysis, XPS, XRD analysis etc.). The so-constructed model was further combined with the ZIF-8 surface to create ZIF-8/FGO interface. The interface model was further characterized in-depth. It was observed that the FGO penetrates the deep pockets of ZIF-8 due to strong interactions between the atoms of ZIF-8 surface and the amine functions of 4AmPy grafted onto the GO surface. This higher degree of affinity was well supported by FTIR, TEM and mechanical testing experiments.

Subsequently, these models were used to predict CO_2 adsorption and separation performances of ZIF-8/FGO that were compared to that of ZIF-8/pristine-GO. GCMC calculations were performed to assess the adsorption properties of CO_2, CH_4 and N_2 gases in terms of affinity and gas uptake as well as in terms of preferential sittings. Both ZIF-8/pristine-GO and ZIF-8/FGO show moderate adsorption selectivity for CO_2 versus the other gases. The amine functional groups of FGO tend to increase CO_2 uptake capacity while maintaining similar CO_2 selectivity. The comparison with experimental data will be performed in the near future to validate these predictions.

REFERENCES

1. Ayrat M. Dimiev, S. E. *Graphene Oxide Fundamentals and Applications*. (**2017**).
2. Zhao, Y., Ding, H. & Zhong, Q. Synthesis and characterization of MOF-aminated graphite oxide composites for CO2 capture. *Appl. Surf. Sci. 284*, 138–144 (**2013**).
3. Petit, C., Mendoza, B. & Bandosz, T. J. Reactive adsorption of ammonia on Cu-based MOF/graphene composites. *Langmuir 26*, 15302–15309 (**2010**).
4. Petit, C. & Bandosz, T. J. Enhanced adsorption of ammonia on metal-organic framework/graphite oxide composites: Analysis of surface interactions. *Adv. Funct. Mater. 20*, 111–118 (**2010**).
5. Zhao, Y., Seredych, M., Zhong, Q. & Bandosz, T. J. Aminated graphite oxides and their composites with copper-based metal–organic framework: in search for efficient media for CO2 sequestration. *RSC Adv. 3,* 9932 (**2013**).
6. Ebrahim, A. M., Jagiello, J. & Bandosz, T. J. Enhanced reactive adsorption of H2S on Cu-

BTC/S- and N-doped GO composites. *J. Mater. Chem. A 3*, 8194–8204 (**2015**).

7. Policicchio, A., Zhao, Y., Zhong, Q., Agostino, R. G. & Bandosz, T. J. Cu-BTC/aminated graphite oxide composites as high-efficiency Co2 capture media. *ACS Appl. Mater. Interfaces 6*, 101–108 (**2014**).

8. Sadeghi, N., Sharifnia, S. & Do, T.-O. Enhanced CO2 photoreduction by a graphene-porphyrin metal-organic framework under visible light irradiation. *J. Mater. Chem. A 6*, 18031–18035 (**2018**).

9. Senthilnathan, J. & Yoshimura, M. Low energy liquid plasma for direct reduction and formation of rGO-aminopyridine hybrid for electrical and environmental applications. *J. Hazard. Mater. 340*, 26–35 (**2017**).

10. Hoseini, S. J., Khozestan, H. G. & Fath, R. H. Covalent attachment of 3-(aminomethyl)pyridine to graphene oxide: A new stabilizer for the synthesis of a palladium thin film at the oil-water interface as an effective catalyst for the Suzuki-Miyaura reaction. *RSC Adv. 5*, 47701–47708 (**2015**).

11. Cho, Y. H. *et al.* Water and ion sorption, diffusion, and transport in graphene oxide membranes revisited. *J. Memb. Sci. 544*, 425–435 (**2017**).

12. Guo, Y., Jia, Z. & Cao, M. Surface modification of graphene oxide by pyridine derivatives for copper(II) adsorption from aqueous solutions. *J. Ind. Eng. Chem. 53*, 325–332 (**2017**).

13. Dreyer, D. R., Todd, A. D. & Bielawski, C. W. Harnessing the chemistry of graphene oxide. *Chem. Soc. Rev. 43*, 5288 (**2014**).

14. Jena, K. K., Narayan, R. & Alhassan, S. M. Highly branched graphene siloxane−polyurethane-urea (PU-urea) hybrid coatings. *Prog. Org. Coatings 111*, 343–353 (**2017**).

15. Bonakala, S. *et al.* Understanding of the Graphene Oxide / Metal-Organic Framework Interface at the atomistic scale. *ACS Appl. Mater. Interfaces 10*, 1–6 (**2018**).

16. Dreyer, D. R., Park, S., Bielawski, C. W. & Ruoff, R. S. The chemistry of graphene oxide. *Chem. Soc. Rev.* 228–240 (**2010**). doi:10.1007/978-3-319-15500-5_3

17. Vandevondele, J. *et al.* Quickstep: Fast and accurate density functional calculations using a mixed Gaussian and plane waves approach. *Comput. Phys. Commun. 167*, 103–128 (**2005**).

18. Perdew, J. P., Burke, K. & Ernzerhof, M. Generalized Gradient Approximation Made Simple. *Phys. Rev. Lett. 77*, 3865–3868 (**1996**).

19. Grimme, S. Semiempirical GGA-Type Density Functional Constructed with a Long-Range Dispersion Correction. *J Comput Chem 27*, 1787–1799 (**2006**).

20. Elstner, M. *et al.* Self-consistent-charge density-functional tight-binding method for simulations of complex materials properties. *Phys. Rev. B 58,* 7260–7268 (**1998**).

21. Jorgensen, W. L., Maxwell, D. S. & Tirado-Rives, J. Development and Testing of the OPLS All-Atom Force Field on Conformational Energetics and Properties of Organic Liquids. *J. Am. Chem. Soc. 118*, 11225–11236 (**1996**).

22. Allen, M. P. & Tildesley, D. J. *Computer simulation of liquids*. doi:10.1016/j.cpc.2008.01.029

23. Breneman, C. M. & Wiberg, K. B. Determining atom-centered monopoles from molecular electrostatic potentials. The need for high sampling density in formamide conformational analysis. *J. Comput. Chem. 11,* 361–373 (**1990**).

24. Frisch, M. J. *et al.* Gaussian 09, Revision B.01. *Gaussian 09, Revision B.01, Gaussian, Inc., Wallingford CT* (**2009**).

25. Lee, H. *et al.* Metal-organic frameworks grown on a porous planar template with an exceptionally high surface area: Promising nanofiller platforms for CO2 separation. *J. Mater. Chem. A 5*, 22500–22505 (**2017**).

26. Peng, D. Y. & Robinson, D. B. A New Two-Constant Equation of State. *Ind. Eng. Chem. Fundam. 15*, 59–64 (**1976**).

27. Zhong, C. *CADSS 1.3 : Complex Adsorption and Diffusion Simulation Suite*. (**2011**).

28. Vlugt, T. J. H., García-Pérez, E., Dubbeldam, D., Ban, S. & Calero, S. Computing the heat of adsorption using molecular simulations: The effect of strong Coulombic interactions. *J. Chem. Theory Comput. 4*, 1107–1118 (**2008**).

Article 1

THE JOURNAL OF PHYSICAL CHEMISTRY C

Article

Cite This: *J. Phys. Chem. C* 2019, 123, 4984–4993

pubs.acs.org/JPCC

Unraveling the Enhancement of the Interfacial Compatibility between Metal–Organic Framework and Functionalized Graphene Oxide

Anusha Lalitha,[‡,#] Jae Eun Shin,[§,#] Satyanarayana Bonakala,[‡] Jee Yeon Oh,[§] Ho Bum Park,[*,§] and Guillaume Maurin[*,‡]

[‡]Institut Charles Gerhardt Montpellier UMR 5253 CNRS, Université de Montpellier, Place E. Bataillon, 34095 Montpellier Cedex 05 France

[§]Department of Energy Engineering, Hanyang University, Seoul 04763, Republic of Korea

S *Supporting Information*

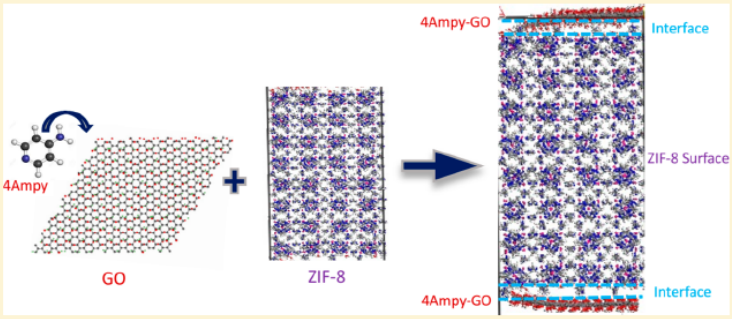

ABSTRACT: Advanced modeling and experimental characterization tools were coupled to gain an unprecedented in-depth characterization of the interface formed when a hybrid porous solid ZIF-8 is incorporated as filler onto an amine-functionalized graphene oxide (GO) matrix. As a preliminary stage, an aminopyridine-functionalized GO was synthesized, and a realistic atomistic model was computationally built integrating their structural and chemical features deduced from X-ray photoelectron spectroscopy and X-ray diffraction experiments. An atomistic representation of the ZIF-8/functionalized GO interface was further simulated and carefully analyzed in terms of the nature and the strength of interactions between the two components and the GO conformation with a special emphasis on the impact of the functionalization. It was revealed that grafting the aminopyridine function at the GO significantly enhances the interactions with the terminal functions present at the MOF interface associated with an in-depth penetration of the functionalized GO into the pockets of the ZIF-8. The so-predicted high compatibility between the two components was then supported by Infrared experiments collected on the prepared composite. Complementary transmission electron microscopy experiments further revealed a homogeneous dispersion of the ZIF-8 nanoparticles into the GO matrix with the absence of MOF agglomeration and mechanical testing evidenced a significant enhancement of the tensile strength for the corresponding composite. This fundamental exploration unambiguously demonstrates the key role played by the GO functionalization to achieve optimal interfacial MOF/GO properties, and this opens promising perspectives for processing thin films required for future applications.

I. INTRODUCTION

Graphene oxide (GO), a derivative of graphene with diverse oxygen-containing functionalities such as hydroxyl, epoxy, diol, ketones, and carboxyl,[1−3] has attracted tremendous interest for use in electronic devices[4−6] owing to its highly tunable electronic properties. Since GOs can also be made as thin films, they have been further considered for various applications in the fields of catalysis,[7,8] energy storage/conversion,[9−11] and biomedicine[12−14] etc. Furthermore, due to their excellent mechanical properties, they have been widely considered as composite systems in combination with different materials including polymers, inorganic and hybrid porous solids.[15] Their association with one of the most recent classes of porous materials, the metal−organic frameworks (MOFs), has been the subject of intense research over the last decades. MOF/GO composites have demonstrated great promise in various areas, including gas capture/separation,[16−21] electrochemistry,[22,23] electrocatalyst,[24−26] supercapacitors,[27] energy storage,[28] etc. More recently, the functionalization of GOs by diverse functional groups, including metals[29] or nonmetals like

Received: January 2, 2019
Revised: January 30, 2019
Published: January 30, 2019

DOI: 10.1021/acs.jpcc.9b00028
J. Phys. Chem. C 2019, 123, 4984–4993

nitrogen,[30,31] sulfate,[32] or even polymers,[33] attached either covalently or noncovalently to the highly reactive oxygen functionalities, have been proposed as an effective strategy to strengthen the interfacial interactions with the MOFs as fillers, thus leading to an enhancement of the mechanical properties of the resulting composites.[34] Functionalized GOs with amine-containing molecules have been particularly explored in combination with a series of MOFs as they change their chemistry (by selective interaction with amine group) and microstructure (by generating micropores) at the interface which is of interest in adsorption[32,35−37] and catalysis.[38] It is to be noted that the 4-aminopyridine functionalized GO has been only rarely considered so far[39,40] although the concomitant presence of amine function and aromatic ring can be expected to act synergistically to favor a high affinity with the incorporated MOF. This motivated us to synthesize the corresponding functionalized GO as well as its composite with one of the most investigated MOF, the zinc-based zeolite imidazole framework ZIF-8.[41] A series of advanced characterization and modeling tools was coupled to identify the role played by the GO functionalization on the MOF/GO interface, i.e., the nature and strength of the interactions, the surface coverage, the GO conformation at the MOF surface as well as on the dispersion of the MOF nanoparticles in the GO matrix and the mechanical properties of the composite. Such a fundamental understanding is highly relevant to further guide the design of optimal MOF/GO composites that besides showing promising performances for a targeted application, are easily prepared as homogeneous thin films/membranes with high mechanical resilience which are both crucial prerequisites for further processing at the industrial scale.

To that purpose, we expanded our previously developed molecular modeling approach[42−47] integrating density functional theory and force field based-molecular dynamics simulations to derive an atomistic representation of the functionalized GO integrating the nature and concentration of functional groups, i.e., epoxy, hydroxyl, carboxylic, and amine functions, as deduced from our own X-ray photoelectron spectroscopy analysis. This was followed by a computational construction of a model for the resulting ZIF-8/functionalized GO interface that was scrutinized and compared to the scenario encountered for the pristine-GO composite derivative.[44] These conclusions gained at the microscopic scale were further supported by infrared spectroscopy experiments. The impact of the GO functionalization on the dispersion of MOF nanoparticles onto the GO matrix as well as on the tensile strength of the resulting composite, was finally revealed by transmission electron microscopy and mechanical testing, respectively.

II. METHODS

II.1. Experimental Section. *II.1.1. Graphene Oxide Synthesis.* Graphene oxide was synthesized from purified natural graphite powder (99.99%, SP-1, 100 Mesh, Bay Carbon Inc.) following Hummers' method.[48,49] Initially, graphite powder and sulfuric acid (95%, H_2SO_4 DaeJung Chemicals) were mixed in a double-walled glass reactor at 5 °C and stirred for 10 min. Potassium permanganate (99.3%, Junsei Chemical) was added to the solution and stirred for 12 h at 35 °C. A total of 500 mL of deionized water was then gradually added into the resulting GO solution in the glass reactor below 5 °C. The as-prepared GO suspension was then poured into a beaker and further diluted by 2 L of deionized water. Hydrogen peroxide (H_2O_2-30%, Sigma-Aldrich) was added into the GO solution until its color turned from brown to golden yellow. After stirring for 30 min, GO solution was vacuum filtrated by using a glass fiber filter (WHATMAN) and further washed out with 10 wt % HCl aqueous solution. The GO was subsequently vacuum-dried in a desiccator for 2 days and washed with 3 L of acetone followed by filtration. Finally, the final product was dried in a desiccator under vacuum for 3 days.

II.1.2. Aminopyridine−GO Synthesis. As-synthesized GO powder was mixed with 50 mL of $SOCl_2$ solution (0.69 mol) and stirred for 10 min. The mixture was then refluxed for 3 h at 90 °C under N_2 atmosphere and further evaporated to remove the excess of $SOCl_2$ in order to obtain activated GO. After evaporating, dried activated GO was dispersed in 20 mL of THF (0.28 mol). 3.764 g of aminopyridine (4AmPy, 94.11 g/mol, 98%, Sigma-Aldrich) was dissolved in 80 mL of THF and further added into the as-prepared activated GO solution. The mixture was then refluxed at 80 °C for 5 h and stirred at room temperature for 10 h. After reaction, the solution was centrifuged at 5000 rpm for 3 min and washed with THF to remove the excess of 4AmPy. The final product was finally dried under vacuum. The loaded amount of 4AmPy is approximately 20 wt % in 4AmPy-GO based on the TGA analysis reported in Figure S1".

II.1.3. ZIF-8 Synthesis. A 0.366 g sample of zinc nitrate hexahydrate ($Zn(NO_3)_2 \cdot 6H_2O$, 99%, Sigma-Aldrich) and 0.811 g of organic ligand (i.e., 2-methyl imidazole, 99%, Sigma-Aldrich) were individually dispersed in 15 and 20 mL of methanol, respectively, prior to being mixed together and stirred for 5 h at room temperature.[47,50] The as-synthesized product was further washed with methanol four times and centrifuged to remove the excess of organic linkers and impurities.

II.1.4. Fabrication of ZIF-8/4ampy-GO Composite. As-synthesized 4AmPy-GO powder was dispersed in EtOH (1 mg/mL) and sonicated for 1 h using a bath-sonication system. Different quantities of ZIF-8 nanoparticles were added to this 4AmPy-GO solution and stirred for 1 h to achieve a well-dispersed mixture. The ZIF-8/4AmPy-GO composite was thus fabricated and subsequently filtered under vacuum on the anodic aluminum oxide (AAO) support (WHATMAN, 0.2 μm). The so-obtained ZIF-8/4AmPy-GO composite was further dried under vacuum at room temperature for 24 h.

II.1.5. Characterization of GO and 4AmPy-GO. The *Fourier transform infrared (FT-IR)* spectra of the pristine GO and 4AmPy-GO were measured using a Nicolet 6700 (Thermo electron scientific instruments, USA) in the range from 4000 to 600 cm^{-1}. The corresponding FT-IR data are reported in Figure S2. The distinct characteristic peaks observed for the pristine GO at 3450, 1710, 1230, and 1065 cm^{-1} are attributed to the stretching vibration of the CO−H, C═OOH, C−O−C, and C−OH groups, respectively.[51] Regarding 4AmPy-GO, the FT-IR spectrum shows peaks at 1400 and 1120 cm^{-1} associated with the C═N and C−N stretching modes of the pyridine group, respectively.[52] Two additional peaks appear at 3130 and 1645 cm^{-1} characteristics of the N−H stretching mode and N−H bend, respectively.[40,53] The presence of these latter features indicates a successful chemical bonding of 4AmPy at the surface of the GO nanosheet.[40,53] *X-ray photoelectron spectroscopy (XPS)* was used to confirm the nature of the chemical bonding and the atomic ratios (C/O and C/N) for both GO and 4AmPy-GO. This was performed using an ESC system (XPS-theta probe, Thermo Fisher

DOI: 10.1021/acs.jpcc.9b00028
J. Phys. Chem. C 2019, 123, 4984−4993

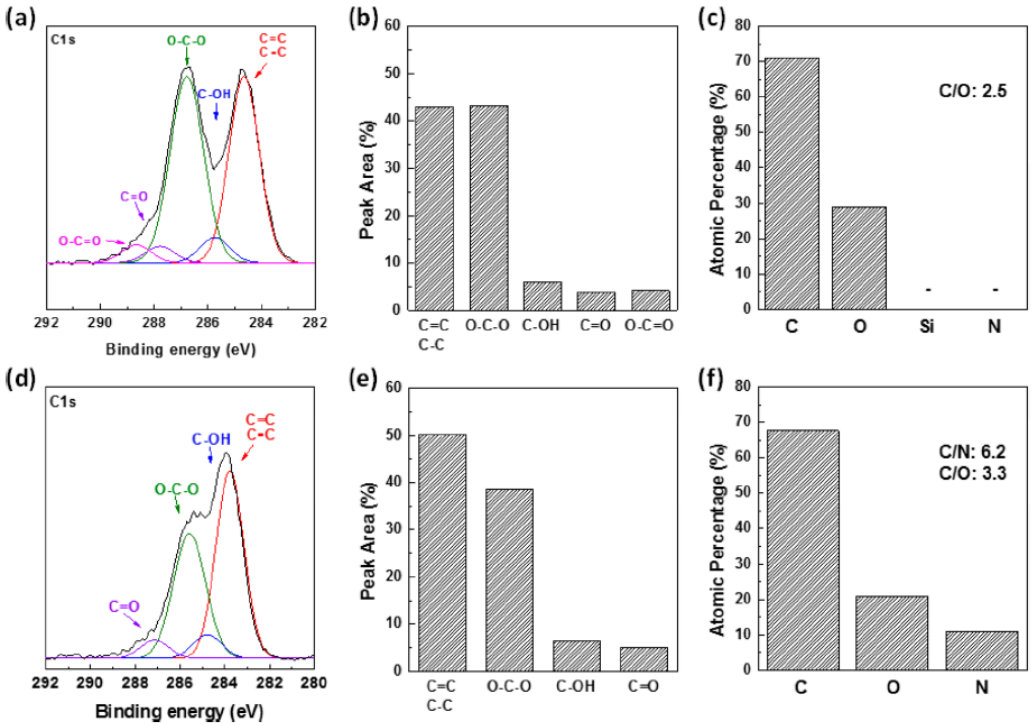

Figure 1. XPS spectra of the (a) pristine GO and (d) 4AmPy-GO. Peak areas of each oxygen functional groups of the pristine GO (b) and 4AmPy-GO (e) deduced from the analysis of the XPS spectra. Atomic percentages of C, O, and N in the pristine GO (c) and 4AmPy-GO (f).

Scientific Co., USA) equipped with a monochromatic Al Kα source (C correction: 284.5 eV). The corresponding results are summarized in Figure 1. The C 1s XPS spectrum for the pristine GO indicates a considerable degree of oxidation with five components which correspond to carbon atoms bounded to different oxygen functional groups on GO: the non-oxygenated ring C═C at 284.6 eV, the C−O (C−O−C) at 286.4 eV, the carbonyl (C═O), the carboxylic (O═C−OH) and the hydroxyl (C−OH) groups at 287.8, 290.4, and 285.5 eV respectively.[54] The C/O ratio for the pristine GO was found to be 2.5.

The C 1s XPS spectrum of 4AmPy-GO contains most of the characteristic peaks discussed above except that assigned to the carboxylic functions. This clearly indicates that the amine groups of 4AmPy are combined with the edge groups of the GO sheets. Further, the C/O ratio was found to be slightly higher than that for the pristine GO, i.e., 3.3, because of a partial reduction of the GO during the preparation of 4AmPy-GO. In addition, the N percentage is approximately 10% after functionalization leading to a C/N ratio of 6.2. *Powder X-ray diffraction (PXRD)* patterns for GO, 4AmPy-GO, and ZIF-8 were recorded on a diffractometer (D8 Advance, Bruker, Germany) fitted with a monochromatic Al Kα source (λ = 1.5406 Å) at 40 kV and 40 mA (1.6 Kw) in the range of 5−30°, and a scan rate of 1 deg/min. The corresponding data are reported in Figure S3c. We first checked that the PXRD pattern collected for our synthesized ZIF-8 is the same as previously reported for this MOF. Furthermore, the main characteristic peak position for both GOs allowed us to estimate the interlayer distance. It was found that the interlayer spacing for 4AmPy-GO is larger (about 13.1 Å) than that of the pristine GO (7.7 Å[55]) and this is consistent with an intercalation of the aminopyridine in the GO layers.

Transmission electron microscopy (TEM) was carried out using TEM 2100F (JEOL, Tokyo, Japan) to characterize the structural and textural features of pristine GO, 4AmPy-GO as well as of ZIF-8/4AmPy-GO. The structure and the morphology of pristine GO and 4AmPy-GO are reported in Figure S4, parts a and b. One can observe that GO presents a smooth surface morphology while 4AmPy-GO exhibits a winkled and folded surface. The wrinkled structure is due to the presence of the functionalized groups attached at the surface of the GO nanosheet, consistent with previous findings.[53] *Mechanical properties* of both GOs and their composites with ZIF-8 were probed using an Instron Universal Testing System (AGS-J-500N, Norwood, MA). The height and width of samples were 13 mm and 2 mm respectively, and the tensile test rate was 1.0 mm/min. To measure the mechanical properties of composites, we prepared thick films using a vacuum filtration method, where the ZIF-8 and 4AmPy-GO solutions were mixed in a volume ratio.

II.2. Computational Section. *II.2.1. Construction of 4AmPy-GO Model.* The periodic GO−OH[44] model we developed previously (Figure 2a) was considered as a starting point. This model contains epoxy (−O−), and hydroxyl (−OH) functional groups attached to its basal plane. The incorporation of the 4AmPy function proceeds via a reaction with the epoxy motifs (Figure 2b). Following the previously proposed mechanism,[56] the -NH_2 function of 4AmPy reacts in such a way to break the C−O−C bridge leading to the

DOI: 10.1021/acs.jpcc.9b00028
J. Phys. Chem. C 2019, 123, 4984−4993

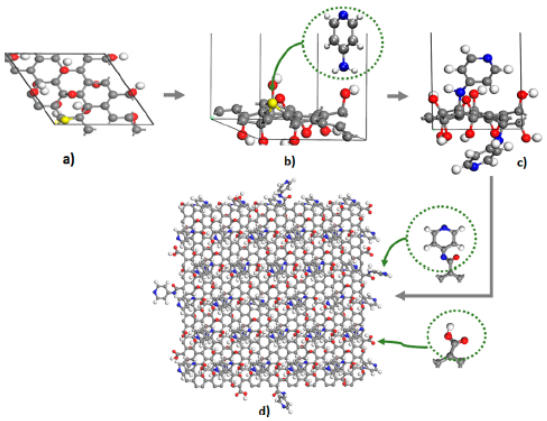

Figure 2. Schematic illustration of the stepwise construction of the atomistic model for 4AmPy-GO: (a) initial periodic GO−OH model (top view, marked epoxy group in yellow), (b) 4AmPy (encircled in green) and reactive epoxy motifs (highlighted in yellow), (c) resulting 4AmPy grafting, and (d) final nonperiodic model labeled as 4AmPy-GO, where $-CO_2H$ and 4AmPy are incorporated on the edges.

formation of a C−OH group and a pyridine-NH complex, releasing H^+ as illustrated in Figure 2c. Two epoxy rings were thus opened on both sides of the GO layer to graft 4AmPy (Figure 2c) in order to reach C/N and C/O ratios of 6 and 3 respectively as experimentally evidenced. The so-obtained periodic model was then optimized at the DFT-level using QUICKSTEP module in CP2K package[57] that allowed a full relaxation of both atomic position and cell dimensions. The Gaussian and plane waves (GPW) dual basis set method was applied, which employs Gaussian-type atom-centered basis functions to describe the wave functions and an auxiliary plane wave basis to describe the density. The PBE functional[58] was considered with a D3[59] dispersion correction developed by Grimme. A double-ζ basis set[60] with pseudopotentials of Goedecker−Teter−Hutter (GTH)[60] describing core electrons were used for all elements. Charge density in plane waves were expanded up to an energy cut off 240 Ry. This DFT-optimized model (Figure S5) and the resulting cell parameters (Table S1) are reported in the Supporting Information.

A refined model was further derived from the so-obtained periodic structure by incorporating $-CO_2H$ functions at the edges of the graphene oxide layer, which subsequently also reacts with 4AmPy (see Figure 2d) as evidenced by the XPS analysis (Figure 1). This reaction involves the $-NH_2$ function of 4AmPy and the $-CO_2H$ groups releasing H_2O and leading to the formation of amide complexes.[56] The so-constructed nonperiodic model labeled as 4AmPy-GO corresponds to C/N and C/O ratios of ∼6.26 and ∼3.7, respectively, in excellent agreement with the experimental findings. Furthermore, the atomic compositions of this microscopic model in terms of C, O, and N are 70%, 19%, and 11% respectively, which match well the corresponding experimental data of 66%, 20%, and 10%.

The so-obtained 4AmPy-GO model of dimension 40 Å x 40 Å was further geometry optimized at the force field level using molecular dynamics (MD) simulations in the NVT ensemble at 298 K using the Hoover thermostat with a relaxation time of 0.5 ps. Equation of motion was computed by the velocity Verlet algorithm with a time step of 1 fs. The OPLS-2005[61] all atom force field parameters were considered to describe the bonded and nonbonded potentials of this model. The nonbonded potentials correspond to the sum of a 12−6 Lennard-Jones (LJ) contribution and a Coulombic term. The crossed LJ parameters were computed by using the Lorentz−Berthelot mixing rules. The van der Waals interactions were truncated at 10 Å while the long-range electrostatic interactions were calculated using the Ewald summation method.[62] The atomic partial charges were calculated through electrostatic potential scheme using CHELPG[63] approach applied to representative fragments with PBE functional 6-311g(d,p) basis set implemented in Gaussian package.[64] The molecular fragments used for calculating the charges of 4AmPy are illustrated in Figure S6. The charges of other functional groups were kept the same as in the initial GO−CO_2H model.[44] The full set of charges are listed in Table S2. with the atom labels described in Figure S7. An illustration of the geometry optimized 4AmPy-GO model is provided in Figure 3. The resulting interlayer distance of 10 Å is in good

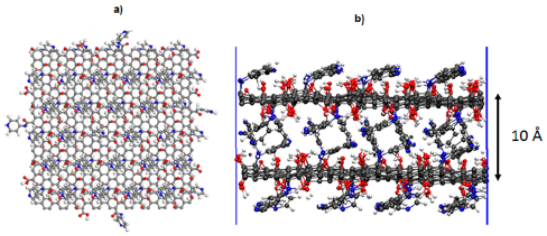

Figure 3. Geometry-optimized model for 4AmPy-GO generated by the force field based-MD simulations: (a) Top view and (b) lateral view showing the interlayer distance of 10 Å. Color scheme for GO layers: C, gray; O, red; H, white; N, blue.

agreement with the distance obtained at the DFT-level (see Figure S5, 11 Å). These observations allow the validation of the selected force field parameters and charges used to describe the 4AmPy-GO atomistic model. The relative deviation between the simulated and experimental interlayer distances deduced from the analysis of the PXRD data (13 Å) can be most probably explained by a difference between the considered distribution of the functional groups in the modeled layer and a more disordered partition of these functions in the real system.

II.2.2. Construction of ZIF-8/4AmPy-GO Composite. The 4AmPy-GO model was combined with the ZIF-8 surface[45] to create the composite using the force field-based MD computational strategy we developed and recently applied to a series of MOF/GO[44] and MOF/polymer interfaces.[43,45,47] The most stable [011] ZIF-8 surface was taken from our previous work[44,46] where the under-coordinated atoms were saturated with two types of terminations: OH groups and imidazole moieties bonded to the Zn external atoms. The dimension of the considered ZIF-8 surface model is 51 Å × 48 Å × 97 Å. 4AmPy-GO model fits well along the lengths of ZIF-8 in x and y directions, with 4AmPy-GO layers being 40 Å × 40 Å. Eight layers of 4AmPy-GO were stacked on top of each other one by one and placed along the z axis i.e., normal to the ZIF-8 model. This number of layers was chosen to exclude mutual interactions between ZIF-8 to ZIF-8 surfaces along the z axis.[43] In these calculations, all atoms of ZIF-8 were treated as charged LJ sites and the surface model was considered as

DOI: 10.1021/acs.jpcc.9b00028
J. Phys. Chem. C 2019, 123, 4984−4993

flexible in a similar way than in our previous investigation.[45] The interactions between the GOs and ZIF-8 were described by the sum of LJ potential and Coulombic terms with the crossed-interactions computed by applying the Lorentz–Berthelot mixing rules. Several sets of MD simulations were performed for equilibration. MD simulations in the NVT ensemble using the Hoover thermostat with a relaxation time of 0.5 ps were run in a sequence of temperatures (30, 100, and 298 K) each for 2 ns, with a 1 fs time step to carefully equilibrate the system followed by a 5 ns production run. An illustration of the optimized ZIF-8/4AmPy-GO composite is presented in Figure 4.

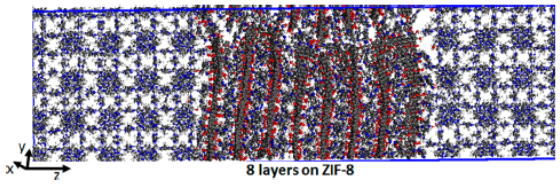

Figure 4. Illustration of the constructed ZIF-8/4AmPy-GO interface: Color scheme for GO layers follows the same color code as Figure 3. ZIF-8: C, gray; N, blue; Zn, gray; O, red; H, white.

III. RESULTS AND DISCUSSION

As a first step, the normalized atomic density for both components of the composite was calculated by scanning the system along the *z* axis, the black and red lines corresponding to 4AmPy-GO and ZIF-8, respectively.

This density profile is divided into three zones as it can be seen in Figure 5a: (i) region B corresponds to a bulk-like behavior of 4AmPy-GO (until 34 Å) where the density oscillates around an equilibrium value, and (ii) region A is the interfacial region (from 34 to 42 Å), where the equilibrated normalized atomic density of both 4AmPy-GO and ZIF-8 decreases and tends to zero. The lower and upper (~the density is zero) cross-sectional length of 4AmPy-GO and ZIF-8 is marked with a dashed orange line. The *z* length of this delimited zone, also called penetration depth, almost occupies the whole region A and corresponds to a width of about 8 Å. (iii) A third region is associated with the pure ZIF-8 bulk phase (from 33 to 130 Å). An illustration of the interfacial region A is depicted in Figure 5b. It is clearly observed that 4AmPy-GO penetrates the deep pockets of ZIF-8, forming a mesh and even twisting the ZIF-8 surface (marked with dashed orange line). This behavior deviates with what we previously observed for the pristine GO for which we had found only a partial penetration into the ZIF-8 with a corresponding depth of about 5 Å. This observation evidence that the amine functionalization of the graphene oxide affects the interlocking between the two components at the interface.

To understand the origin of such a higher penetration depth of 4AmPy-GO in the interfacial region, the preferential interactions between the two components of the composite were further explored. Radial distribution functions (RDFs) between different MOF/graphene oxide atom pairs were calculated to characterize such interactions. The [011] ZIF-8 surface contains (−OH) groups and imidazole moieties (−NH) bonded to the Zn external atoms, in an alternate fashion while the 4AmPy-GO has epoxy, hydroxyl, carboxylic, and 4AmPy at the basal plane and the edges. All these functional groups are potential interacting sites between the two components. The most relevant results are shown in Figure 6. One can observe that the shortest interacting distances imply the H atoms of $-NH_{ZIF-8}$ and the O atoms of the edged carbonyl function of 4AmPy (Figure 6a) with a mean separating distance of 2.5 Å. Similarly, the H atoms of $-OH_{ZIF-8}$ and the N atoms of the basal pyridine 4AmPy groups imply interactions with a mean characteristic distance of 3.1 Å (Figure 6b). Compared to the scenario with the pristine ZIF-8/GO[44] case where the same groups −NH and −OH of the ZIF-8 interacted uniformly with all the oxygen-containing groups of GO, i.e., epoxy, hydroxyl, and carbonyl at the edges, here we observed that the MOF/graphene oxide interactions are mostly dominated by the presence of the amine groups in 4AmPy-GO since the intensity of the corresponding RDF plots is much higher compared to that corresponding to the interactions with the other groups of the graphene oxide (see Figure 6a). This emphasizes that the

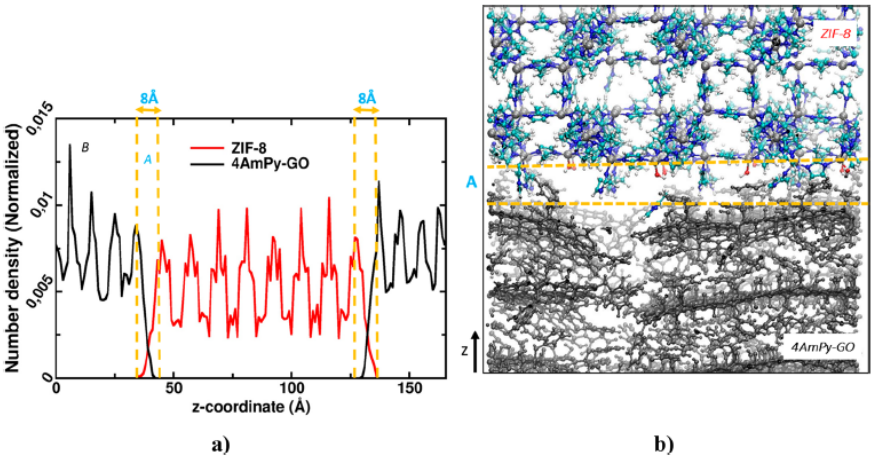

Figure 5. (a) Normalized atomic density profiles for 4AmPy-GO and ZIF-8 in the composite. (b) Representative snapshot of the resulting interface.

DOI: 10.1021/acs.jpcc.9b00028
J. Phys. Chem. C 2019, 123, 4984–4993

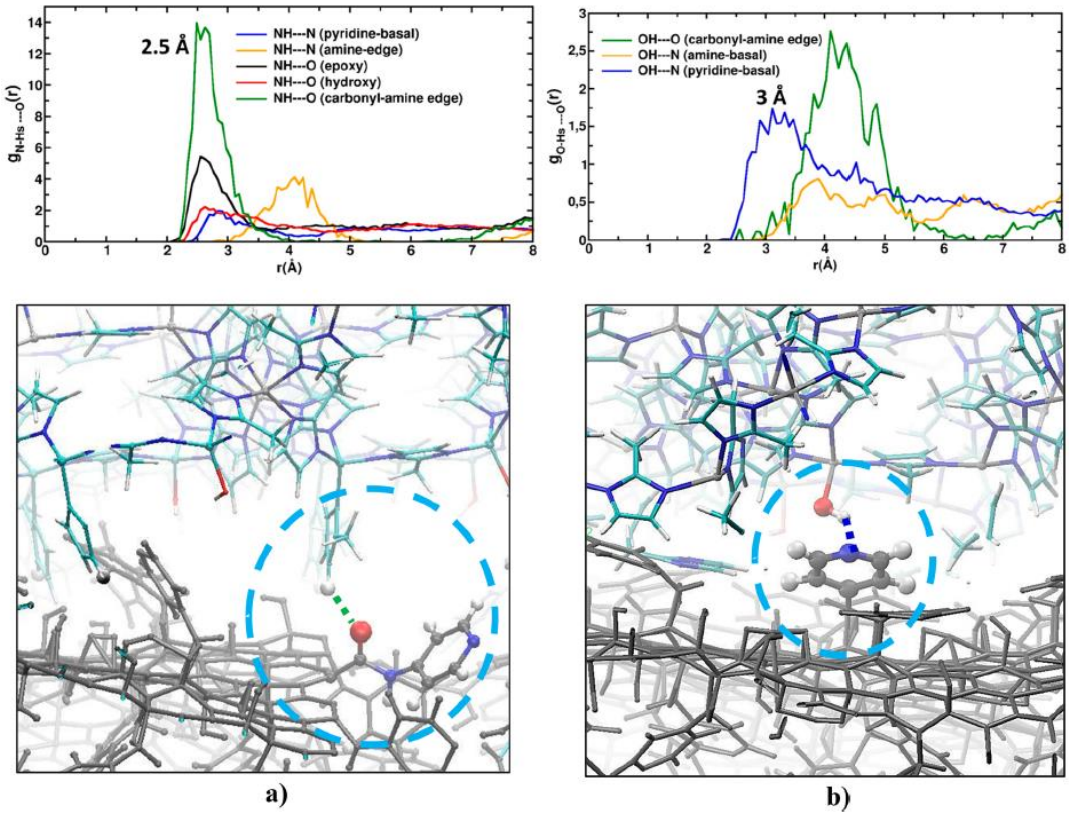

Figure 6. Radial distribution functions plotted for different ZIF-8/4AmPy-GO atom pairs above. (a) –NH (ZIF-8) and (b) –OH (ZIF-8) terminations with all the oxygen and nitrogen containing groups of 4AmPy-GO. Subsequent snapshots are shown below as illustrations. The color scheme of ZIF-8 and GOs are kept the same as in the above figures.

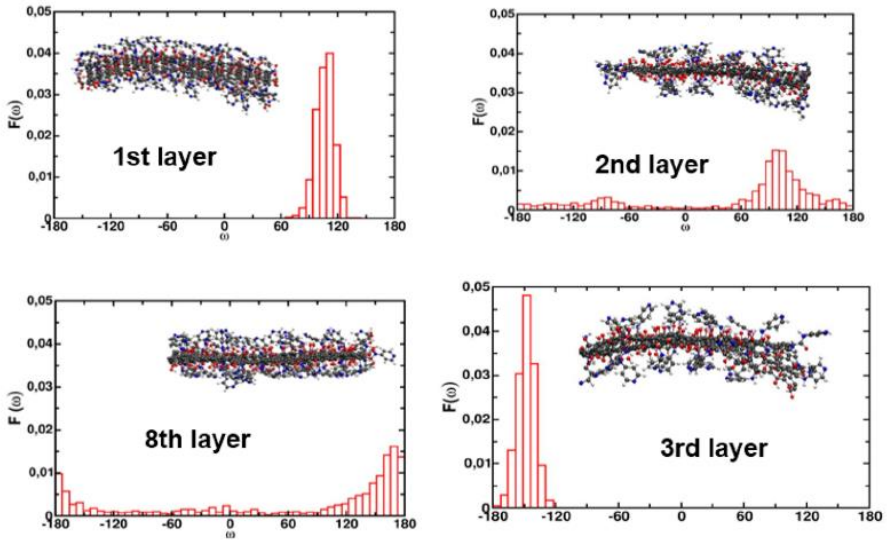

Figure 7. Dihedral angle distributions of the first, second, third, and eighth layers of 4AmPy-GO attached to the ZIF-8 surface averaged over the MD simulations.

DOI: 10.1021/acs.jpcc.9b00028
J. Phys. Chem. C 2019, 123, 4984–4993

amine functionalization contributes to enhance the interactions at the interface with the MOF, thus implying a higher MOF/graphene oxide affinity at the origin of an in-depth penetration of the 4AmPy-GO at the ZIF-8 surface.

To shed light on the local conformation of the 4AmPy-GO layers with respect to the ZIF-8 surface, their dihedral angle distributions were further analyzed. The corresponding data averaged over all the MD trajectory are reported for the first, second, third, and eighth layers, and their respective layer snapshots are presented in Figure 7. We can observe that the 4AmPy-GO layer planarity (exactly 0° to 180°) is not maintained when the graphene oxide is in close contact with the ZIF-8 surface. The geometry of the first layer is distorted as revealed by the presence of a well-pronounced distribution around 90°. This behavior is attributed to the strong interactions between −NH atoms of ZIF-8 and the 4AmPy group of the graphene oxide. One can further observe that when we move toward the eighth layer, a uniform distribution of angle is obtained; this behavior is similar to the case of a bulk layer.

Experimentally, the FT-IR spectra recorded for the 4AmPy-GO composites prepared for different containing ZIF-8 concentrations (see Figure 8) confirmed the interactions

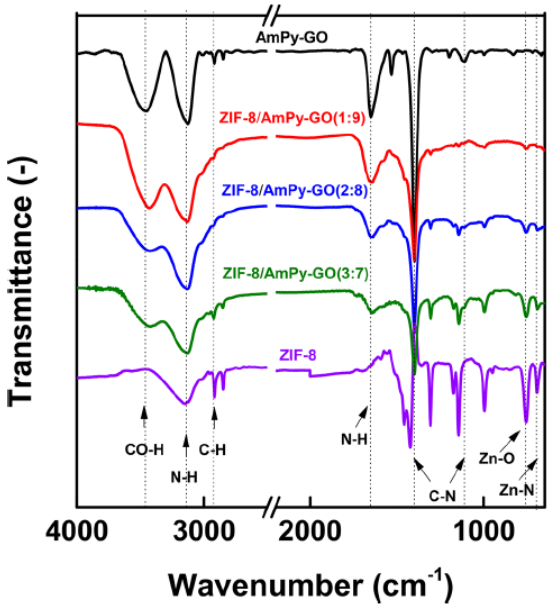

Figure 8. FT-IR spectra of the ZIF-8/4AmPy-GO composites corresponding to different contents of ZIF-8. Comparison with the data collected for the pure 4AmPy-GO.

between the ZIF-8 surface and the amine groups of 4AmPy-GO. Indeed the FT-IR spectra recorded for the composites revealed the presence of a peak at ~3200 cm^{-1} assigned to the N−H vibration mode.[52] Interestingly, the intensity of this peak decreases when the ZIF-8 concentration increases. This supports that the vibration of the N−H groups of 4AmPy-GO is gradually perturbed by the interactions with the ZIF-8 surface.

Moreover, the structure of ZIF-8/4AmPy-GO nanosheets was further explored by TEM. Figure 9 reveals that the ZIF-8

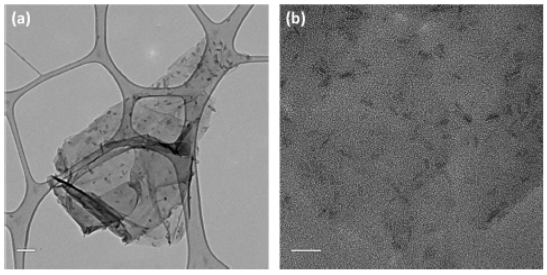

Figure 9. TEM images of ZIF-8/4AmPy-GO nanosheets. (ZIF-8:4AmPy-GO = 3:7) Scale bar = 0.2 μm (Figure 9a) and 50 nm (Figure 9b), respectively.

nanoparticles are homogeneously attached at the surface of the 4AmPy-GO nanosheet. This behavior differs with that of the pristine GO-based composite which showed aggregation of ZIF-8 nanocrystals.[50] This observation supports a better compatibility between ZIF-8 nanoparticles and the 4AmPy-GO resulting from the higher affinity between the two components as predicted by our molecular simulations.

We further explored the mechanical properties of both GOs and their composites. Figure S8 first reports the tensile stress/strain curves of the pristine GO and 4AmPy-GO obtained using a Universal Testing System (UTS). We can observe that the mechanical strength of 4AmPy-GO is enhanced compared to the pristine GO, indicating that the functionalization makes the graphene oxide more rigid and mechanically stable due to its high interaction between the layer and the 4AmPy groups. We then measured the tensile strength and calculated the Young modulus to evaluate the impact of ZIF-8 on the mechanical behavior of 4AmPy-GO. Figure S9 shows that both tensile strength and Young modulus become higher when the ZIF-8 concentration increases. Therefore, this observation evidence that the homogeneously distributed ZIF-8 particles at the 4AmPy-GO surface tends to enhance the mechanical properties of the graphene oxide.

Figure 10 reveals that the tensile strength of ZIF-8/4AmPy-GO composite is much higher than its pristine GO derivative. We also observed that the increment of its tensile strength (from 65.3 to 80.9 MPa) when ZIF-8 concentration increases is much more pronounced than for ZIF-8/pristine GO (from 39.9 to 48.8 MPa). This behavior is attributed to the relatively strong interactions between the ZIF-8 surface and the 4AmPy

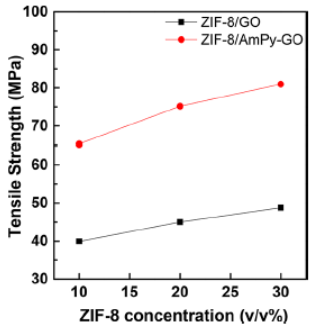

Figure 10. Tensile strength of ZIF-8/pristine GO and ZIF-8/4AmPy-GO composites containing different concentrations (v/v%) of ZIF-8.

DOI: 10.1021/acs.jpcc.9b00028
J. Phys. Chem. C 2019, 123, 4984−4993

groups attached at the graphene oxide surface as evidenced by molecular simulations and confirmed experimentally.

IV. CONCLUSION

This joint computational/experimental approach reports an unprecedented in-depth characterization of a MOF/functionalized GO composite in terms of morphology of the interface formed between the two components, their adhesion strength and the atomistic origin of their high compatibility. Force field-based Molecular Dynamics simulations built a realistic atomistic model for the 4AmPy-GO incorporating the C/N and C/O ratios deduced from the XPS analysis performed on the synthesized corresponding functionalized GO. This model was further combined with the ZIF-8 surface and a careful computational inspection of the resulting composite revealed a penetration of the functionalized GO into the pockets of the ZIF-8 which is much more pronounced than that predicted for the pristine GO derivative. This high affinity between the two components was further attributed to relatively strong interactions between the atoms at the external surface of ZIF-8 and the amine functions of 4AmPy grafted at the GO surface. Further FT-IR and TEM experiments performed on the composite confirmed this prediction revealing a homogeneous distribution of the ZIF-8 nanoparticles attached at the surface of the 4AmPy-GO nanosheets. Mechanical testing further revealed a much higher tensile strength for the ZIF-8/4AmPy-GO composite compared to its pristine GO derivative. This work unambiguously demonstrates that the GO functionalization drastically enhances the compatibility between the two components. This paves the way toward the processing of homogeneous and mechanical stable films of great importance for future applications.

■ ASSOCIATED CONTENT

Supporting Information

The Supporting Information is available free of charge on the ACS Publications website at DOI: 10.1021/acs.jpcc.9b00028.

Additional figures and tables showing DFT-optimized 4AmPy-GO models, force field parameters, and atomic charges for 4AmPy-GO layers, FTIR spectra, and PXRD, TEM and tensile plots for the ZIF-8/4AmPy-GO composite (PDF)

■ AUTHOR INFORMATION

Corresponding Authors

*(G.M.) E-mail: guillaume.maurin@univ-montp2.fr.

*(H.B.P.) E-mail: badtzhb@hanyang.ac.kr.

ORCID

Ho Bum Park: 0000-0002-8003-9698

Guillaume Maurin: 0000-0002-2096-0450

Author Contributions

#These authors contributed equally to the work

Notes

The authors declare no competing financial interest.

■ ACKNOWLEDGMENTS

The research leading to these results has received funding from the European Community H2020 (GRAMOFON GA 727619) G.M. thanks the Institut Universitaire de France for its support. The authors are thankful for the support from the Korea Research Institute of Chemical Technology grant funded by the Korean government (Ministry of Science and ICT) in 2018 (CRC-14-1-KRICT).

■ REFERENCES

(1) Wang, X.; Xing, W.; Zhang, P.; Song, L.; Yang, H.; Hu, Y. Covalent Functionalization of Graphene with Organosilane and Its Use as a Reinforcement in Epoxy Composites. *Compos. Sci. Technol.* **2012**, *72* (6), 737−743.

(2) Kochmann, S.; Hirsch, T.; Wolfbeis, O. S. Graphenes in Chemical Sensors and Biosensors. *TrAC, Trends Anal. Chem.* **2012**, *39*, 87−113.

(3) Roghani-Mamaqani, H.; Haddadi-Asl, V.; Khezri, K.; Salami-Kalajahi, M. Edge-Functionalized Graphene Nanoplatelets with Polystyrene by Atom Transfer Radical Polymerization: Grafting through Carboxyl Groups. *Polym. Int.* **2014**, *63* (11), 1912−1923.

(4) Becerril, H. A.; Mao, J.; Liu, Z.; Stoltenberg, R. M.; Bao, Z.; Chen, Y. Evaluation of Solution-Processed Reduced Graphene Oxide Films as as Transparent Conductors. *ACS Nano* **2008**, *2*, 463−470.

(5) Gómez-Navarro, C.; Weitz, R. T.; Bittner, A. M.; Scolari, M.; Mews, A.; Burghard, M.; Kern, K. Electronic Transport Properties of Individual Chemically Reduced Graphene Oxide Sheets. *Nano Lett.* **2007**, *7* (11), 3499−3503.

(6) Eda, G.; Fanchini, G.; Chhowalla, M. Large-Area Ultrathin Films of Reduced Graphene Oxide as a Transparent and Flexible Electronic Material. *Nat. Nanotechnol.* **2008**, *3* (5), 270−274.

(7) Huang, J.; Zhang, L.; Chen, B.; Ji, N.; Chen, F.; Zhang, Y.; Zhang, Z. Nanocomposites of Size-Controlled Gold Nanoparticles and Graphene Oxide: Formation and Applications in SERS and Catalysis. *Nanoscale* **2010**, *2* (12), 2733−2738.

(8) Tang, Z.; Shen, S.; Zhuang, J.; Wang, X. Noble-Metal-Promoted Three-Dimensional Macroassembly of Single-Layered Graphene Oxide. *Angew. Chem., Int. Ed.* **2010**, *49* (27), 4603−4607.

(9) Li, F.; Jiang, X.; Zhao, J.; Zhang, S. Graphene Oxide: A Promising Nanomaterial for Energy and Environmental Applications. *Nano Energy* **2015**, *16*, 488−515.

(10) Kumar, P.; Maiti, U. N.; Lee, K. E.; Kim, S. O. Rheological Properties of Graphene Oxide Liquid Crystal. *Carbon* **2014**, *80* (1), 453−461.

(11) Meng, X.; Zhu, J.; Bi, H.; Fu, Y.; Han, Q.; Wang, X. Three-Dimensional Nickel Hydroxide/Graphene Composite Hydrogels and Their Transformation to NiO/Graphene Composites for Energy Storage. *J. Mater. Chem. A* **2015**, *3* (43), 21682−21689.

(12) Huang, P. J. J.; Liu, J. DNA-Length-Dependent Fluorescence Signaling on Graphene Oxide Surface. *Small* **2012**, *8* (7), 977−983.

(13) Shen, J.; Shi, M.; Yan, B.; Ma, H.; Li, N.; Hu, Y.; Ye, M. Covalent Attaching Protein to Graphene Oxide via Diimide-Activated Amidation. *Colloids Surf., B* **2010**, *81* (2), 434−438.

(14) Huang, P. J. J.; Liu, J. Molecular Beacon Lighting up on Graphene Oxide. *Anal. Chem.* **2012**, *84* (9), 4192−4198.

(15) Huang, X.; Qi, X.; Boey, F.; Zhang, H. Graphene-Based Composites. *Chem. Soc. Rev.* **2012**, *41* (2), 666−686.

(16) Kumar, R.; Jayaramulu, K.; Maji, T. K.; Rao, C. N. R. Hybrid Nanocomposites of ZIF-8 with Graphene Oxide Exhibiting Tunable Morphology, Significant CO2 Uptake and Other Novel Properties. *Chem. Commun.* **2013**, *49* (43), 4947.

(17) Zhou, Y.; Zhou, L.; Zhang, X.; Chen, Y. Preparation of Zeolitic Imidazolate Framework-8 /Graphene Oxide Composites with Enhanced VOCs Adsorption Capacity. *Microporous Mesoporous Mater.* **2016**, *225*, 488−493.

(18) Petit, C.; Mendoza, B.; Bandosz, T. J. Hydrogen Sulfide Adsorption on MOFs and MOF/Graphite Oxide Composites. *ChemPhysChem* **2010**, *11* (17), 3678−3684.

(19) Hu, Y.; Wei, J.; Liang, Y.; Zhang, H.; Zhang, X.; Shen, W.; Wang, H. Zeolitic Imidazolate Framework/Graphene Oxide Hybrid Nanosheets as Seeds for the Growth of Ultrathin Molecular Sieving Membranes. *Angew. Chem., Int. Ed.* **2016**, *55* (6), 2048−2052.

(20) Decoste, J. B.; Peterson, G. W. Metal-Organic Frameworks for Air Purification of Toxic Chemicals. *Chem. Rev.* **2014**, *114* (11), 5695−5727.

DOI: 10.1021/acs.jpcc.9b00028
J. Phys. Chem. C 2019, 123, 4984−4993

(21) Li, W.; Zhang, Y.; Su, P.; Xu, Z.; Zhang, G.; Shen, C.; Meng, Q. Metal-Organic Framework Channelled Graphene Composite Membranes for H2/CO2 Separation. *J. Mater. Chem. A* **2016**, *4* (48), 18747−18752.
(22) Luanwuthi, S.; Krittayavathananon, A.; Srimuk, P.; Sawangphruk, M. In Situ Synthesis of Permselective Zeolitic Imidazolate Framework-8/Graphene Oxide Composites: Rotating Disk Electrode and Langmuir Adsorption Isotherm. *RSC Adv.* **2015**, *5* (58), 46617−46623.
(23) Mehek, R.; Iqbal, N.; Noor, T.; Nasir, H.; Mehmood, Y.; et al. Novel Co-MOF/Graphene Oxide Electrocatalyst for Methanol Oxidation. *Electrochim. Acta* **2017**, *255*, 195−204.
(24) Jahan, M.; Liu, Z.; Loh, K. P. A Graphene Oxide and Copper-Centered Metal Organic Framework Composite as a Tri-Functional Catalyst for HER, OER, and ORR. *Adv. Funct. Mater.* **2013**, *23* (43), 5363−5372.
(25) Yang, L.; Tang, B.; Wu, P. Metal-Organic Framework-Graphene Oxide Composites: A Facile Method to Highly Improve the Proton Conductivity of PEMs Operated under Low Humidity. *J. Mater. Chem. A* **2015**, *3* (31), 15838−15842.
(26) Liu, D.; Jin, Z.; Bi, Y. Charge Transmission Channel Construction between a MOF and RGO by Means of Co-Mo-S Modification. *Catal. Sci. Technol.* **2017**, *7*, 4478−4488.
(27) Xu, X.; Shi, W.; Li, P.; Ye, S.; Ye, C.; Ye, H.; Lu, T.; Zheng, A.; Zhu, J.; Xu, L.; Zhong, M.; Cao, X. Facile Fabrication of Three-Dimensional Graphene and Metal-Organic Framework Composites and Their Derivatives for Flexible All-Solid-State Supercapacitors. *Chem. Mater.* **2017**, *29* (14), 6058−6065.
(28) Ramaraju, B.; Li, C. H.; Prakash, S.; Chen, C. C. Metal-Organic Framework Derived Hollow Polyhedron Metal Oxide Posited Graphene Oxide for Energy Storage Applications. *Chem. Commun.* **2016**, *52* (5), 946−949.
(29) Zhang, J.; Liu, X.; Zhou, H.; Yan, X.; Liu, Y.; Yuan, A. Pt-Doped Graphene Oxide/MIL-101 Nanocomposites Exhibiting Enhanced Hydrogen Uptake at Ambient Temperature. *RSC Adv.* **2014**, *4* (55), 28908−28913.
(30) Jayaramulu, K.; Masa, J.; Tomanec, O.; Peeters, D.; Ranc, V.; Schneemann, A.; Zboril, R.; Schuhmann, W.; Fischer, R. A. Nanoporous Nitrogen-Doped Graphene Oxide/Nickel Sulfide Composite Sheets Derived from a Metal-Organic Framework as an Efficient Electrocatalyst for Hydrogen and Oxygen Evolution. *Adv. Funct. Mater.* **2017**, *27* (33), 1700451.
(31) Nancy Anna Anasthasiya, A.; Khaneja, M.; Jeyaprakash, B. G. Electronic Structure Calculations of Ammonia Adsorption on Graphene and Graphene Oxide with Epoxide and Hydroxyl Groups. *J. Electron. Mater.* **2017**, *46* (10), 5642−5656.
(32) Ebrahim, A. M.; Jagiello, J.; Bandosz, T. J. Enhanced Reactive Adsorption of H2S on Cu-BTC/S- and N-Doped GO Composites. *J. Mater. Chem. A* **2015**, *3* (15), 8194−8204.
(33) Yang, S.; Zou, Q.; Wang, T.; Zhang, L. Effects of GO and MOF@GO on the Permeation and Antifouling Properties of Cellulose Acetate Ultrafiltration Membrane. *J. Membr. Sci.* **2019**, *569*, 48−59.
(34) Dimiev, A. M.; Eigler, S. *Graphene Oxide: Fundamentals and Applications*; John Wiley & Sons, Ltd.: 2016.
(35) Zhao, Y.; Seredych, M.; Zhong, Q.; Bandosz, T. J. Aminated Graphite Oxides and Their Composites with Copper-Based Metal−organic Framework: In Search for Efficient Media for CO2 Sequestration. *RSC Adv.* **2013**, *3* (25), 9932.
(36) Zhao, Y.; Ding, H.; Zhong, Q. Synthesis and Characterization of MOF-Aminated Graphite Oxide Composites for CO2 Capture. *Appl. Surf. Sci.* **2013**, *284* (10), 138−144.
(37) Policicchio, A.; Zhao, Y.; Zhong, Q.; Agostino, R. G.; Bandosz, T. J. Cu-BTC/Aminated Graphite Oxide Composites as High-Efficiency Co2 Capture Media. *ACS Appl. Mater. Interfaces* **2014**, *6* (1), 101−108.
(38) Sadeghi, N.; Sharifnia, S.; Do, T.-O. Enhanced CO2 Photoreduction by a Graphene-Porphyrin Metal-Organic Framework under Visible Light Irradiation. *J. Mater. Chem. A* **2018**, *6* (37), 18031−18035.
(39) Senthilnathan, J.; Yoshimura, M. Low Energy Liquid Plasma for Direct Reduction and Formation of RGO-Aminopyridine Hybrid for Electrical and Environmental Applications. *J. Hazard. Mater.* **2017**, *340*, 26−35.
(40) Hoseini, S. J.; Khozestan, H. G.; Fath, R. H. Covalent Attachment of 3-(Aminomethyl)Pyridine to Graphene Oxide: A New Stabilizer for the Synthesis of a Palladium Thin Film at the Oil-Water Interface as an Effective Catalyst for the Suzuki-Miyaura Reaction. *RSC Adv.* **2015**, *5* (59), 47701−47708.
(41) Park, K. S.; Ni, Z.; Côté, A. P.; Choi, J. Y.; Huang, R.; Uribe-Romo, F. J.; Chae, H. K.; O'Keeffe, M.; Yaghi, O. M. Exceptional Chemical and Thermal Stability of Zeolitic Imidazolate Frameworks. *Proc. Natl. Acad. Sci. U. S. A.* **2006**, *103* (27), 10186−10191.
(42) Semino, R.; Durholt, J. P.; Schmid, R.; Maurin, G. Multiscale Modeling of the HKUST-1/Polyvinyl Alcohol) Interface: From an Atomistic to a Coarse Graining Approach. *J. Phys. Chem. C* **2017**, *121* (39), 21491−21496.
(43) Benzaqui, M.; Semino, R.; Menguy, N.; Carn, F.; Kundu, T.; Guigner, J. M.; McKeown, N. B.; Msayib, K. J.; Carta, M.; Malpass-Evans, R.; et al. Toward an Understanding of the Microstructure and Interfacial Properties of PIMs/ZIF-8 Mixed Matrix Membranes. *ACS Appl. Mater. Interfaces* **2016**, *8* (40), 27311−27321.
(44) Bonakala, S.; Lalitha, A.; Shin, J. E.; Moghadam, F.; Semino, R.; Park, H. B.; Maurin, G. Understanding of the Graphene Oxide/Metal-Organic Framework Interface at the Atomistic Scale. *ACS Appl. Mater. Interfaces* **2018**, *10*, 33619. See the Supporting Information.
(45) Semino, R.; Ramsahye, N. A.; Ghoufi, A.; Maurin, G. Microscopic Model of the Metal-Organic Framework/Polymer Interface: A First Step toward Understanding the Compatibility in Mixed Matrix Membranes. *ACS Appl. Mater. Interfaces* **2016**, *8* (1), 809−819.
(46) Semino, R.; Ramsahye, N. A.; Ghoufi, A.; Maurin, G. Role of MOF Surface Defects on the Microscopic Structure of MOF/Polymer Interfaces: A Computational Study of the ZIF-8/PIMs Systems. *Microporous Mesoporous Mater.* **2017**, *254*, 184−191.
(47) Semino, R.; Moreton, J. C.; Ramsahye, N. A.; Cohen, S. M.; Maurin, G. Understanding the Origins of Metal−organic Framework/Polymer Compatibility. *Chem. Sci.* **2018**, *9*, 315−324.
(48) Hummers, W. S.; Offeman, R. E. Preparation of Graphitic Oxide. *J. Am. Chem. Soc.* **1958**, *80* (6), 1339.
(49) Shin, J. E.; Kim, H. W.; Yoo, B. M.; Park, H. B. Graphene Oxide Nanosheet-Embedded Crosslinked Poly(Ethylene Oxide) Hydrogel. *J. Appl. Polym. Sci.* **2018**, *135*, 45417.
(50) Lee, H.; Park, S. C.; Roh, J. S.; Moon, G. H.; Shin, J. E.; Kang, Y. S.; Park, H. B. Metal-Organic Frameworks Grown on a Porous Planar Template with an Exceptionally High Surface Area: Promising Nanofiller Platforms for CO2 Separation. *J. Mater. Chem. A* **2017**, *5* (43), 22500−22505.
(51) Dreyer, D. R.; Todd, A. D.; Bielawski, C. W. Harnessing the Chemistry of Graphene Oxide. *Chem. Soc. Rev.* **2014**, *43* (15), 5288.
(52) Guo, Y.; Jia, Z.; Cao, M. Surface Modification of Graphene Oxide by Pyridine Derivatives for Copper(II) Adsorption from Aqueous Solutions. *J. Ind. Eng. Chem.* **2017**, *53*, 325−332.
(53) Jena, K. K.; Narayan, R.; Alhassan, S. M. Highly Branched Graphene Siloxane−polyurethane-Urea (PU-Urea) Hybrid Coatings. *Prog. Org. Coat.* **2017**, *111*, 343−353.
(54) Bagri, A.; Mattevi, C.; Acik, M.; Chabal, Y. J.; Chhowalla, M.; Shenoy, V. B. Structural Evolution during the Reduction of Chemically Derived Graphene Oxide. *Nat. Chem.* **2010**, *2* (7), 581−587.
(55) Cho, Y. H.; Kim, H. W.; Lee, H. D.; Shin, J. E.; Yoo, B. M.; Park, H. B. Water and Ion Sorption, Diffusion, and Transport in Graphene Oxide Membranes Revisited. *J. Membr. Sci.* **2017**, *544*, 425−435.
(56) Dreyer, D. R.; Park, S.; Bielawski, C. W.; Ruoff, R. S. The Chemistry of Graphene Oxide. *Chem. Soc. Rev.* **2010**, *39*, 228−240.

DOI: 10.1021/acs.jpcc.9b00028
J. Phys. Chem. C 2019, 123, 4984−4993

(57) Vandevondele, J.; Krack, M.; Mohamed, F.; Parrinello, M.; Chassaing, T.; Hutter, J. Quickstep: Fast and Accurate Density Functional Calculations Using a Mixed Gaussian and Plane Waves Approach. *Comput. Phys. Commun.* **2005**, *167* (2), 103−128.
(58) Perdew, J. P.; Burke, K.; Ernzerhof, M. Generalized Gradient Approximation Made Simple. *Phys. Rev. Lett.* **1996**, *77*, 3865−3868.
(59) Grimme, S. Semiempirical GGA-Type Density Functional Constructed with a Long-Range Dispersion Correction. *J. Comput. Chem.* **2006**, *27*, 1787−1799.
(60) Elstner, M.; Porezag, D.; Jungnickel, G.; Elsner, J.; Haugk, M.; Frauenheim, T.; Suhai, S.; Seifert, G. Self-Consistent-Charge Density-Functional Tight-Binding Method for Simulations of Complex Materials Properties. *Phys. Rev. B: Condens. Matter Mater. Phys.* **1998**, *58* (11), 7260−7268.
(61) Jorgensen, W. L.; Maxwell, D. S.; Tirado-Rives, J. Development and Testing of the OPLS All-Atom Force Field on Conformational Energetics and Properties of Organic Liquids. *J. Am. Chem. Soc.* **1996**, *118* (45), 11225−11236.
(62) Allen, M. P.; Tildesley, D. J. *Computer Simulation of Liquids* **2017**, DOI: 10.1093/oso/9780198803195.001.0001.
(63) Breneman, C. M.; Wiberg, K. B. Determining Atom-Centered Monopoles from Molecular Electrostatic Potentials. The Need for High Sampling Density in Formamide Conformational Analysis. *J. Comput. Chem.* **1990**, *11* (3), 361−373.
(64) Frisch, M. J.; Trucks, G. W.; Schlegel, H. B.; Scuseria, G. E.; Robb, M. A.; Cheeseman, J. R.; Scalmani, G.; Barone, V.; Mennucci, B.; Petersson, G. A.; et al. *Gaussian 09*, Revision B.01; Gaussian, Inc.: Wallingford, CT, 2009.

DOI: 10.1021/acs.jpcc.9b00028
J. Phys. Chem. C 2019, 123, 4984−4993

GENERAL CONCLUSIONS AND PERSPECTIVES

This work allowed an unprecedented systematic exploration of the MOF/GO interfaces at atomistic scale using an innovative computational approach integrating quantum and force field-based calculations. The considered MOFs were selected based on a preliminary experimental screening made within the EU H2020 RIA GRAMOFON project which identified a series of candidates with attractive CO_2 adsorption properties. All these MOFs are ultra-small pore MOFs with pore/gate openings of 3.0-4.0 Å which allow a selective trapping of CO_2 over N_2 by either molecular sieving or thermodynamic (interactions) effects. Two GO systems were explored, the pristine material integrating diverse oxygen containing potential active sites (GO) as well as the amine-functionalized version (FGO). The overall objective of GRAMOFON was to assemble together these MOFs and GOs materials to design multi-functional hybrid composites with high accessible surface areas, good mass transfer characteristics, and improved thermal properties leading to enhanced desorption properties when subjected to microwave irradiation, and mechanically stable materials for CO_2 capture. To aid such a development of novel composite systems, the computational strategy I devised aimed to assess the feasibility and hence stability of all these MOF/GO composites by a systematic assessment of the compatibility between their constitutive components that can be measured by their affinity at the interface they formed. In this context, quantum and force field-based modelling were coupled to first model reliable GO and FGO microscopic models based on the information gained experimentally on the prepared materials as well as MOF surface models before constructing the MOF/GO interfaces. Special attention was paid to carefully characterize these MOF/GO interfaces in terms of interacting sites, MOF surface coverage and conformational arrangement of the GO on the MOF surfaces. As a first illustration on the ZIF-8/GO composite, all oxygen functional groups on the GO layers were shown to interact strongly with the terminal -NH groups of the imidazole and –OH molecules of the inorganic node of ZIF-8 surface. In particular, the involvement of the $–CO_2H$ groups present at the edge of GO led to strong distortions at the interfacial region close to the MOF surface. These predictions were further supported by complementary experimental data, i.e. TEM images and Mechanical strength measurements which confirmed the relatively high affinity between GO nanosheets and ZIF-8 nanoparticles.

This computational strategy was further applied to systematically explore the effect of nature of the MOFs on the MOF/GO compatibility. Regarding MIL-69(Al)/GO, two different facets of MIL-69(Al) were combined with GOs. A rod-like growth mechanism of 1D MIL-69(Al) due to GO layer was unravelled in excellent agreement with experiments. It was exhibited that the GOs interacts strongly with (010) surface than (001) surface of MIL-69(Al) by forming strong bonds

between its hydroxyl and carboxyl functions with MOF surface atoms reinforcing π−π like interactions. These results motivated self-scrolling of GO sheets followed by an anisotropic crystal growth of MIL-69(Al) along [001] direction. In MIL-91(Ti)/GO, the main interactions at the interface leading to high interfacial properties were showcased. The oxygen functional groups of the GO improve the contacting area with the MOF through the favourable hydrogen bonding. In general, it was observed that the carboxyl groups at the edge of GOs play a key role in the compatibility of these composites.

As a further step, a microscopic model of the amine functionalized GO (FGO) was constructed and combined with ZIF-8 surface model to provide an in-depth characterization of the resulting interface. It was demonstrated that FGO penetrates the deep pockets of ZIF-8 due to strong interactions between the surface atoms of ZIF-8 surface and the amine functions of 4AmPy grafted onto the GO surface. This higher degree of affinity was well supported by FTIR, TEM and mechanical testing experiments.

Finally, to get a precise microscopic description of the adsorption phenomena in the MOF/GO composites, i.e. on ZIF-8/GO and ZIF-8/FGO, Monte Carlo simulations were conducted to predict their CO_2 adsorption and separation performances. Through these simulations, adsorption properties of CO_2, CH_4 and N_2 gases in terms of affinity and gas uptake as well as in terms of preferential sites were defined. Both GO/ZIF-8 and FGO/ZIF-8 show moderate adsorption selectivity for CO_2 compared to other gases. It was demonstrated that the amine functional groups of FGO tend to increase CO_2 uptake capacity while maintaining similar CO_2 selectivity.

The so-developed multi-scale methodology represents a roadmap to study a wide range of MOF/GO systems to design composites with even higher compatibility. This study paves way for the development of several mixed matrix membranes in near future provided that adequate all-atom force field parameters are available for such systems and to further control the feasibility of these advanced MMMs. An extension of this work will be to simulate the permeability properties of these MOF/GO composites using a combination of Monte Carlo and Molecular Dynamics simulation tools.

Even though these atomistic simulations on MOF/GO systems lead to valuable insights, some relevant properties still cannot be computed due to system size restrictions like mechanism of aggregation of MOF nanoparticles in a GO matrix. A possible way to bridge this gap is to use Coarse-Graining (CG) molecular simulations. In CG as compared to all-atom (AA) based

simulations, the number of degrees of freedom is greatly reduced enhancing computational efficiency. As a result, an increase of orders of magnitude in the simulated time and length scales can be achieved. The basic principle of the CG approach is to group several atoms into a single interacting site called "bead". This implies discarding certain degrees of freedom from the model system, but care should be taken to reproduce the dynamic properties of the target systems. Future directions of this work will be to implement CG strategy to study full MOF nanoparticles embedded in the GO matrix in order to shed light on important phenomena such as aggregation, also widen the application areas by adding surfactants/capping agents or varying the reaction solutions for these technologically promising composites.

Abstract

Recently, most of the research attention has been focused on controlling global warming resulting from the emission of greenhouse gases. The advantage of developing adsorbents for physisorption-based CO_2 capture resides in the reduction of energy penalty and easier recyclability. Composite systems (MOF/GO) made from the assembly of graphene oxide (GO) with Metal organic frameworks (MOFs) together with tailored functionalities have been recently revealed as promising candidates to selectively adsorb CO_2 over diverse gases including N_2 and CH_4. In this PhD, an innovative computational methodology integrating density functional theory calculations and force field-based molecular dynamics simulation has been applied to provide a first atomistic picture of the interactions at the MOF/GO interface with the main objective to characterize the nature of the interactions between the two components, the surface coverage, the GO conformation that all together are expected to play a key role in the compatibility of the composite. As a first step, a careful attention has been paid to develop a structural model for the GO containing –hydroxyl, -epoxy and –carboxylic groups consistent with the experimental observation on the C/O ratios. As a proof of concept, the zinc-based zeolite imidazole framework ZIF-8 has been considered and its MOF surface model has been taken from our previous work. The MOF/GO interface has been further built and detailed analysis of the MOF/GO interfaces has been generated. A systematic computational exploration of the impact of the nature of the MOFs as well as of the functionalization of GO has been further deployed. Subsequently, the adsorption and separation performances were modelled for these MOF/GO systems using Monte Carlo simulations. These computational findings were supported by experimental data collected within the frame of the H2020 EU GRAMOFON and paves way towards a more rationale development of mixed matrix membranes.

Keywords: Molecular Simulations, Force Field, Molecular Dynamics, Monte Carlo, graphene oxide, metal-organic frameworks, mixed matrix membranes, composites, interfaces, CO_2 capture.

Résumé

La problématique du réchauffement de la planète causé par l'émission de gaz à effet de serre est actuellement un enjeu sociétal majeur. La capture de CO_2 par l'utilisation de matériaux poreux apparait comme une solution viable. Des composites construits à partir de l'assemblage d'oxyde de graphène (GO) et de matériaux hybrides poreux de type MOFs ont récemment été proposés comme des candidats prometteurs pour l'adsorption sélective du CO_2 vis-à-vis d'autres gaz, comme N_2 et CH_4. Dans cette thèse, une attention particulière a été portée à la construction de modèles structuraux pour le GO incorporant différentes fonctionnalités chimiques. Une méthodologie computationnelle innovante intégrant des approches quantiques et classiques (Dynamique Moléculaire) a été ensuite mise en œuvre pour construire des modèles microscopiques des composites MOF/GO et caractériser leurs interfaces en termes de taux de recouvrement, nature des sites d'interaction et déformation du GO, des paramètres qui jouent un rôle majeur dans la compatibilité du composite. Cette étude a été menée de façon systématique en faisant varier la nature à la fois du MOF et de la fonctionnalisation du GO. Par la suite, les performances de séparation de ces systèmes ont été modélisées à l'aide de simulations Monte Carlo. Cet effort computationnel a été mené en lien étroit avec des données expérimentales issues de différentes collaborations au sein du projet H2020 EU GRAMOFON. Les conclusions de cette thèse ouvrent la voie à un développement plus rationnel des membranes à matrice mixte MOF/GO.

Mots-clés : Simulations moléculaires, Champs de force, Dynamique Moléculaire, Monte Carlo, Oxyde de Graphène, Matériaux hybride poreux, MOFs, Composites, Membranes mixtes. Interfaces, Capture CO_2.